A Thesis Submitted for the Degree of PhD at the University of Warwick

The properties of cool DZ white dwarfs

by

Mark A. Hollands

Thesis

Submitted to the University of Warwick

for the degree of

Doctor of Philosophy

Department of Physics

September 2017

THE UNIVERSITY OF
WARWICK

Contents

Declarations

I submit this thesis to the University of Warwick graduate school for the degree of Doctor of Philosophy. This thesis has been composed by myself and has not been submitted for a degree at another University.

An appreciable quantity of thesis includes material from published/submitted papers written by myself which are detailed below

- Hollands et al. (2015), *The incidence of magnetic fields in cool DZ white dwarfs.* Chapter 6 makes use of material from this work.
- Hollands et al. (2017), *Cool DZ white dwarfs - I. Identification and spectral analysis.* Chapter 3 includes material from this publication.
- Hollands et al. (submitted 2017), *Cool DZ white dwarfs - II. Compositions and evolution of old remnant planetary systems.* Chapters 4 and 5 include material from this recently submitted paper. While not yet published, this paper is included here in the event that it is accepted before the assessment of this thesis.

In addition, the introduction and conclusions make use of material from all three of these papers.

The work presented herein was carried out by myself with one exception in Chapter 3. Section 3.3 is based on calculations performed by Vadim Alekseev, and was written by Vadim Alekseev and Detlev Koester. This section was originally part of Hollands et al. (2017) and is kept here for a complete description of the model atmospheres used in this work and the improvements in physics that made this thesis possible.

Abstract

Over the last few decades it has become clear that metals present within the atmospheres of more than one quarter of white dwarfs signify recent accretion of minor bodies from their planetary systems. Spectral analysis of these metal-polluted white dwarfs allows determination of the accreted body composition, providing the most direct method for measuring the makeup of exoplanetary material. So far, most detailed abundance analyses have mostly been limited to a few systems at a time.

In this thesis, I present a sample of 231 cool DZ white dwarfs identified from SDSS spectroscopy. These stars exhibit strong metal lines from multiple elements, permitting detailed abundance analyses of each. Furthermore their low effective temperatures of 9000–4400 K imply corresponding cooling ages of 1–8 Gyr, allowing me to examine some of the oldest planetary systems in orbit of stellar remnants.

Across the sample, I found a huge diversity in the metal abundance ratios, with Fe/Ca varying by a factor 100. I developed a simple method for interpreting the rocky geology of the accreted parent bodies, indicating that some were composed of $> 80\,\%$ crust material, and with $> 80\,\%$ core material for others. Using the calculated white dwarf ages, I identified a downwards trend of the highest levels of metal pollution for the oldest systems, suggesting their mass reservoirs of exoplanetesimals become depleted on a $\simeq 1$ Gyr time scale.

Finally, Zeeman split metal lines are found in the spectra of 33 of these systems, with surface magnetic fields in the range 0.25–30 MG. Investigation of this rare combination of metals and magnetism has consequences for the formation of white dwarf magnetic fields, and motivates new research in atomic physics.

Chapter 1

Introduction

White dwarfs are the final states for almost all stars, and as this thesis aims to demonstrate, are some of the most interesting astrophysical objects, owing to their extreme physical properties, which have led to research in many areas of astronomy as well as fundamental physics. While in many ways simple objects, in some sense it is their simplicity that make white dwarfs attractive objects to study, as they can be modeled to high level of accuracy. It is then the deviations from the simplest cases that allow us to increase our knowledge, for example: exotic atmospheric chemistry, stellar pulsations, or magnetic fields.

1.1 A brief history of white dwarfs

To have the most basic understanding of what a white dwarf is, requires at least some knowledge of quantum mechanics. However, the first white dwarf stars were identified more than a century before the wave of discovery leading to the theory of quantum mechanics. Unsurprisingly these objects remained enigmatic until the theoretical machinery required to understand their peculiar properties was available.

The first white dwarf to be identified, 40 Eridani B (Herschel, 1785), was found as a binary companion to the K-type main sequence star, 40 Eridani A (a third, C component, a faint M-dwarf, was discovered later). Within a Hertzsprung-Russel diagram it became clear that 40 Eri B was extremely faint for its colour (Hertzsprung, 1915), and spectroscopy revealed it to have an A-type spectrum, despite its K-type companion being much brighter (Lindblad, 1922). Via the Stefan-Boltzmann law, these observations suggested a tiny radius and hence a density orders magnitude greater than anything previously encountered in nature.

A faint companion to the F-type star Procyon, had been suspected by Bessel

(1844), due to variability in its proper-motion. The white dwarf companion, Procyon B, was identified half a century later by Schaeberle (1896). This discovery letter is a mere four sentences in length, and with the opening line "This morning I discovered a companion to Procyon", demonstrates how much the scientific process has changed in a single century. This star is much cooler than 40 Eri B, at $\simeq 8000\,\mathrm{K}$, but again a small radius was needed to explain the relative brightnesses of Procyon and Procyon B.

The nearest, and arguably most famous white dwarf, Sirius B, was again inferred astrometrically by Bessel (1844), and accidentally discovered by Alvan Graham Clark in 1862 (Holberg & Wesemael, 2007). After the faint companion to Sirius was observed spectroscopically (Adams, 1915), an astounding discovery was made. Although Sirius B is 10 magnitudes fainter than Sirius A, both have A-type spectra, again implying a small radius. Furthermore, astrometry had already revealed Sirius to have a mass close to $1\,\mathrm{M}_{\odot}$– only half that of the primary star. Comparing the mass of Sirius B with those of 40 Eri B and Procyon B, shows another odd property of white dwarfs: despite being roughly twice as massive as the other two stars, Sirius B is physically smaller, and thus has an order of magnitude larger density. This is of course contrary to both main-sequence stars, and our everyday experience that an objects size is positively correlated with its mass (described in more detail in Section 1.2).

The final member of the 'classical white dwarfs' is van Maanen's star or vMa2 (van Maanen, 1917). This star has a few interesting properties that separate it from the others. Firstly, note that unlike the previous three objects, vMa2 is *not* followed by a B, i.e. it is not a member of a multiple system. It is a single star, and holds the records for the first known and closest of the isolated white dwarfs. vMa2 piqued the interest of van Maanen due to its extreme proper-motion of three arcseconds per year, despite its relatively faint apparent magnitude of 12.3 (van Maanen, 1917). Surprisingly, the spectrum obtained by van Maanen (1917) showed an early F-type spectrum due to the presence of several strong metal lines – the significance of these metallic features was not understood for many decades, however it is now recognised that these lines are in fact the first observational data containing the signature of an extrasolar planetary system (Zuckerman, 2015; Farihi, 2016). A complete explanation of how this star fits into the picture of extrasolar planetary systems is given in Section 1.5. Several years after the original observations of vMa2, van Maanen (1920) obtained a parallax of $246 \pm 6\,\mathrm{mas}$ indicating vMa2 was only about $4\,\mathrm{pc}$ away, making vMa2 "by far the faintest F-type star known". It was soon realised that this star too belonged to the same class of "faint white stars" populated by the companions to Sirius, Procyon, and 40 Eri (Luyten, 1922a).

In the following years, many more of these high proper-motion, faint white stars were discovered (e.g. Luyten, 1922b,c), which due to their inferred small sizes, came to be known as white dwarfs. It was clear from their inferred densities that these stars were separate to the more commonly observed “ordinary” stars (Milne, 1931c). However, until the mid-1920s, an explanation for the properties of white dwarfs remained out of reach.

1.2 White dwarf structure

The extreme pressures and temperatures expected in dense white dwarf interiors indicated they should be composed of a fully ionised plasma (Saha, 1920; Eddington, 1926). With the simultaneous development of atomic theory and quantum mechanics, it became clear that the white dwarf interiors, unlike ‘normal’ stars, could not be modelled as classical ideal-gases (Eddington, 1926). Fowler (1926) applied the newly developed Fermi-Dirac statistics (Fermi, 1926; Dirac, 1926) to the electrons in white dwarf interiors, resolving how material could exist in such a dense state. At these densities, the average separation between electrons is shorter than their thermal de-Broglie wavelength, and so the electron gas becomes *degenerate*. The electrons are then forced to occupy the lowest available energy states in both physical- and momentum-space. From this Fowler (1926) explained that the apparent force required to oppose gravitational collapse arose from statistical means. By reducing the available volume, and hence the available states in physical-space, electrons would be forced into higher momentum-states. The high-momentum of these spacially confined electrons thus manifests itself as a pressure, balancing further gravitational collapse. While white dwarf interiors are generally considered to be “hot”, the average thermal energy per electron is much lower than the Fermi-energy, and thus the degenerate electron gas can be modeled as being at zero temperature.

Further development along these lines explained that as more mass is added to a white dwarf a greater deal of pressure is required to oppose gravitational collapse. To provide the increased degeneracy pressure the star therefore decreases in radius, forcing the electrons into the necessary higher momentum states.

Because the internal pressure of a white dwarf is dominated by electron degeneracy, which depends on the density, and in turn is set by the stellar mass, the equilibrium radius is largely independent of the temperature. Thus, as white dwarfs radiate their internal energy, to first approximation, they maintain a constant radius.

1.2.1 Mass limit

The late 1920s and early 1930s saw rapid development in the field of stellar structure, with a considerable amount of work devoted to polytropic gas-spheres (e.g. Russell, 1931; Milne, 1931b,a) with an equation of state given by

$$P \propto \rho^{1+1/n}, \tag{1.1}$$

where P is the pressure, ρ is the density and n is the polytropic-index. Following Stoner (1930) noting that the electrons interior to white dwarfs must become relativistic, Chandrasekhar (1931b) considered the equation of state for a white dwarf as composite polytropes for relativistic ($n = 3$) and non-relativistic ($n = 3/2$) electron-degenerate gases. This soon led Chandrasekhar to the conclusion that white dwarfs should have a maximum mass, which in the fully degenerate relativistic case, was found to be $0.91\,\mathrm{M}_\odot$(Chandrasekhar, 1931a). This limiting mass corresponded to the extreme of a radius tending to zero.

Of course, we now know that this mass limit should be somewhat higher. Later, Chandrasekhar (1935) presented full calculations for the white dwarf mass-radius relationship with the mass-limit in units of M_3 as shown in Fig. 1.1. A formula is given for the limiting-mass as

$$M_3 = 5.728\,\mathrm{M}_\odot/\mu^2, \tag{1.2}$$

where the mass subscript denotes the polytropic index $n = 3$, and μ is the ratio of nucleons to electrons in the white dwarf interior. Although the internal composition of white dwarfs was not known at the time, substituting $\mu = 2$ for a fully ionised C/O mixture,[1] results in a mass-limit of $1.43\,\mathrm{M}_\odot$, close to the present-day accepted value, and now lovingly known as the Chandrasekhar mass. Some additional refinements were made by Chandrasekhar (1939) considering the effects of electron degeneracy at finite temperature. The derivation of white dwarf structure would eventually contribute to Chandrasekhar being awarded the 1983 Nobel prize in Physics, along with Fowler.

Although the many decades since Chandrasekhar's derivation have seen vast improvements in our understanding of white dwarf physics, the improvements to the mass-radius relation have only led to minor modifications, with the Chandrasekhar mass only minimally changed over the years (e.g. Hamada & Salpeter, 1961).

---

[1] Chandrasekhar's original $0.91\mathrm{M}_\odot$ mass-limit resulted from assuming $\mu = 2.5$.

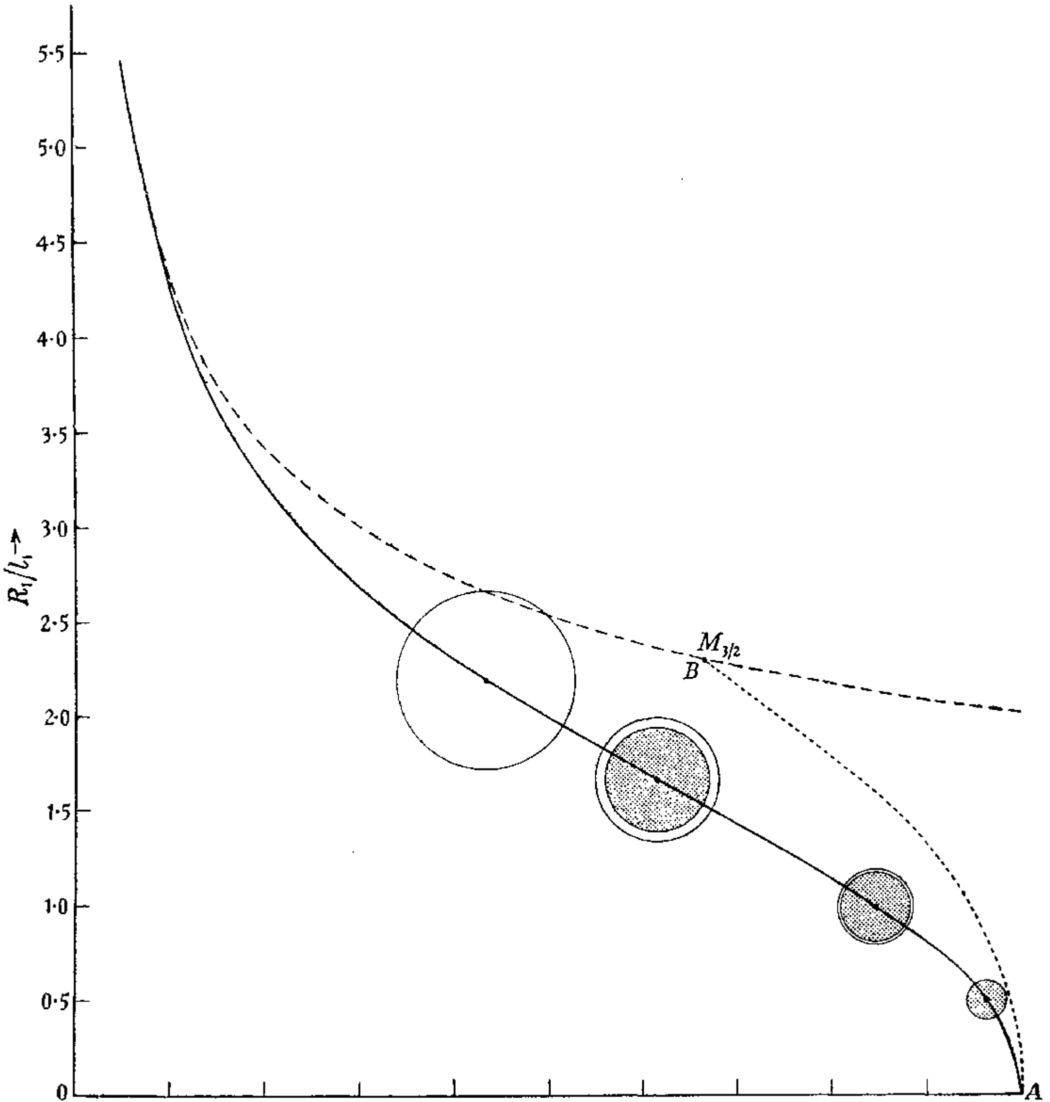

Figure 1.1: The white dwarf mass-radius relation as first presented by Chandrasekhar (1935). The dotted and dashed lines correspond to non-relativistic and fully relativistic polytropes respectively. The dotted solid line considers the increasing effects of relativity as the white dwarf mass is increased.

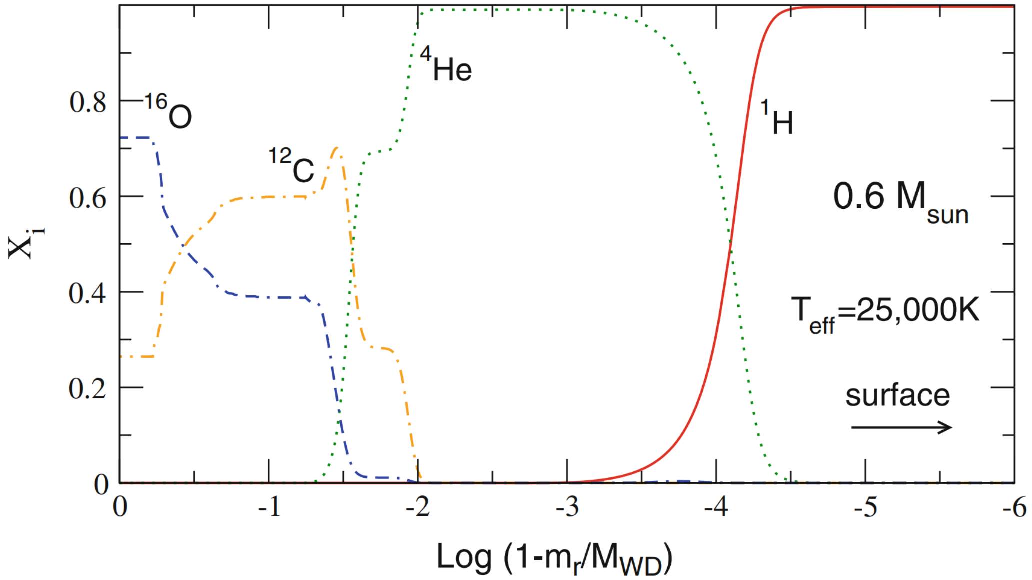

Figure 1.2: Chemical stratification of a carbon-oxygen white dwarf with a hydrogen dominated atmosphere. Almost all of the mass is contained within carbon and oxygen, with helium contributing about 1 % of the total mass, and hydrogen only one part in 10^4. Original figure from Althaus et al. (2010).

1.2.2 Internal composition

White dwarfs are the product of the stellar evolution for stars with $M < 8\,\mathrm{M}_\odot$. Once the progenitor stars reach the red giant branch, the temperature and pressure within their cores become sufficiently high to ignite burning helium. This helium, the product of hydrogen burning during the main-sequence, is transmuted into carbon via the triple-alpha process. Additional burning of carbon with another helium nucleus results in the formation of oxygen (Herwig, 2013). For initial masses closer to $8\,\mathrm{M}_\odot$, the production of Mg and Ne also occurs.

For most white dwarfs the result of stellar evolution is thus a core of carbon and oxygen surrounded by a thin layer of helium and an even thinner layer of hydrogen (Althaus et al., 2010) as depicted in Fig. 1.2. For approximately one quarter of white dwarfs, a very late thermal pulse can move a newly formed white dwarf back to the asymptotic giant branch (AGB), where the remaining hydrogen is burned, resulting in a stellar remnant with a helium atmosphere (Koester, 2013). Due to the strong gravitational fields of white dwarfs, the heavy elements settle towards the core, with light elements at the surface (Schatzman, 1949).

1.2.3 Convection and diffusion

Two physical processes that are important to understand in the context of this thesis are convection and diffusion. Schatzman (1949) described that for a hydrogen atmosphere in radiative equilibrium, heavy elements should sink below the photosphere extremely quickly. This gave a natural explanation to white dwarfs with pure hydrogen atmospheres , but left questions on the metal-rich atmosphere of vMa2. However, Schatzman (1949) was quick to point out that convection would severely impede the efficiency of gravitational diffusion. While convection would keep heavy elements mixed in the outer envelope, diffusion at the base of the convection zone would still lead to the eventual depletion of metals.

It was since found that cool white dwarfs develop convection zones in their outer helium envelopes (e.g. Böhm, 1968; Böhm & Cassinelli, 1970). For helium atmosphere white dwarfs, these convection zones thus extend to the surface of the star (Fontaine & van Horn, 1976). Calculations by Vauclair et al. (1979) showed that even with the impeded rate of gravitational settling in these cool helium atmosphere white dwarfs, accretion of some outside source of matter would be needed to explain the presence of metals in their atmospheres. While the conventional wisdom was that gravitational settling timescales were essentially dependent on atomic weights, Paquette et al. (1986a,b) showed this was not strictly true. They showed that ions of moderately different masses could diffuse at similar rates, with their calculations accounting for plasma screening effects needed within the white dwarf envelopes. While calculated diffusion rates have improved since, the work by Paquette et al. (1986a,b) is considered a major milestone in understanding the physics affecting the diffusion of metals out of the bases of white dwarf convection zones (Fontaine et al., 2015).

More recent calculations of convection zone sizes and diffusion timescales using the diffusion model of Paquette et al. (1986a,b) are given by Koester (2009). To demonstrate the differences between diffusion within hydrogen and helium dominated atmospheres, the sinking timescales of Fe as functions of T_{eff} are shown in Fig. 1.3 (for $\log g = 8$). The figure demonstrates that for hydrogen atmospheres, the timescales can be on the order of days, and thus detecting metals is only possible for such white dwarfs that are actively accreting. For helium atmosphere white dwarfs, these timescales instead reach millions of years in the coolest objects. However at these T_{eff}, the stars have already been cooling for $\gtrsim 1\,\mathrm{Gyr}$, and so the diffusion timescales remain relatively short compared with the white dwarf age. For white dwarfs with helium dominated atmospheres, the convection zone masses reach $\simeq 10^{-5}$ of the total white dwarf mass, calculated at $\log g = 8$. While certainly constituting a large volume when accreted metals are mixed throughout, recall from Fig. 1.2 that the helium layer constitutes about 1 % of the stellar mass. Thus, at their most sizeable the extent of the convection zones for white dwarfs with pure hydrogen/helium atmospheres, are still far from reaching the carbon/oxygen core[2].

1.3 White dwarf cooling

One of the most remarkable properties of white dwarfs is their predictable rate of cooling. This is because white dwarfs do not generate any new heat through nuclear processes. Instead the bulk of a white dwarf is an isothermal sphere of electron-degenerate carbon and oxygen[3] due to the very high thermal conductivity of the degenerate matter. The hot interior is in effect a large reservoir of thermal energy surrounded by non-degenerate layers at the surface which slowly radiate away this finite amount of heat.

Mestel (1952) was the first to develop a white dwarf cooling model finding a power law dependence between the age and stellar luminosity,

$$t_{\mathrm{cool}} \propto {L_{\mathrm{wd}}}^{-5/7}. \tag{1.3}$$

Consequently, Schmidt (1959), recognised that white dwarfs could be used as cosmochronometers in his attempts to estimate the local star formation history. Later, Winget et al. (1987) established that white dwarfs could be used to estimate the age of the Galactic disc, and in turn the age of the Universe. This is because the white dwarf luminosity distribution was found to steadily increase towards the faintest objects, but then discontinuously drop to zero $L_{\mathrm{wd}} \sim 10^{-4}\,\mathrm{L}_{\odot}$ (Liebert et al., 1988). This was naturally explained if the white dwarfs near this luminosity-cutoff had descended from the first stars formed within the disc of the Milky Way.

Since the first cooling model by Mestel (1952), continuous improvements in accuracy have been made by incorporating important physical processes that affect the cooling rate. van Horn (1971) described two important improvements to this cooling model. Firstly, thermal energy could be carried away from the white dwarf interior via neutrino+antineutrino pair production. Secondly, Salpeter (1961) had shown that in the interiors of cool white dwarfs, the ions will form a crystal lattice. Thus at the stage of crystallisation, the associated latent heat will impede white dwarf cooling until the core has fully crystallised.

---

[2] White dwarfs with atmospheric carbon dredged up from the core are discussed in section 1.4.1.

[3] For white dwarfs formed from progenitor stars close to $8\,\mathrm{M}_{\odot}$, other possibilities such as O/Mg/Ne cores are also possible, but are far less common.

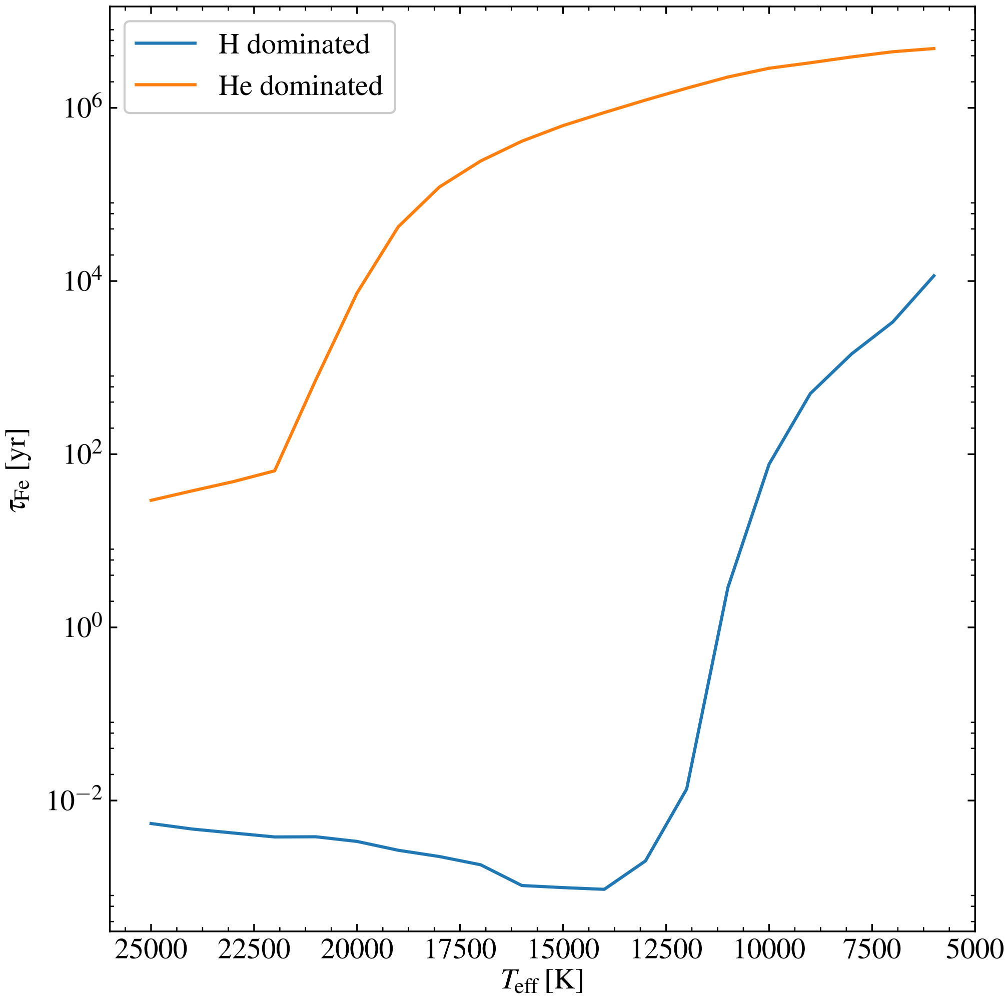

Figure 1.3: Diffusion timescales of Fe are shown for both white dwarfs with hydrogen and helium dominated atmospheres as a function of T_{eff} and with $\log g = 8$. It is clear that sinking timescales for helium atmospheres are always several orders of magnitude longer than compared with hydrogen atmospheres of the same temperature. Data are the most recent versions of those presented by Koester (2009).

Cooling models continue to rise in sophistication and therefore accuracy, and now include important physical effects of, for instance, atmospheric composition, and surface-core coupling via convection (Fontaine et al., 2001). The most up to date cooling models are thought to be accurate to about 2 % (Salaris et al., 2013). However, to improve precision T_{eff} and white dwarf masses are required. In the impending era of Gaia[4], the precise white dwarf masses that will be inferred from stellar parallaxes is expected to result in great advancements in white dwarf cosmochronology. In Chapter 5 I take advantage of white dwarf cooling models to estimate the ages of the DZ white dwarfs we identify, and therefore explore the evolution of remnant planetary systems over time.

1.4 White dwarf atmospheres and spectra

The photons detected in an astrophysical spectrum carry information on the physical conditions from which they were emitted. For stars, photons emanate from the outermost layers, i.e. the photosphere. With a sufficiently complete understanding of the physical processes that result in an observed spectrum, models can be constructed to infer the physical conditions within the stellar atmosphere. This is absolutely the case for white dwarfs, and so in this thesis I use detailed models (developed by Detlev Koester) to interpret properties of many white dwarfs.

1.4.1 Spectral classification

Photometrically, white dwarfs appear as faint blue or white points of light, allowing little more than the T_{eff} to be estimated. However, white dwarfs with similar photometry may have very different spectra, and generally fall into just a few categories. While a classification scheme for white dwarfs had emerged following their discovery, Sion et al. (1983) streamlined white dwarf spectral classification (in the optical, 3000-10000 Å) resulting in the system that is used today. All white dwarf spectral classifications are preceded with the letter "D", denoting a degenerate object. The primary white dwarf categories are DA, DB, DO, DC, DQ, and DZ.

The DAs are characterised by spectra consisting of only H I lines, and are the most commonly encountered white dwarfs. Their naming comes from their resemblance to the spectra of A-type stars.

The DBs are the next most commonly encountered spectral type, so-called

---

[4] Gaia is an ongoing space-mission performing precision astrometry. The much anticipated second data-release (DR2) is scheduled for April 2018, and is expected to contain 5-parameter astrometric solutions for ~ 1 billion stars.

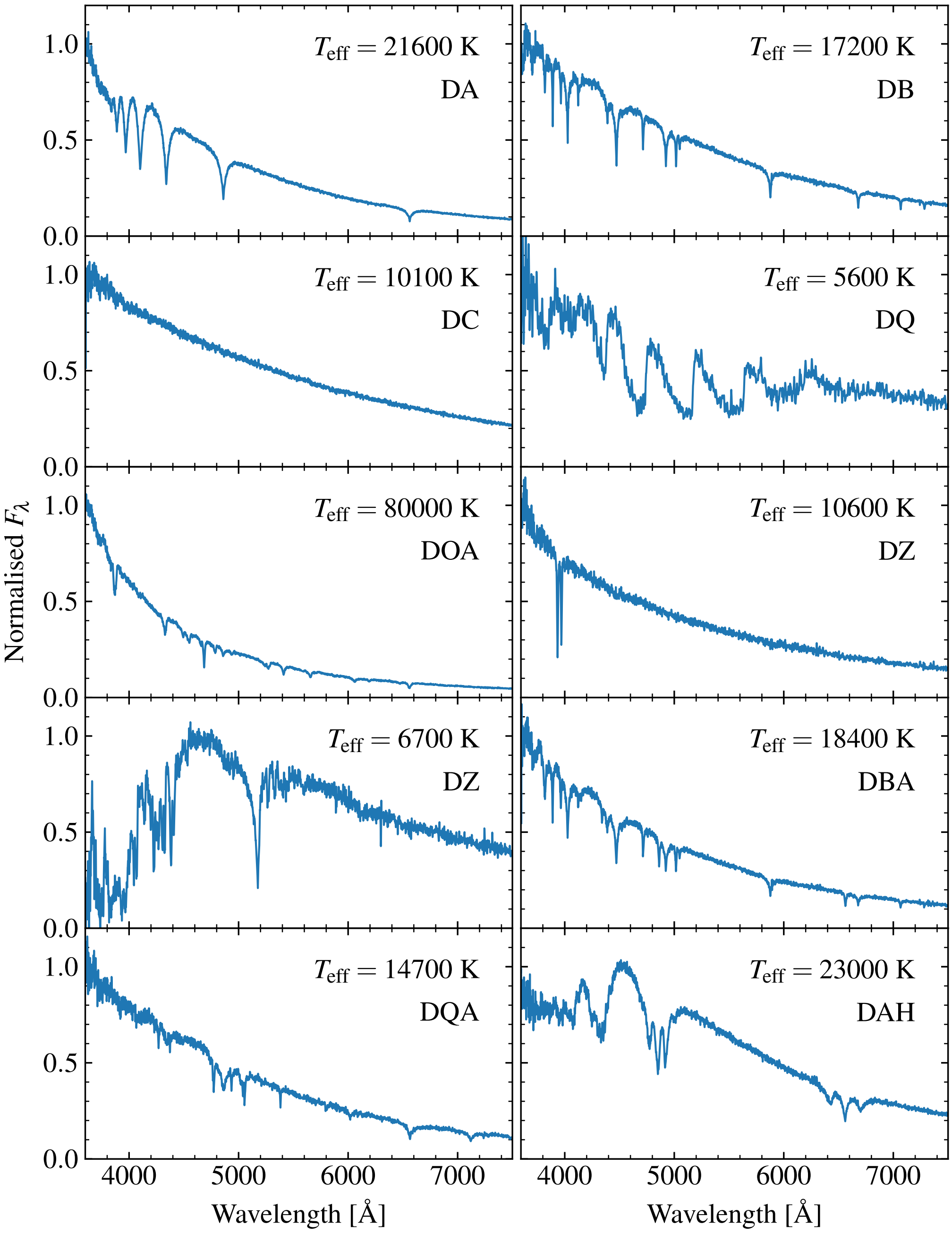

Figure 1.4: White dwarf spectra are seen to vary wildly with spectral type and $T_{\rm eff}$. The data are from SDSS, with classifications and $T_{\rm eff}$ measurements from Kepler et al. (2015).

due to their resemblance to B-type main-sequence stars. This is because their spectra exhibit He I lines.

DC white dwarfs do not show absorption lines of any type, where the "C" indicates a continuum spectrum. There can be a variety of reasons for this. When DAs cool below $T_{\mathrm{eff}} \simeq 6000\,\mathrm{K}$, hydrogen lines vanish, and so DAs transition to DCs at this T_{eff}. For DBs, this transition occurs at $\simeq 11000\,\mathrm{K}$, and so DCs with $T_{\mathrm{eff}} \simeq 6000$–$11\,000\,\mathrm{K}$ have helium dominated atmospheres, whereas those below 6000 K can have atmospheres dominated by either hydrogen or helium. Finally, hotter DC white dwarfs can exist if an extremely strong magnetic field $B_{\mathrm{S}} > 100\,\mathrm{MG}$ is present, as the magnetic field geometry causes spectral lines to become washed out, resulting in a featureless spectrum.

DO stars show spectral lines of He II, and therefore can be seen as precursors to DB stars, with the transition T_{eff} occurring in the range 40 000–50 000 K. Due to the initial rapid cooling, the He II lines do not remain visible for very long, and so DOs are not found in large numbers, even ignoring their favourable selection bias due to their immense luminosity (particularly in the ultra-violet). Their name comes from analogy to O-type main sequence stars.

DQ white dwarfs show carbon features in their spectra (for this spectra class, features in the UV are also considered), which are normally from Swan-bands of unstable C_2 molecules that form temporarily in the white dwarf atmosphere, or also sometimes from C I lines. For cool white dwarfs with helium dominated atmospheres (too cool to show helium lines), deep-convection zones extending from the surface to the core can dredge up carbon into the atmosphere. There are also the more recently discovered hot-DQs (Dufour et al., 2005), which have carbon-dominated atmospheres, and show C II lines instead.

Finally there are the DZs which have spectra containing lines only from metals. These are essentially cool DCs which have accreted metals. Indeed, Farihi et al. (2010a) found that these two white dwarf categories share the same spatial and kinematic distributions. As the title may give some indication, DZs are the main-focus of this thesis, and are introduced in greater detail in Section 1.5.

Beyond these primary classifications, compound categories are also possible where more than one type of line is present, with the different classifiers are ordered in terms of line dominance, e.g. DAB, DBA, DAZ, DBZ, DQA. As many classifiers can be used as needed, for instance the nearby star WD 1917−017 is classed as a DBQA.

Secondary spectral characteristics can also be appended to the primary (or compound classification). If emission lines are present these can be denoted with

"E". For magnetism, two categorisations are possible depending on whether the magnetism was discovered through polarimetry ("P") or Zeeman splitting of spectral lines ("H"). Variability is sometimes included with a "V", although this is usually identified photometrically. For instance DQE, DAP, DZH, DBV. Some authors also include a terminating number to indicate $T_{\rm eff}$, calculated as $50400\,{\rm K}/T_{\rm eff}$ (Sion et al., 1983), e.g. a DA with $T_{\rm eff} = 13000\,{\rm K}$ may be written as DA4. This is rarely expressed beyond one significant figure and never more than two. In Fig. 1.4, ten spectra are shown demonstrating the huge difference among the various spectral classes.

White dwarf classifications do come with some health warnings. It is usually tempting to think of white dwarf spectral classification as also classifying the atmospheric composition, however these two categorisations do not exactly overlap. For instance Gentile Fusillo et al. (2017) concluded that the DAZ, GD 17, has a helium dominated atmosphere, since it is too cool to show He I lines, but has enough trace hydrogen to form Balmer lines. Another caveat is that these classifications are never final, and subject to change with improving instrumentation, e.g. classification from DC to a DA with weak hydrogen lines. Finally these classifications are generally limited to optical wavelengths, except in the case of DQs, where UV wavelengths may be considered.

1.4.2 Atmospheric parameters

The main physical characteristics accessible through white dwarf atmospheric modelling are:

- Effective temperature
- The surface gravity
- Element abundances
- Surface magnetic fields
- Redshift
- Rotation velocity ($v \sin i$)

Effective temperature ($T_{\rm eff}$) is a simple way to assign a singular temperature to a stellar atmosphere. Observed spectra are integrated over a range of atmospheric layers from which photons are emitted and escape into space. Each of these layers will have a different temperature according to some gradient set by the various sources of opacity. The coolest and outermost layers have a very low density and thus contribute little of the observed flux, while at the other extreme, the deepest atmospheric layers are obscured by all those above them, and so while intrinsically bright, also contribute little to the flux emitted into space. It stands to reason that some intermediate layer dominates the emergent spectrum which to some degree can be considered the stellar temperature.

$T_{\rm eff}$ is defined by considering flux emitted over all wavelengths. Integrating over the entire flux density $F(\lambda)$,

$$f = \int_0^\infty F(\lambda)\,\mathrm{d}\lambda, \tag{1.4}$$

yields the total flux, f, which is the total power radiated per unit area of the stellar surface. We can then use the Stefan-Boltzmann law to determine the effective temperature, i.e.

$$f = \sigma T_{\rm eff}^4, \tag{1.5}$$

where σ is the Stefan-Boltzmann constant. Of course the Stefan-Boltzmann law is principally defined for calculating the flux radiated from a perfect blackbody. Therefore $T_{\rm eff}$ is to be interpreted as the temperature of a perfect blackbody radiating the same total flux as an observed spectrum.

Surface gravity has an obvious meaning, at least for white dwarfs, where the atmosphere is comparatively thin compared to the stellar radius. However its effect on astrophysical spectra is perhaps not so apparent. The surface gravity naturally results in a denser atmosphere and higher atmospheric pressure. This leads to a broadening of spectral lines through a variety of mechanisms, which are collectively referred to as pressure broadening.

One important effect is impact broadening, whereby an atom undergoing a transition may be interrupted by collision of another atom. This effectively reduces the transition timescale therefore increasing uncertainty in the transition energy.

The close proximity of atoms, ions, and electrons under these conditions results in splitting of atomic energy levels via the Stark effect (Mihalas, 1978; Tremblay & Bergeron, 2009). Integrated over the pressure structure of the atmosphere, this also leads to broadening of spectra lines.

Element abundances are measured from the presence of spectral lines. For white dwarfs such lines are almost always in absorption, as they attenuate the starlight from the deeper layers of the atmosphere. Because each ion has a unique set of spectral lines, it is thus possible to identify not only individual elements, but also their ionisation states. Naturally, the higher the abundance of an element is, the more starlight its lines absorb, and so model atmospheres can be used to determine the number density of absorbers in the photosphere. For ions with multiple absorption lines excited from different lower energy levels, the relative line strengths provide an independent constraint on $T_{\rm eff}$, as the level populations are temperature dependent.

Surface magnetic fields are typically measured through the Zeeman splitting of spectral lines. Through modelling of the Zeeman components it is possible to not only measure the strength of the field, but also constrain its geometry. For weak magnetic fields, spectropolarimetry can instead be used to measure circular polarisation of spectral lines. A more detailed introduction to white dwarf magnetism is given in Section 1.6.

Redshift is simply the shift of spectral lines due to relativistic effects. For main sequence stars, this is dominated by the line-of-sight velocity. For white dwarfs, this includes an important contribution from gravitational redshift. For single white dwarfs which are the focus of this thesis, it is impossible to measure these two components separately, and in general the resolution of the data I use is largely insensitive to their sum. However, in white dwarf+main sequence spectroscopic binaries, these two radial velocity components can be decorrelated (e.g. Holberg et al., 2012). The period-averaged velocity of the main-sequence component yields the systemic velocity of the binary, which when subtracted from the period-averaged velocity of the white dwarf gives its gravitational redshift (which is conventionally measured in $\rm km\,s^{-1}$).

Rotation velocity causes broadening of spectral lines via the Doppler effect. If we consider a rotating white dwarf viewed from its equator, half of the stellar disc moves towards us and is blueshifted, with the other half moving away and thus redshifted. Therefore a spectrum, which is integrated over the whole stellar disc, includes contributions from all of these shifts resulting in broadened spectral lines. More likely the star is viewed at an angle away from the equator, and so the width of the velocity-profile is reduced by a factor of $\sin i$, where i is the inclination between the observer and rotation-axis.

1.4.3 Fitting model atmospheres to data

The goal of building a model atmosphere is to include as many aspects as possible outlined in Section 1.4.2 as input parameters, and using all relevant physics (Mihalas, 1978), replicate the emergent spectrum integrated over the stellar disc.

For white dwarfs, the most important of these are $T_{\rm eff}$, $\log g$, and chemical abundances. For non-DAs, the inclusion of magnetic fields remains an ongoing challenge, although progress is being made in this area (Dufour et al., 2015). Radial-velocity and rotational-broadening, affect spectra in a way that can be included a posteriori.

For the two main classes of white dwarfs, the DAs and DBs, the compositions are fixed to pure hydrogen and pure helium respectively, and so the only two remaining parameters are T_{eff} and $\log g$. Therefore, for DAs and DBs, commonly one constructs a grid of models in the T_{eff}-$\log g$ plane. Models at intermediate points can then be calculated via interpolation. This allows DA and DB spectra to be fitted very quickly through a χ^2-minimisation routine or similar since the model grid only needs to be calculated once.

For the DZs we consider in this work, such grids are, for all practical purposes, impossible to produce. Each element included in the model would add an additional axis to the grid. For ten elements, T_{eff}, and $\log g$, sampled with 20 points per dimension, a grid of 4×10^{15} spectra would be required. Given four minutes of calculation time per spectrum (which I found to be typical for the models discussed in the following subsection), approximately two Hubble times would be required to calculate the entire grid. For the DZs here, a more reasonable approach is to employ some fitting technique, be it Markov Chain Monte Carlo, χ^2-minimisation, or manual adjustment, and to recalculate the model spectrum for each step in parameter space. This is undeniably a slow process, but a necessary one to correctly model the spectra we encounter in this work.

1.4.4 Koester DZ models

In this work I use models constructed by Detlev Koester. Specifically I use a branch of this code principally set up for the calculation of cool DZ models. The code consists of three main programs written in FORTRAN. These are KAPPA, ATM, and SYN, which are run in this order to produce a spectrum. For DZ white dwarfs, these atmospheres can be calculated assuming local-thermodynamic-equilibrium (LTE). In LTE atmospheres, the mean free photon path is much shorter than the length scales for gradients in temperature and pressure. Therefore, for any small region of atmosphere, the populations of different ionisation states and their energy levels, can be safely calculated using only the local state variables of temperature and pressure. This simply amounts to using the Saha ionisation equation (a function of temperature and pressure) to determine the populations for different ions, and using the Boltzmann distribution (only a function of temperature) to calculate the populations within an ion's energy levels. This approximation *vastly* decreases the complexity of calculating atmospheric models. For very hot white dwarfs, such an approximation is invalid and non-LTE (NLTE) models must be used instead (Hubeny & Lanz, 1995).

The KAPPA program is used to first calculate opacity and equation of state tables, where κ commonly denotes opacity. The κ-table is essentially a large 3-dimensional grid of opacity values as a function of temperature, pressure, and wavelength. The table is then calculated for a fixed set of chemical abundances. Thus the main inputs to KAPPA are the abundances for each element, and the values of temperature, pressure, and wavelength to calculate the opacity table at. Once the temperature/pressure/wavelength values have been decided these can be kept fixed for all modelling, with only the abundances varied for KAPPA, as these are the only inputs that constitute free-parameters of the model.

The ATM program is used to calculate the LTE atmospheric structure, or in other words the temperature and pressure profiles throughout the atmosphere, considering radiative and convective energy transfer. While there are multiple inputs to ATM depending on the desired complexity of the model, the two astrophysically relevant parameters are the T_{eff} and the $\log g$. For LTE atmospheres, the boundary condition at the deepest layer of the atmosphere is a black body spectrum. Then using the equations of radiative transfer and the previously generated κ-table, the atmospheric structure is iteratively computed.

Finally SYN calculates the emergent flux, given the atmospheric structure. This makes use of a variety of atomic data which includes wavelengths, energy levels, oscillator strengths ($\log gf$ values), and line broadening theories. For the latter of these, simple Lorentzian approximations are appropriate for many of the small lines. For some of the stronger lines with asymmetric line wings, a more complex van der Waals broadening theory is used (Walkup et al., 1984). For the very strongest lines, i.e. the Ca II H+K lines, and the Mg II 2800 Å doublet, where the line wings extend more than 1000 Å from the line centre, more sophisticated broadening theories must be used, with their details described in Chapter 3.

1.5 Planetary systems of white dwarfs

1.5.1 Exoplanetary systems overview

Over the last two decades the study of extrasolar planetary systems has revealed that worlds around other stars exhibit an unexpected level of diversity, including system architecture, masses, and orbital parameters. Using the method of transmission spectroscopy, it is now also possible to probe the chemistry of exoplanet atmospheres. These have been found to contain atomic (e.g. Charbonneau et al.,

2002) and molecular species (Swain et al., 2008), including multiple detections of water, e.g. Kreidberg et al. (2014b), and in some cases clouds (Kreidberg et al., 2014a). However, at the present, the study of bulk exoplanetary properties is mostly limited to measuring their masses and radii, and hence their bulk density. Exoplanet structures and compositions based on the comparison of these measurements with planet formation models, (e.g. Lissauer et al., 2011) are very uncertain for two reasons. Firstly, mass and radius measurements are typically subject to large uncertainties, and secondly the internal make-up of planets is degenerate with respect to their bulk densities (Rogers & Seager, 2010).

To directly probe the composition of a rocky exoplanet necessarily requires looking inside it and thus destroying it. There are a several cases of exoplanets known to be disintegrating in front of their host stars due to the dusty tails detected from asymmetric transits in their stellar light curves (Rappaport et al., 2012; Sanchis-Ojeda et al., 2015). However, even in these cases, the composition of the disrupting material can only be indirectly inferred from the dust properties (van Lieshout et al., 2014), and is only representative of the outer layers.

Instead, the study of exoplanetesimals accreted onto the surfaces of white dwarfs provide the most detailed and accurate insight into the composition of extrasolar planetary material (Zuckerman et al., 2007), as will be seen throughout the following subsections (and indeed this thesis).

1.5.2 The mystery of white dwarf metal pollution

The story of white dwarf planetary systems is an interesting one, as it begins with the discovery of the metal polluted DZ white dwarf vMa2 by van Maanen (1917) (see Fig. 1.5), but took almost 90 years before a planetary origin was envisaged for its atmospheric metals (Jura, 2003; Debes et al., 2012). The first spectral analysis of vMa2 was performed by Weidemann (1958, 1960), which was also the first quantitative spectral analysis performed for any white dwarf. Weidemann (1960) was able to measure abundances of Ca, Mg, Fe and concluded that hydrogen could not be the dominant atmospheric constituent, and thus vMa2 must have a helium dominated atmosphere. As mentioned in Section 1.1, it is now recognised that the Ca II lines observed in van Maanen's original vMa2 spectrum constitute the first data imprinted with the signature of an extrasolar planetary system (Zuckerman, 2015; Farihi, 2016).

Since the discovery of vMa2, many other white dwarfs have been found with atmospheres contaminated with metals (e.g. Hintzen & Tapia, 1975; Cottrell et al., 1977; Shipman et al., 1977; Wehrse & Liebert, 1980; Liebert & Wehrse, 1983; Zuck-

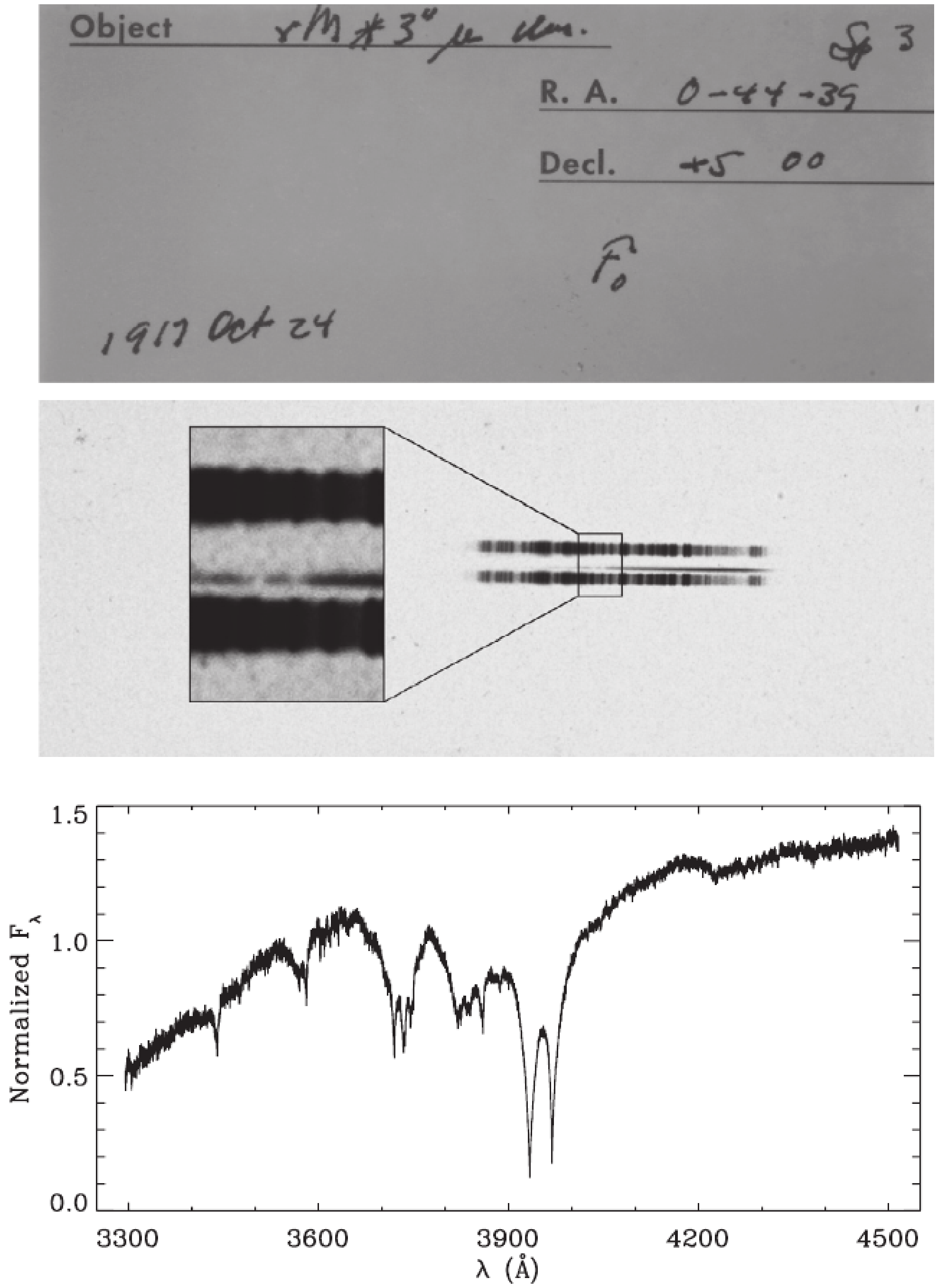

Figure 1.5: (Top/Middle) The first spectrum of vMa2 (van Maanen, 1917) was taken by Walter Adams and classified as an F-type star due to the prominent Ca H+K absorption lines, still visible on the original plate almost one century later. (Bottom) A more recent UVES spectrum clearly shows these same Ca lines as well as transitions from Mg and Fe. Figure from Farihi (2016).

erman & Reid, 1998; Dufour et al., 2007; Koester & Kepler, 2015). Due to gravitational settling, these heavy elements are expected to sink below the observable photosphere on time scales many orders of magnitude shorter than the white dwarf cooling age (Koester, 2009). Therefore the observed atmospheric contamination by metals at 25–50 % (Zuckerman et al., 2003; Koester et al., 2014) of white dwarfs can only be explained by recent or ongoing accretion of metal-rich material (Vauclair et al., 1979).

Because exoplanetary systems were not known to exist at that time, much effort was expended in explaining the atmospheric metals of white dwarfs via other mechanisms. Dredge up of core material offered an attractive explanation, but Vauclair et al. (1979) showed that convection zones could not extend deep enough into the stellar interior for this process to occur. Instead many authors argued for the accretion of grains from the interstellar medium (ISM) (e.g. Wesemael, 1979; Aannestad & Sion, 1985). While this explanation was the accepted source of metal pollution for many decades, it was plagued with several physical problems. The near Solar-composition of the ISM naturally means that it is dominated by hydrogen with metallic grains as traces (Wilson & Matteucci, 1992). Yet most of the known metal polluted white dwarfs have helium atmospheres[5] including vMa2. To solve this conundrum, explanations that allowed for the accretion of interstellar dust grains but not hydrogen gas were proposed (Michaud & Fontaine, 1979; Wesemael & Truran, 1982). An additional problem comes from the fact that DAZ white dwarfs, with their very short diffusion timescales for heavy elements, are generally not found in regions of enhanced ISM density (Aannestad et al., 1993). Therefore for the white dwarfs in low density regions, ISM accretion cannot explain their atmospheric metals.

1.5.3 The dusty disc of G 29−38

The first clue that eventually lead to the correct interpretation of white dwarf pollution came from observations of the DA white dwarf G 29−38. Zuckerman & Becklin (1987) sought to identify white dwarfs with close brown dwarf companions by looking for excesses in infrared flux. Since white dwarfs are very faint in the infra-red exhibiting only a Rayleigh-Jeans tail, any additional flux seen at these wavelengths must be emitted at a low temperature but from a surface area significantly larger than the white dwarf. Observations of G 29−38 showed the infrared excess (Fig. 1.6) that Zuckerman & Becklin (1987) were looking for. While hopeful that this marked

---

[5] The predominance of helium atmospheres among the known metal-polluted white dwarfs is a selection effect, owing to the stronger transparency of helium, thus resulting in stronger lines that are more readily detected than for hydrogen atmospheres.

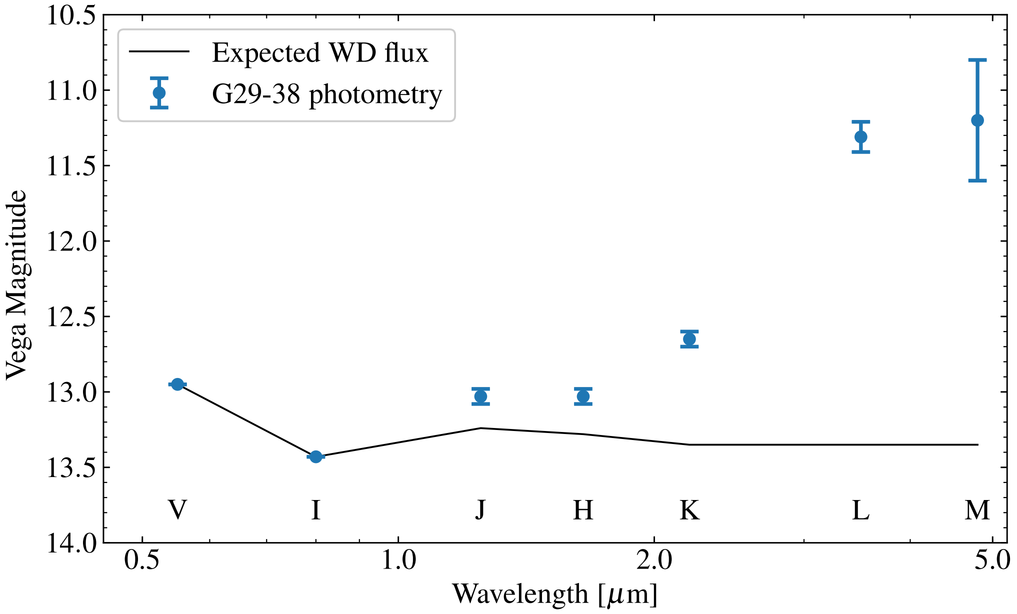

Figure 1.6: Beyond about 1.5 μm, G 29−38 exhibits a large flux excess compared to that expected for a 12 000 K white dwarf alone. Photometric points are the original data presented by Zuckerman & Becklin (1987).

the first discovery of a white dwarf + brown dwarf binary, Zuckerman & Becklin (1987) did not rule out the possibility that a large quantity of dust close to the white dwarf could also produce a similar signature.

Thankfully G 29−38, is also a variable star (McGraw & Robinson, 1975) with an amplitude of $\simeq 11\,\%$,[6] which was exploited by Graham et al. (1990) to reveal that only dust emission could explain the presence of infrared flux. Graham et al. (1990) found that the infrared excess was modulated with the same phase and frequency as the white dwarf, implying that the source of the emission had to be both close to the star and made from small particles that could thermally respond to changes in the stellar flux on a short time scale. In essence, the infrared flux could only be explained by a circumstellar disc of opaque dust which thermally reprocessed the incident stellar flux.

Later, Koester et al. (1997) identified metal lines in the spectrum of G 29−38, thus revising its spectral class from DA to DAZ. Because G 29−38 has a hydrogen dominated atmosphere, and thus short sinking times for heavy elements, it was thus apparent that G 29−38 was accreting metals from its circumstellar dust disc. While

---

[6] Trivia: McGraw & Robinson (1975) first published their detection of variability in G 29−38 along with the discovery of one other pulsating white dwarf, G 38−29.

this certainly provided a first step in elucidating the origin of atmospheric metals, at the time this simply meant rephrasing the question to the origin of the dust disc, which for the time being was still presumed to be related to ISM accretion.

1.5.4 A solution at last

Duncan & Lissauer (1998) were first to consider the long term stability of the Solar system beyond the Sun's main-sequence lifetime. They found that orbiting objects not destroyed during the Sun's giant phases could remain on stable orbits once the Sun becomes a white dwarf. More generally Debes & Sigurdsson (2002), found that planetary objects around stars with initial semi-major axes $> 5\,\mathrm{AU}$, can be expected to survive as they move onto wider orbits during the mass-loss associated with stellar evolution. However, they also found that some objects in multi-planet systems on previously stable orbits, could become unstable due to the reduced attraction from the central star. They also speculated on such instability being able to drive comets inwards which could pollute the white dwarf.

Following the work of Debes & Sigurdsson (2002), the seminal paper by Jura (2003) is considered the turning point where the ISM accretion hypothesis began to fall out of favour, and instead a planetary interpretation was to be given for the material in close orbit of G 29−38 and in the atmospheres of many white dwarfs. Jura (2003) showed that the dust orbiting G 29−38 could be modelled as a flat, opaque annulus of material, extending between the dust sublimation radius and the Roche radius of the white dwarf.

The Roche radius, sometimes referred to as the Roche limit, is the distance from a massive celestial object that causes a second loosely bound object (held together only by its own self gravity) to disintegrate due to tidal forces. The Roche radius takes a simple form, and can be calculated from only the mass of the primary object, and the density of the loosely bound secondary object, given by the simple expression (Davidsson, 1999)

$$R^3_{\mathrm{Roche}} = \frac{9M_1}{4\pi\rho_2}. \tag{1.6}$$

For a typical white dwarf mass of $M_1 = 0.6\,\mathrm{M}_\odot$ and typical rock density of $\rho_2 = 3\,\mathrm{g\,cm^{-3}}$, this implies a tidal disruption radius close to $1\,\mathrm{R}_\odot$. Note that equation 1.6 has no dependence on the size of the planetesimal. Jura (2003) proposed that an asteroid venturing within this critical distance of G 29−38 would have been tidally disrupted. The resulting dust would then be circularised into a debris disc which over time would accrete onto the stellar surface, leading to the appearance of metallic absorption lines in the stellar spectrum. Compared with previous speculation on the accretion of comets, the proposed disruption of an asteroid is more consistent with the volatile depleted, Ca-rich material observed in the atmosphere.

Since the works of Debes & Sigurdsson (2002) and Jura (2003), the dynamics of perturbing asteroids within white dwarf Roche radii as well as the accretion mechanisms within debris discs has become a booming area of research (Nordhaus et al., 2010; Bonsor et al., 2011; Bonsor & Wyatt, 2012; Mustill & Villaver, 2012; Debes et al., 2012; Veras et al., 2013, 2014a,b; Frewen & Hansen, 2014; Mustill et al., 2014; Veras et al., 2015; Veras & Gänsicke, 2015a,b; Bonsor & Veras, 2015; Veras et al., 2016a; Hamers & Portegies Zwart, 2016; Brown et al., 2017; Petrovich & Muñoz, 2017; Veras et al., 2017b), yielding vast progress in exploring the rich variety of system architectures that can lead to exoplanetesimal accretion by white dwarfs. In any case the arguments put forward by Jura (2003) have consistently been able to explain new observations of metal-polluted white dwarfs, as well as those observed with debris discs.

1.5.5 More on discs

Since the original observations of G 29−38, more than forty white dwarfs with circumstellar debris discs are now known from infra-red excesses (von Hippel et al., 2007; Jura et al., 2007b; Farihi et al., 2008; Brinkworth et al., 2009; Farihi et al., 2010b; Melis et al., 2010; Debes et al., 2011; Kilic et al., 2012; Farihi et al., 2012; Brinkworth et al., 2012; Bergfors et al., 2014; Rocchetto et al., 2015; Dennihy et al., 2016; Barber et al., 2016), and in all cases these white dwarfs are found to be metal polluted.[7] Despite the ever increasing number, it actually took 18 years before the second disc hosting white dwarf was discovered at GD 362 (Kilic et al., 2005; Becklin et al., 2005). The atmosphere of this star is extremely metal-rich, and while first identified as a DAZ (Gianninas et al., 2004), the star was later shown to have a helium dominated atmosphere (Zuckerman et al., 2007), with hydrogen only present as a trace element. The total metal abundance remains the highest detected for any white dwarf, demonstrated by the detection of trace elements Sc, V, Co, Cu, and Sr. In particular, the latter two of these have yet to be detected in the atmosphere of any other white dwarf. These large metal abundances and the bright infrared excess indicate that GD 362 is still accreting metals at a high rate.

It has been customary since the work of Jura (2003) to fit the white dwarf in-

---

[7] PG 0010+280, possesses an infrared excess and so far no metals have been detected in its photosphere (Xu et al., 2015). However, in this case the infrared colours are indicative of an irradiated substellar companion.

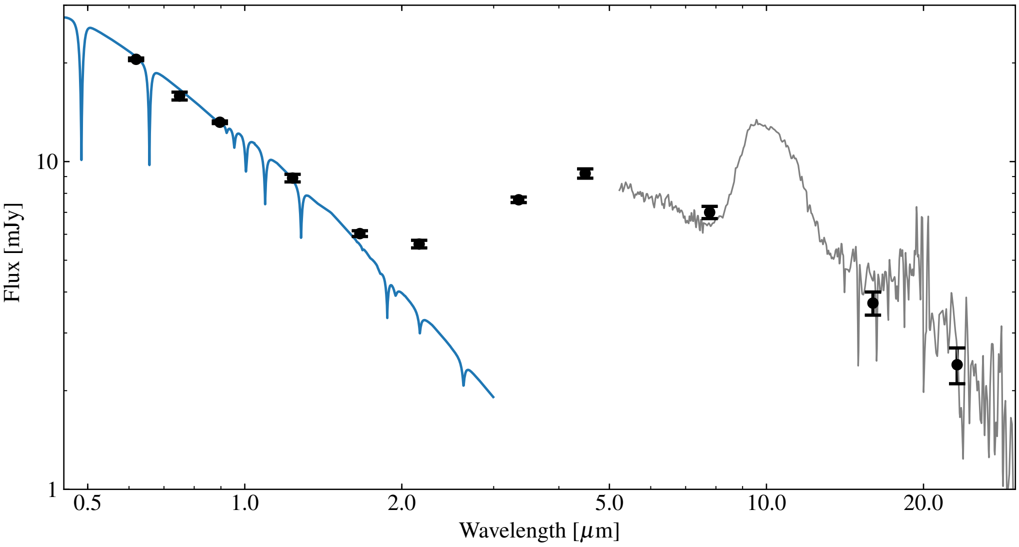

Figure 1.7: The Spitzer observations of Reach et al. (2005, 2009) demonstrate unambiguous 10 μm silicate emission at G 29−38. Photometry are from SDSS, APASS, 2MASS, WISE, and Spitzer. A 12 000 K DA model is plotted against the optical photometry to emphasise the flux excess beyond 1.5 μm.

frared photometry with a model based on concentric rings each emitting a blackbody spectrum. Of course this is only an approximation, although certainly a useful one for determining disc parameters, however the underlying disc spectrum is more complicated. Spectroscopic observations of G 29−38 with Spitzer[8] (Reach et al., 2005, 2009) revealed strong 10 μm silicate emission (Fig. 1.7) which has been attributed to a mixture of enstatite and forsterite dust grains. In addition to G 29−38, only a few objects, including GD 362, have proved to be sufficiently bright enough for spectroscopic follow-up with Spitzer (Jura et al., 2007a, 2009). With JWST[9] available in the near future, it will be possible to detect molecular emission at additional objects, and includes the prospect of carrying out detailed mineralogy in the brightest systems like G29−38.

While the metallic discs of these white dwarfs are usually detected via the infrared emission of dust grains, some are also visible through material in the gas phase. The first gaseous disc was identified at SDSS J122859.93+104032.9 by

---

[8] Spitzer is an infra-red space telescope with imaging and spectroscopic instrumentation covering 3.6–160 μm. Its primary mirror has a diameter of 0.85 m.

[9] JWST is an upcoming space telescope expected to launch in 2019. It is chiefly designed for infra-red observations with an array of imaging and spectroscopic instruments covering 0.7–27 μm in wavelength. Among space-based observatories, its 6.5 m diameter primary mirror will provide an unprecedented collecting area and spatial resolution.

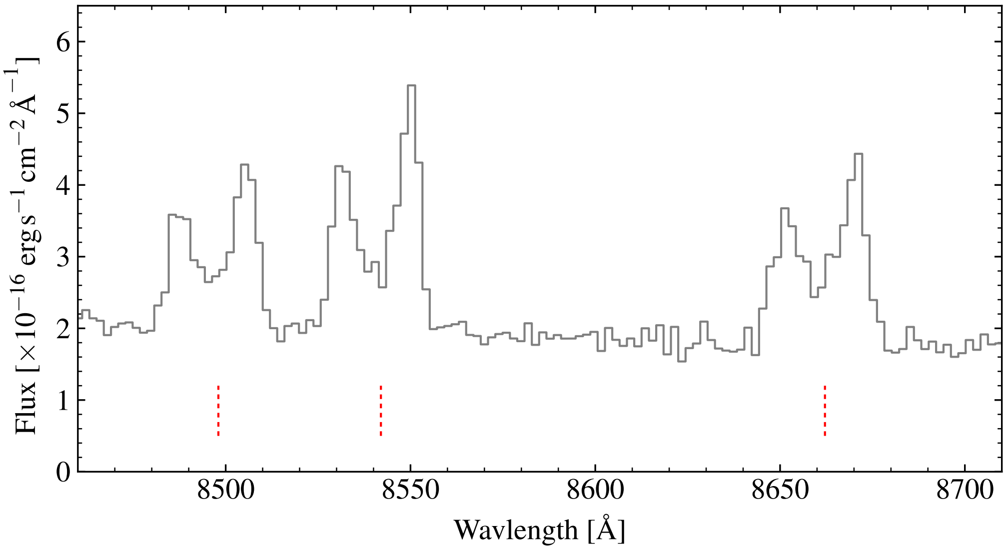

Figure 1.8: Gaseous emission observed at SDSS J122859.93+104032.9 from the infrared Ca II triplet. The double peaked structure is indicative of a disc, with material moving towards and away from the observer on each side of the disc. The laboratory wavelengths are marked by the red dotted lines.

Gänsicke et al. (2006). The SDSS[10] discovery spectrum is shown in Fig. 1.8, unambiguously exhibiting double-peaked emission profiles from the Ca II triplet. Such emission profiles are commonly encountered for astrophysical discs, including cataclysmic variables and active galactic nuclei. Essentially the double-peaked structure results from the distribution of Doppler-shifts for gas moving towards and away from the observer on each side of the disc. Furthermore, SDSS J1228+1040 is found to exhibit an infrared excess (Brinkworth et al., 2009) as well as an atmosphere rich in metals (Gänsicke et al., 2012).

In principle, all white dwarf discs ought to contain a gaseous component, with the gas-to-dust fraction reaching unity close to the white dwarf. In practice, gas discs are rarely detected except in the case of very high accretion rates. Since this time, the number of confirmed detections of gaseous discs totals seven (Gänsicke et al., 2007, 2008; Gänsicke, 2011; Farihi et al., 2012; Dufour et al., 2012; Melis et al., 2012; Wilson et al., 2014), with a candidate gas disc reported by Guo et al. (2015).

An exciting aspect to the gaseous components to these discs is their recently discovered variability. Wilson et al. (2014) were the first to observe a dynamically active disc, showing that SDSS J161717.04+162022.4 displayed only weak gas

---

[10] The Sloan Digital Sky Survey (SDSS) is described in Section 1.7.

emission (if at all) in its 2006 SDSS spectrum, but peaked later in 2008 SDSS observations, and subsequently decayed in strength over the next six years. Wilson et al. (2014) speculated that this could indicate impact of an additional exoplanetesimal onto an already existent debris disc, producing new gas. In their monitoring of SDSS J1228+1040, Manser et al. (2016a) were able to exploit twelve years observations to show slow precession of the disc. From Fig. 1.8, it is clear that in all three components, the red peaks are stronger suggesting an asymmetric disc. The data presented by Manser et al. (2016a) showed this asymmetry eventually equalising, before transitioning to a structure dominated by the blue peaks, which they were able to visualise (in velocity space) via Doppler tomography. Manser et al. (2016b) also identified similar gaseous variability at SDSS J104341.53+085558.2 (originally identified by Gänsicke et al. 2007), which they argued could be explained through general relativistic precession of the disc. In summary, the gas components to these discs often vary on observable timescales, and thus offer a window into the dynamic nature of exoplanetesimal accretion onto white dwarfs.

1.5.6 WD 1145+017

While this picture of evolved planetary systems has adequately explained observations for more than a decade, the most unambiguous evidence surfaced only recently, with deep, asymmetric transits in the K2 lightcurve of WD 1145+017 (Fig. 1.9, leading to the discovery of disintegrating planetesimal fragments orbiting near the Roche radius of this star ($P_{\rm orb} \simeq 4.5\,{\rm hr}$) (Vanderburg et al., 2015). Additionally WD 1145+017 has an infrared excess as well as photospheric metal lines in its spectrum. While no gas emission is observed, the almost edge-on view of the disc permits gaseous *absorption* features (mostly Fe II) to be detected instead (Xu et al., 2016).

Because WD 1145+017 is currently the only example where we witness the tidal disruption of a planetesimal in real time, naturally this exciting object is being actively monitored in great detail (Gänsicke et al., 2016b; Alonso et al., 2016; Rappaport et al., 2016; Gary et al., 2017; Redfield et al., 2017). On short timescales, individual transit features are seen to emerge and disappear over a few days (Gänsicke et al., 2016b). In the longer term the level of activity at WD 1145+017 has been seen to rise since its initial discovery, before beginning to decline in late 2015, and then rapidly rising again in April 2016 (Gary et al., 2017). The circumstellar absorption features are also seen to vary on similar timescales (Redfield et al., 2017). Thus, the duration over which tidal disruption will remain visible at WD 1145+017 is presently unconstrained.

From a theoretical perspective, WD 1145+017, poses many questions on the

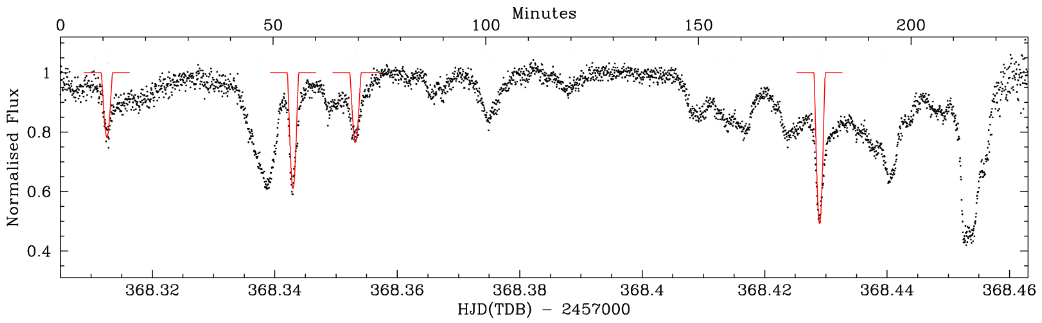

Figure 1.9: Over a single orbital period, multiple debris fragments cause numerous transits blocking up to 60 % of the stellar flux. The high cadence ULTRASPEC data shows that even the most narrow transits last for several minutes, with the asymmetry of the longer transits indicating tails of dust produced through tidal disruption. Original figure from Gänsicke et al. (2016b).

dynamics of the disrupting planetesimal fragments. Veras et al. (2017a) performed simulations of asteroid breakup for different compositions and orbital parameters. They found that the fragments must be in circularised orbits, and must be a differentiated body with a core and mantle to avoid immediate breakup (for a loose rubble pile) or non-disruption (for a solid metallic body). Veras et al. (2016b) were also able to place mass constraints for the orbiting bodies for various numbers of fragments based on transit phase shifts. Gurri et al. (2017) found that fragments with masses $> 10^{23}$ g would become unstable within a two years if not highly circular orbits.

Unfortunately, the prospect of detecting a statistically large sample of systems like WD1145+017 within the near future is low considering the chance alignment required, and the potentially small fraction of time for which transits are visible during an accretion episode. However, WD 1145+017 will continue to be an important case study for understanding the process of planetesimal accretion.

1.5.7 Compositions of extrasolar planetesimals

As we have seen so far, remnant planetary systems can be identified through four different signatures. Many hundreds of white dwarfs are now known to show traces of heavy elements in the atmospheres indicating recent accretion of material into the photosphere. Of these, several tens show infrared excesses indicative of dusty circumstellar discs. From the objects with confirmed dusty discs, a handful are observed with a circumstellar gaseous component, usually from double peaked emission lines, but occasionally from broad absorption features. In only one system are transits from a disintegrating planetesimal observed. Evidently these signatures form a hierarchy in terms of detectability, with all four observed at WD 1145+017. The most commonly encountered observables of those above, white dwarfs exhibiting metal lines in their spectra, offer the unique ability to allow *direct* measurement of extrasolar planetary material compositions, as suggested at the start of this section.

Since the detailed model of Jura (2003) convincingly arguing that white dwarfs with metal lines have accreted debris from their remnant planetary systems, it was realised that spectral analysis of a white dwarf, which yields atmospheric abundances, could be used to infer the composition of the accreted parent bodies. Such an analysis was first performed by Zuckerman et al. (2003), although at the time it remained unclear whether this scenario was definitively the correct interpretation. Since then many metal-polluted white dwarfs have been analysed by a number of authors in order to study the compositions of the disrupted parent bodies (Zuckerman et al., 2007; Koester, 2009; Klein et al., 2010; Zuckerman et al., 2010; Melis et al., 2011; Koester et al., 2011; Klein et al., 2011; Gänsicke et al., 2012; Dufour et al., 2012; Jura et al., 2012; Xu et al., 2013; Vennes & Kawka, 2013; Farihi et al., 2013a,b; Xu et al., 2014; Kawka & Vennes, 2014; Raddi et al., 2015; Wilson et al., 2015; Kawka & Vennes, 2016; Farihi et al., 2016; Melis & Dufour, 2017; Xu et al., 2017).

In several cases the derived abundances imply the accretion of material from planetesimals having undergone differentiation. For instance the relatively high Ca and Al content at NLTT 43806 points to lithospheric material (Zuckerman et al., 2011), whereas the large Fe and Ni relative abundances at Ton 345 are better explained by a planetesimal enhanced in core-material (Wilson et al., 2015).

Analysis of two systems, GD 61 and SDSS J124231.07+522626.6 (Farihi et al. 2013a and Raddi et al. 2015, respectively) have also revealed the accretion of water-rich asteroids. In both cases, the oxygen abundances were found to be vastly greater than expected from the accretion of minerals containing MgO, SiO_2, CaO etc. (bearing in mind that the dominant rock-forming elements Mg, Al, Si, Ca, and Fe are all easily detected). Because only a fraction of this oxygen could be explained through metal-oxide bearing minerals, and the non-detection of carbon rules out CO and CO_2, the excess oxygen strongly suggests a water-rich origin. Furthermore, both white dwarfs are DBAZs, with trace hydrogen within the helium dominated atmosphere, forming clear Balmer lines. The hydrogen to oxygen relative abundances are sufficiently high to be consistent with water accretion. Contrary to the atmospheric metals, hydrogen will not sink below the helium dominated photosphere. This has caused some authors to speculate that the trace hydrogen in the atmospheres of many DAB/DBA white dwarfs are a signature of past accretion of water-rich asteroids (Raddi et al., 2015; Gentile Fusillo et al., 2017). For both GD 61 and SDSS J124231.07+522626.6 the water mass-fractions of the asteroids were estimated to be a few 10 %, similar to the Solar System asteroid Ceres.

Until recently all metal-polluted white dwarfs have shown abundance-patterns consistent with an origin from within the snow line. However, Xu et al. (2017) recently demonstrated that WD 1425+540 has an atmosphere enriched in the volatile elements C, N, and S, and an abundance pattern that is overall consistent with a Kuiper-belt like object. In summary, the planetary systems around stellar remnants are found to be as diverse as those around main-sequence stars, including our own Solar system.

1.5.8 DZ white dwarfs

In this thesis I focus on a subclass of metal polluted white dwarfs, the cool DZs. Recall from Section 1.4.1 that DZ white dwarfs are characterised by having only metal lines in their spectra, and that most known DZ stars have atmospheres dominated by helium, due to the diminished strength of the helium lines below $T_{\rm eff} \simeq 11\,000\,{\rm K}$. Additionally, the low opacity of helium results in metal lines that are both deep and broad even at low abundances of $\log[{\rm Z/He}] \lesssim -9\,{\rm dex}$. In hydrogen-dominated atmospheres with $T_{\rm eff} \lesssim 6000\,{\rm K}$ the Balmer lines also vanish, and, if contaminated by metals, they too may be classed as DZs. In practice these are rarely observed, as the higher opacity of hydrogen atmospheres requires larger metal abundances to form detectable spectral lines. Furthermore, the longer sinking timescales of heavy elements within helium atmospheres (Fig. 1.3) allow metals to remain detectable for many Myr after the end of an accretion episode. Regardless of background element, DZ white dwarfs are cool objects by definition. Because white dwarf cooling is relatively well understood (Fontaine et al., 2001; Salaris, 2009), their effective temperatures can be used to estimate the white dwarf ages. Thus DZs allow study of planetary material within the oldest remnant planetary systems.

The cool DZs – as opposed to DZs with $T_{\rm eff} > 9000\,{\rm K}$ – were chosen for study here due to the plethora of intense spectral features in the optical (see Fig. 1.4 for comparison of a cool and warm DZ). For much warmer DZs, usually only the Ca II H+K doublet is seen, which does not permit analysis of the composition for the accreted parent body.

In Fig. 1.10 we show the spectrum of the DZ white dwarf SDSS J1535+1247 (a star which is discussed further in Chapter 3) with the major metal transitions labelled. The strongest features in the DZ spectra are almost always the Ca II H+K

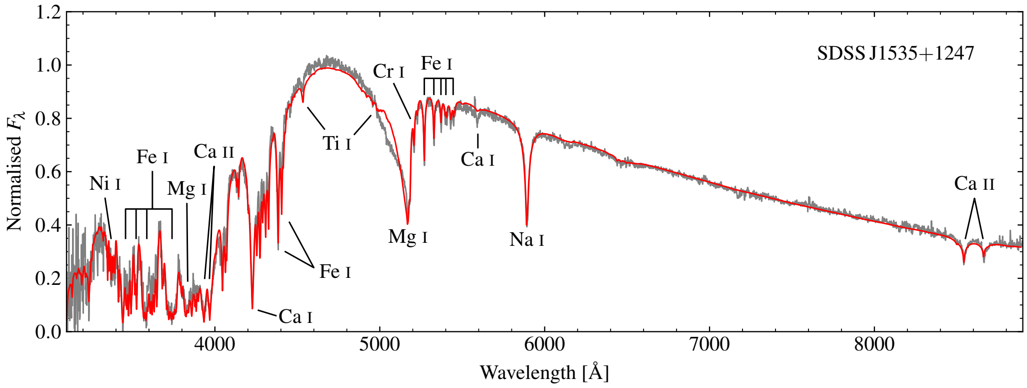

Figure 1.10: SDSS J1535+1247 is typical of the other DZs discussed throughout this thesis both in terms of its spectrum and composition of the accreted material, albeit with the highest signal-to-noise ratio. The main spectral features are labelled. The many unlabelled lines in the range 4000–4400 Å are almost all from Fe I, with the exception of a Cr I triplet centred on 4275 Å. Our best fitting model (Chapter 3) is shown in red.

resonance lines which are visible over the full range of $T_{\rm eff}$ for the objects in this work. Other strong Ca features include the 4227 Å Ca I resonance line, and the infra-red Ca II triplet (although its bluest component is rarely strong enough to be visible). The next most easily detected elements are Mg and Fe, whose lines have lower oscillator strengths, but are typically $\simeq 1$ dex higher in abundance than for Ca. Fe is constrained mostly by a forest of unresolved lines in the 3400–3900 Å region, but also by multiplets near 4400 Å and 5400 Å. The Mg I-b triplet, centred on 5171 Å, is the most prominent Mg feature, especially because of its asymmetric profile which results from a satellite line formed in high density helium atmospheres (Allard et al. 2016a; Hollands et al. 2017/Chapter 3). Additionally, lines of Na, Cr, Ti, and Ni can be detected for many cool DZs, where all of these are seen for SDSS J1535+1247.

To conclude this introduction on cool DZs, it is worthwhile to point out that the prototype metal polluted white dwarf, vMa2, falls into the class of cool DZs. Thus it is with great privilege that I write a thesis on the same class of object within a month of the discovery spectrum's centenary (Fig. 1.5). For the objects I present in chapters 3 through 6, the metal abundances are much higher, in some cases by over three orders of magnitude, however it cannot be ignored that the discovery of vMa2 is where the story of remnant planetary systems began.

1.6 Magnetic white dwarfs

White dwarfs have been known to harbour magnetic fields since the detection of circularly polarised light from GJ 742 (Kemp et al., 1970). In the following decades a plethora of magnetic white dwarfs have been identified either from Zeeman splitting of absorption lines in their spectra or by spectropolarimetry (Kawka et al., 2007, and references therein). The advent of large scale spectroscopic surveys, in particular the SDSS, has in the last decade increased the number of known magnetic white dwarfs to several hundred (Gänsicke et al., 2002; Schmidt et al., 2003; Vanlandingham et al., 2005; Kleinman et al., 2013; Kepler et al., 2013, 2015).

Magnetic white dwarfs are unrivaled laboratories for testing atomic physics under strong fields. While neutron stars/magnetars undoubtedly have greater surface fields by many orders of magnitude, white dwarfs are significantly more abundant and their atmospheres can be directly probed with spectroscopy. They therefore provide unique tool for measurements of atomic processes in magnetic fields spanning 1 to 1000 MG.[11]

Despite the ever growing list of these previously rare objects, several questions continue to remain without a definite answer: What is the origin of these magnetic fields? And what is the fraction of white dwarfs that are magnetic, and how does this vary with cooling age/temperature?

1.6.1 Origin of white dwarf magnetism

Two distinct models have been proposed to explain the emergence of fields $\gtrsim 1\,\mathrm{MG}$ in isolated white dwarfs. In the fossil field hypothesis, the magnetic fields of the chemically peculiar Ap/Bp stars are thought to be amplified due to flux conservation during post-main sequence evolution resulting in white dwarfs with fields in the MG regime (Woltjer, 1964; Angel & Landstreet, 1970; Angel et al., 1981; Wickramasinghe & Ferrario, 2000). A more recent hypothesis (Tout et al., 2008) considers a binary origin, where a system undergoing a common envelope leads to magnetic dynamo generation. We comment further on magnetic field generation in Chapter 6.

1.6.2 Incidence of magnetism

The incidence of magnetism in white dwarfs remains poorly established due to selection effects. Independent studies are difficult to reconcile with one another as each suffers from its own set of biases. This problem becomes significantly more

---

[11] The record for a continuous field generated in an Earth-based laboratory is 0.45 MG (Brandt et al., 2001).

pronounced when focusing on subsets of the total white dwarf population where small number statistics dominate.

Recent volume limited samples of nearby white dwarfs present the most unbiased estimates of the magnetic incidence when considering all white dwarf sub types, and suggest incidences of $21 \pm 8\,\%$ for white dwarfs within 13 pc of the Sun, and $13 \pm 4\,\%$ for those within 20 pc (Kawka et al., 2007). However these magnetic white dwarfs are dominated by fields lower than 100 kG and strongly magnetic objects with fields above 10 MG. Only 1 out of the 15 magnetic white dwarfs in the compilation of Kawka et al. (2007) has a field strength between 1 and 10 MG (the range that we discuss in this work).

More recently, Sion et al. (2014) have presented a volume limited white dwarf sample within 25 pc from the Sun. They find a magnetic incidence of 8 % when considering magnetic fields above 2 MG only. Other studies have investigated the magnetic incidence with much larger, but magnitude-limited samples. For instance Kleinman et al. (2013) identified over 12 000 DAs from spectra in the 7th data release of the SDSS, of which they classified more than 500 as magnetic (Kepler et al., 2013), leading to a much lower incidence of 4 %. However, because this sample is magnitude-limited, it is intrinsically biased. Most degenerates in the local sample have temperatures below 10 000 K, whereas 84 % of the white dwarfs from Kepler et al. (2013) are hotter than this. The discrepant numbers between the local sample of cool/old white dwarfs and hotter/younger white dwarfs, have been the basis for some authors to claim an age-dependency of the magnetic incidence (Fabrika & Valyavin, 1999; Liebert et al., 2003).

Analysing the small sample of white dwarfs with accurate parallaxes, Liebert (1988) noted that magnetic white dwarfs appear to be under-luminous for their colour, suggesting they have smaller radii, and hence higher masses, than non-magnetic white dwarfs. Later, Liebert et al. (2003) derived a mean mass of $0.93\,\mathrm{M}_\odot$ for eight magnetic white dwarfs from the Palomar Green (PG) survey, based on model atmosphere analyses, compared to $\sim 0.6\,\mathrm{M}_\odot$ for non-magnetic ones. While there is hence independent evidence for higher-than-average masses for magnetic white dwarfs, caveats to bear in mind are that there are still few magnetic white dwarfs with precise parallaxes, and even for those systematic uncertainties in the analysis of their spectra limits the accuracy of the desired masses (Külebi et al., 2010).

A common theme among all the above investigations is that the true magnetic incidence is expected be higher, as the various biases (e.g. signal-to-noise, magnetic broadening, magnitude-limited surveys) tend to work against the identification of magnetic white dwarfs.

1.6.3 Measurement of white dwarf magnetic fields

The magnetic fields of white dwarfs are detected and measured using two main techniques. The first method is to measure the circular polarisation of light from a white dwarf, as with the first detected magnetic white dwarf GJ 742 (Kemp et al., 1970). This method can be extended to spectropolarimetry, where the polarisation signature is measured as a function of wavelength (e.g. Landstreet & Angel, 1975; Friedrich et al., 1996; Kawka et al., 2007; Vornanen et al., 2013). This method has the advantage of being able to measure fields down to a few kG (Kawka et al., 2007), but comes with the disadvantage of low quantum efficiency and thus is suited only to the brightest of white dwarfs.

The second technique exploits the Zeeman effect through the observed splitting of spectral lines. Within SDSS, the combination of spectral resolution and intrinsic Balmer line widths places a lower limit of $\simeq 2\,\mathrm{MG}$ for magnetism at DA white dwarfs (Kepler et al., 2013). Zeeman splitting is the most common detection method for white dwarf magnetism, as it does not require special instrumentation beyond basic spectrographs, and is thus the method we give our attention to for the remainder of this thesis. An example spectrum of magnetic DA white dwarf (DAH) is shown in Fig. 1.11.

To describe the Zeeman effect, for simplicity we first turn to the hydrogen atom. The Hamiltonian for the bound electron in the absence of a magnetic field is simply given by

$$H = \frac{p^2}{2m_e} - e^2/r + V_{\mathrm{SO}}, \tag{1.7}$$

where the terms corresponds to the kinetic energy operator, the potential energy between the electron and nucleus, and the spin-orbit effect (Wickramasinghe & Ferrario, 2000). The wavefunction, $|\psi\rangle = |n, l, m_l, m_s\rangle$, is fully characterised by the four usual quantum numbers, n, l, m_l, and m_s, which are the principle, orbital, magnetic and spin quantum numbers respectively.

The spin-orbit effect arises from coupling of orbital and spin angular momenta. Due to relativistic motion, the electric field of the nucleus has a magnetic component in the electron's frame of reference, which induces a torque on the electron depending on its total angular momentum, resulting in shifts in atomic energy levels. Thus spectral lines are seen to exhibit splitting, referred to as fine structure. This effect can be derived from considering the first-order relativistic correction to

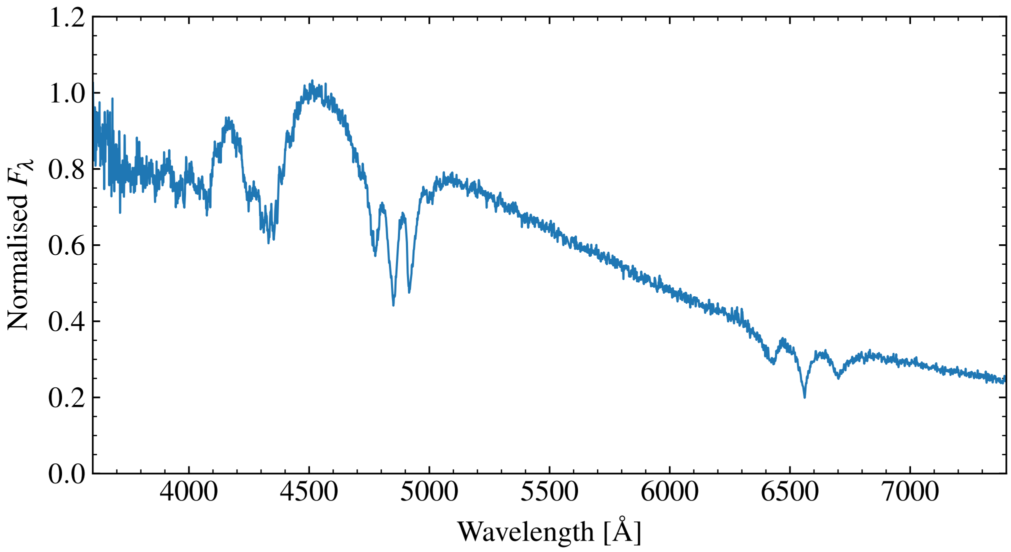

Figure 1.11: The full sized spectrum of the DAH from Fig. 1.4 shows unambiguous Zeeman splitting of the Balmer lines into three components each. Measuring the energy separation between components reveals an surface-averaged field of 6.5 MG.

the kinetic energy. In the case of multi-electron atoms, the spin-orbit effect can be notably large. For instance the Ca II H+K doublet shows separation of 35 Å, where the upper energy level splits into states of different total angular momentum.

We now consider the application of a magnetic field in the z direction to the Hamiltonian, arriving at

$$H = \frac{p^2}{2m_e} - e^2/r + V_{\mathrm{SO}} + \frac{\mu_B B}{\hbar} J_z + \frac{m_e \mu_B^2 B^2}{2\hbar^2} r^2 \sin^2\theta, \tag{1.8}$$

where the first and second of the new terms correspond to the paramagnetic/linear-Zeeman and diamagnetic/quadratic-Zeeman effects respectively, and where J_z is the total angular momentum operator (Wickramasinghe & Ferrario, 2000).

If we consider the case of a weak applied field, such that the linear and quadratic terms are much smaller than V_{SO}, then the splitting can be treated as a perturbation on the zero-field atom. In this regime the quadratic effect is negligible, and so splitting is linear in the applied field. The line profiles can be complex, and while rarely observed for DAHs we show in Chapter 6 that this can be a common regime for magnetic white dwarfs with metal lines (as also shown by Zuckerman et al. (2011), Farihi et al. (2011b) and Kawka & Vennes (2014) for DAZH white dwarfs with $B \sim 10^5$).

Next we turn to a higher field where the linear term is sufficiently large to disrupt spin-orbit coupling, but is still much smaller than the quadratic effect. Since spin and orbital momentum have decoupled J_z can be replaced with L_z. In the case that the linear Zeeman effect term dominates over the quadratic effect, then each level splits into $2l+1$ states corresponding to the different m_l quantum numbers. This specific case is commonly encountered for magnetic white dwarfs and is called the Paschen-Back regime. The selection rules for transitions only allow for $\Delta m_l = 0, \pm 1$ and so all transitions are split into three, referred to as the π and $\sigma^{\pm}$ components, respectively. The energy separation between each adjacent component is thus simply $\mu_B B/\hbar$, allowing easy measurement of the field. We show the example DAH from Fig. 1.4 in full-size in Fig. 1.11, demonstrating Zeeman-splitting of the spectral lines into three components. The splitting of Hα appears larger than for Hβ when displayed in terms of wavelength. Converting to wavenumber, (which is proportional to photon energy), shows the splitting to be identical.

For very strong magnetic fields, the contribution of the quadratic term in equation (1.8) can no longer be ignored. Unlike the linear term, which only depends on B and the m_l quantum number, the quadratic Zeeman effect has dependence on the electron's position relative to the atom (and the direction of the magnetic field). Thus, for hydrogen, the extent of the quadratic effect is proportional to n^4 (from the r^2 dependence), and so the higher-order Balmer lines are affected the most.

Calculation of the mixed linear and quadratic Zeeman effects cannot be solved analytically. Therefore the energy eigenvalues and oscillator strengths must be calculated numerically, and have been tabulated by Roesner et al. (1984) and Forster et al. (1984), among others. The result on the wavelengths of the Balmer lines is found to be complex. Where the linear Zeeman effect lifts the degeneracy between states of the same n, l, but different m_l, the quadratic Zeeman effect lifts the degeneracy between states with the same l. Thus additional splitting and line-shifts are observed. This is shown for the first 10 Balmer lines in Fig. 1.12 (Schimeczek & Wunner, 2014b), a diagram often referred to as a spaghetti-plot.

For atoms heavier the hydrogen, a multi-electron Hamiltonian must be used instead, where the electrons exert electrostatic forces on each other (Schimeczek & Wunner, 2014a). Thus the calculation of the energy eigenvalues under high fields rapidly increases in complexity with each added electron, and is most challenging when the linear and quadratic Zeeman effects are comparable to each other, or to the electrostatic potential. Thus calculations for the full-range of fields encountered at white dwarfs has been limited to only light atoms (Ruder et al., 1994; Thirumalai & Heyl, 2014).

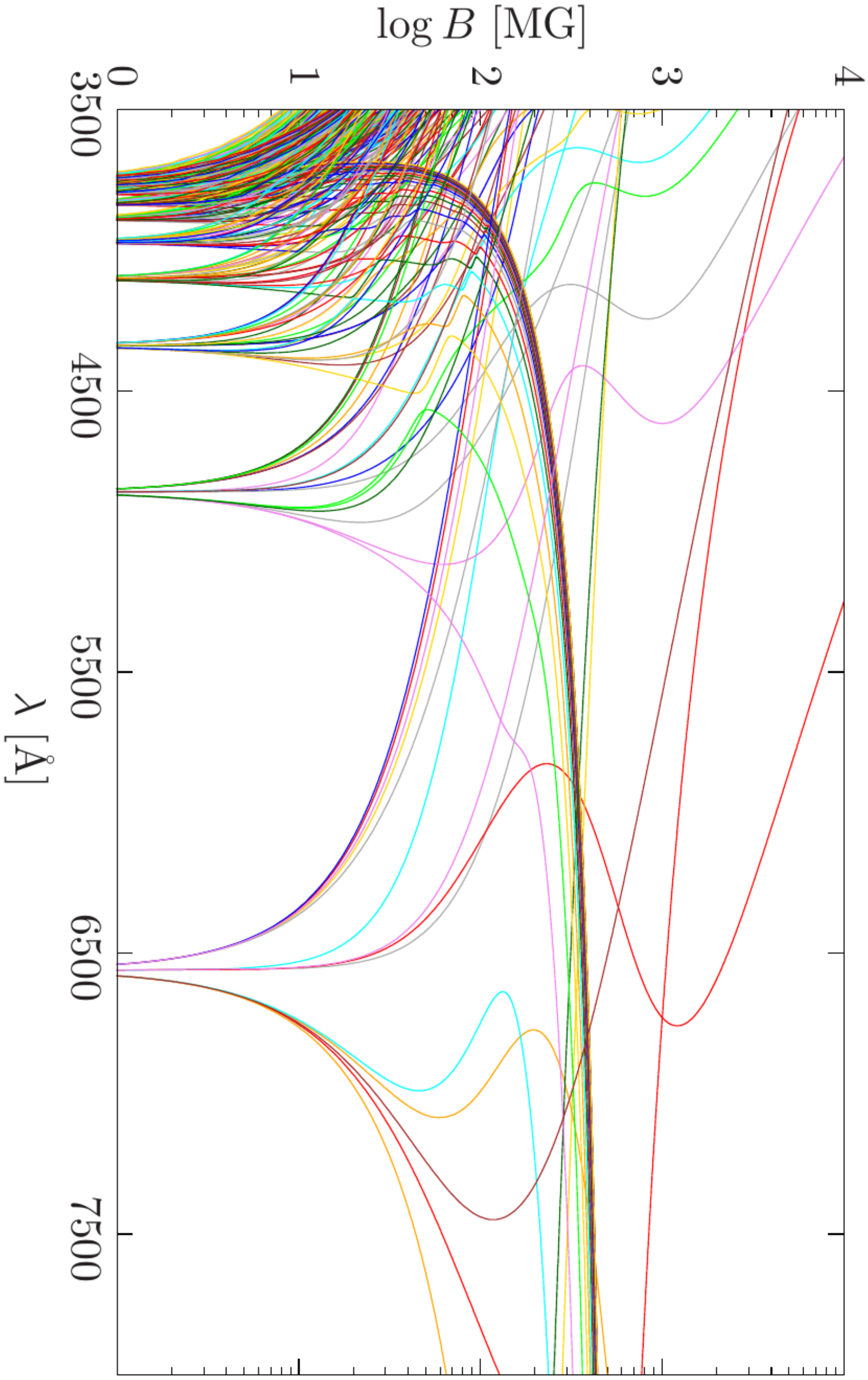

Figure 1.12: The first 10 Balmer lines are shown for field strengths typically encountered in high-field white dwarfs. Beyond 10 MG the splitting-pattern becomes extremely complicated. The variety of colours serve only to distinguish transitions. Original figure from Schimeczek & Wunner (2014b).

1.7 SDSS

The Sloan Digital Sky Survey (SDSS) is one of the most productive astronomical surveys of recent years, and due to the vast variety of data it has output, has lead to the identification of most of the currently known white dwarfs (Kleinman et al., 2004; Eisenstein et al., 2006; Kleinman et al., 2013; Kepler et al., 2015, 2016). The survey itself is composed of several missions of varying goals, consisting of a mixture of imaging and spectroscopy across optical wavelengths. Imaging took place up to data release 7, but has since focussed entirely on spectroscopy. The most recent data release is DR14, covering SDSS surveys I, II, and III, and the first two data releases of the ongoing SDSS IV. The survey footprint covers $\simeq 14000$ square degrees of the Northern sky, focussing on observations out of the Galactic plane.

The SDSS telescope, located at Apache point observatory in New Mexico, features a 2.5 m diameter primary mirror and 3 degree wide field-of-view of (Gunn et al., 2006). SDSS imaging took place over almost a decade for the first 7 data releases. The SDSS camera makes use of five broadband filters. These SDSS filters cover the entirety of the optical, and in order of bluest to reddest are simply known denoted u, g, r, i, and z (or $ugriz$). The transmission profiles for each filter are shown in Fig. 1.13.

SDSS provided vast quantities of spectroscopy for both point- and extended-sources. Rather than being limited to one (or a in some cases a handful) of objects, as is the case for long-slit spectroscopy, SDSS makes use of multi-fibre spectrographs, which permit many spectra to be taken from a single field simultaneously. This involves attaching many fibre-optic cables to a plate in the telescope field-of-view (the targets are selected in advance), with the other end of the fibers directed towards dispersive elements in front of CCDs. Up to DR8, a 640-fiber spectrograph (know simply as the SDSS spectrograph) was used, covering wavelengths from 3800–9200 Å, and with a resolution of $\simeq 2000$. From DR9 onwards, the SDSS spectrograph was replaced with BOSS (Baryon Oscillation Spectroscopic Survey), which has a similar resolution, but a wavelength coverage of 3600–10400Å and instead has 1000 fibers for an increased number of spectra per pointing. Both spectrographs, feature both blue and red optimised CCDs covering the range of the optical. A dichroic beam splitter is used to direct light to the separate detectors. SDSS also features a number of lesser-used instruments, including infra-red spectrograph, which are not used in this work.

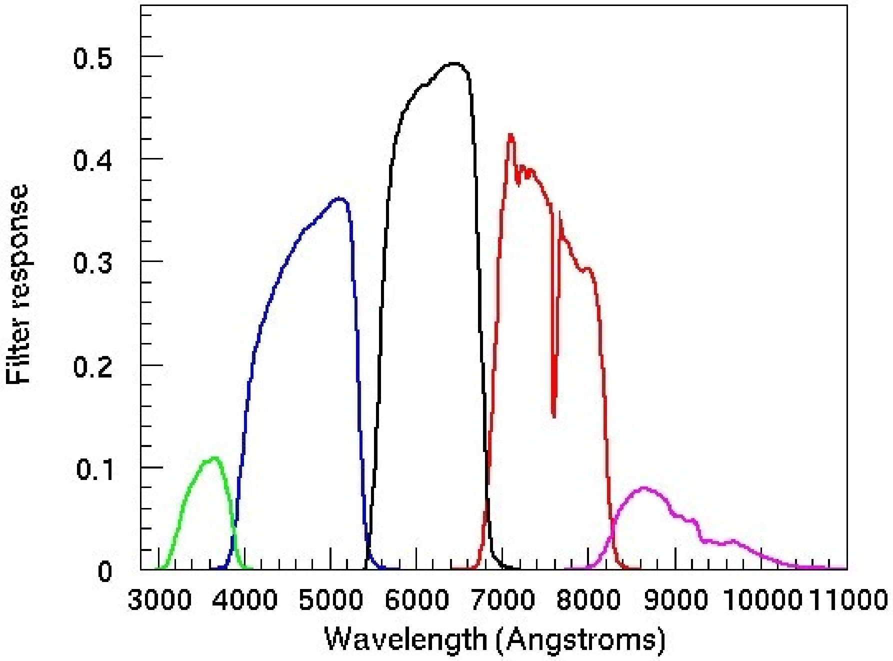

Figure 1.13: Filter transmission curves for the SDSS *ugriz* passbands from left to right. Original figure from `http://www.sdss3.org/instruments/camera.php`.

1.8 Outline of the thesis

This concludes the introduction to white dwarfs and their accompanying planetary systems. The remainder of the thesis is structured as follows. Within Chapter 2 I describe two scientific techniques employed throughout the thesis, specifically the reduction of CCD spectra, and using Bayesian statistics with Markov Chain Monte Carlo methods for analysing data. In Chapter 3, I introduce my sample of 231 cool DZ white dwarfs, the methods developed for their identification, their spectral analysis and some of their basic stellar properties. In Chapter 4, I present my analysis of the DZ sample in terms of characterising the compositions of material within their planetary systems, and exploring some of the most chemically interesting systems in detail. In Chapter 5, I use the wide span of cooling ages for my DZ sample to explore the evolution of remnant planetary systems. In Chapter 6, I change tack, instead exploiting the accreted metals to investigate the magnetic properties of cool white dwarfs. Finally, I present my conclusions in Chapter 7.

Chapter 2

Scientific techniques

In this chapter I introduce two scientific techniques that I employ elsewhere in this thesis. Section 2.1 concerns the reduction of spectroscopic data, which is relevant to Chapters 3 and 6, where I present my own spectroscopic follow up observations. In Section 2.2 I introduce the concept of Bayesian statistics, and how to fit Bayesian models to data using Markov-Chain Monte-Carlo.

2.1 Observational spectra reduction

An astrophysical spectrum represents the interaction of light and matter under various physical conditions at the observed object, and as such spectroscopy is one of the primary technique used to understand astrophysical sources.

Unlike sashimi, spectra are generally not consumed in their raw form, and obtaining a physically meaningful spectrum from the raw data is no simple process. This is demonstrated by Fig. 2.1, which shows two raw CCD images (blue and red arms), compared with the fully calibrated and combined spectrum.[1]

It is clear that the raw data contain many unwanted features which must be corrected for during the reduction process. The most obvious feature in Fig. 2.1 are the numerous vertical lines in the background, particularly in the red arm. These are sky emission lines radiated by atoms and molecules in the Earth's atmosphere. At both ends of the spectrum, little light hits the CCD, yet significant variation is still seen. On short spatial scales we see low level noise, and on the longest scales we see the effects of vignetting and long scale sensitivity variation across the CCD. Across the whole image, but much more noticeable at the ends, are a multitude of bright

---

[1] Usually CCD spectra are oriented with the dispersion-axis in the vertical direction. This is not possible with the constraints of the page. Therefore references in the text to CCD columns and rows refer to pixels in the dispersive and spatial directions respectively.

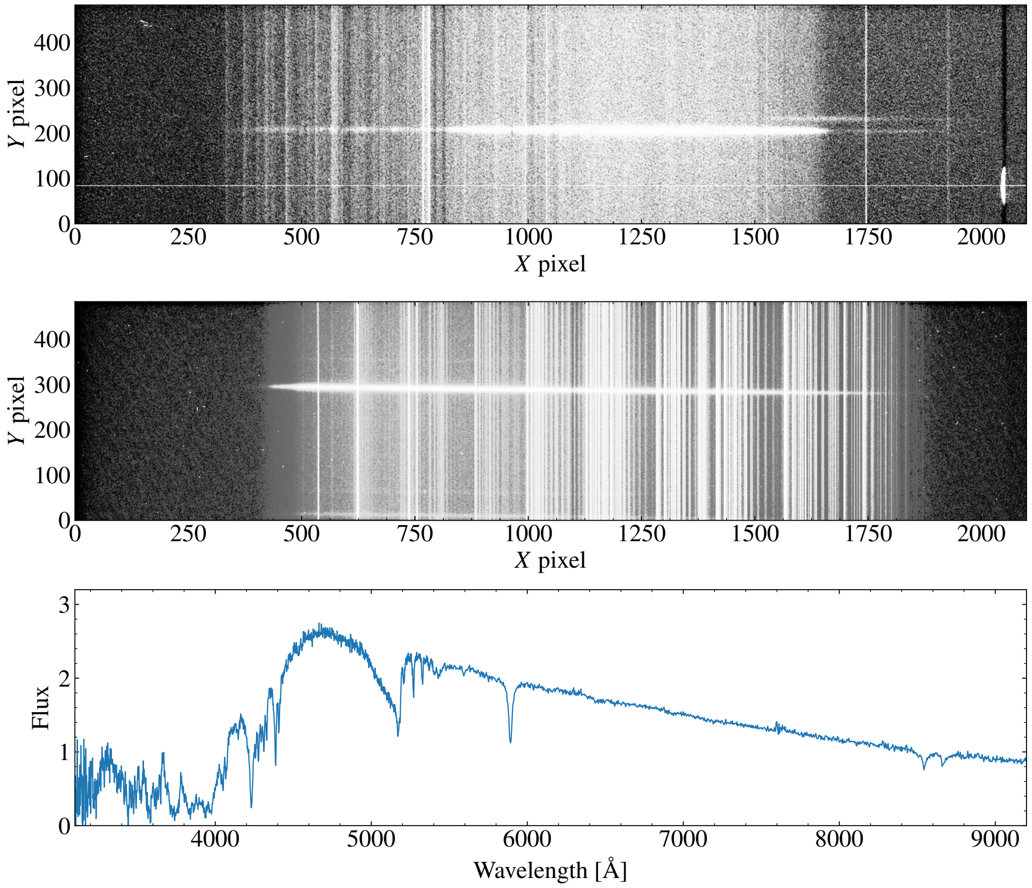

Figure 2.1: Blue (top) and red (middle) CCD frames from the WHT ISIS instrument and the corresponding spectrum after calibration (bottom). For the CCD frames, the dispersion direction is along the x-axis, and spatial direction along the y-axis. The CCD images have been histogram equalised to reveal all of their relevant features. For the reduced spectrum, flux units are in $10^{-16}\,\mathrm{erg\,cm^{-2}\,s^{-1}\,\AA^{-1}}$. The bright horizontal spectral traces in the CCD frames correspond to the dispersed light of the target star. The blue CCD shows a ghost spectrum from an internal reflection of the source onto the CCD. The numerous vertical features, particularly in the red arm are sky emission lines. In this example, the target is the nearby DZ white dwarf SDSS J1535+1247.

spots. These are the result of charged particles hitting the CCD over the duration of the exposure, in this case fifteen minutes. These are usually referred to as 'cosmic rays', although in reality they almost always originate from the radioactive atoms within the surrounding instrumentation (Howell, 2006). These too must be corrected for if they overlap the spectral trace of the target. In this particular instrument, the blue arm exhibits a charge leakage region, which also results in a bright column of pixels. While clearly an unintended feature, this does not affect the reduction since it is sufficiently far from the target spectrum.

In this section I am primarily referring to long-slit spectroscopy, although many of the challenges and techniques described are still relevant to other forms of spectroscopy such as Echelle spectra. In long-slit spectroscopy, a slit is placed in the optical path of the target between the secondary mirror and detector (Howell, 2006). With no other optical elements between the slit and detector, this produces a narrow image on the CCD, with only a few objects along this strip, hopefully including the target. If the slit width is comparable to or lower than the seeing, decreasing the slit width will improve spectral resolution. The downside of using slits narrower than the seeing is that not all of the target's starlight will pass through the slit resulting in a decreased signal to noise ratio. Furthermore, atmospheric dispersion of starlight can cause wavelength dependent flux losses, increasing the difficulty of flux calibration. This can be mitigated by aligning the slit along the direction of atmospheric dispersion, or using an atmospheric dispersion corrector (Howell, 2006).

To form a spectrum, light that has passed through the slit is collimated before being directed to a dispersive element, with the dispersive direction perpendicular to the slit direction. This dispersive element is either a prism, diffraction grating, or a combination of the two (known as a grism). If a grating is used, multiple dispersion orders may overlap, in which case a filter is needed to select the desired order.

Finally, photons arriving at the CCD during integration liberate electrons from the semiconductor into a potential well. At the end of integration, the photoelectrons are shuffled into a readout device. The readout process does not directly count electrons in each pixel. Instead an analogue voltage is measured designed to be proportional to the number of electrons. This voltage is then digitised into Analogue Digital Units (ADUs) which are generally referred to simply as counts (Howell, 2006). The mean ratio between counts and photoelectrons is the gain, although this is typically designed to be close to one. Because of the analogue step in this process, readout results in additional noise that must be included a component of measurement uncertainties. The noise can be mitigated by reading out the detector more slowly, or in other words, measuring the voltage across the pixel over a longer time span. Readout noise is visible in Fig. 2.1 as the uncorrelated noise at the ends of the CCDs. A final note on readout is that at photoelectron numbers in the region of several 10 000, pixels starts to saturate and the gain becomes non-linear. If a high signal-to-noise (S/N) ratio is desired, multiple exposures can be taken such that counts remain in the linear regime. The final result after readout are images like those in Fig. 2.1.

The process of spectral calibration consists of 7 main steps, which are detailed in the following subsections.

2.1.1 Bias subtraction

In CCD detectors, a bias voltage is applied to the readout chip such that even with an integration time of zero, a few thousand counts are still measured. One reason for this relevant to astronomers is that it ensures readout noise errors are not clipped during digitisation, since ADUs cannot be negative. Correction to the data requires taking bias images, which are essentially zero-second exposures, i.e. readout of the chip is performed without charge integration (Howell, 2006). This allows the measurement of both the bias level and the readout noise across the chip. This can be done in the day time and so typically many tens of bias are taken. The readout noise is estimated by simply selecting a sufficiently large region in one of the images and taking the standard deviation. The bias level may vary by a few counts across the chip, and so to estimate the average, one stacks all bias frames and takes the median producing a "master bias" image, which is relatively free of readout noise. The master bias is then subtracted from all science and calibration images which is referred to as debiasing.

2.1.2 Flat fielding

The pixels across a CCD do not have precisely the same sensitivity, and so pixel-to-pixel variations must be corrected for, in a process referred to as flat fielding (Howell, 2006). While flat fields are required for both photometry and spectroscopy, for spectroscopy the calibration source must have a smooth spectral response. Typically a tungsten filament lamp is used as this has a spectral profile close to a black body.

A spectrum is taken of the lamp projected onto a diffusely reflecting surface. The 2D frame is then the combination of the lamp spectrum and the throughput in the dispersive and spatial directions, with the pixel-to-pixel variations and readout noise superimposed on this. Often many flat fields are needed, and potentially more than one hundred if good sensitivity at blue wavelengths is needed (which is often

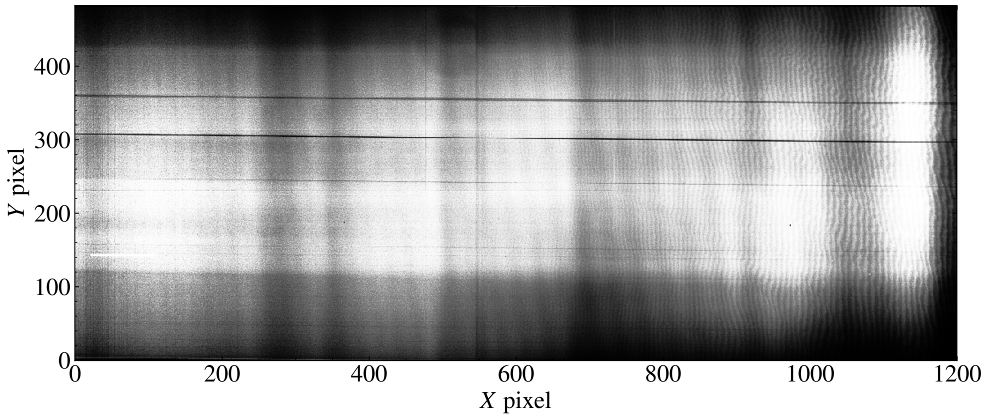

Figure 2.2: A flat field for a red-optimised CCD. A variety of features are seen which includes lower sensitivity columns, fringing – especially towards the right of the frame, and reduced throughput at the extremes of the spatial direction (towards the top and bottom of the image). Histogram normalisation has been applied for increased contrast.

the case for spectra presented in this thesis). This is because the tungsten lamp will contain few counts at blue wavelengths but increases rapidly towards redder wavelengths. Therefore, exposure times must be limited so that a single flat field does not saturate at red wavelengths, but sufficient exposures must be taken to ensure high signal-to-noise at blue wavelengths.

After bias subtraction, these flat frames are scaled to the same level, and the median taken producing a *masterflat* frame. To make the masterflat actually flat the spectral response of the lamp must be removed. The masterflat is collapsed along the spatial direction, and the resulting 1-D profile fitted with a lower-order polynomial or spline. The masterflat is then divided by the polynomial/spline in the dispersive direction, with the resulting image having a mostly constant value, with the exception of pixel-to-pixel variations. An example of masterflat field is shown in Fig. 2.2.

Often a reciprocal image of the flat-field is made, and is referred to as a balance-frame. The balance frame can then be used to multiply the science frames during the extraction process.

2.1.3 Sky subtraction

Spectroscopy taken from ground-based telescopes will rather obviously be superimposed with a spectrum of the Earth's atmosphere. This must be carefully subtracted from the data as part of the extraction process (Howell, 2006), which is described in more detail in Section 2.1.4. However the first steps of extraction are necessary to be discussed at this point.

The process of sky subtraction is demonstrated graphically in Fig. 2.3. Firstly the position of the target spectrum across the dispersive direction, or trace, is determined by fitting a polynomial or spline to the peak in spatial pixels. Two sets of regions are then selected. Firstly a region bounding the spectrum profile of fixed width, but following the spectral trace. This region is used for both sky subtraction and extraction. Secondly, two regions on either side of the spectral trace are selected, again with their widths fixed but following the trace of the target spectrum. These regions contain only the sky spectrum, whose purpose are to estimate the sky contribution in the region in between, and therefore remove it from the spectrum profile.

For this purpose, a polynomial is fit to each row in the sky region, where higher-order polynomial terms may be necessary for very wide sky regions. The polynomial is then evaluated for the pixels in the region containing the spectrum profile. The result is an image in the profile region containing the expected sky background, which can then be subtracted from the data during the extraction process. This method is especially import in the case where skylines have a significant degree of curvature, or are misaligned with the CCD pixels. In these cases, some CCD rows will show rapidly increases or decreases in flux, where the row crosses the boundary of a sky emission line.

2.1.4 Extraction of the 1D spectrum

The next stage of the reduction is to turn the 2D CCD spectrum into a 1D spectrum. In all previous steps, the uncertainties in readout, flat-fielding and sky-subtraction should have been tracked, and so the uncertainty in the 1D spectrum can also be estimated during extraction.

The simplest extraction method, sometimes called 'normal' extraction, is to simply sum the counts along each row in the target spectrum. While this provides an unbiased estimate of the mean flux in each pixel row, it tends to result in poor signal-to-noise ratios for faint objects, as the variance in the sum is uniformly weighted for pixels with and without significant amounts of the target flux. Therefore making the extraction region wider always increases the variance in the sum, but making this region too narrow will eventually start to remove pixels containing the target.

One alternative extraction method is to perform a weighted Gaussian profile fit to each row in the spectrum, where the Gaussian centroid is known from the spectral trace determined at the beginning of Section 2.1.3. The total flux is then

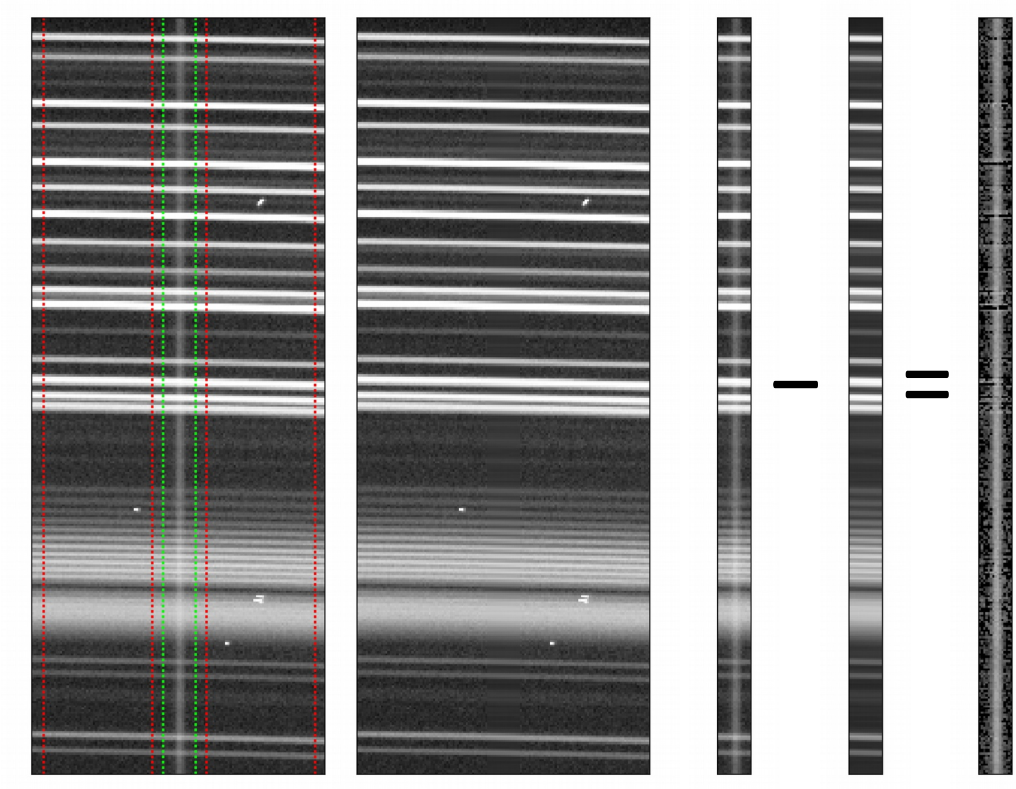

Figure 2.3: **Left**: A section of a CCD frame with strong sky emission lines running horizontally. Note that these do not run exactly parallel to the CCD and have some small amount of curvature. Sky fitting regions are indicated by the red dotted lines, with the spectrum region indicated by the green dotted lines. **Centre**: Each row is fitted with a polynomial to estimate the flux in the spectrum region. For demonstrative purposes, the target region has been replaced with the estimated sky flux, which can just be made out due to the absence of readout noise. **Right**: The estimated sky flux is subtracted from the target region leaving only the target flux. Some of the brightest skylines do however leave residuals in the data, which can be partially removed by co-adding multiple spectra.

proportional to the product of the height and width of the fitted Gaussian. In principle this method can be used to measure fluxes in saturated spectra, by only fitting the unsaturated wings.

In the case of faint targets, where every photon counts, a better technique is needed. The optimal-extraction algorithm, developed by Horne (1986), essentially solves this issue, and has become the standard algorithm for spectral extraction. The algorithm is optimal in the sense that it performs a weighted sum across a CCD row, where the weights are chosen to give the maximum possible signal-to-noise ratio. This is achieved by first estimating the flux fractions for pixels along each row. One way to do this is Gaussian profile fitting along rows as described previously, but then fitting those Gaussians with polynomials along columns to smooth out row-to-row noise, and then finally renormalising, so that each row sums to 1. The result is a new image, P_{xy}, where rows and columns are indexed by x and y respectively. If the sky-subtracted data is D_{xy}, and its variance V_{xy}, then Horne (1986) demonstrates that the optimal flux estimate in each row, f_y^{opt}, is given by

$$f_y^{\mathrm{opt}} = \frac{\sum_x P_{xy} D_{xy} / V_{xy}}{\sum_x P_{xy}^2 / V_{xy}}, \tag{2.1}$$

and the variance of f_y^{opt} by

$$\mathrm{var}[f_y^{\mathrm{opt}}] = \frac{1}{\sum_x P_{xy}^2 / V_{xy}}. \tag{2.2}$$

In the case where the image is background dominated (readout noise or sky dominated), improvements in signal-to-noise of 30 % are typical in comparison to normal extraction.

While (2.2) cannot be directly improved, the results do dependent on the choice of method used to calculate P_{xy}. Marsh (1989) devised an improved method for calculating P_{xy}, which is particularly beneficial in the case where the spectral profile is not parallel with the CCD columns and when the profile shows curvature.

For the faint white dwarfs encountered in this thesis, the optimal extraction algorithm is necessary to achieve the best results. Thus, in the chapters where I present data reduced by myself, I always use the combination of the Horne (1986) and Marsh (1989) methods (found in the PAMELA packages of the STARLINK project).

At this point in the reduction we now have 1D spectra, however the data units are in terms of pixel and counts, rather than wavelength and energy-flux. This is demonstrated in Fig. 2.4, where some of the spectra used to produce the final

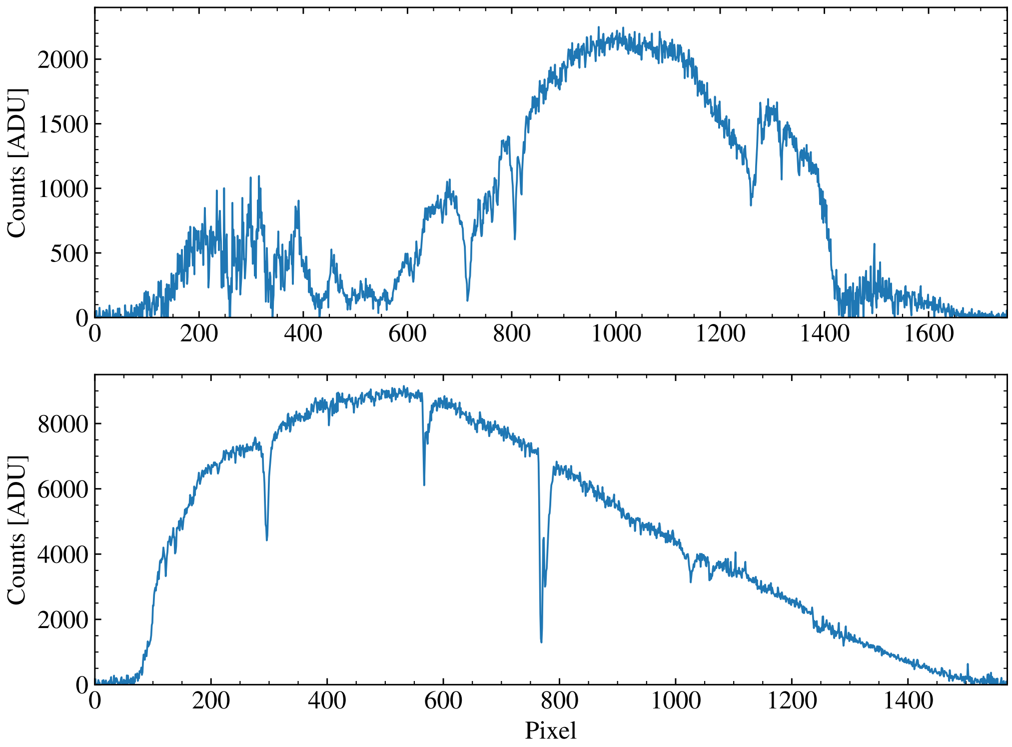

Figure 2.4: Optimally extracted spectra for SDSS J1535+1247, with the blue and red spectra displayed at the top and bottom respectively. These same data were used to produce the fully calibrated data in Fig. 2.1, demonstrating the significant differences between this intermediate stage and the final product. Note that due to the use a dichroic-beam splitter, the blue and red data overlap at their extremities (where the throughput for the dichroic is approximately equal in the red and the blue).

spectrum in 2.1 are shown. Furthermore, huge differences are seen in the relative scaling as a function of wavelength, especially at either end of the data. This is the result of wavelength dependent throughput, which drops off rapidly at extremes of wavelength in either direction. For all spectral calibration in this thesis, I perform all subsequent calibration steps using the software MOLLY which is included in the STARLINK project.

2.1.5 Wavelength calibration

Calibration of counts to fluxes requires knowledge of the wavelengths for each spectral pixel, therefore wavelength calibration is always the first step in processing the 1D spectra. This step is not particularly difficult, but is generally time consuming.

Spectrographs always include an arc-emission (gas-discharge) lamp, which emits a spectrum rich in sharp lines with well known, stable wavelengths (Howell, 2006). Ideally the lamp will have many lines spanning the whole range of the instrument setup being used.

If extremely precise wavelength calibration is not particularly important, it may only be necessary to take a single exposure of the arc lamp at the beginning of the night. If however, the goal of the observations are high precision radial-velocity measurements of the target star, then arc spectra will need to be taken throughout the night. In the most extreme case, each observation should be bracketed by a pair of arc spectra. This is necessary, as any flexure of the telescope as it moves across the sky will cause subtle changes in which wavelengths fall onto each pixel.

The 2D arc spectra, similar to sky spectra appear as a multitude of horizontal lines (cf. Fig. 2.3). For each target spectrum the arcs are extracted over the same pixel range, producing a variety of 1D arc-emission spectra.

To complete the wavelength calibration, one of the arc spectra is selected and plotted. Then as many of the lines as possible are identified against a comparison chart (referred to as an “arc-map”). For each of these lines, the centroid in terms of pixel and it’s wavelength is recorded. The full list of pixel-wavelength pairs is then fit with a polynomial to provide a conversion between wavelength.

Even if only one arc exposure was taken, each target spectrum, will require an associated 1D arc extracted over the same pixel range as the target. Depending on the science goals, the original wavelength solution may be inappropriate to apply to all objects for a whole night. Instead, the centroids for each emission line are tweaked with respect to the original identifications, and the pixel-to-wavelength polynomial refit to provide a new wavelength solution that can be applied to the target spectra.

In the case of multiple arcs per night, the number of line tweaks and refits will be significantly increased, but this is typically automated in calibration software. However, to actually apply the wavelength solution to the target spectra, many choices will be available, which can be filtered by the time they were taken, on-sky position, and extraction position. Where the very highest wavelength-precision is required, and each target exposure is bracketed by a pair of arcs, these polynomial coefficients can be interpolated to target's central time of exposure.

In some cases, arc-lamp exposures may not provide sufficient accuracy. In these cases, the sky spectrum (which was subtracted previously) can itself be used as a calibration source. Using sky spectra has the advantage that they are observed simultaneously with the target, and so include all the same systematic effects such as CCD flexure. However, most strong sky emission lines appear towards the red end of the optical, whereas the blue half of the optical is mostly free from sky features. The difference is seen clearly in Fig. 2.1, demonstrating that sky emission lines are only an effective option for wavelength calibration of red sources.

One final, but very important step is required to complete wavelength calibration: heliocentric correction. The Earth orbits the Sun at $\simeq 30\,\mathrm{km\,s^{-1}}$, and an observer at the Earth's equator will also experience an additional motion of $\simeq 0.5\,\mathrm{km\,s^{-1}}$around the Earth's rotation axis. This induces blue/redshifts in the data relative to the Solar reference frame. Correcting this requires information on both the time of day and time of year, as well as the location of the observatory on the Earth and the position of the target on the sky. Once performed, this allows all data to be compared in a common frame-of-reference. If one's data ever appears to show RV variability occurring at a period of 1 year or 1 sidereal day, to avoid any possibility of future embarrassment, the first thing to check should always be whether heliocentric correction was correctly applied to the data.

2.1.6 Flux calibration

With the wavelengths calibrated, the fluxes also require correction. To do this, at various times throughout the observing night, a 'standard star', or 'flux standard', is also observed. Ideally, this should be at a similar elevation above the horizon as the target, and so should suffer from similar systematic effects. Standard stars are chosen on the basis that they have simple, stable spectra that can be modeled accurately. Therefore the absolute spectrum of the standard star can be calculated, which, when compared with its observed spectrum (in terms of counts and wavelength) provides a wavelength-dependent correction (Howell, 2006). The flux-solution, which is essentially a rescaling factor as a function of wavelength, can then be multiplied with all spectra.

Flux calibration is generally the least accurate part of spectral-reduction, where accuracy better than a few percent is rarely possible. However, there are a few things that can be done to improve accuracy. If accurate calibration of blue wavelengths is required, then choosing a flux standard with high effective temperature is desirable, as these will be brightest at blue wavelengths, where instrumental throughput is often at its poorest. For this reason, hot DA white dwarfs make excellent flux standards, but also because modeling their absolute spectra can be achieved through fitting only the profiles of the hydrogen Balmer lines. With models and uncalibrated standard-star spectra in hand, fitting their ratio can be further improved by masking wavelength regions with strong spectral features. Finally, if the ratio curve varies rapidly towards the extremes of wavelength, it can be more accurate to fit its logarithm than the ratio itself.

2.1.7 Telluric removal

Because spectra acquired from the ground must necessarily look through the Earth's atmosphere, molecular absorption bands, particularly from water, will be present in the observed spectra. These are referred to as telluric absorption, or simply tellurics, where two such features are clearly seen in Fig. 2.4 at pixel values of 570 and 770. Note that in the bottom panel of Fig. 2.1, these have been removed (although some residuals remain near 7600 Å).

Telluric removal is generally an optional feature during reduction, i.e. if the affected wavelengths are not of scientific importance, then there is little to be gained by removing them. However, it is may be at least aesthetically pleasing to remove them anyway.

Generally this is performed as an additional step during flux calibration, as it also requires the use of the standard star. To remove tellurics, first the standard star spectrum is continuum normalised to one, with only stellar and telluric absorption features remaining. Then all wavelengths, except for those containing tellurics, are fixed to exactly one, which is needed to avoid inducing further noise into the target spectra at wavelengths without tellurics. Additionally any noisy pixels that exceed one should be clipped as telluric absorption strictly removes flux. The resulting spectrum is simply called the telluric spectrum. When flux calibrating spectra, the target fluxes are typically divided by the telluric spectrum scaled by the airmass[2] of the target and standard. Alternatively, the scaling of the telluric spectrum can

---

[2] Airmass is a dimensionless quantity expressing the column density of air observed through, compared with the amount at zenith, which by definition always has an airmass of 1.

be fitted to the target during flux calibration to best remove absorption features.

Hopefully this section has demonstrated the challenges encountered in converting raw CCD frames into fully calibrated, scientifically useful spectra, and that care must taken to get the very most out of observational data.

2.2 Bayesian statistics and MCMC

The process of fitting a model to some data is a sufficiently broad concept that it constitutes its own field of research. However, whatever approach is used to do this, when we fit models to data, fundamentally we are only asking a few basic questions.

Firstly, we might ask “Which regions of the model’s parameter space best describe my data?”. This is generally answered by defining some goodness-of-fit metric which we attempt to optimise with respect to the model parameters, and then looking at the sensitivity of the optimal value of the metric to adjustment of those parameters. One of the most common methods to achieve this is to minimise the χ^2 between the data and model, and to then calculate the curvature around the χ^2-minimum, in effect providing estimates of optimal parameter values and their (co)variances.

A second question could be “Given an optimised model, does this model actually describe the data well?”. In the case of a poorly chosen model, this may be apparent ‘by-eye’. For χ^2 minimised fits, the reduced χ^2 ($\chi^2_{\rm red}$), which is χ^2 divided by the number of degrees-of-freedom, is used as indicator of whether a best-fit is a good fit. In this case a $\chi^2_{\rm red}$ close to one indicates an acceptable fit. $\chi^2_{\rm red}$ much greater than one suggest either underestimated data uncertainties or a poor choice of model, whereas values smaller than 1 suggest errors on the data are overestimated.

A final question may be “Given an optimised model that is in good agreement with the data, is this model better than some alternative model?” Often this alternative model is the null-hypothesis, which is generally a subset of the model we are trying to test. An simple astrophysical example is measuring a weak emission-line in a spectrum. The null-hypothesis is that there is no emission line, which could consist of just fitting to the continuum level of the data with some low-order polynomial. The alternative model, could then consist of the same degree polynomial added to a Gaussian line profile fixed to the expected wavelength and width of emission. The χ^2 for both models can then can be compared using a statistical method such as an F-test to quantify whether an emission line model is a significant improvement over the null hypothesis.

In recent years the adoption of Bayesian statistics has become prevalent within the astrophysics community (Sharma, 2017), due to its ability to accurately estimate model parameters and their uncertainties by including prior information which is otherwise ignored in a typical least-squares fit. In Chapter 6, I use Bayesian techniques to fit models to magnetic white dwarf spectra, and so these techniques are detailed here.

2.2.1 Bayesian statistics

In frequentist statistics, probability is interpreted as the rate that an event will occur. For example, if we consider a single radioactive atom, and ask whether that atom will decay during some time interval, the frequentist will measure an ensemble of identical atoms and measure the decay rate. However, returning to the single atom, the frequentist may say that the atom either decays with 100 % probability or it does not.

In Bayesian statistics, probability is instead viewed as a degree of belief, which to many people is the most intuitive way to think about probability. In the previous example about nuclear decay, a Bayesian could state that an atom has a 10 % chance of decay during 10 s, whereas a frequentist would be compelled to consider an ensemble of atoms and determine expectation value for the fraction of atoms decaying over 10 s.

However, Bayesian statistics is more than an interpretation. Our degree of belief in something typically comes from a variety of sources, which on their own may not be particularly informative, but when combined, provide a more refined understanding. This ability to combine degrees of belief is encoded in the famous Bayes' theorem (Koch, 2007) which is typically written

$$P(A|B) = \frac{P(B|A)\,P(A)}{P(B)}. \tag{2.3}$$

In this notation $P(A)$ simply refers to the probability of A being true, while $P(A|B)$ refers to to the probability of A being true *given* that B is true.

As a example, let $P(J)$ equal the probability that it is January, i.e. 1/12, and let $P(S)$ be the probability of it snowing on any given day, independent of the time of year, which we will take to be 1/1000 – or about once every 3 years (about right for the UK at least). We can now consider the contingent probability that it will snow given that it is a day in January, $P(S|J)$, which let's say is 1/200 (or a 14 % chance it will snow at least once over the whole of January).

Now let us imagine you have awoken one day with amnesia, and there is only one question on your mind, "Is it January?". Initially, the *prior probability* of this being the case is just $P(J)$. However you open the curtains and see that it is snowing. We can now update our knowledge of whether it is January using Bayes' theorem. In other words we calculate $P(J|S)$, which using the above numbers, we arrive at 5/12. This is referred to as the *posterior probability* of it being January. Perhaps you find one further piece of evidence, a calendar on the wall, set to the month of December. We can then reapply Bayes' theorem in light of this new information, using our previous posterior as our new prior – a process known as Bayesian updating. We now find that it is unlikely to be January, although perhaps the Calendar has not been updated yet.

In the above example, both J and S, are discrete quantities whose probability distributions can only take on the values of True or False. However Bayes' theorem, and Bayesian statistics can be extended to continuous distributions, which is of great practical importance to the modeling scientific data.

A common use-case is that we have some $\vec{x}$ and $\vec{y}$ data vectors with the $\vec{\sigma}$ as the y-uncertainties. We then wish to fit a model, M, to our data, where M takes a parameter vector, $\vec{\theta}$, as an argument. Essentially, we wish to calculate the probability distribution for $\vec{\theta}$, given our data, $P(\vec{\theta}|\vec{x},\vec{y},\vec{\sigma})$. Applying Bayes' theorem we then have

$$P(\vec{\theta}|\vec{x},\vec{y},\vec{\sigma}) = \frac{P(\vec{\theta})\,P(\vec{y}|\vec{\theta};\vec{x},\vec{\sigma})}{P(\vec{y}|\vec{x},\vec{\sigma})}. \tag{2.4}$$

The first term, $P(\vec{\theta})$, is our prior knowledge of $\vec{\theta}$, which can be interpreted as the expected distribution of our parameters in the absence of additional information. For example, if the white dwarf mass was a free parameter in a model, in the absence of any data, our current knowledge for the mass is that it is drawn from the observed white dwarf mass distribution (e.g. Tremblay et al., 2016), and so this distribution can be used as a prior on the model. Compared with fitting via χ^2-minimisation, the use of priors has the effect of weighting the results to more commonly encountered values. In the previous example, extremely high or low white dwarf masses are disfavoured unless the data strongly supports one of these cases. Furthermore, the prior can restrict impossible results for regions of parameter space with zero probability density. For instance, a basic least-squares fit may indicate a mass of $1.3 \pm 0.2\,\mathrm{M}_{\odot}$, naively indicating some chance of a white dwarf exceeding the Chandrasekhar mass. Applying a suitable prior, will force the result to conform with reality, thus making the measurement more accurate. Note that this suggests a non-Gaussian parameter distribution, and so a simple (mean)$\pm(1-\sigma$ error) may be an unsuitable way to communicate the result.

The next term $P(\vec{y}|\vec{\theta};\vec{x},\vec{\sigma})$, is the likelihood of our data. This can be described as the expected distribution of data for fixed parameter values and measurement errors (Cowles, 2013). For data with normally distributed uncertainties, the likelihood reduces to a simple form. For a single data-point, it's likelihood is simply

$$P(y_i|\vec{\theta};x_i,\sigma_i) = \frac{1}{\sqrt{2\pi}\sigma_i}\exp\left[-\frac{\left(y_i - M(x_i,\vec{\theta})\right)^2}{2\sigma_i^2}\right]. \tag{2.5}$$

The likelihood for the full data-vector is simply the product of likelihoods for our N data points,

$$P(\vec{y}|\vec{\theta};\vec{x},\vec{\sigma}) = \frac{1}{(2\pi)^{N/2}}\prod_i^N \frac{1}{\sigma_i}\exp\left[-\frac{\left(y_i - M(x_i,\vec{\theta})\right)^2}{2\sigma_i^2}\right]. \tag{2.6}$$

To simplify, we can drop the normalising terms, and move the product inside the exponential, which becomes a sum

$$P(\vec{y}|\vec{\theta};\vec{x},\vec{\sigma}) \propto \exp\left[-\sum_i^N \frac{\left(y_i - M(x_i,\vec{\theta})\right)^2}{2\sigma_i^2}\right]. \tag{2.7}$$

Written in this way, it is now clear that the sum can be rewritten in terms of χ^2, and so (2.7) reduces to

$$P(\vec{y}|\vec{\theta};\vec{x},\vec{\sigma}) \propto \exp(-\chi^2/2). \tag{2.8}$$

Therefore, maximising the likelihood is identical to minimising χ^2.

The final term, $P(\vec{y}|\vec{x},\vec{\sigma})$, is called the *evidence* and strictly speaking, should be written as $P(\vec{y}|\vec{x},\vec{\sigma};M)$, or the probability of our data given our model, M (Cowles, 2013). Note that unlike the other terms in (2.4) this is not a distribution, but a scalar value (since its arguments are all constants). The evidence can also be seen as a normalising constant for the posterior, assuming the prior and likelihood are both correctly normalised. In the case of fitting two competing models, the ratio of their evidences, tells us which model is statistically more probable. In practice the evidence is difficult to calculate, as it requires integration of $P(\vec{\theta})P(\vec{y}|\vec{\theta};\vec{x},\vec{\sigma})$, along all dimensions of $\vec{\theta}$, which is numerically expensive.

Often we only have a single model we wish to fit, and so this is not an issue.

Furthermore, the absolute scaling of the posterior is not important if all we really want is the shape of the distribution. In logarithmic form the posterior distribution is then written as

$$\log(P(\vec{\theta}|\vec{x},\vec{y},\vec{\sigma})) = \log(P(\vec{\theta})) - \tfrac{1}{2}\chi^2 + \text{const}, \tag{2.9}$$

where all proportionality terms are relegated to the trailing constant. If the priors on each component of $\vec{\theta}$ are independent, then we can also express (2.9) as

$$\log(P(\vec{\theta}|\vec{x},\vec{y},\vec{\sigma})) = \sum_i \log(P(\theta_i)) - \tfrac{1}{2}\chi^2 + \text{const}. \tag{2.10}$$

Computationally and practically, log-probabilities are much easier to deal with than the probabilities themselves. For instance, with a dataset of 30 000 points, the minimised χ^2 is also expected to be $\simeq 30\,000$ (for a good fit). The unnormalised likelihood, $\exp(-\chi^2/2)$, is then $\simeq 4 \times 10^{-6515}$, which can be represented by neither double precision nor quadruple precision floating-point numbers. The log-likelihood is simply $-15\,000$, which presents no such problem. Furthermore, multiplying probability distributions (i.e. different priors and the likelihood) and probability ratios, translate to simple addition and subtraction respectively. Finally, many commonly encountered probability distributions contain exponentials and so, ignoring normalisation factors, may even be simpler to write down and faster to compute in logarithmic form, e.g. the normal and exponential distributions.

This now gives us a convenient way to write down the posterior distribution for $\vec{\theta}$, for the typical case where our data are normally distributed deviates, and we are only fitting a single model. However, being able to write down the functional form for a distribution does not lead to an easy way to estimate the mean/median or (co)variances for the different components of $\vec{\theta}$. If we could only draw samples from our posterior distribution, it would then be a simple process of calculating the mean and variance of each parameter, and the covariance between each pair of parameters.

2.2.2 Markov Chain Monte Carlo

Markov Chain Monte Carlo (MCMC) is a numerical technique which is precisely suited to the problem of drawing samples from arbitrarily complex distributions (Cowles, 2013). There are many different implementations of MCMC, but they all share the same fundamental properties. A chain is constructed where each step in the chain is dependent only on the previous one (the Markov condition), but where the steady state equilibrium of the chain is distributed according to a predefined target distribution (Cowles, 2013). This essentially allows one to use the end of the chain as a method for drawing samples from the target distribution.

Typically, the chain is initialised somewhere near the distribution maximum (but probably out of equilibrium) and the chain is allowed to evolve. Successive steps in the chain are calculated according to a proposal distribution around the current position. If the probability density is higher at the proposed position, then the jump takes place. If on the other hand the density is lower, it may still take place with some probability according to the ratio of the current and proposed densities. It is this process that allows the chain to initially move towards the distribution maximum (known as the burn in phase), but then take on the target distribution at equilibrium.

In the relevant sections of this work I use an implementation of MCMC called EMCEE which is written in the PYTHON programming language (Foreman-Mackey et al., 2013). EMCEE uses an ensemble sampler to perform MCMC, which means at any given step in the chain consists of a set number of walkers spaced throughout the parameter space (Goodman & Weare, 2010). From another point of view, each walker has its own chain, however the chain trajectories are *not* independent. To move between positions i and $i+1$ a jump is proposed from the distribution of all other walkers at step i. This has the advantage that the jump distribution takes on the shape of the target distribution, significantly reducing the time taken to burn in the chain, as well as limiting the number algorithm parameters to two, i.e. the number of steps and the number of walkers. By comparison, in a traditional Metropolis-Hastings implementation of MCMC, the jump distribution is usually from a fixed covariance matrix that the user must tune by hand before running the MCMC routine.

In practice EMCEE is easy to use. The user provides a function for calculating the log-probability of the target distribution (i.e. equation (2.10)), which itself takes the parameter vector as an argument.

The user must also provide an initial walker distribution for the zeroth step, where a typical choice is a "Gaussian-ball" near the maximum of the target distribution. The ensemble is then allowed to evolve over a set number of steps. The result is a 3-dimensional array of shape N_{walkers}, N_{steps}, and $N_{\text{parameters}}$.

After the chain has burnt-in, we can then form a set of independent samples from the target distribution, although care must be taken. All walkers in a given step of the converged chain can be considered as independent samples. However these samples are correlated with those from the immediately previous steps. Thus if we require more samples than N_{walkers}, we can do this by combining multiple steps in the chain, *but* they should ideally be separated by a sufficient number of steps to ensure independence.

With the generated samples it is now possible to determine the marginal distributions of the data. These are the distributions for a single component of $\vec{\theta}$ integrated over all of its other dimensions Cowles (2013). For instance if $\vec{\theta}$ is N-dimensional, the marginal distribution of θ_1 is given by

$$P(\theta_1|\vec{x},\vec{y},\vec{\sigma}) = \int P(\theta_1,\theta_2,\theta_3,\ldots,\theta_N|\vec{x},\vec{y},\vec{\sigma})\,\mathrm{d}\theta_2\,\mathrm{d}\theta_3\ldots\mathrm{d}\theta_N. \tag{2.11}$$

While this looks complicated, with MCMC generated samples, the distribution of θ_1 is found by simply ‘ignoring’ the values along the other components of $\vec{\theta}$. The marginal distribution can then be displayed via a histogram of the samples. The width of the marginal distribution automatically contains the contributions in variance from all other parameters, regardless of whether the other parameters are scientifically interesting. These uninteresting but necessary parameters of the model are referred to as nuisance-parameters (Cowles, 2013). We can also investigate the marginal joint-distributions between a pair of parameters, i.e.

$$P(\theta_1,\theta_2|\vec{x},\vec{y},\vec{\sigma}) = \int P(\theta_1,\theta_2,\theta_3,\ldots,\theta_N|\vec{x},\vec{y},\vec{\sigma})\,\mathrm{d}\theta_3\ldots\mathrm{d}\theta_N. \tag{2.12}$$

The 2D marginal distributions are useful to investigate the covariance between two parameters. These can be shown graphically as either a scatter plot, or 2D histogram.

2.3 Astrophysical example

To demonstrate the power of fitting with Bayesian techniques, I have constructed a simple example that might encountered in an astrophysical setting: measurement of a spectral emission line. The functional form I have chosen is a straight-line (for the continuum) added to a Gaussian profile, which has the functional form

$$y = C + mx + A\exp\left(-\frac{1}{2}\left[\frac{x-x_0}{w}\right]^2\right), \tag{2.13}$$

where C, m, A, x_0, and w are the free parameters of the model. Note that this is a model is non-linear in the parameters, and even for a least-squares fit cannot be fitted analytically. However, if the values of x_0 and w could be fixed, the model would be linear in the remaining parameters.

I initialised this by generating some fake data, with true parameters of $C = 2$, $m = -0.2$, $A = 4$, $x_0 = 1.6$, and $w = 0.6$. I sampled 30 uniformly spaced x-values between -2 and 5. The corresponding y-values are Gaussian deviates around (2.13) evaluated at the "true parameters".

For priors, I gave the C, m parameters uniform prior over all space, i.e. all values are weighted equally. For A and w, I gave uniform priors for all positive values, where the probability density is set to zero for negative values, restricting the fit from fitting negative amplitudes and widths for the emission line. Strictly speaking, these are all "improper" prior distributions since they cannot be normalised. Despite this, the posterior distribution, constructed according to (2.10), still has a finite integral. As an example of integrable and non-trivial prior, I gave the emission line centroid, x_0, a "laboratory measurement" of 1.60 ± 0.01, which is included in the fit as a Gaussian prior.

For the MCMC fit, I initialised 100 walkers, with each parameter normally distributed close to the true-values, and with widths within an order of magnitude of the final results. I then ran the MCMC for 300 steps to allow for sufficient burn-in of the chain. In Fig. 2.5, 20 of the walkers are plotted showing that the chain is converged for all parameters by about step 100 (the initial distributions can be seen from the spread of walkers at step 0). I therefore conservatively ignored the first 200 steps (dashed blue line), with samples chosen at every 10 of the remaining steps, resulting in 1000 independent samples of the posterior distribution.

The marginalised distributions of these 1000 samples are displayed in Fig. 2.6. While the histograms, show the distributions integrated over all other parameters, the scatter plots show the joint-distributions between each pair of parameters (again marginalised over the remaining parameters). The m vs. C and w vs. A panels show small amounts of negative correlation indicating that if one of the parameters in each pair is changed by small positive amount, the other from the pair must also be changed by a small, but negative amount to maintain a good fit to the data. The true values are indicated by the red dashed lines, which demonstrate that the fit is generally within about 1-σ of the true parameter values – the A parameter is closer to 2-σ away, but this is not a rare occurrence for a five parameter model.[3] Note that in principle, we do not need to plot all dimensions of the parameter-vector, for instance we might only be interested in the line parameters, A, x_0, and w. In this case the continuum parameters, m and C would be nuisance-parameters – necessary to correctly estimate the errors in the line parameters, but perhaps uninteresting in their own right. Therefore it may be appropriate to plot 2.6, only showing the marginal distributions of the parameters of interest.

Finally in Fig. 2.7 the data (black points) with true model (red) and fit model (blue) are shown. The blue shaded region indicates the 2-σ confidence region of the fit. A highly useful property of generating samples from the fit, is that they can be manipulated to calculate other useful quantities ensuring correct propagation of uncertainties and covariances. For spectral lines, one such quantity is the equivalent-width. This is defined as the width of a rectangle with height equal to 1, and area equal to that of the spectral line after continuum normalisation. In the case of our model in equation (2.13), the equivalent width, EW, is calculated as

$$\mathrm{EW} = A \int_{-\infty}^{+\infty} \frac{\exp\left(-\frac{1}{2}\left[\frac{x-x0}{w}\right]^2\right)}{C+mx}\,\mathrm{d}x. \tag{2.14}$$

By calculating the equivalent width for each independent posterior sample we obtain a distribution of equivalent-widths, whose mean and standard deviation provide a measurement. From the example, the true values lead to an equivalent-width of 3.60, with the MCMC samples providing a measurement of 3.73 ± 0.29 – within 1-σ from the correct value.

This example has hopefully demonstrated the usefulness of Bayesian statistics combined with MCMC to estimate model parameters, as well as draw samples from their joint probability distribution, which can be used for calculating other useful quantities.

---

[3] While one Gaussian deviate has a $\simeq 4.6\,\%$ probability of existing beyond 2-σ from the mean (its p-value), for five independent deviates (Fig. 2.6 shows they are close to independent), the probability that one or more are located beyond 2-σ in the marginalised distributions is $1-(1-0.046)^5 \simeq 0.208$.

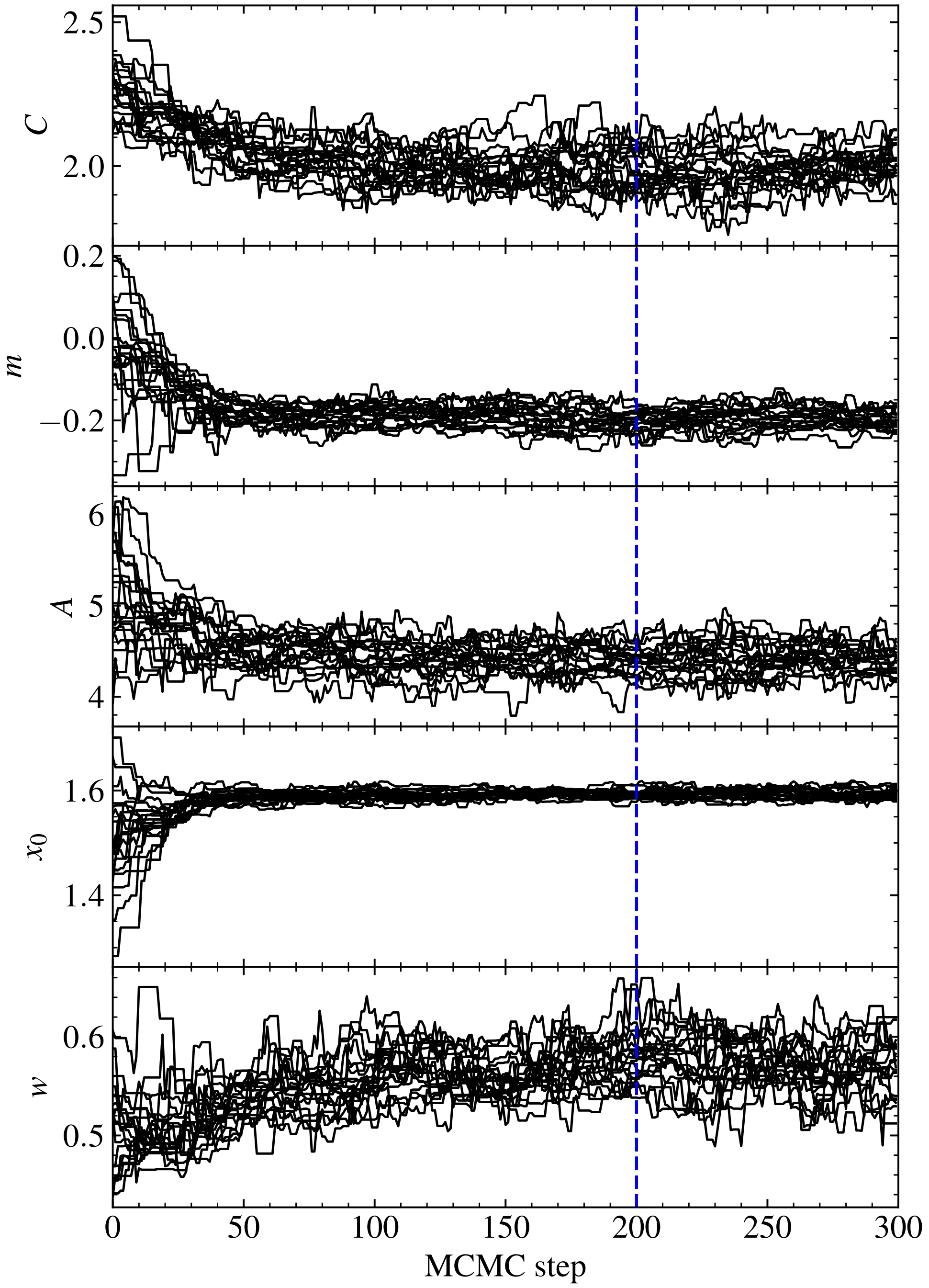

Figure 2.5: MCMC chains for the five parameters in the MCMC example. Only the first 20 walkers are plotted for clarity. The blue dashed line indicates the cutoff point after which every 10th step in the chain is used for independent samples.

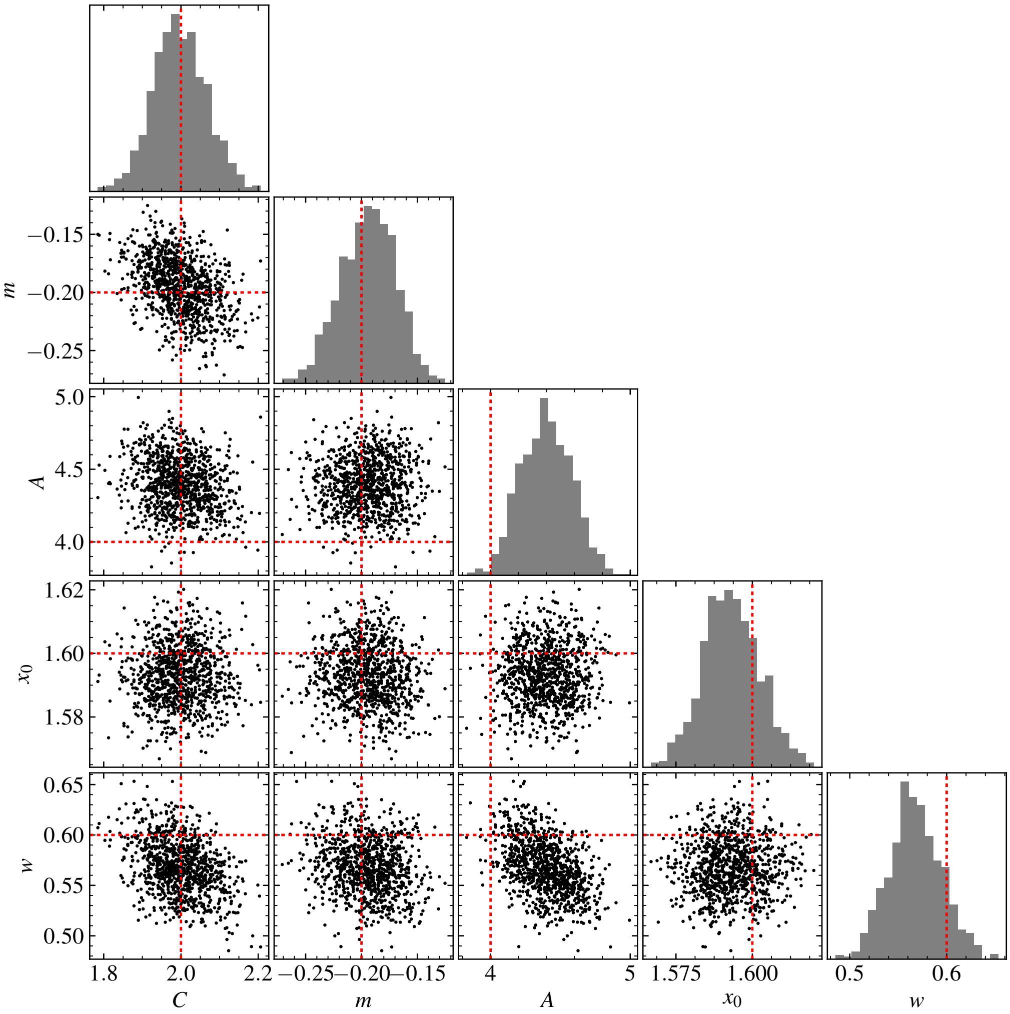

Figure 2.6: Corner plot for the MCMC example. The histograms show the marginalised distributions for each of the five parameters. The scatter plots show the marginalised joint-probability distributions between each pair of parameters, where each point represents an independent MCMC sample from the fit. The red dashed lines indicate the locations of the true values.

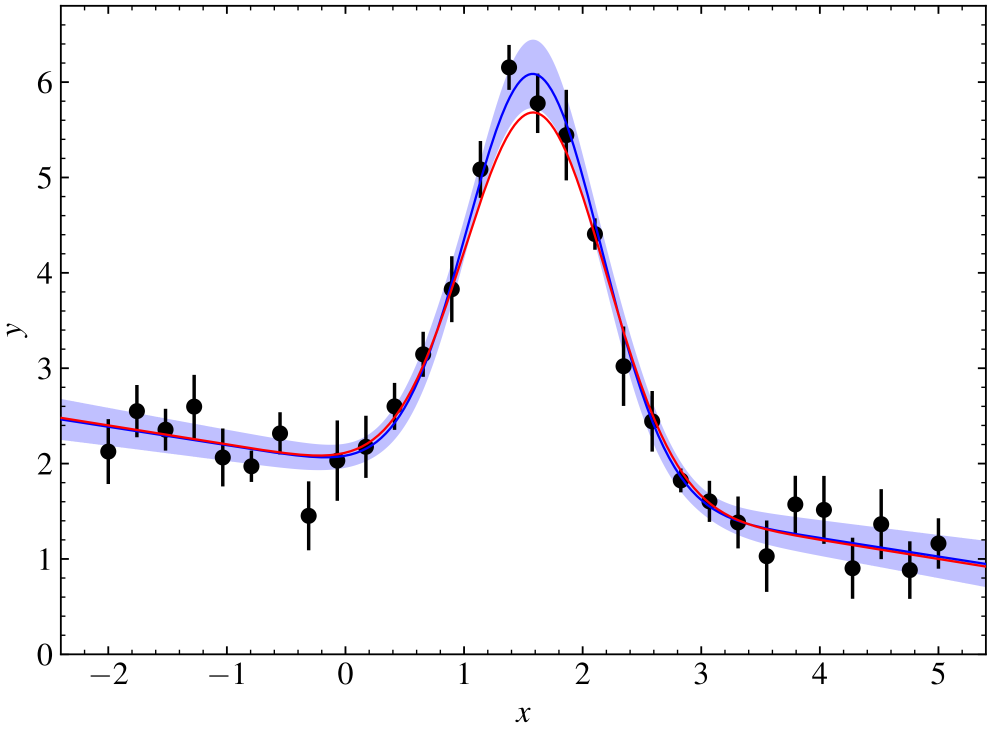

Figure 2.7: The data from the MCMC example are shown by the black points with their corresponding error-bars. The red line indicates the model evaluated at the true parameter values. The blue line, which is partially obscured by the red line, is the model evaluated at the mean of marginalised parameter distributions. The faint blue region indicates the 2-σ confidence region on the fit.

Chapter 3

A large sample of DZ white dwarfs

Over the last 15 years, the Sloan Digital Sky Survey (SDSS, see Section 1.7) has been an invaluable source of white dwarf discoveries, providing spectroscopy for $> 40\,000$ stellar remnants of all spectral types and spanning all temperature regimes (Kleinman et al., 2004; Eisenstein et al., 2006; Kleinman et al., 2013; Kepler et al., 2015, 2016). In this chapter we add our own contribution to the above list through our identification of a sample of cool DZ white dwarfs.

Prior atmospheric analyses of DZ white dwarfs by Bergeron et al. (2001) and Dufour et al. (2007), found a wide range in the level of observed metal pollution across the $T_{\rm eff}$ range of their samples (see Fig. 9 of Dufour et al., 2007). However, below $\simeq 7000\,$K only one object, G165-7 (SDSS J1330+3029 throughout this work), was found with log[Ca/He] $> -9\,$dex. The authors noted that this could be explained as a selection bias. The majority of the DZs analysed by Dufour et al. (2007) came from the SDSS white dwarf catalogue of Eisenstein et al. (2006), which was subject to a colour-cut excluding objects with $(u-g)$ sufficiently red to overlap the main-sequence. This colour-cut would also preclude the identification of SDSS objects spectrally similar to G165-7 ($u - g = 1.96 \pm 0.03\,$mag), which was instead included by Dufour et al. (2007) as one of twelve additional systems from Bergeron et al. (1997) and Bergeron et al. (2001).

The suspicion of selection effects by Dufour et al. (2007) was soon proved correct by Koester et al. (2011) (hereafter KGGD11) who searched specifically for DZs with strong metal-pollution and low $T_{\rm eff}$ similar to G165-7. KGGD11 noted that such white dwarfs would follow cooling tracks extending below the main-sequence in $(u-g)$ vs. $(g-r)$ (see Fig. 3.1), exhibiting colours not possible for other types of stars due to extremely strong H+K line absorption in the SDSS u-band. In total KGGD11, identified 26 cool DZs ($T_{\mathrm{eff}} < 9000\,\mathrm{K}$) with spectra strongly line-blanketed by metals, occupying a previously sparse corner of the T_{eff} vs. log[Ca/He] plane.

Here, we extend the work of KGGD11 to SDSS DR12, finding 231 cool DZ white dwarfs with strong metal lines. These stars provide not only detailed information on ancient exoplanetary chemistry, but also serve as laboratories for state of the art atomic physics under the extreme conditions found in white dwarf atmospheres.

3.1 White dwarf identification

3.1.1 Spectroscopic search

We adopted two distinct methods to identify DZ white dwarfs from the SDSS DR12 spectra. The first (*method 1*) makes use of various data cuts (colour, proper-motion, etc.) to filter the number of objects requiring visual inspection. Following the release of SDSS DR12, we employed a new identification scheme (*method 2*) where we fit all SDSS spectra with DZ templates. This method was found to be superior to *method 1* as it required fewer spectra to be visually inspected, and allowed a larger range of colour space to be explored. We still describe the first method briefly as the initial results it provided were used to calibrate the template fitting approach.

Method 1

The first method is essentially an extension of the work by KGGD11 to subsequent SDSS data releases. We restricted our search for further cool DZs firstly to SDSS point-sources, and then performing a colour-colour cut in $(u-g)$ vs. $(g-r)$ (dashed region in Fig. 3.1), similar to that used by KGGD11. This region avoids the main sequence and contains the 17 coolest and most metal polluted DZs found by KGGD11. While this area of colour-space was chosen to avoid other types of stellar objects, it is instead home to quasars with Ly-α breaks occurring in the u-band, which were intensely targeted for spectroscopy in SDSS-III (Ross et al., 2012). While this targeting strategy leads to cool DZ stars being serendipitously observed, these quasars required filtering from our colour selection.

We removed quasars using a combination of proper-motion and spectroscopic redshifts: We required a $> 3\sigma$ detection of proper-motions, where SDSS proper-motion errors are typically 2–6 $\mathrm{mas\,yr^{-1}}$. The total proper-motion is chi-distributed with two degrees-of-freedom, whereas the 1-σ errors correspond to single

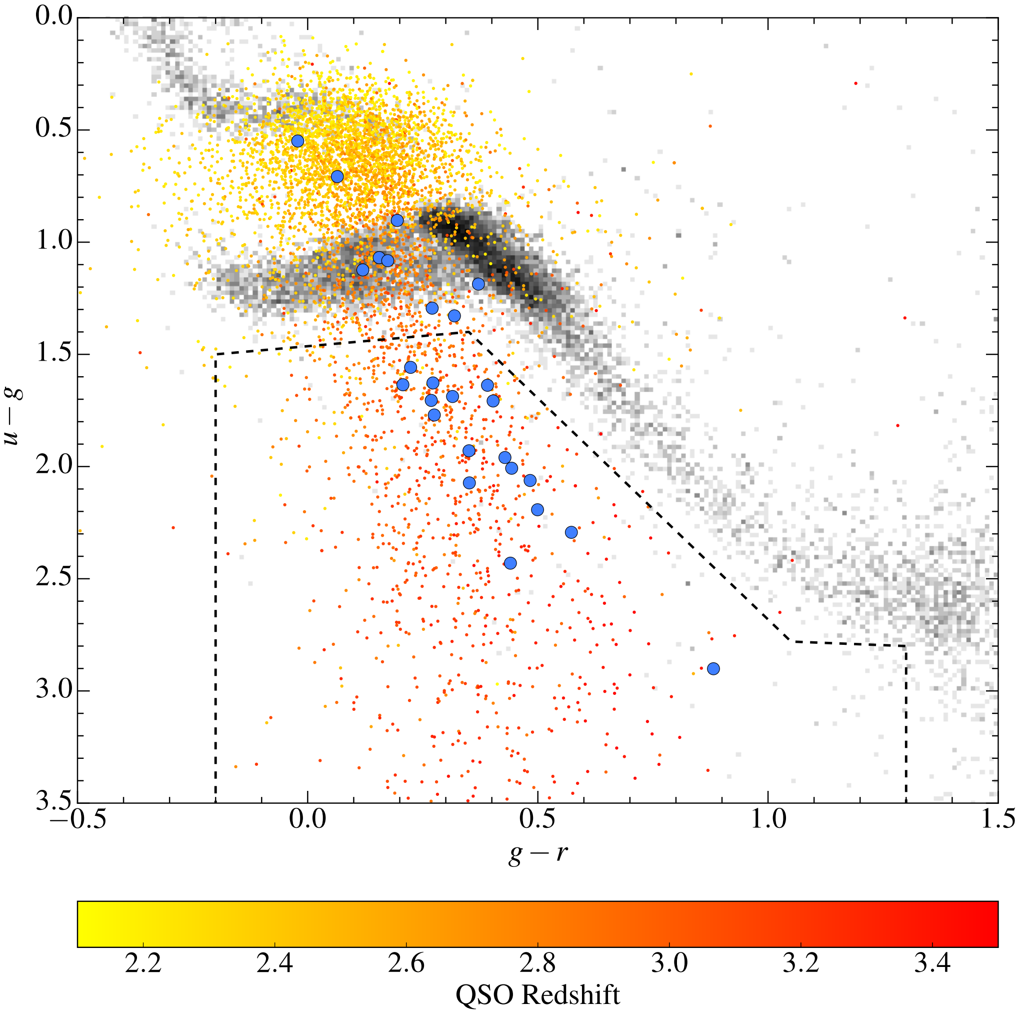

Figure 3.1: Our colour-cut (dashed line) is similar to that used by KGGD11, although their $u - g < 3.2$ constraint is removed. The cut includes 17 of the original KGGD11 sample (blue points) which are the coolest and most metal-rich of their stars. A random sample of SDSS quasars is shown by the smaller coloured points – their colour corresponding to the redshift, illustrating the degeneracy between DZs and QSOs in this colour-space.

components, therefore $\simeq 1\,\%$ of the $\simeq$477 000 quasar spectra[1] will have measured proper-motions in excess of our 3σ-cut. Using *only* proper-motion to filter quasars was insufficient as these are not always available for faint, $g > 20$ objects, due to lack of cross-detections in USNO-B. Additionally a few high proper-motion systems ($> 100\,\mathrm{mas\,yr^{-1}}$) have such large displacement between SDSS and USNO-B photometry that cross-matching fails. For instance, SDSS J1144+1218 (KGGD11) has no available SDSS proper-motion, but is found in PPMXL with a celestial motion of $617 \pm 6\,\mathrm{mas\,yr^{-1}}$(see Table B.4).

We supplemented our proper-motion cut with a cut on redshift, z, to remove additional quasars, and avoid missing DZs with no SDSS proper-motion – systems only needed to pass one of the two tests to make it to the next stage. For the redshift cut we imposed $z - 3\sigma_z < 0.01$, removing both quasar and galaxy spectra from our sample. The relative rarity of cool DZ spectra in SDSS can lead to incorrect spectral classification and subsequently an incorrect redshift estimate from the SDSS pipeline. Therefore we allowed objects with the `zwarning` flag not equal to zero to "automatically pass" our redshift test (zero indicates a z value that is deemed to be correct). However of the 17 KGGD11 DZs within our colour-cut, five were found with $1.38 < z < 1.41$ and `zwarning`$= 0$, indicating that DZ stars can be misclassified as quasars with no warning flags raised in this narrow redshift range. Therefore an exception to our redshift cut was made for the few SDSS spectra with $1.3 < z < 1.5$.

Our combined proper-motion/redshift cut successfully removed most QSOs and galaxies, thus reducing the size of the sample of purely colour-selected spectra by 33 % to around 100 000. At this stage, all 17 DZs from KGGD11 were still contained within the selection.

As this sample was still rather large for visual inspection, we sought to remove additional contaminants. Most of the remaining spectra were of K/M dwarfs at the border of our colour-cut. We performed template fitting for spectral subclasses K1–M9 to remove these cool main sequence stars. For M dwarfs we used the templates from Rebassa-Mansergas et al. (2007). For subclasses K1, K3, K5 and K7 we created templates by combining multiple (at least 20 per subclass) high signal-to-noise (S/N) SDSS spectra which we identified in the CasJobs database (Li & Thakar, 2008) using the `class` and `subclass` attributes.

We fitted each of the 100 000 spectra against all stellar templates, obtaining a reduced chi-squared (χ^2_{red}) for each fit. The template with lowest χ^2_{red} for a given spectrum was recorded as the best-fitting template. The median S/N was also recorded for each SDSS spectrum.

---

[1] See `http://www.sdss.org/dr12/scope/` for a breakdown of all SDSS DR12 spectroscopy.

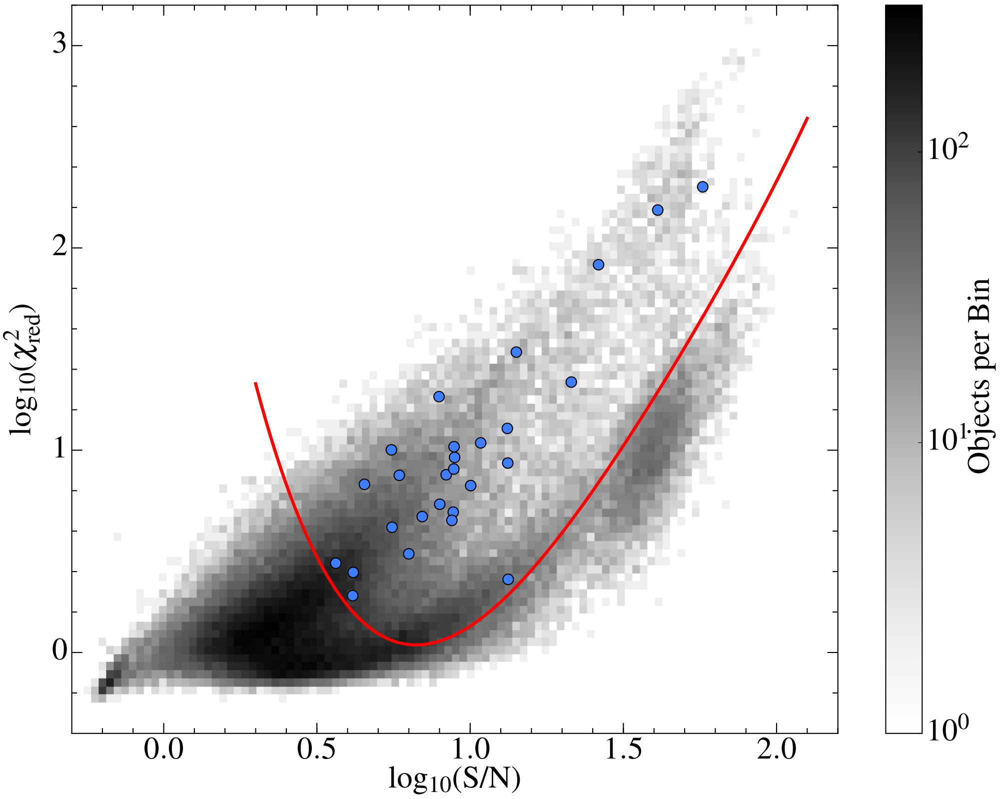

Figure 3.2: Density map in the $\chi^2_{\rm red}$-S/N plane for proper-motion/redshift selected objects. Blue points are the DZs identified by KGGD11 that fall within our colour-cut. Several of these systems have more than one SDSS spectrum (see Table B.1 for number of SDSS spectra per object), hence there are more than 17 points shown here. The red curve indicates a 4th-order polynomial in log-log space which defines our final cut.

The resulting distribution in the S/N vs. $\chi^2_{\rm red}$ plane (Fig. 3.2) is bimodal at high-signal to noise indicating probable main sequence stars in the lower cluster, and objects spectrally different to the K/M star templates in the upper branch. The bulk of spectra are found at low signal-to-noise/low $\chi^2_{\rm red}$, and so are of too poor quality for meaningful analysis. The KGGD11 DZs were used to define a cut-off for the remaining spectra as indicated by the red line. This has the effect of removing the high S/N and low $\chi^2_{\rm red}$ (main sequence) objects, as well as very low S/N spectra.

The $\chi^2_{\rm red}$-S/N cut reduced the sample size down to $\simeq 35\,000$ spectra which we visually inspected for DZ white dwarfs. In total we identified 126 spectra corresponding to 103 unique DZ stars. Some objects had additional spectra which were not identified via *method 1* (e.g. because of low S/N), but were found upon searching for spectra with the same SDSS `ObjID`. This brought the total number of DZ spectra to 138 for the 103 systems.

Method 2

While we successfully identified more than 100 cool, metal-rich DZs with *method 1*, its scope was severely limited by our initial colour-cut. Of the 26 DZ white dwarfs in the KGGD11 sample, 9 were excluded by this cut (Fig. 3.1), suggesting that many more DZs may have colours overlapping the main-sequence in $(u-g)$ vs. $(g-r)$. Additionally, the u-band errors for DZs in SDSS are sometimes > 1.0 mag, and so while the true $u-g$ value should place a system below the main sequence in Fig. 3.1, the measured colour could instead escape our colour cut. Furthermore, the possibility remained that systems could fail both our proper-motion and redshift tests, or also fall under our $\chi^2_{\rm red}$-cut in Fig. 3.2.

Method 2 essentially uses only the SDSS spectra for identification, and so allows us to identify objects that would otherwise be photometrically degenerate with main sequence stars. To provide zeroth-order estimates of atmospheric parameters for our spectral fitting (described later in section 3.4), we generated a grid of DZ models of varying $T_{\rm eff}$ and log[Ca/He]. The grid spanned $4400\,{\rm K} \leq T_{\rm eff} \leq 14\,000\,{\rm K}$ in steps of 200 K and $-10.5 \leq \log[{\rm Ca/He}] \leq -7$ in steps of 0.25 dex (735 DZ model spectra). For all models in the grid the surface gravity, $\log g$, is fixed to the canonical value of 8. Other elements were fixed to bulk Earth abundances (McDonough, 2000) relative to Ca. We found our model grid could also be used as templates to identify DZ white dwarfs through fitting to the SDSS spectra.

We supplemented our DZ grid with the 768 highest quality SDSS spectra with average S/N > 100. These consisted entirely of main sequence stars of spectral-types B through K, bringing the total number of templates to 1503.

With these template spectra at hand we fitted each template against *all* 2.4M SDSS spectra with mean $\mathrm{S/N} > 3$ – this S/N cut removes not only the poorest quality spectra, but also quasars where the bulk of the signal is contained within a few narrow emission lines. For each fit the template spectra were linearly interpolated onto the same wavelength grid as the SDSS spectrum under consideration – the high S/N requirement of the non-DZ templates meant the effects of interpolating noise were kept to a minimum. Secondly, a reduced χ^2 was calculated between the SDSS spectrum and interpolated template with only a scaling factor as a free parameter. Ignoring the small flux errors on the non-DZ templates, the optimum scaling factor, A, has the simple analytic form

$$A = \frac{\sum_i f_i\, t_i/\sigma_i^2}{\sum_j t_j^2/\sigma_j^2}, \tag{3.1}$$

where the f_i and σ_i are the fluxes and errors on the SDSS spectra and the t_i are the unscaled fluxes on the interpolated templates. For each SDSS spectrum, the template with the lowest χ^2_{red} was considered to be the best fit.

SDSS spectra which best fit a non-DZ template were immediately discarded, reducing the 2.4M spectra to $\simeq 244\,000$. All SDSS DZ spectra identified via *method 1* still remained after this cut. Next we applied a single colour cut of $u - g > 0.50$, essentially enforcing that white dwarfs in our sample contain significant absorption in the blue end of their spectra. This has the effect of removing DZ stars with $T_{\mathrm{eff}} > 9000\,\mathrm{K}$ for the most metal rich objects and $T_{\mathrm{eff}} > 6500\,\mathrm{K}$ for the lowest metallicities in our grid. Hotter objects are not the focus of this work.

Although only $\simeq 10\,\%$ of objects best-fit a DZ template, the best fit does not imply a good fit. Thus we next cut on χ^2_{red}vs. S/N, similarly to *method 1* (Fig. 3.2). The cut is a parabola in $\log(\chi^2_{\mathrm{red}})$ vs. $\log(S/N)$, whose scale we chose to keep all objects identified through *method 1*. This is shown in Fig. 3.3.

At $\mathrm{S/N} > 7$, the distribution in Fig. 3.3 becomes trimodal in χ^2_{red} with only the upper cluster filtered by our cut. We found the majority of points in the intermediate distribution had best fitting templates with the lowest two values of log[Ca/He] (-10.5 and -10.25 dex) in our model grid. This is because those templates are relatively featureless and so had a tendency to match other types of main-sequence stars. Therefore we chose to remove all spectra matching the low Ca-abundance templates, leaving only $\simeq 10\,600$ spectra for visual inspection.[2]

---

[2] While this final cut inevitably biases us towards high-metallicity systems, objects with $\log[\mathrm{Ca/He}] < -10$ do not permit meaningful chemical analyses of the accreted material, with Ca as potentially the only detected element.

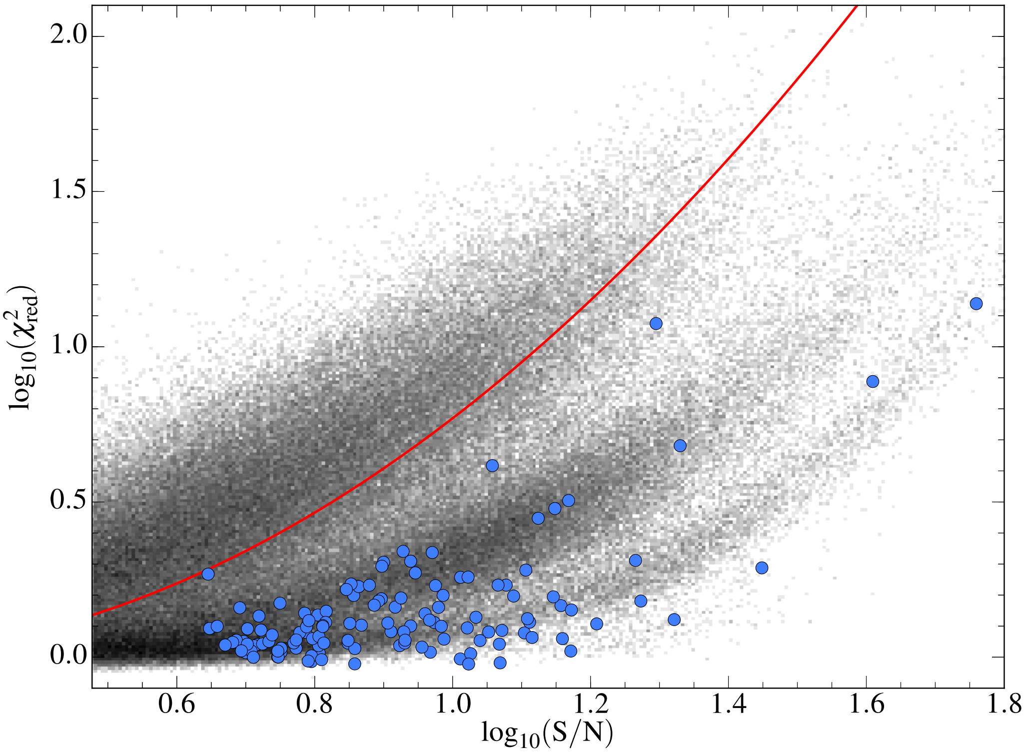

Figure 3.3: Density map in the $\chi^2_{\rm red}$-S/N plane for objects with best fits to DZ templates. Blue points correspond to the DZ spectra identified using *method 1*. Our $\chi^2_{\rm red}$-cut is indicated by the red parabola.

Table 3.1: Coordinates, SDSS spectral identifiers, and photometry for the ultracool white dwarfs we have serendipitously discovered.

SDSS J	Plate-MJD-Fib	u [mag]	g [mag]	r [mag]	i [mag]	z [mag]	Ref.
003908.33+303538.9	6526-56543-0006	21.73 ± 0.26	20.39 ± 0.03	20.44 ± 0.04	20.97 ± 0.09	21.15 ± 0.44	
025754.92+042807.5	4256-55477-0926	22.72 ± 0.33	21.15 ± 0.04	20.65 ± 0.04	21.06 ± 0.07	21.20 ± 0.26	
100103.42+390340.4	1356-53033-0280	21.30 ± 0.11	20.01 ± 0.03	19.58 ± 0.02	19.95 ± 0.04	20.52 ± 0.23	1
133739.40+000142.8	0299-51671-0357	20.79 ± 0.05	19.54 ± 0.02	19.13 ± 0.02	19.52 ± 0.02	20.02 ± 0.08	2
140237.31+080519.1	4863-55688-0792	21.96 ± 0.19	21.41 ± 0.05	21.33 ± 0.06	21.51 ± 0.13	20.96 ± 0.18	
144440.01+631924.4	6983-56447-0685	21.72 ± 0.12	20.37 ± 0.03	20.22 ± 0.03	20.08 ± 0.03	20.13 ± 0.13	
170320.12+271106.8	5013-55723-0128	22.50 ± 0.18	21.42 ± 0.03	20.84 ± 0.03	21.16 ± 0.06	21.15 ± 0.23	
225817.87+012811.1	4290-55527-0290	21.10 ± 0.09	19.82 ± 0.02	19.62 ± 0.02	20.07 ± 0.03	20.52 ± 0.15	
231130.14+283444.8	6292-56566-0964	22.67 ± 0.20	21.14 ± 0.02	20.95 ± 0.03	21.27 ± 0.05	21.10 ± 0.17	
234931.16−080245.6	7146-56573-0460	22.43 ± 0.42	21.03 ± 0.03	20.82 ± 0.05	20.97 ± 0.08	20.39 ± 0.17	

References: (1) Gates et al. (2004), (2) Harris et al. (2001)

Table 3.2: Breakdown of methods 1 & 2 for the visually inspected SDSS spectra. For each spectral type, the *number/number* format indicates the total spectra, and the number of unique systems respectively.

Method	1	2
Main-sequence stars	29545/27660	6645/6253
Carbon stars	148/126	15/12
Quasars	4477/3575	2013/1895
Galaxies	128/123	9/9
WDMS binaries	33/30	0/0
Cool DZ WDs	126/103	291/229
Other WDs	61/59	773/715
Unclassifiable spectra	54/52	808/784
Total	34572/31728	10554/9897

We identified 291 DZ spectra via visual inspection corresponding to 229 unique white dwarfs, including all of those identified through *method 1*. Serendipitously, *method 2* also led us to identify 10 ultracool white dwarfs, of which only 2 are previously known (Harris et al., 2001; Gates et al., 2004). Ultracool white dwarfs have temperatures below 4000 K, yet exhibit blue colours due to collision induced absorption of H_2 in their atmospheres. The 10 systems are listed in Table 3.1 and their spectra are displayed in Fig. 3.4. Since we do not find all previously known SDSS ultracool white dwarfs (Harris et al., 2000; Gates et al., 2004; Harris et al., 2008), a targeted search via template fitting would likely find additional such objects.

Comparison of methods 1 & 2

Method 2 was clearly superior to *method 1* for identifying DZ white dwarfs as it allowed us to identify additional systems and required manual inspection of fewer spectra. A comparison of all visually inspected spectra between the two methodologies is shown in Table 3.2. Note that the listed spectra for *method 2* are only a superset of *method 1* with respect to cool DZ white dwarfs. For instance *method 1* shows some sensitivity to carbon stars, as these are not rejected by the K/M star template fitting shown in Fig. 3.2, but *are* rejected by the DZ template fitting in *method 2*.

Our final sample of cool DZ white dwarfs is listed in Table B.1, which includes coordinates, plate-MJD-fiber identifiers, and SDSS photometry. For systems where multiple SDSS spectra are available, only one row is listed, where the plate-

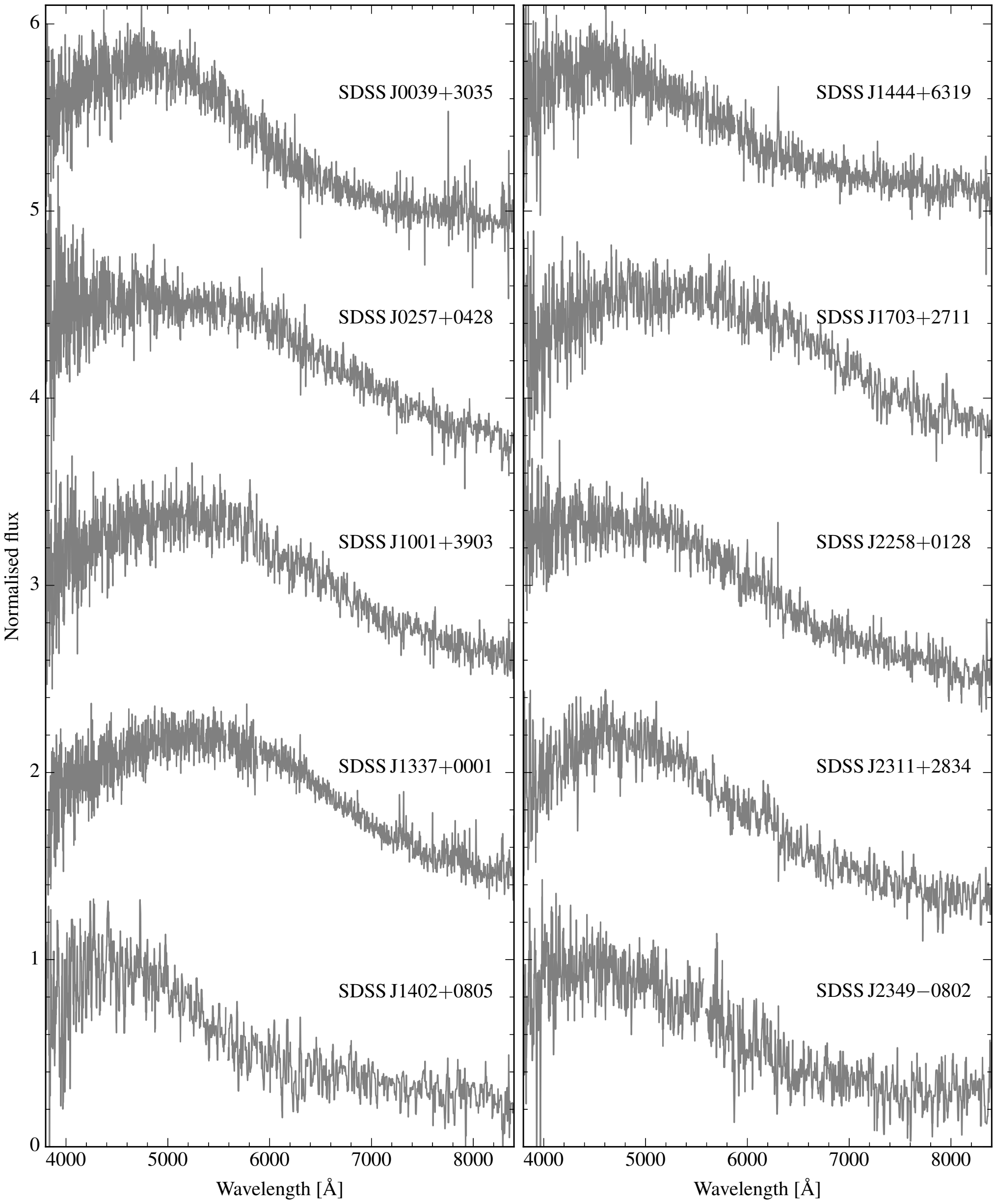

Figure 3.4: Ultracool white dwarf spectra. Each spectrum is normalised to 1, and offset by 1.2 from one another. Smoothing is applied according to the spectral signal-to-noise. Full coordinates and plate-MJD-fiber identifiers are provided in Table 3.1.

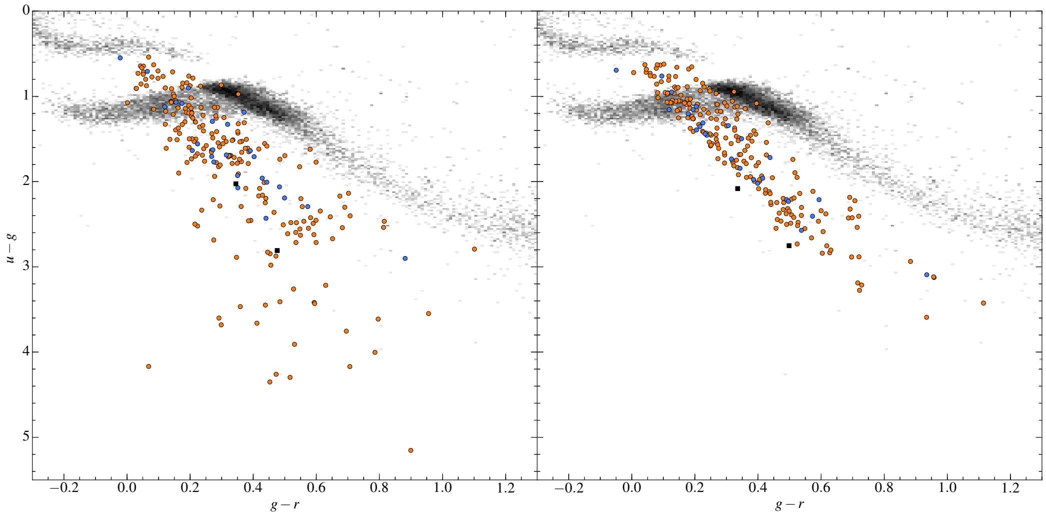

Figure 3.5: Colour-colour diagrams of our white dwarf sample. The left panel shows the observed SDSS colours, whereas those on the right are the synthetic colours from our best fit models. Objects also in the KGGD11 sample are shown in blue, photometrically identified DZs as black squares, and the remainder of our sample in orange. The increased scatter for the observed colours is dominated by uncertainty on the u-band fluxes which in some cases can exceed 1 mag.

MJD-fiber ID corresponds to the spectrum fitted in section 3.4. We also show an updated $(u-g)$ vs. $(g-r)$ colour-colour diagram for our sample in Fig. 3.5. The left panel shows the observed colours for our sample, whereas the right panel shows the synthetic colours computed from our best-fitting models (section 3.4). The difference in spread is due to the large u-band errors, which are biggest for very cool systems and those with strong metal absorption in the spectral range covered by the SDSS u filter.

3.1.2 Photometric search

We also attempted to identify potential DZ white dwarfs purely from SDSS photometry and astrometry, with the intention of subsequent spectroscopic follow-up. We filtered for point sources with clean photometry (using the `type` and `clean` flags), and the colour-cut indicated by the black dashed line Fig. 3.1 was applied. Since the number of photometric sources dwarfs the already large size of the spectroscopic database, we also imposed a maximum magnitude of $g < 18.5$ to filter on only the brightest objects. We also required the magnitudes in all bandpasses > 15 in order to avoid objects with saturated photometry. DZ white dwarfs within the specified brightness limit ought to have reasonably large proper-motions. We therefore required proper-motions to be at least $50\,\mathrm{mas\,yr^{-1}}$, with a detection of at least 3σ above zero.

The combination of these cuts resulted in a small sample of 217 objects. Many of these were in crowded fields and so their proper-motions were not considered trustworthy. In total, six known DZ stars with spectra were recovered. These are SDSS J0116+2050, SDSS J0916+2540, SDSS J1214−0234, SDSS J1330+3029, SDSS J1336+3547, and SDSS J1535+1247.

Two objects (SDSS J0512−0505 and SDSS J0823+0546) were identified as clear DZ white dwarfs contenders, and were both followed up in Dec 2013 using the William Herschel Telescope (WHT – details of the spectroscopic reduction are summarised in section 3.2). The observations confirmed both targets to be cool DZ white dwarfs and we include them in all relevant figures and tables throughout this work, These two systems bring our full DZ sample to 231 unique objects. As six of the eight objects our photometric search highlighted as possible DZ white dwarfs already had SDSS spectra, this indicates a high spectroscopic completeness for DZ white dwarfs in the range $15 > g > 18.5$.

3.1.3 Note on magnetic objects

Prior to Hollands et al. (2015) the only known magnetic DZ white dwarfs (DZH) were LHS2534 (Reid et al., 2001), WD0155+003 (Schmidt et al., 2003) and G165−7 (Dufour et al., 2006), which were identified through Zeeman split lines of Mg I, Na I, Ca II, and Fe I. All 3 systems have SDSS spectra and are included in our sample with respective names SDSS J1214−0234, SDSS J0157+0033, and SDSS J1330+3029. In the early stages of this work, before the release of SDSS DR12, we had identified a further 7 magnetic DZs which have already been published (Hollands et al., 2015).

Since the release of DR12, we have identified further DZH including some we had missed from DR10 (fields $\lesssim 1\,\mathrm{MG}$ are only detectable from close inspection of the sharpest lines, with further objects found through the expanded colour-selection of method 2). Our full list of magnetic DZs is given in Table 6.1.

Magnetic white dwarfs are interesting astrophysical objects in their own right, and so we discuss these systems at length in Chapter 6. However, their presence requires some mentioning here, as the magnetic fields affect the quality of our spectroscopic fits which do not incorporate magnetism, and varying degrees caution should be applied when considering results for these stars. In the best cases (lowest fields) like SDSS J1330+3029, the effect of magnetism on line shapes/equivalent widths is minimal and so our T_{eff}/abundance values can be trusted as much as the non-magnetic case. In the highest field cases like SDSS J1536+4205 the effect is much greater with the uncertainty in $T_{\rm eff}$ around 500 K and abundances uncertainties likely around 0.5 dex. SDSS J1143+6615 is a special case where the field is so high, that attempting to fit with a non-magnetic model was found to be a pointless exercise. Therefore, within this chapter, the star is included only as a DZ identification (it is instead discussed thoroughly in in Chapter 6).

3.2 Additional spectra

The 26 DZ white dwarfs analysed by KGGD11 were identified before the introduction of BOSS, and their spectra only extended as blue as $\simeq$ 3800 Å, i.e. covering the cores of the Ca H+K doublet, and its red wing. However the blue wing extends several hundred Å further. Synthetic $(u - g)$ colours calculated by KGGD11 from their best fit models were found to be in poor agreement with the reported SDSS colours, typically over-predicting u-band flux by about 50 %, and in the worst case by a factor 2.9 (SDSS J2340+0817). This result indicated our models required an additional source of opacity bluewards of 3800 Å.

The newer BOSS spectrograph offers bluer wavelength coverage down to $\simeq$ 3600 Å. The spectra of DZs observed from DR9 onwards include additional absorption lines of Mg and Fe in this wavelength range, as predicted by the model spectra. However, while our models predicted further absorption features between 3000 and 3600 Å (particularly from Fe), they remained insufficient to explain the additional opacity required in the u-band.

To determine the source of ground-based UV opacity, we acquired spectra of 18 DZs with the William Herschel Telescope (WHT) down to 3000 Å using the Intermediate dispersion Spectrograph and Imaging System (ISIS). The observations were made during December 2013 and 2014, with a basic observing log given in Table 3.3. The same instrument setup was used on all nights. ISIS uses a dichroic beam splitter to separate the light onto two CCDs optimised for blue and red wavelengths. For the ISISB arm we used the R300B grating, and the 158R grating on the ISISR arm, with central wavelengths of 4300 Å and 7300 Å respectively. Using a 1.2" slit, this setup leads to spectral resolutions of about 5 Å in the blue arm and 9 Å in the red arm. For both CCDs we used 2 × 2 binning to reduce readout noise.

For the 2013 observations we focused on obtaining bluer spectra of bright targets taken before the introduction of BOSS, and confirming two photometrically/astrometrically selected DZ candidates (section 3.1.2). Thick cloud dominated the first half of December 28th, with some sporadic thin cloud during the remainder of the night. Therefore the only good quality data obtained was for

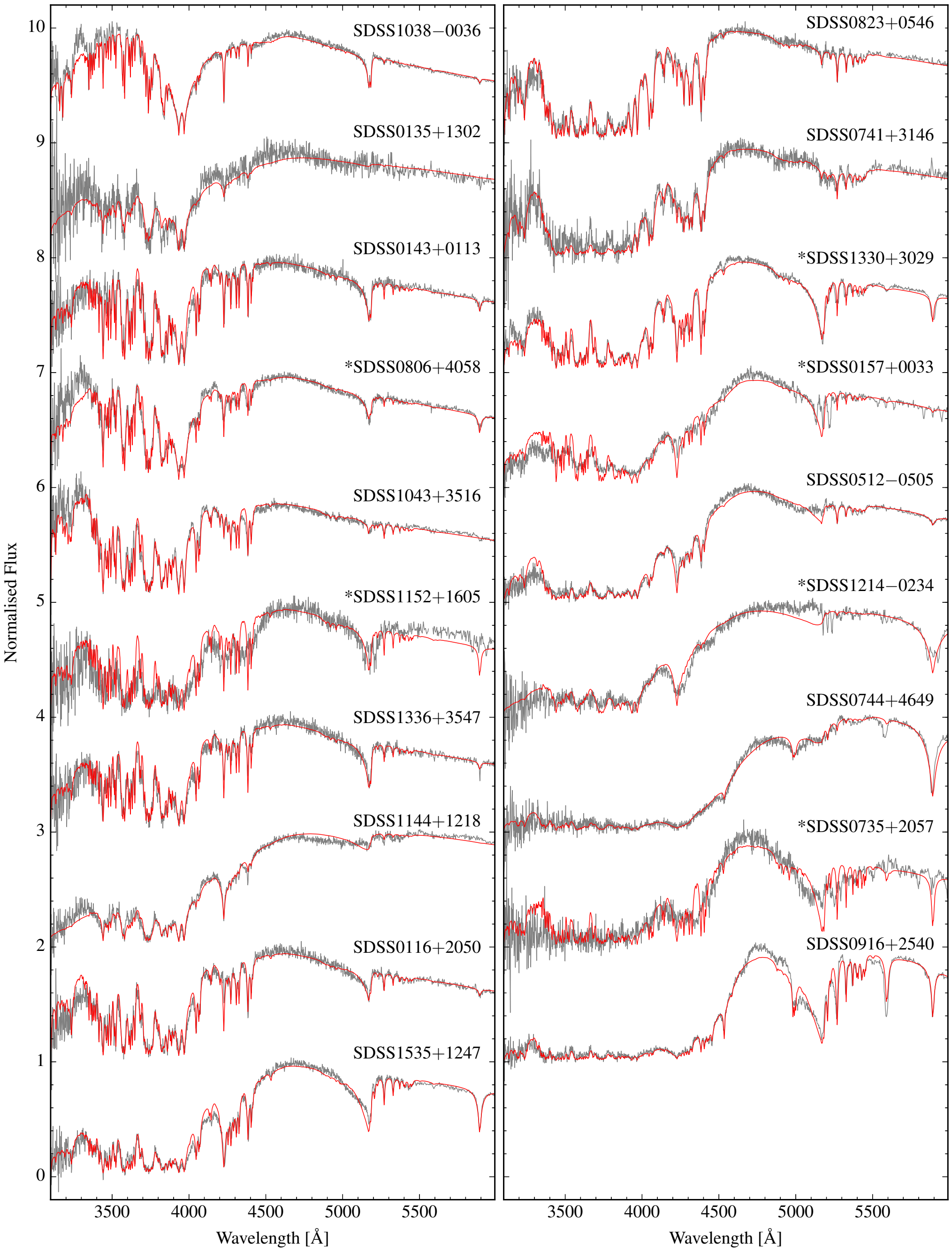

Figure 3.6: WHT spectra taken down to the atmospheric cutoff (grey), ordered by approximate level of absorption below 4500 Å. Spectra are peak normalised to 1 and offet by 1 from one another. Magnetic objects are indicated by asterisks. Best fitting models (see Section 3.4) are shown in red.

Table 3.3: Observation log of WHT spectra. The observation date corresponds to the start of the night. t_{exp} is the total exposure time for each target.

SDSS J	Obs. date	t_{exp} [s]	$\langle$Airmass$\rangle$	Note
SDSS J0823+0546	28/12/2013	3000	1.09	a
SDSS J0116+2050	29/12/2013	2700	1.02	b,c
SDSS J0135+1302	29/12/2013	3000	1.12	c
SDSS J0512−0505	29/12/2013	2700	1.28	a
SDSS J0735+2057	29/12/2013	12600	1.09	c
SDSS J0916+2540	29/12/2013	3600	1.02	b
SDSS J1038−0036	29/12/2013	1800	1.22	b
SDSS J1214−0234	29/12/2013	3000	1.34	
SDSS J1330+3029	29/12/2013	1200	1.20	b
SDSS J1336+3547	29/12/2013	1800	1.13	b
SDSS J1535+1247	29/12/2013	1200	1.66	b
SDSS J0806+4058	23/12/2014	7200	1.05	c
SDSS J1043+3516	23/12/2014	4800	1.03	b
SDSS J1144+1218	23/12/2014	3300	1.05	b
SDSS J0143+0113	24/12/2014	2400	1.13	b,c
SDSS J0157+0033	24/12/2014	7200	1.19	b
SDSS J0741+3146	24/12/2014	9000	1.03	c
SDSS J0744+4649	24/12/2014	7200	1.19	c
SDSS J1152+1605	24/12/2014	6900	1.05	b,c

Notes: (a) Photometrically identified DZs, confirmed with these spectra. (b) Object appears in KGGD11. (c) Has at least one BOSS spectrum.

SDSS J0823+0546 (taken during a clear part of the night). All other objects observed on the 28th were re-observed on the 29th with stable, clear conditions throughout the night. The flux calibration of spectra taken during 2013 was found to be excellent including for SDSS J0823+0546 (the only object successfully observed on December 28th).

For the 2014 observations we instead concentrated on obtaining improved spectra for objects where the existing SDSS spectra were poor, as well as following up some objects from SDSS DR10 with atypical spectra, e.g. SDSS J0744+4649. The first half of December 23rd was strongly affected by Saharan dust, only permitting observations in the second half of the night. On the 24th, while some small amount of dust still persisted in the air, it remained fairly stable throughout the night and so the flux calibration of objects taken on this night were found to be of reasonable quality.

Standard spectroscopic techniques were used to reduce the data, as described in Section 2.1, with software from the STARKLINK project. For each night multiple bias frames were combined to produce a master-bias image which was subtracted from each frame. Multiple flat fields were also taken per night, and co-added to produce a master-flat field. Images were then divided by the master-flat to remove pixel dependent variations. Extraction of 1-D spectra was performed using the optimal-extraction method via routines in the PAMELA package. Wavelength and flux calibrations along with telluric removal were subsequently performed in MOLLY.[3]

The flux calibration of SDSS J1144+1218 was strongly affected by the aforementioned dust. We corrected the spectrum by fitting the difference between synthetic magnitudes and SDSS photometry (in all SDSS filters) with a 3rd-order polynomial, providing a wavelength dependent correction. The calibrated spectra are shown in Fig. 3.6 with their best fitting models (modelling discussed in sections 3.3 and 3.4).

Comparison with the WHT spectra and model atmospheres revealed that the missing source of opacity came from lines of Ni and Ti. The missing lines were added to our line list used for calculation of DZ models described in the subsequent sections of this chapter.

3.3 Model atmospheres

The methods and basic data for the calculation of model atmospheres and synthetic spectra are described in Koester (2010) and KGGD11. Atomic line data were ob-

---

[3] MOLLY software can be found at `http://deneb.astro.warwick.ac.uk/phsaap/software/`

tained from the VALD (Piskunov et al., 1995; Ryabchikova et al., 1997; Kupka et al., 1999) and NIST databases (Kramida et al., 2016). Since many of the metal lines are extremely strong and have a significant influence on the atmospheric structure, we have included approximately 4500 lines not only in the calculation of synthetic spectra but also for the atmospheric structure calculation. The blanketing effect is very important and with every change of abundances new tables of the equation of state and absorption coefficients were calculated to obtain consistent results.

The strongest lines considered are the resonance lines H+K of Ca II located at 3968/3934 Å, and h+k of Mg II at 2803/2796 Å. Although the latter are in the UV outside the range of the optical spectra, they still influence the models in the visible range. In KGGD11 approximate unified line profiles were used for these lines, but the quasi-molecular data – in particular dipole moments – were not available at that time. We have since calculated all missing data and redetermined the line profiles for this work.

3.3.1 Ab-initio potentials and dipole moments for quasi-molecules of Ca^+He, Mg^+He, and MgHe

Ab-initio calculations were performed using the MOLCAS package (Aquilante et al., 2010). Electronic energies were calculated at the CASSCF (complete active space self-consistent field) level. Calculations of the dynamic electron correlation effects for the multiconfigurational CASSCF wave functions are based on the second order perturbation theory, the CASPT2 method in MOLCAS (Finley et al., 1998). The spin-orbit interaction energy was included using the state interaction program RASSI (restricted active space state interaction) in MOLCAS (Malmqvist et al., 2002). The RASSI program also calculates dipole moments of optical transitions between electronic states. Some details on the results of the present calculations are given below.

Mg^+He: The calculations included electronic states of Mg^+He correlating with the ground $2p^63s$ state and excited 3p and 4s states of the Mg^+ ion. Calculated potentials and dipole moment functions for some transitions are shown in Fig. 3.7. The ground $^2\Sigma^+$ state has a shallow potential well ($D_e \approx 50$ cm^{-1}, re ≈ 3.5 Å). Interaction of Mg $2p^63p$ with He gives $^2\Pi_{1/2,3/2}$ states, and a $^2\Sigma^+$ state. A slight difference between the $^2\Pi_{1/2}$ and $^2\Pi_{3/2}$ states is not seen in the plot scale. The dipole moment of 3p $^2\Pi$ – 3s $^2\Sigma^+$ transitions is nearly constant. The 3p $^2\Sigma^+$ state interacts with a higher lying 4s $^2\Sigma^+$ state. Due to this interaction the dipole moment of the resonance 3p $^2\Sigma^+$ – 3s $^2\Sigma^+$ transition decreases (Fig. 3.7). Calculations were

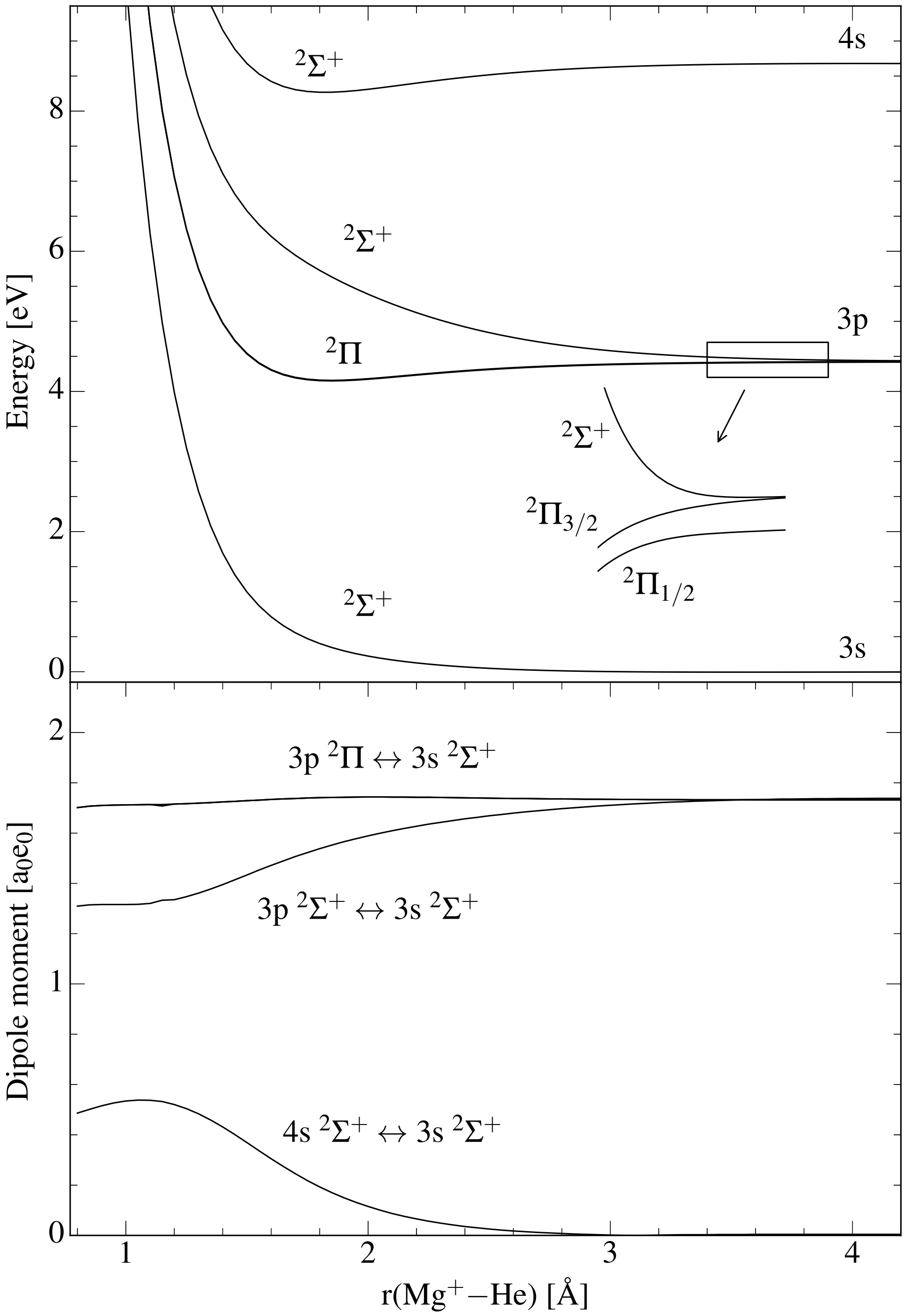

Figure 3.7: Potential energies (top) and dipole moments (bottom) for the Mg^+He molecule. The resonance lines at 2796 and 2803 Å are the transitions from the 3s to the 3p states. The insert shows the small difference between the $^2\Pi_{3/2}$ and $^2\Pi_{1/2}$ states due to the spin orbit interaction. Likewise the corresponding dipole moments overlap on the larger scale.

performed using relativistic atomic natural orbital (ANO) type basis sets (Almlöf & Taylor, 1987). The data shown in Fig. 3.7 were obtained using

Mg.ano-rcc.Roos.17s12p6d2f2g.9s8p6d2f2g
He.ano-rcc.Widmark.9s4p3d2f.7s4p3d2f

which are the largest ANO type basis sets in the MOLCAS basis set library. The accuracy of CASSCF/CASPT2 calculations with the ANO basis sets has been discussed in detail in Roos et al. (2004). Smaller ANO type basis sets for the He atom (VQZP and VTZP) were tested as well. The deviations from the results obtained with the largest basis sets (Fig. 3.7) were found rather small (at least the differences would not be seen in the scale of Fig. 3.7). For calculations of quasi-molecular bands corresponding to the 3p $^2\Pi$ – 3s $^2\Sigma^+$ and 3p $^2\Sigma^+$ – 3s $^2\Sigma^+$ transitions, the asymptotic energies were adjusted to match the energies of the Mg^+(3p $^2P_{1/2,\,3/2}$) doublet.

The Mg^+He molecule has been the subject of several theoretical studies (Monteiro et al., 1986; Allard et al., 2016b). Comparison of the present results with other studies is given in Allard et al. (2016b).

MgHe: The present calculations include electronic states of MgHe molecule correlating with the ground $3p^6 4s^2$ and excited singlet and triplet 4s4p and 4s5s states of the Ca atom. Calculated potentials and dipole moments of some transitions are shown in Fig. 3.8. The results were obtained with the same basis sets as for Mg^+He molecule.

The MgHe molecule was studied using ab initio methods by Demetropoulos & Lawley (1982) and very recently by Leininger et al. (2015) and Allard et al. (2016a). The latter study reports potentials and transition dipole moments only for the triplet 3p $^3\Sigma^+$, 3p $^3\Pi$, and 4s $^3\Sigma^+$ states. Comparison reveals close similarities with the present results including in particular crossing of 4s $^3\Sigma^+$ – 3p $^3\Sigma^+$ and 4s $^3\Sigma^+$ – 3p $^3\Pi$ transition dipole moment functions at r(Mg–He) ≈ 2.2 Å (dashed lines in lower part of Fig. 3.8).

Ca^+He: The present calculations include electronic states of Ca^+He molecule correlating with the ground $3p^6 4s$ and excited 3d, 4p, and 5s states of the Ca^+ ion. Potentials and dipole moments of some transitions calculated with the basis sets

Ca.cc-pV5Z.Peterson.26s18p8d3f2g1h.8s7p5d3f2g1h,
He.cc-pV5Z.Dunning.8s4p3d2f1g.5s4p3d2f1g

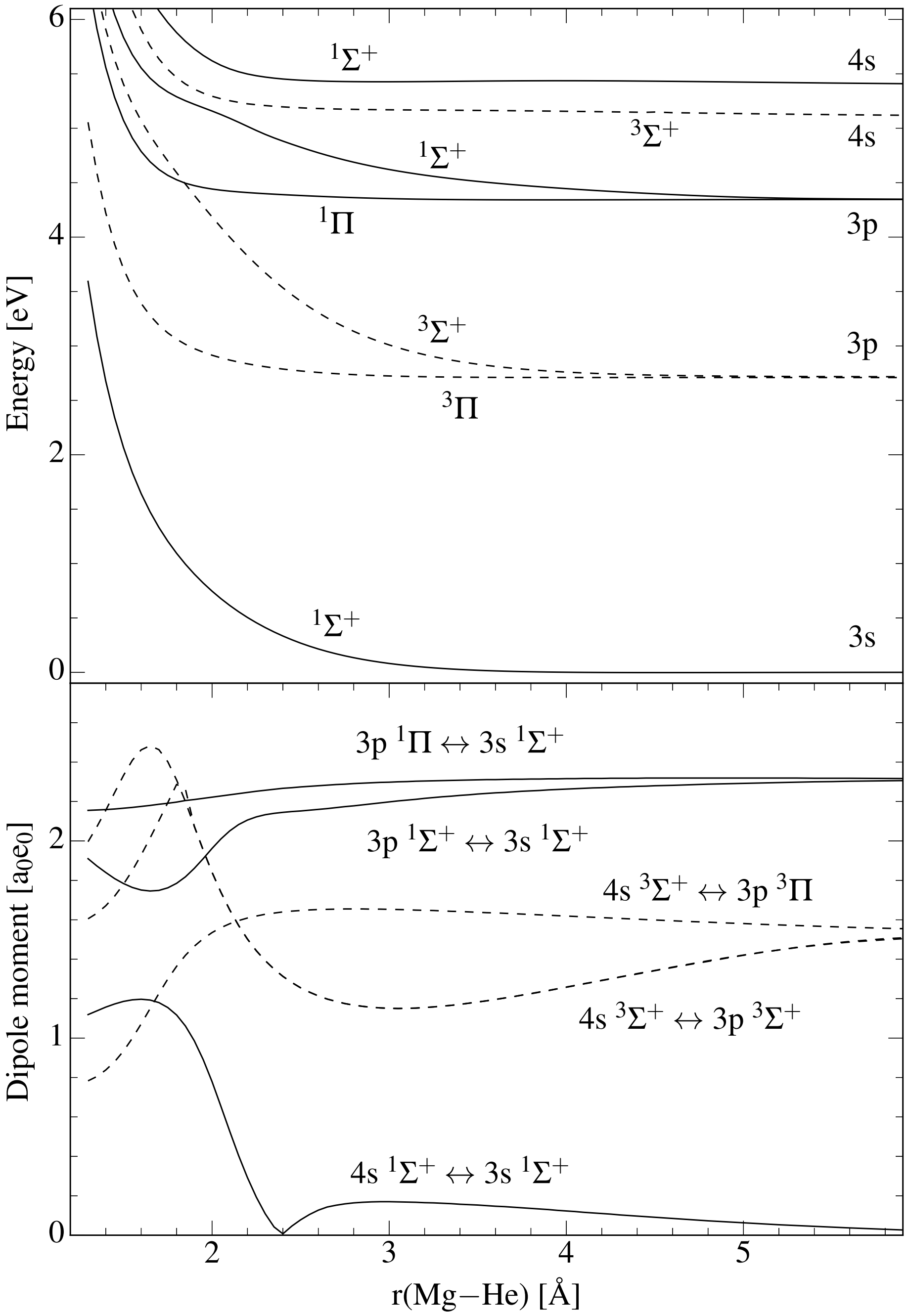

Figure 3.8: Potentials (top) and dipole moments (bottom) for the singlet (solid lines) and triplet (dashed lines) states of MgHe molecule.

are shown in Fig. 3.9. The Ca$^+$He states correlating with 3d ^{2}D$_{3/2,\,5/2}$ are metastable. The 3d $^2\Delta_{3/2,\,5/2}$ and $^2\Pi_{1/2,\;3/2}$ states are weakly bound (D$_e$ $\leq$ 400 cm^{-1}) and 3d $^2\Sigma^+$ is strongly repulsive. Due to interaction between 3d $^2\Sigma^+$ and 4p $^2\Sigma^+$ states, the asymptotically forbidden 3d $^2\Sigma^+$ – 4s $^2\Sigma^+$ transition acquires a considerable dipole moment as r(Ca$^+$–He) decreases (Fig. 3.9). In turn, the dipole moment of the resonance 4p $^2\Sigma^+$ – 4s $^2\Sigma^+$ transition decreases (Czuchaj et al., 1996).

The Ca$^+$He molecule has been the subject of several theoretical studies (Giusti-Suzor & Roueff, 1975; Monteiro et al., 1986; Czuchaj et al., 1996). Line profiles of Ca II H+K resonance lines perturbed by He calculated with the present potentials and transition dipole moments have been discussed in Allard & Alekseev (2014).

3.3.2 Unified line profiles

For the calculation of line profiles we used the semi-classical unified theory as described in Allard & Kielkopf (1982) and many later papers by Allard and coworkers. In particular we use the concept of the "modulated dipole" as developed in Allard et al. (1999), which takes into account the change of the transition probability with emitter-perturber distance, as well as the modification of perturber densities through the Boltzmann factor, depending on the interaction potential. For this work we need profiles extending to more than 1000 Å from the line centre; in a unified theory, which aims to describe the line core and far wing simultaneously this needs profiles extending over a dynamic range of 12 and more orders of magnitude. This required a complete rethinking and reimplementation of all algorithms for the calculation of the auto-correlation function and Fourier transforms; while the physics is taken unchanged from the papers cited above the numerical code was completely rewritten. Improved algorithms and numerous small changes now allow us to cover the profile over more than 10 orders of magnitude without excessive noise and artefacts. We mention only one of the more significant improvements: the calculation of the one-perturber correlation function (see Allard & Kielkopf, 1982) involves integrals of the type

$$\int V(x)\,\sin(2\pi x)\,\mathrm{d}x, \tag{3.2}$$

where V is slowly varying and the sin a rapidly oscillating function. By replacing $V(x)$ over small intervals with a linear approximation the integral can be calculated analytically, avoiding the greatest source of noise in previous calculations.

Line profiles calculated with these new algorithms were used for the resonance

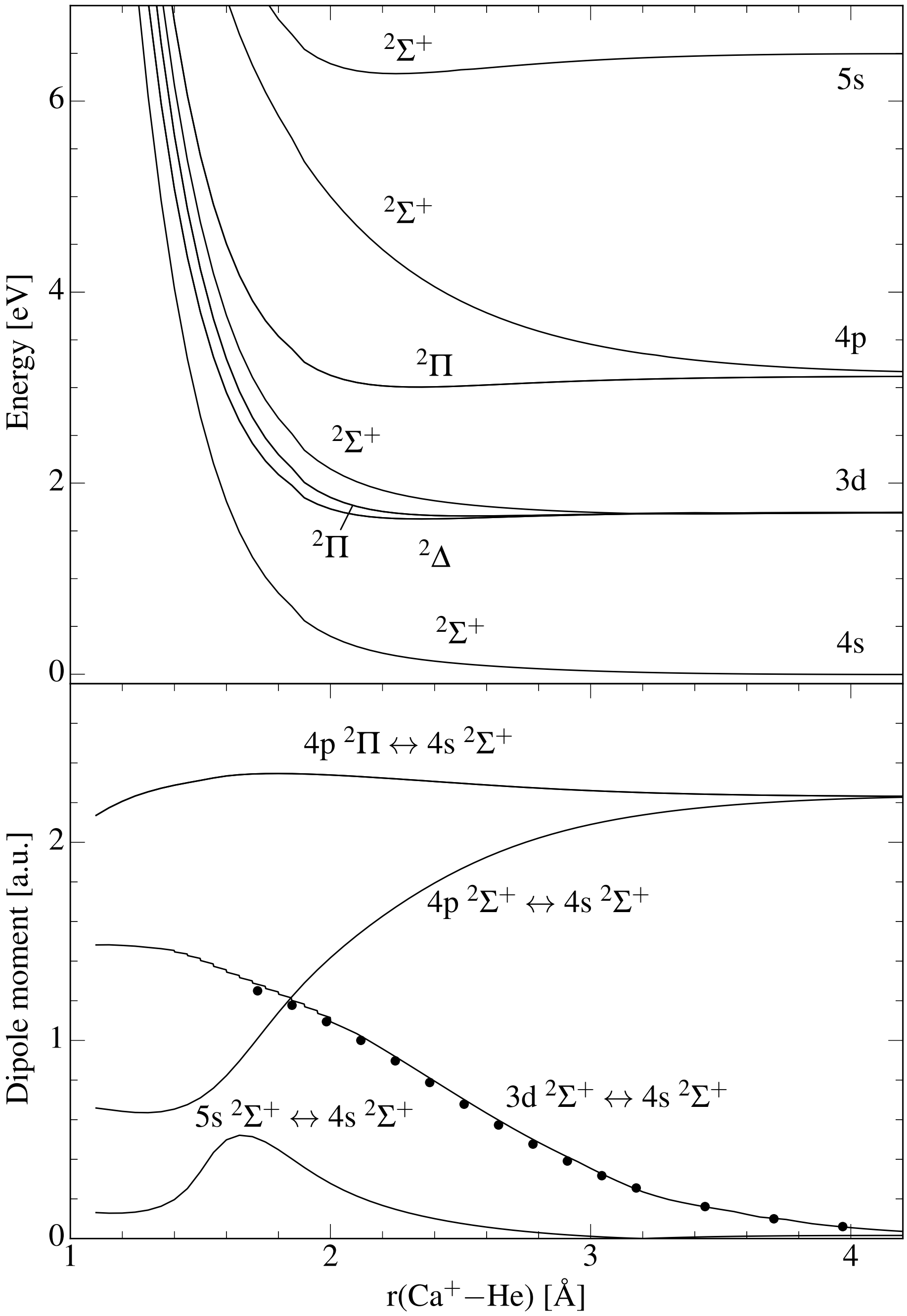

Figure 3.9: Potential energies (top) and dipole moments (bottom) for the Ca$^+$He molecule. The transitions for the Ca II H+K resonance lines are from the 4s to the 4p states. Some of the Czuchaj et al. (1996) results are shown by dotted lines for comparison.

lines of Ca II and Mg II.

After the bulk of this project was complete, new calculations for the Mg I triplet 5168/5174/5185 Å were presented by Allard et al. (2016a). Using atmospheric parameters from KGGD11 ($T_{\rm eff} = 6000\,$K) they show a reasonable fit to the Mg I triplet in SDSS J1535+1247. Our fits to this object with the KGGD11 parameters and also with the new value $T_{\rm eff} = 5770\,$K were of similar quality with our first calculated line profile tables. This table had a spacing of logarithmic perturber density of 0.5 dex, with a high end at 21.0, 21.5, 22.0. When analysing the structure of the atmosphere, we realised that the logarithmic neutral perturber density was close to 22 already near $\tau_{\rm Rosseland} = 2/3$, and much of the line profile was formed at densities larger than 21. As can be seen in Fig. 3 of Leininger et al. (2015) the maximum absorption changes very rapidly with increasing perturber density, moving to the blue of the central wavelength. To better describe the line profile we calculated new profile tables with a finer spacing (0.2 dex) of the log density between 21 and 22. With these tables, the calculated profiles did not fit the spectrum, but showed the maximum absorption far to the blue of the low density maximum. As we do not know the details of the calculations in Allard et al. (2016a), we cannot explain the differences. However, we note that the conditions for this triplet in this object are close to or possibly beyond the limits of the unified theory as discussed in Allard & Kielkopf (1982) (e.g. eqs. 106, 108). Because of these current uncertainties for the Mg I triplet we have decided to use the interpolation algorithm of Walkup et al. (1984), already used and described in KGGD11, which gives a reasonable fit. The same method was also used for other medium strong lines with notable asymmetries.

3.4 Atmospheric analysis

The process of fitting the white dwarfs in our sample is made difficult by both the complexity of the emergent flux and the practical challenge of dealing with the various systematics which affect the SDSS spectra.

Typically one begins the analysis of white dwarf spectra by fitting of the model spectrum to the data at some chosen – preferably line free – continuum regions. Atmospheric parameters are then obtained by fitting to only absorption lines. Such a procedure removes the effects of interstellar reddening and poor flux calibration, allowing for precise estimation of $T_{\rm eff}$ and $\log g$ for DA and DB stars. For the cool DZ stars in our sample, the intense line blanketing at wavelengths below $\simeq 5500\,$Å results in no clearly defined continuum. We therefore chose to work with the flux-calibrated spectra for the fitting of our atmospheric models. However, the flux calibration accuracy for some of the spectra still presented a major hurdle.

The SDSS spectra obtained using the original spectrograph (released DR1–DR8) show very good flux calibration as synthetic g, r, and i magnitudes calculated from these spectra agree well with SDSS photometry. This has previously been investigated in great detail by Genest-Beaulieu & Bergeron (2014), who reach a similar conclusion. In general, flux calibrations taken by the newer BOSS spectrograph from DR9 onwards (most of the new objects in this work were observed using BOSS) are typically much lower in quality for two reasons. Firstly, for objects targeted as QSO candidates, the BOSS flux calibration is purposely incorrect. To improve sensitivity for the Ly-α forest of quasars, the fibers are offset in the bluewards direction of atmospheric dispersion (Dawson et al., 2013). These offsets were not applied for the flux calibration fibers, which are centred at 5400 Å, and so QSO targets have spectra which appear too blue. Because our DZ sample overlaps the colour-space of quasars, many of the white dwarf spectra are affected by this issue. In principle this can be rectified as DR13 provides post-processing corrections for BOSS flux calibrations according to the procedure of Margala et al. (2015). However, high proper-motions (median value of $60\,\mathrm{mas\,yr^{-1}}$, and maximum of $600\,\mathrm{mas\,yr^{-1}}$ for our sample) lead to a second source of systematic error resulting in unreliable flux calibrations. The spectroscopic fibers (2 arcsec in diameter for BOSS), are placed according to positions obtained via SDSS imaging, taken up to and including DR7. Therefore significant displacement of sources between photometric and spectroscopic observations results in further calibration error of spectral fluxes.

Since the fitting of our model atmospheres requires fairly good flux calibration we apply a simple correction to affected spectra. The BOSS spectrograph fully covers the wavelengths of the SDSS g, r, and i filters, allowing us to calculate synthetic magnitudes in these bands. The differences between the SDSS and synthetic magnitudes against their effective wavelengths are then fitted with a first order polynomial (including uncertainties on both the SDSS and synthetic photometry). Converting the fit from magnitudes to spectral flux units provides a wavelength dependent correction, which we multiply with the original spectrum. Iterating this procedure three times ensures good agreement of the spectrum with its g, r, and i magnitudes. To demonstrate the effectiveness of this procedure, one system, SDSS J1058+3143, is shown in Fig. 3.10 with both its SDSS and BOSS spectra. The BOSS spectrum is distorted by the original flux calibration, but is seen to agree well with photometry following our correction. In cases like SDSS J1058+3143 where BOSS and SDSS spectra were available, it was usually preferable to use the

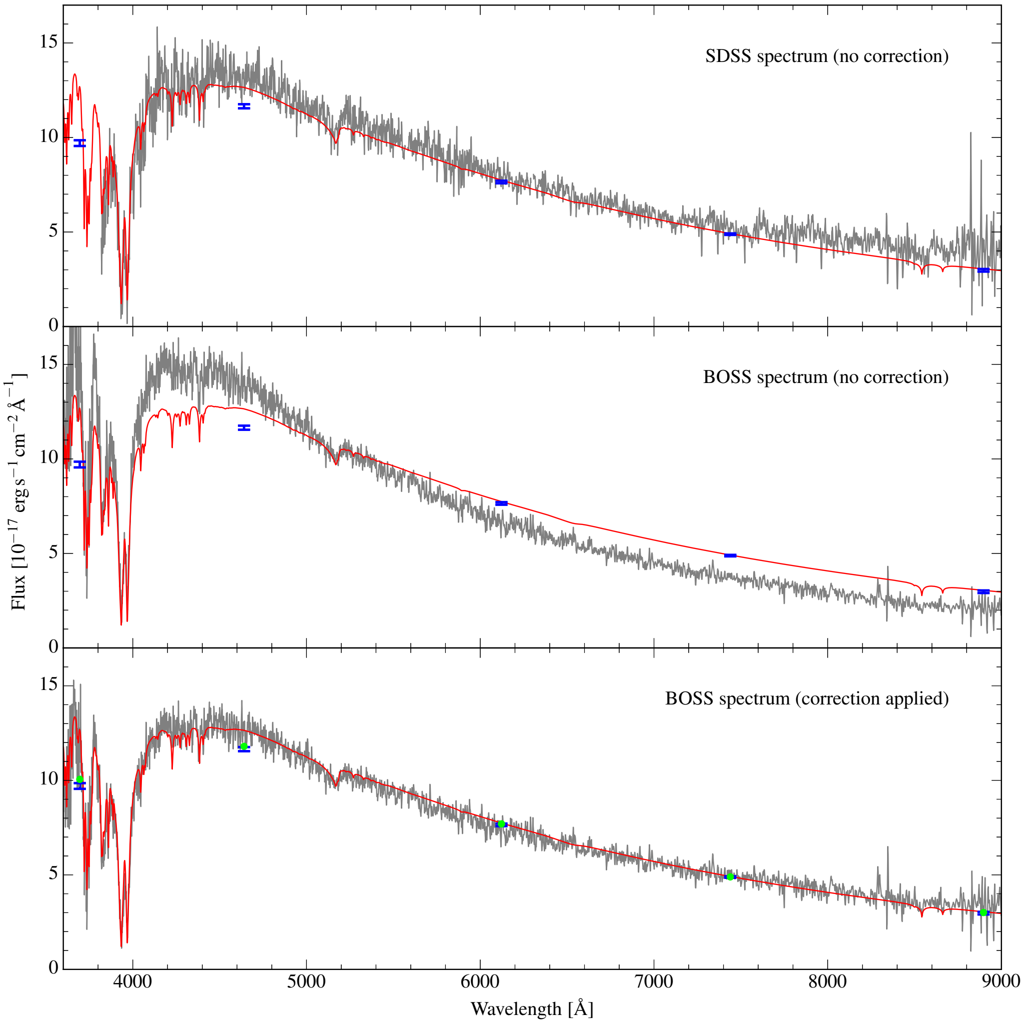

Figure 3.10: The pre-BOSS spectrum of SDSS J1058+3143 (top) is seen to match the SDSS photometry (blue points). The BOSS spectrum with its original flux calibration (middle) overestimates flux at blue wavelengths, and underestimates it at red wavelengths. Applying our corrective procedure to the BOSS spectrum (bottom) effectively removes the distortion to the flux calibration. In all panels our best fitting model is shown in red. In the bottom panel the model's synthetic magnitudes are also displayed (green) showing the close agreement in all bands when fitting to the corrected spectra. Displayed spectra are smoothed with a 3-point boxcar for clarity. The u-band points are placed redwards of their effective wavelength (3595 Å) in order to appear within the bounds of the figure.

corrected BOSS spectra (unless the BOSS spectra were of very low quality) as these go to bluer wavelengths ($\simeq 3600$ Å versus $\simeq 3800$ Å for the original spectrograph), covering additional spectral lines, in particular Mg and Fe. The SDSS spectrum that fitting was performed on is given in the plate-MJD-fiber column in Table B.1.

To model the corrected spectra, we first made zeroth order estimates by fitting a grid of DZ models, spanning a wide range in T_{eff} and metal abundances (the same model grid described in section 3.1.1). T_{eff} is varied from 4400 to 14 000 K in 200 K steps, and log[Ca/He] from -10.5 to -7.0 in 0.25 dex steps. All other elements are held at bulk Earth abundances relative to Ca, and the $\log g$ is set to 8.0 in all cases. The χ^2 between each grid point and the target spectrum was calculated. The grid of χ^2 values was then fit with a bi-cubic spline to estimate the location of minimum χ^2 in the plane of T_{eff} and Ca abundance, and the corresponding parameters were then used as a starting point for a detailed fit. From this point, parameters in the model were manually iterated in small steps (typically 100 K or less in T_{eff} and 0.05–0.3 dex for abundances), until satisfactory agreement between spectrum and model was found. The χ^2_{red} between model and data served as an approximate indicator of goodness of fit, but due to the various model and calibration uncertainties described, could not always be relied upon. Instead agreement between photometry and the relative strengths of absorption lines could be used to gauge required adjustment in T_{eff}, and then the abundances could be fine tuned from residual differences in each absorption line. Due to the complicated way in which T_{eff} and abundances affect line strengths, further adjustments of these parameters were often needed, in some cases (depending strongly on the spectral S/N) requiring several tens of models.

Two caveats to our fits are that they are performed at a fixed $\log g$ of 8, and unless in obvious disagreement with the data, at a fixed hydrogen abundance of $\log[\text{H}/\text{He}] = -4$ dex. Here we discuss the effect of these caveats on our parameter estimation.

Firstly we note that it is not possible to estimate surface gravities from the spectra of cool helium atmosphere white dwarfs, as the effect of changing $\log g$ on the emergent spectrum can generally be compensated by adjustment of the other model parameters. In other words $\log g$ is strongly correlated with the other atmospheric parameters, and so increases the uncertainties in the parameters derived from our fits compared with those at a fixed value $\log g = 8.0$. We attempted to quantify the effect of $\log g$ on our uncertainties, by refitting SDSS J1535+1247 at multiple $\log g$ values and examining the shift in T_{eff} and abundances. Genest-Beaulieu & Bergeron (2014) find the SDSS spectroscopic $\log g$ distribution to have a standard deviation of

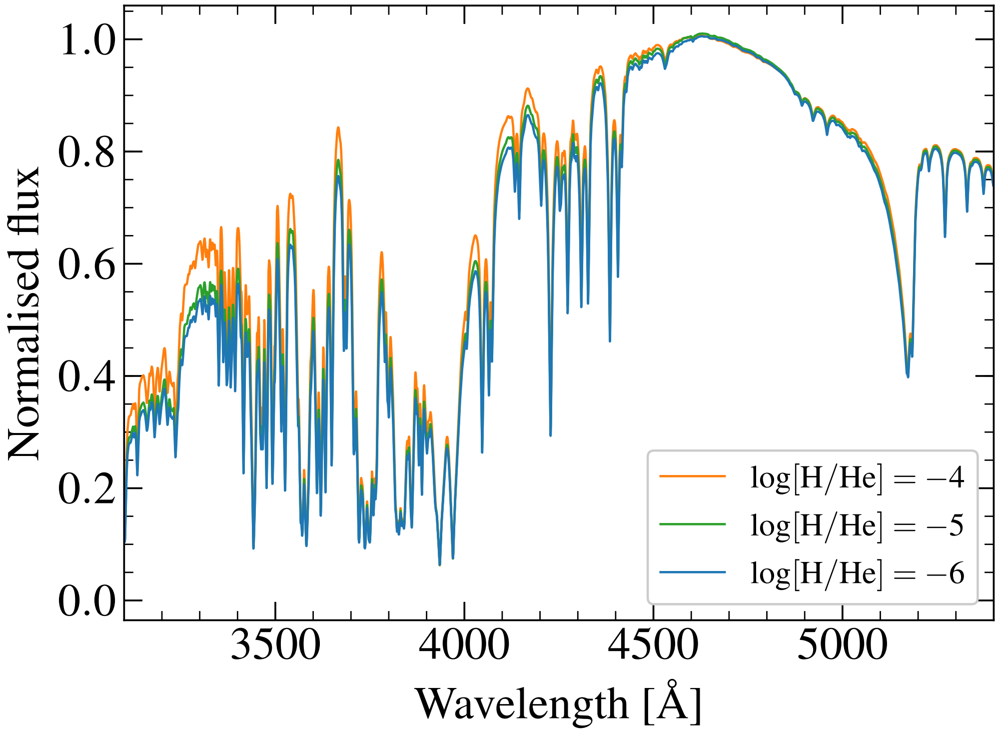

Figure 3.11: The best fitting model for SDSS J1336+3547 is shown in red. The green and blue models are recomputed at decreased hydrogen abundances with all other atmospheric parameters held constant. No discernible change is seen for abundances below $\log[\mathrm{H/He}] = -6$. Normalisation is with respect to the $\log[\mathrm{H/He}] = -4$ model.

0.2 dex. We therefore repeated our fits to SDSS J1535+1247 at $\log g = 7.8$ and 8.2. We found that a 0.2 dex increase in $\log g$ leads to 75 K increase in T_{eff}, and 0.19 dex increases in abundances, with the opposite effects for a 0.2 dex decrease. Fortunately, because all abundances correlate with $\log g$ to the same degree, abundance ratios are minimally effected. Therefore using a fixed $\log g$ value will not significantly impact the investigation of accreted body compositions (Chapter 4).

By default hydrogen abundances were set to $\log[\mathrm{H/He}] = -4$ dex in our models, as we do detect trace hydrogen at this level (and higher) in several of the brightest systems. This value of -4 dex was only adjusted if the models showed departure from the data and hence we report hydrogen abundances only in those cases. The presence of trace hydrogen does increase the electron density within the atmosphere slightly and so, in principle, modifies the metal line profiles compared with a hydrogen deficient atmosphere. However, we demonstrate in Fig. 3.11 that this effect is negligible, where we decrease the hydrogen abundance from log[H/He] = −4 to −6 dex with all other atmospheric parameters held constant for the system SDSS J1336+3547. For transitions such as the Ca H+K lines, Ca I 4228 Å line, and the Mg-b blend ($\simeq$ 5170 Å) the difference between line profiles is small enough as to be undetectable even in the highest quality spectra presented in this work. The largest difference is seen at blue wavelengths between 3000 Å and 4500 Å, where the continuum flux can be 15 % greater at −4 dex than at −6 dex. However, for the majority of spectra the signal-to-noise ratio at these wavelengths is so low (typically between 2 and 6) that the effect of a fixed hydrogen abundance does not affect our fits.

Generally the χ^2 between data and models served only as an indicator of fit quality. Direct χ^2 minimisation did not necessarily correspond to the *best* fit as, for instance, any remaining flux calibration error (higher order than our corrections could account for) could dominate the residuals in the fit. Additionally, residuals are affected where the wings of line profiles still require further theoretical improvement. For example the blue wing of the Mg I b-blend at $\simeq$ 5170 Å, does not always fit the data well, particular for the lowest temperatures in our sample. In this situation, we found an adequate solution was to match the equivalent widths between model and spectrum (as well as fitting other Mg features), which does not correspond to χ^2 minimisation.

For a few of the brightest objects where the flux calibration is considered to be exceptionally good, in particular those where we have obtained WHT spectra (SDSS J0116+2050, SDSS J0512−0505, SDSS J0741+3146, SDSS J0744+4649, SDSS J0823+0546, SDSS J0806+4058, SDSS J0916+2540, SDSS J1043+3516, SDSS J1144+1218, and SDSS J1535+1247), direct χ^2 minimisation was considered to be appropriate. Even so, in some cases where line widths between model and spectrum are not in exact agreement (e.g. the Mg I line of SDSS J0512−0505), a better fit was achieved by manually updating some parameters following the least-squares fit.

The atmospheric parameters derived from our fits are given in Table B.2. The final models are shown with their corresponding spectra in the Figs. A.1–A.11 in appendix A. Where we obtained WHT spectra, the models are also shown in Fig. 3.6.

From the fit parameters we also derive convection zone masses and diffusion timescales for each element. For this purpose we calculated the convection zone sizes and diffusion timescales for the same grid of models described before in terms of T_{eff} and Ca abundances.[4] These were then bi-linearly interpolated to estimate diffusion rates and convection zone sizes.

Uncertainties are difficult to estimate from these fits. For the 10 objects mentioned above that we fitted via a least-squares routine, the reported errors on T_{eff} are typically a few K, and for abundances a few 0.01 dex. As these are purely statistical errors they are far too small and fail to account for systematic uncertainty. Even for the very best spectra, we believe the errors on T_{eff} are measured to no better than 50 K (where systematic uncertainty dominates), but can be as large as 400 K for the noisiest spectra. To estimate the error on T_{eff} (σ_T) on a per-object basis, we combine the aforementioned systematic and statistical variances producing the simple relation

$$\sigma_T^2 = (50\,\mathrm{K})^2 + \left(\frac{T_{\text{eff}}}{5\,\mathrm{SN}}\right)^2 . \tag{3.3}$$

The statistical component of σ_T (right-hand term) is assumed to be proportional to T_{eff} divided by the median spectral signal-to-noise ratio between 4500 and 5500 Å (SN). The scaling factor of 5 was chosen to give the expected distribution of errors as described above. The σ_T calculated from equation (3.3) are included in Table B.2, and are used for error propagation in section 3.7.

Uncertainties on abundances are dependent on the element, the line strengths, and the spectral signal-to-noise ratio. We estimate these are typically in the range 0.05–0.3 dex from adjustment of the abundances in the models in comparison with the data. Ca is in general the most well measured element due to the large oscillator strengths of the H+K lines, which remain visible over the entire T_{eff} range of objects in our sample.

As stated previously, all models were calculated at a fixed surface gravity of $\log g = 8$. Even so, uncertainties of 0.2 dex can be assumed from the width of the empirical white dwarf $\log g$ distribution (Genest-Beaulieu & Bergeron, 2014).

For the fitting described throughout this section, we assumed that interstellar reddening has a minor effect on the spectra, as these faint stars are estimated to lay within a few hundred parsecs from the Sun (see section 3.7), and the SDSS footprint avoids the Galactic plane. We show this assumption to be reasonably justified, given the already moderate uncertainties for the more distant, and hence most affected systems. For each object, we calculated the maximum possible reddening along its line of sight using the Schlegel et al. (1998) Galactic dust map, and found the

---

[4] For detailed discussion on these envelope calculations see Koester & Wilken (2006a) and Koester (2009) with the most up to date tables available at `http://www1.astrophysik.uni-kiel.de/~koester/astrophysics/astrophysics.html`

maximum $E(B-V)$ values to have a median of 0.029. For three nearby, bright systems (SDSS J0116+2050, SDSS J1043+3516, and SDSS J1535+1247) which span a variety of $T_{\rm eff}$ and can be safely considered unreddened, we applied an artificial reddening of $E(B-V)=0.029$ and refit the spectra to quantify the effect.

We found the typical effect on $T_{\rm eff}$ to be a decrease of $\simeq 130\,{\rm K}$, and abundances decreasing by $\simeq 0.1\,{\rm dex}$. While this is comparable to our estimated errors for the brightest systems, for the more distant objects, where reddening reaches its maximum, our estimated $T_{\rm eff}$ and abundance uncertainties exceed the systematic effect from reddening. We therefore conclude that reddening does not significantly affect our results, due to the intrinsic faintness of these low $T_{\rm eff}$ objects. For white dwarfs hotter than 12000 K (Genest-Beaulieu & Bergeron, 2014), reddening cannot be neglected as high quality data can be obtained out to many hundreds of parsecs.

One exception in our sample is SDSS J0447+1124, which was observed in SDSS stripe 1374. This star has a maximum r-band extinction of 1.3 mag, and maximum $E(B-V)=0.47$. Therefore our parameter estimates for this object should be treated with an appropriate degree of skepticism.

3.5 Comparison with other DZ samples

Our sample of DZ white dwarfs focuses on high metallicities at low $T_{\rm eff}$. We have compared our work with that of Dufour et al. (2007) and Koester & Kepler (2015), who investigated metal pollution in warmer helium atmosphere white dwarfs.

Koester & Kepler (2015) carried out a systematic analysis of 1107 DB stars in SDSS, and as part of that work measured Ca abundances. The authors obtained firm measurements of log[Ca/He] for 77 objects in their sample, and upper limits for the remaining stars. These 77 DBZ span 11 000–18 000 K in $T_{\rm eff}$.

The Dufour sample consists of 146 DZ white dwarfs with $T_{\rm eff}$ of 6000–12 000 K. One additional system (plate-MJD-fiber = 0301-51942-0030) is reported at $T_{\rm eff}=4600\,{\rm K}$, however inspection of its spectrum shows this to be a K-type main-sequence star and we therefore remove it from our comparison. As this sample is intermediate in $T_{\rm eff}$ with respect to our sample and that of Koester & Kepler (2015), there is some minor overlap. One system is common to Koester & Kepler (2015) and Dufour et al. (2007), and four systems from Dufour et al. (2007) appear in our work (SDSS J0956+5912, SDSS J1038−0036, SDSS J1112+0700, SDSS J1218+0023). For these five stars we adopt the parameters from Koester & Kepler (2015) and our analysis here.

The minimal overlap between the samples is unsurprising. As Koester &

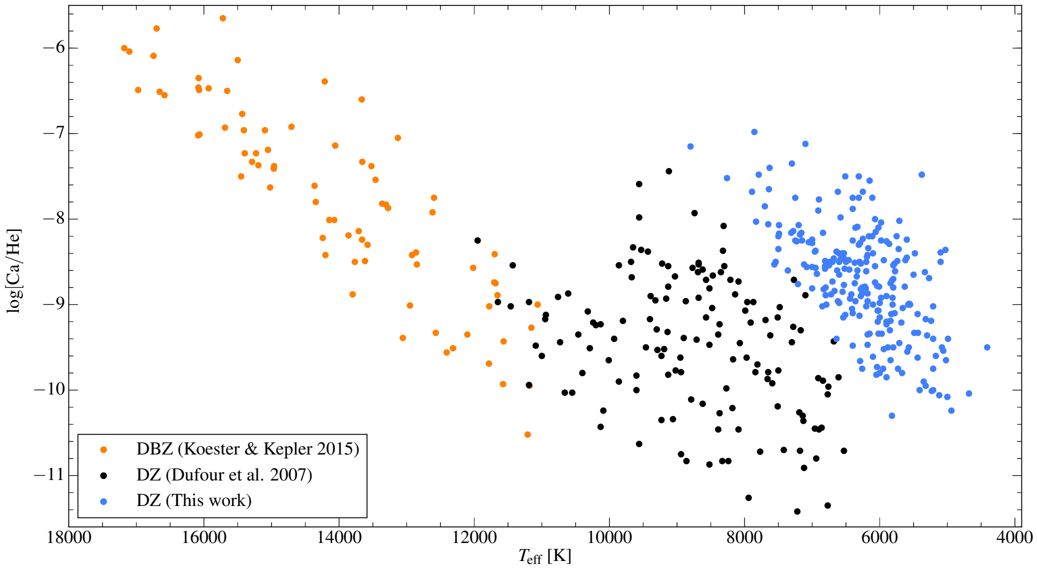

Figure 3.12: Atmospheric Ca abundances against T_{eff} for our DZ sample along with the DBZ/DZ samples of Koester & Kepler (2015) and Dufour et al. (2007).

Kepler (2015) and Dufour et al. (2007) search for DB(Z)s and DZs respectively, the presence of He lines in the SDSS spectra set apart these two samples. The *maximum* $u-g$ colour-cut adopted by Eisenstein et al. (2006) (from which the DZs in Dufour et al. (2007) were selected), is only slightly higher than our *minimum* $u-g$ colour-cut (see section 3.1.1), and so as expected there are only a few objects common to both our sample and that of Dufour et al. (2007).

The distribution of these three samples in log[Ca/He] vs. T_{eff} are displayed in Fig. 3.12. Prominent upper and lower boundaries are observed for the combined distribution, with the objects from Dufour et al. (2007) joining smoothly with the other two samples. The lower bound simply reflects the detection limit for Ca as a function of T_{eff} in He dominated atmospheres, and thus has no physical interpretation. For systems with lower Ca abundances than this bound, only upper limits can be obtained. The upper boundary of the distribution contains significant structure which was not expected. For the DBZs in the Koester & Kepler (2015) sample and the warmest DZs of the Dufour et al. (2007) sample, the maximum observed log[Ca/He] is seen to decrease with decreasing T_{eff}, reaching a minimum of $\simeq -9$ dex between 10 000 K and 11 000 K.

At $\simeq$ 10 000 K, maximum Ca abundances are seen to rapidly increase by more than an order of magnitude over a narrow T_{eff} range, merging smoothly into our DZ distribution (blue points) where the maximum Ca abundances reach $\simeq -7$ dex at about 8000 K. Interestingly, the Dufour et al. (2007) DZ sample appears to show both these effects.

Noticing the downwards trend within their DBZ sample, Koester & Kepler (2015) converted Ca abundances to accretion rates by considering the $T_{\rm eff}$-dependence of the convection zone masses and Ca diffusion timescales (see their Figs. 4, 10, and 11). The $T_{\rm eff}$-dependence of the maximum Ca accretion rates remained in the resulting distribution, yet the authors note that no such trend is seen for DAZ white dwarfs over the same $T_{\rm eff}$ range (Koester et al., 2014). Because there is no reason to think the range of accretion rates should differ between hydrogen and helium atmosphere white dwarfs, Koester & Kepler (2015) concluded an incomplete understanding of deep convection zone formation may be responsible.

This decrease in log[Ca/He] persists down to $\simeq 10\,000$ K in the DZ sample of Dufour et al. (2007), demonstrating that it is not sensitive to differences in the input physics and numerical methods in the two different atmospheric codes. The sharp increase in Ca abundances by two orders of magnitude between 10 000–8000 K seen in the Dufour et al. (2007) DZ sample before merging smoothly into our own sample suggests either a rapid decrease in convection zone sizes, an increase in diffusion timescales, or some combination of these two factors.

An alternative hypothesis for the abrupt rise in log[Ca/He], is that a dynamical instability occurs after $\simeq 0.7$ Gyr of white dwarf cooling ($T_{\rm eff} \simeq 10\,000$ K), spontaneously increasing the occurrence rate at which planetesimals are accreted (e.g. see Fig. 3 of Mustill et al., 2014). For white dwarfs with hydrogen atmospheres with their short sinking time-scales, such an instability would instead manifest itself as an increase in the DAZ/DA ratio at around the same age which, subject to selection biases, is potentially observed in Fig. 8 (middle panel) of Koester et al. (2014),

A further downwards trend in log[Ca/He] is seen in the upper envelope of the blue points in Fig. 3.12 from $4000\,\mathrm{K} < T_{\rm eff} < 9000\,\mathrm{K}$. We address this in Chapter 5 due to its likely relevance to remnant planetary system evolution.

3.6 Hydrogen abundances

The origin of trace hydrogen at white dwarfs with helium-dominated atmospheres is not fully understood, with proposed explanations including a primordial origin or accretion from the interstellar medium (Bergeron et al., 2015; Koester & Kepler, 2015), however an alternate hypothesis includes the accretion of water rich planetesimals. Oxygen excesses identified at the metal-polluted white dwarfs GD 61 (Farihi et al., 2013a) and SDSSJ124231.07+522626.6 (Raddi et al., 2015), indicate that these systems must have accreted water-rich material as only partial fractions of their respective oxygen budgets could be associated with the other detected elements in the form of metal-oxides. Both Farihi et al. (2013a) and Raddi et al. (2015) therefore suggested that the trace hydrogen present in the helium-dominated atmospheres of GD 61/SDSSJ124231.07+522626.6, could be explained by accretion of water-rich material. Furthermore, Gentile Fusillo et al. (2017) find evidence that trace hydrogen is correlated with the presence of metals, potentially strengthening the argument for water accretion as the solution to DB white dwarfs with trace hydrogen. From a theoretical perspective, Veras et al. (2014c) found that hydrogen delivery from exo-Oort cloud comets is dynamically possible, and could provide the necessary hydrogen on Gyr timescales to explain observations.

Unlike metals which sink out of the white dwarf convection zone, hydrogen remains suspended indefinitely, thus observed abundances would correspond to the total mass from multiple accretion events, integrated over the cooling age of the white dwarf. This suggests that DB white dwarfs with trace hydrogen (but no metal contamination), may have accreted planetesimals in the past, but with the hydrogen as the only remaining evidence of such accretion events.

While not the focus of this work we do obtain hydrogen abundances and upper limits thereof for a handful objects in our sample. As described in section 3.4, we only attempted to constrain hydrogen abundances in our atmospheric modelling if there we found an obvious discrepancy between the model and observed spectra, where the default abundance was set to log[H/He] $= -4$ dex. One possibility was that the model showed a hydrogen line which was not present in the data, in which case an upper-limit estimation is made. These upper-limits depend both on the white dwarf T_{eff} and also the S/N of the spectrum. In the cases where the measurement is *not* an upper-limit, the detection may either correspond to an Hα detection or an increased hydrogen abundance may have been necessary to replicate the spectrum. For white dwarfs too cool to display Hα the presence of hydrogen still contributes significantly to the electron-pressure in the atmosphere. The resulting increase in atmospheric opacity leads to both a narrowing of the metal lines and a redder continuum, for a given T_{eff} and metal abundances. In principle this additional electron pressure may arise from elements other than hydrogen, e.g. sulfur, but because hydrogen is typically present at abundances orders of magnitude higher than metals, it is a reasonable assumption that hydrogen is the principal donor of additional electrons.

All objects where we were able to constrain hydrogen abundances are displayed in Fig. 3.13. Additionally the spectrum of SDSS J0150+1354 which has the

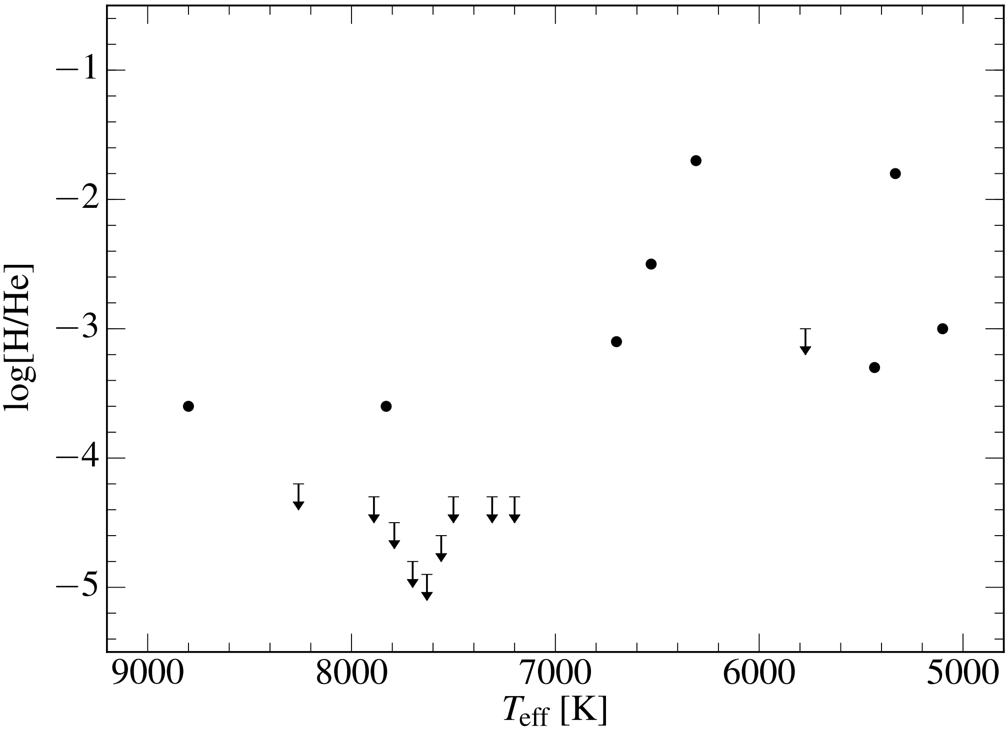

Figure 3.13: Hydrogen abundance as a function of T_{eff}. Firm measurements are indicated by dots, whereas arrows correspond to upper limits only. Hydrogen abundance uncertainties are estimated to be typically around 0.3 dex.

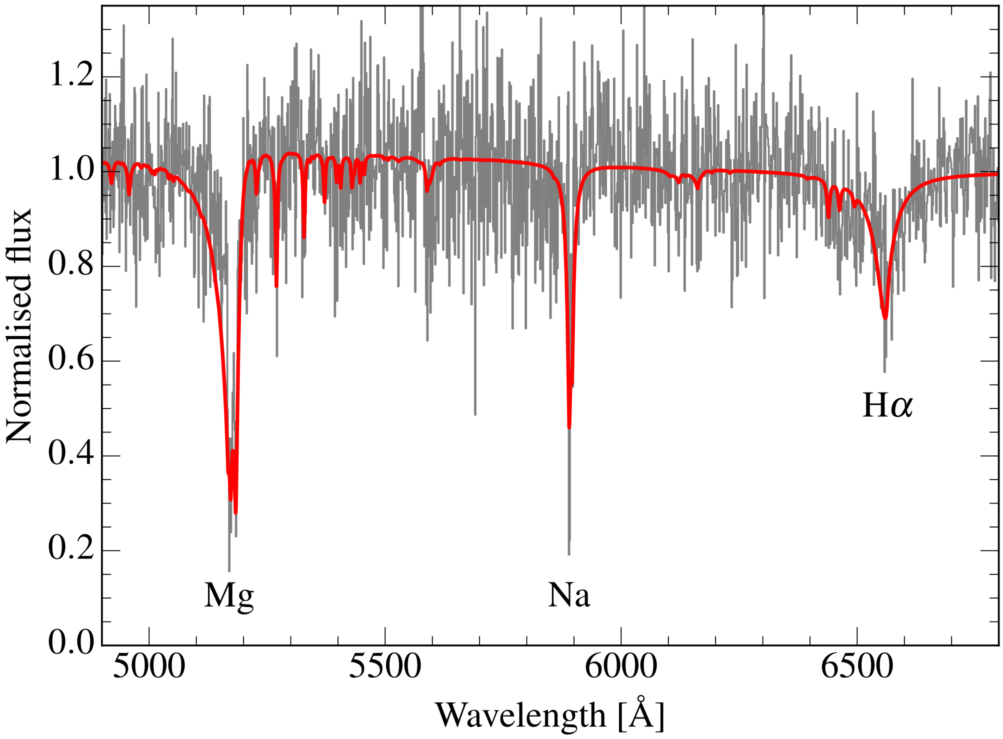

Figure 3.14: Normalised spectrum and best fit model to SDSS J0150+1354, demonstrating the large hydrogen abundance for this cool object. Strong lines are labelled.

largest H abundance in our sample ($\log[\mathrm{H/He}] = -1.7$ dex) is shown in Fig. 3.14, demonstrating the clear Hα detection, and narrow Mg I and Na I lines, even with a cool T_{eff} of 6300 K.

Our sample shows a clear increase in trace hydrogen towards lower T_{eff} within Fig. 3.13. Above 7000 K, (cooling age of 1.5–2.0 Gyr), no objects are found with $\log[\mathrm{H/He}] > -3$ dex. Naively one may be inclined to think Fig. 3.13 provides a strong case for trace hydrogen increasing with cooling age, however this is not the case. If hydrogen accumulation occurred at a constant rate then the inferred hydrogen masses diluted within the white dwarf convection zone should increase linearly with time. The distribution of temperatures in Fig. 3.13 corresponds to cooling ages of about 1–6 Gyr (calculation of cooling ages is discussed in section 3.7), or about 0.8 dex in the logarithm of cooling ages. As convection zone sizes (see Table B.3) are not calculated to change more than about 0.3 dex over the range of the plot, a constant rate of hydrogen accumulation cannot explain the $\simeq 2$ dex increase in abundance observed between the objects above and below T_{eff} of 7000 K in Fig. 3.13.

It is much more plausible that this represents a selection bias related to our colour-cut. For instance, the white dwarf SDSS J1038−0036 has $T_{\mathrm{eff}} = 7700\,\mathrm{K}$ and hydrogen upper-limit of $\log[\mathrm{H/He}] \leq -4.8\,\mathrm{dex}$ from our spectroscopic fit. Recalculating the model spectrum with $\log[\mathrm{H/He}] = -2\,\mathrm{dex}$ (and all other atmospheric parameters kept the same) results in flux redistribution towards blue wavelengths. This changes the $u - g$ colour from 0.71 to 0.42 which falls outside of the colour-cut described in section 3.1.1. It may well be the case that objects do exist with $T_{\mathrm{eff}} > 7000\,\mathrm{K}$ and $\log[\mathrm{H/He}] > -3\,\mathrm{dex}$, but because of their blue colours, are absent in our sample.

The larger number of objects with log[H/He] upper-limits for $T_{\mathrm{eff}} > 7000\,\mathrm{K}$ is also a selection effect. Hotter objects are naturally brighter and thus more likely to have high S/N spectra. Additionally the strength of the Hα line increases with increasing T_{eff} and so observed spectra where log[H/He] is noticeably less than the default model value of $-4\,\mathrm{dex}$ are more likely to be identified. Conversely, below T_{eff} of 7000 K spectra become noisier, Hα lines become weaker, and so typically no visible disagreement is seen for $\log[\mathrm{H/He}] = -4\,\mathrm{dex}$.

None of the above is to say that trace hydrogen is unrelated to the accretion of water-rich objects, simply that the higher abundances seen for the cooler objects in Fig. 3.13 *do not* indicate a time-dependent increase. In conclusion, these results neither favour nor rule out any of the hypotheses for the source of trace hydrogen at white dwarfs with helium dominated atmospheres, i.e. water-rich planetesimals, ISM accretion, or a primordial origin.

3.7 Spatial distribution and kinematics

The calculation of model spectra for a given set of atmospheric parameters (T_{eff}, $\log g$, chemical abundances), yields the emergent spectrum per unit area of the stellar surface. Given the radius of the white dwarf, the absolute spectral flux density can be calculated, which when compared with observational data can be used to infer the distance to the star. We estimate the distances to the DZ stars in our sample propagating the relevant uncertainties via a Monte-Carlo method.

White dwarf radii are a function of both mass and to a much lesser extent T_{eff}, however we have no direct spectral constraint on the masses of our white dwarf sample. Instead, we used the SDSS mass distribution (Kepler et al., 2015) as a prior on the white dwarf mass, and the uncertainties on T_{eff} from Table B.2. These were then propagated through a grid of DB cooling models[5] (Fontaine et al., 2001;

---

[5] The DB cooling models we have used (accessed Sep 2016) can be found at `http://www.astro.`

Bergeron et al., 2001; Holberg & Bergeron, 2006; Kowalski & Saumon, 2006; Bergeron et al., 2011) to calculate posterior distributions on radii. We then calculated synthetic absolute r-band magnitudes from the best-fit models propagating uncertainties from the radii and $T_{\rm eff}$. Finally, distance-moduli and hence distances were determined from the SDSS r-band photometry.

We acknowledge that our distance calculations are not entirely free from bias. Firstly we do not account for interstellar extinction. The SDSS footprint avoids the Galactic plane, minimizing extinction effects, however the most distant stars at a few hundred pc may suffer a small amount. Using the Galactic dust map of Schlegel et al. (1998) we determined the *maximum* extinction possible for each object in our sample, and found a median value of 0.08 mag in the r-band. For the furthest away objects, this implies a typical distance underestimate of 4 % at most. As discussed in section 3.4, SDSS J0447+1124 is an exception, having a maximum r-band extinction of 1.3 mag, and so could be up to 80 % further away than our calculation suggests.

Secondly, we do not account for Lutz-Kelker bias, which places greater statistical weight on larger distances as the prior distribution on distance d is proportional to d^2 for nearby stars uniformly distributed in space. As our our relative distance errors are all near 13 %, Lutz-Kelker bias would lead to a typical underestimate of 3.5 %. Finally there is some evidence that magnetic white dwarfs may be drawn from a different mass-distribution with higher mean than their non-magnetic counterparts (Liebert, 1988; Liebert et al., 2003). If true, then magnetic systems may be closer than our estimates suggest. However considering the above, for vast majority of objects the distance uncertainties remain dominated by the poorly constrained white dwarf masses/radii resulting in relative distance errors of 12–14 %.

Combining the distance estimates with proper-motions (and their uncertainties), we also calculated the tangential velocities for our DZ sample. As described in section 3.1.1, not all objects have a proper-motion measured by SDSS. For a few bright objects with no proper-motion, we instead obtained values from PPMXL. These systems are SDSS J0044+0418, SDSS J0117+0021, SDSS J0842+1406, SDSS J1144+1218, SDSS J1329+1301, and SDSS J2225+2338.

Finally, the grid of cooling models also includes cooling ages for given masses and $T_{\rm eff}$. Like radii, we used a Monte-Carlo method to calculate cooling ages and uncertainties. While we do not discuss ages in this chapter beyond their calculation we make direct use of them in Chapter 5 with relevance to the evolution of remnant planetary systems.

In Table B.4 we list our calculated distances, (and where available) proper-

---

`umontreal.ca/~bergeron/CoolingModels/`.

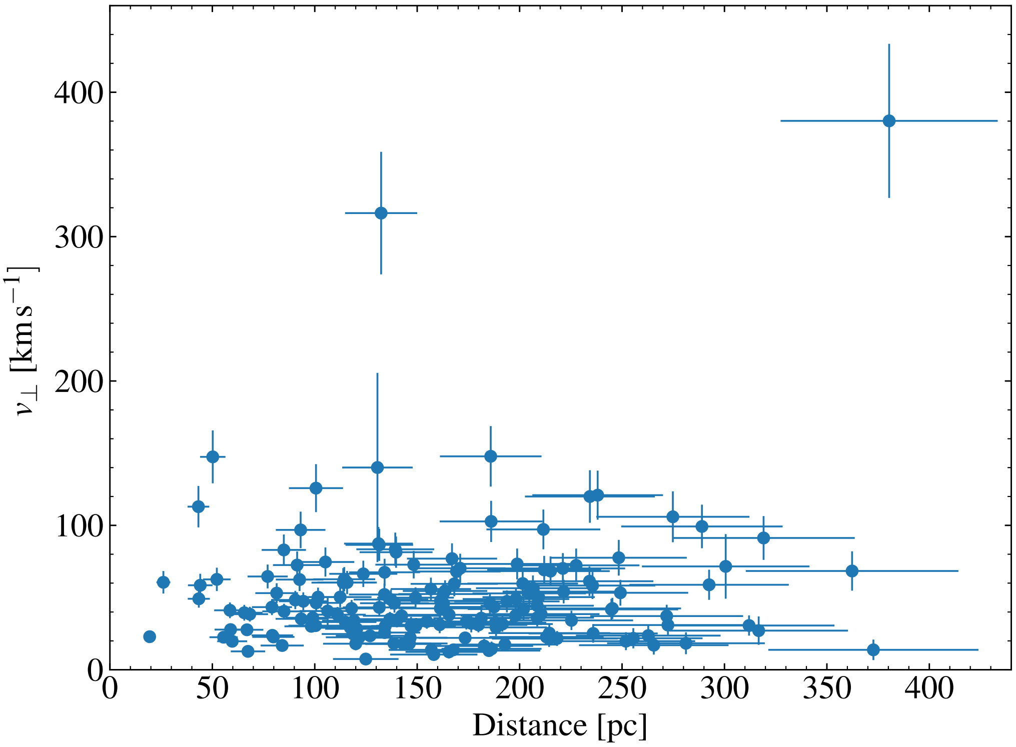

Figure 3.15: Tangential space-velocities against the estimated distance for the DZs in our sample for which a proper-motion measurement is available.

motions, μ, estimated tangential velocities, $v_\perp$, and cooling ages. Note that the calculated posterior-distributions for ages were often asymmetric, and so the quoted values and uncertainties correspond to the median and $\pm 1\sigma$ percentiles. In Fig. 3.15, we show $v_\perp$ against distance (objects with no measured proper-motion are not displayed). Note that while both horizontal and vertical error-bars are shown, $v_\perp$ is strongly correlated with the distance, and so the corresponding error-ellipses are narrow.

In Fig. 3.15 the two systems SDSS J0117+0021 and SDSS J1443+5833 stand out as high $v_\perp$ outliers, with tangential velocities $316 \pm 42\,\mathrm{km\,s^{-1}}$ and $380 \pm 53\,\mathrm{km\,s^{-1}}$ respectively. Such fast moving objects are certainly halo stars. While main-sequence halo stars are typically found with low metallicities, these two objects demonstrate that halo stars *are* hosts to planetary systems which survive stellar evolution to the white dwarf stage. This is further supported by Koester & Kepler (2015) who show two DBZ stars with heights exceeding 400 pc above the Galactic plane.

All other systems in Fig. 3.15 have $v_\perp$ below $150\,\mathrm{km\,s^{-1}}$ indicating these are Galactic disc members, and their distribution in $v_\perp$ appears constant with distance, as would be expected out to only a few 100 pc. The mean $v_\perp$ (still excluding the two probable halo white dwarfs) is $30.14 \pm 0.44\,\mathrm{km\,s^{-1}}$. Although it is impossible to know the total-space velocities, v_tot, for any of these white dwarfs without measuring their radial-velocities, statistically the mean of v_tot is a factor $\Gamma(3/2)^{-2} = 4/\pi$ larger than $v_\perp$ as these are chi-distributed with 3 and 2 degrees of freedom respectively. Including the effect of low number statistics, we estimate the average v_tot for our sample to be $38.4 \pm 1.1\,\mathrm{km\,s^{-1}}$.

One final object worth noting in this section is SDSS J1535+1247, otherwise known as WD1532+129 or G137-24. It was first recognised as a white dwarf by Eggen (1968) photometrically/astrometrically, but was not spectroscopically classed as a DZ until more recently (Kawka et al., 2004). This is by far the brightest DZ in our sample ($r = 15.5$), and evidently from our calculations, the closest to the Sun. While previously known to be a member of the 25 pc local sample (Kawka et al., 2004; Kawka & Vennes, 2006; Sion et al., 2014), our estimate of 19.4 ± 2.5 pc suggests a moderate probability of it also being a member of the 20 pc local sample. The steady revision to closer distances (24 pc in Kawka et al., 2004; Kawka & Vennes, 2006 and 22 pc in Sion et al., 2014) is however no great surprise as the spectroscopic T_eff have also decreased with improvements in both atomic physics and quality of the available spectra. We believe the “rapid cooling” of SDSS J1535+1247 within the recent literature is unlikely to continue, as our fit is strongly constrained by our WHT spectrum at blue wavelengths inaccessible to BOSS (See Fig. 3.6). The remaining uncertainty in the distance to SDSS J1535+1247 comes almost entirely from the unknown mass/radius – all of which will be significantly constrained by Gaia DR2.

Chapter 4

Compositions of extrasolar planetary bodies

Relative metal abundances, obtained through spectral fitting of white dwarfs, inform us on the bulk compositions of the accreted planetesimals. As described in the previous chapter, we have measured the abundances of multiple elements for 230 white dwarfs,[1] allowing us to probe the composition of a large sample of planetesimals formed many Gyr ago. We were able to estimate Ca, Mg, and Fe abundances for all 230 stars in our sample, providing a common set of elements to work with. Conveniently Ca, Mg, and Fe can be used as tracers of crust-, mantle-, and core-like material respectively (Rudnick & Gao, 2003; Palme & O'Neill, 2003; McDonough, 2000). Therefore systems that are overly abundant in one of these elements compared to the mean, can be presumed to have accreted material from planetesimals that have undergone differentiation.

As shown in Table B.2, Na, Cr, Ti, and Ni are not detected at every system. For 101 stars in our sample, Na is detected via the D-doublet centred on 5893 Å, although the two components are unresolved in our spectra due to pressure broadening. Cr and Ti are detected in only 60 and 27 systems respectively due to their typically low mass fractions within the accreted material. Finally, Ni is only detected for eight objects where we have William Herschel Telescope (WHT) follow-up spectra, revealed via a set of Ni lines centred on 3390 Å. We show, particularly throughout Section 4.4, that these elements serve as important diagnostics for confirming the nature of material in the most extreme outliers in the Ca/Mg/Fe abundance parameter space.

---

[1] Recall that the strongly magnetic object SDSS J1143+6615 with $B \gtrsim 20\,\mathrm{MG}$ prohibited a meaningful fit to its spectrum. Thus, SDSS J1143+6615 is excluded from our analysis in this chapter as well as Chapter 5, where we refer to the remaining 230 systems only.

In this chapter we use the measured abundances from our DZ sample to characterise the distribution of accreted parent body compositions. We then compare the most extreme systems with analyses of other metal-polluted white dwarfs, by devising a simple method for estimating crust/mantle/core fractions of the accreted material. Finally, for these DZs with extreme abundance ratios, we discuss their particular ability to inform us on the properties of remnant planetary systems.

4.1 Relative diffusion

An important caveat that must be acknowledged before further discussion on parent body compositions, is the relative diffusion of elements. In white dwarfs with radiative atmospheres, i.e. warm DA stars, the sinking time-scales can be as short as days to years. As this is significantly shorter than the estimated duration of an accretion episode (10^4 to 10^6 yrs, Girven et al. 2012), the assumption of accretion-diffusion equilibrium in the analysis of the accreted debris abundances is fully justified. Diffusion time-scales vary by element with a (non-trivial) dependence on elemental weights, meaning that the atmospheric abundance ratios do not directly represent the composition of the accreted material (Paquette et al., 1986b). However, with calculated gravitational settling time-scales in hand, this is simple to correct for (Koester & Wilken, 2006b; Koester, 2009).

In contrast, in the cool, dense helium atmospheres of DZs discussed here, the assumption of diffusion-accretion equilibrium does not hold true, as the envelopes of these stars are unstable to convection. The outer convection zones (CVZs) extend deep below the stellar atmosphere, and for the objects under consideration here, contain 10^{-6} to 10^{-5} of the total white dwarf mass (Table B.3). The material, once accreted into the photosphere, is diluted by convective mixing throughout the envelope, and settles out into the core on the diffusion time-scale at the base of the CVZ. Consequently, the depletion of metals from the photosphere is strongly impeded. For our sample of cool white dwarfs, these diffusion times span several 10^5 to a few 10^6 yr (Table B.3), comparable to, or longer than the estimated duration of the accretion phase (Girven et al., 2012).[2]

For the majority of DZs it is likely the case that accretion has ceased by the time we observe them, with spectroscopic metals serving as an indicator of at least one accretion event having occurred in the last few Myr. Optically thick discs with sufficient inclination ought to be detectable around the nearest and brightest DZs.

---

[2] For an intuitive illustration of the very different sinking time-scales in DAs and non-DAs as a function of white dwarf age, see Fig. 1 of Wyatt et al. (2014).

However, so far only one DZ is known to possess an infra-red excess indicative of a dust disc (Bergfors et al., 2014). This suggests that many or most of the objects in our sample are not currently accreting, but merely preserve the remains of former planetesimals in their photospheres for a few Myr.

Once accretion has stopped, elements heavier than helium continue their slow diffusion out of the CVZ, remaining spectroscopically visible for several sinking time-scales. However the differences in diffusion velocity for each element leads to the abundance ratios changing over time. This problem is discussed by Koester (2009) in the context of GD 362, which is well demonstrated by their figures 2 and 3.

In the absence of accretion, the rate of change in the abundance ratio between two elements has a simple dependence on their diffusion time-scales. For an element Z with diffusion time-scale τ, its atmospheric abundance (with respect to He) proceeds with time, t, as

$$Z(t)/\mathrm{He} = Z(0)/\mathrm{He} \times \exp\left(-t/\tau\right), \tag{4.1}$$

or in logarithmic form (base 10)

$$\log\left[Z/\mathrm{He}\right](t) = \log\left[Z/\mathrm{He}\right](0) - \ln(10)\, t/\tau. \tag{4.2}$$

If we consider two elements, Z_1 and Z_2, with respective diffusion time-scales, τ_1 and τ_2, manipulation of either equation (4.1) or (4.2), leads to the relation

$$\frac{\mathrm{d}\log\left[Z_2/Z_1\right]}{\mathrm{d}\log\left[Z_1/\mathrm{He}\right]} = \frac{\tau_1}{\tau_2} - 1. \tag{4.3}$$

The two important cases we consider for the remainder of this chapter are Fe vs. Ca, and Mg vs. Ca. In the first case, we find from our envelope calculations (Chapter 3/Table B.3) that τ_{Fe} is usually within 5 % of τ_{Ca}, and so log[Fe/Ca] effectively remains constant with decreasing log[Ca/He], i.e. with increasing time since the end of an accretion episode. In the latter case, we find τ_{Mg} is typically a factor 2.8 ± 0.1 larger than τ_{Ca} for the white dwarfs in our sample. Therefore, equation (4.3) shows that for every one dex decrease in log[Ca/He], the value of log[Mg/Ca] *increases* by 0.64 dex, i.e. a factor four. Kawka & Vennes (2016) present a similar expression to equation (4.3), although defined in terms of time since the end of accretion rather than one of the absolute abundances as we do here.

4.2 Abundance analysis of Ca, Mg, and Fe

Since it is not possible to know how long ago accretion may have stopped we, at least initially, treat the observed abundances as representative of the parent bodies. For the three elements whose abundances we most reliably measure (Ca, Mg, and Fe), their combined composition has two degrees of freedom, and is thus amenable to being displayed graphically. When dealing with atomic abundances, a typical approach is the comparison of the log-abundance ratios, e.g. log[Ca/Mg] vs. log[Fe/Mg]. As one element (Mg in the example) appears twice, the resulting distribution is guaranteed to contain a strong correlation, making the positions of chemically intriguing outliers less obvious. For this reason we display our compositions using a ternary diagram in Fig. 4.1, where we use absolute abundances rather than the logarithmic ratios. Because Ca is typically much less abundant than either Mg or Fe, we rescale Ca by a factor 15 to centre the distribution within the plot (otherwise the data appear compressed within a stripe along the right edge). Our model atmosphere fitting method leads to some minor quantisation which is visually distracting, we therefore initially re-sample the atmospheric abundances with normally distributed deviates with standard deviation 0.01 dex (smaller than the estimated uncertainties which are at best 0.05 dex) to remove this artefact.

The bulk Earth composition (McDonough, 2000), $\oplus$, is located close to the mean of our sample ($\mathrm{Ca} = 0.38$, $\mathrm{Mg} = 0.33$, $\mathrm{Fe} = 0.29$). This suggests that Gyr-old exoplanetesimals are overall similar in composition to the bulk Earth as found in the analyses of younger metal-polluted white dwarfs (Klein et al., 2010, 2011; Gänsicke et al., 2012; Xu et al., 2014).

Typical uncertainties for the photospheric abundances measured from fitting the white dwarf spectra are estimated to be in the range 0.05–0.3 dex. For the poorest quality fits (low signal-to-noise spectra and low abundances), this can translate to large scatter within Fig. 4.1, with its extent amplified at the centre of the plot. For uncorrelated and identical Ca/Mg/Fe uncertainties, the error in the position in dimensionless plot units is approximately half that of the abundance errors in dex at the centre of the diagram. For example, 0.2 dex uncertainties on Ca/Mg/Fe abundances translates to a positional error of 0.1 at the centre of the figure. Due to the non-linear mapping between abundances and coordinates in the ternary diagram, the positional errors are vastly decreased towards the corners, and therefore systems located in these three regions represent compositionally unusual objects even if their abundance uncertainties are large and statistically independent. As the spectral signal-to-noise ratio is increased, the abundance errors of Ca/Mg/Fe

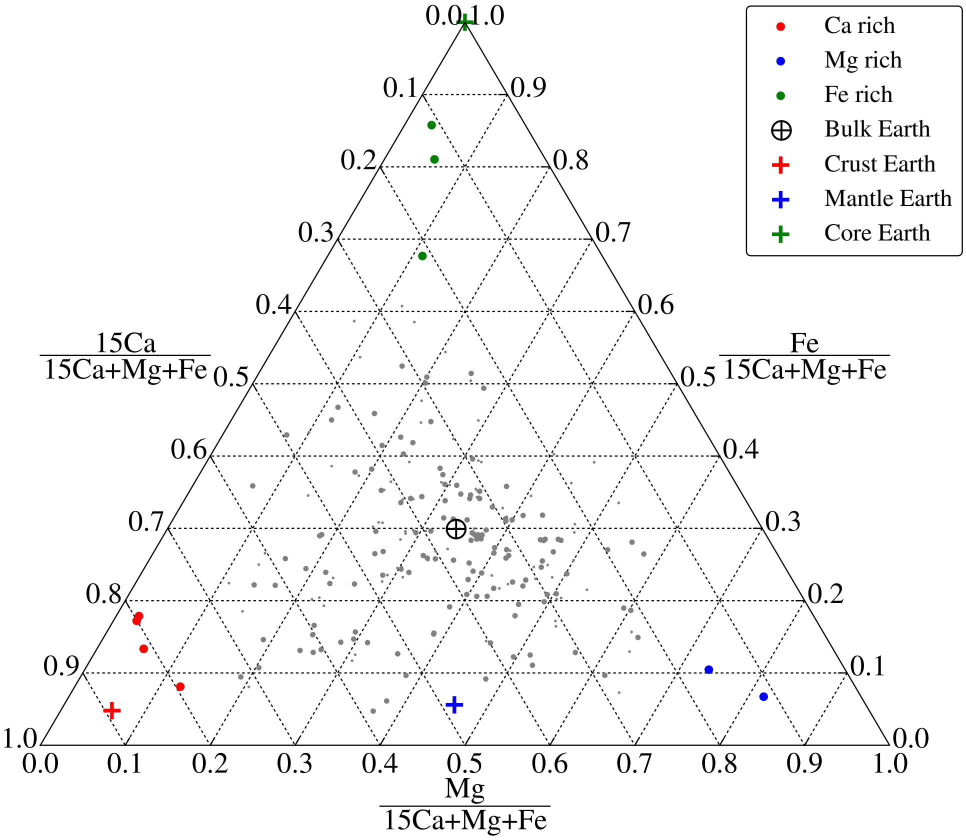

Figure 4.1: Ternary diagram of the Ca, Mg, and Fe abundances in our white dwarf sample, as measured from the spectroscopic fits. On average the Mg/Fe abundance ratio is found to be $\simeq 1$, whereas the Ca/Fe and Ca/Mg ratios are typically an order of magnitude lower. For display purposes Ca is therefore scaled by a factor 15, and consequently numbers on the axes do not correspond to relative abundance fractions. Outliers particularly rich in one of the three elements appear closer to the corners, where the highlighted systems are discussed in detail in Section 4.4. The remaining DZs are categorised into higher and lower quality measurements indicated by the larger and smaller grey points respectively.

become positively correlated and so the uncertainties in relative abundances, e.g. log[Fe/Ca], become smaller still, translating to positional uncertainties of a few 0.01 even at the centre of the diagram.

To increase the visual weight of the systems within Fig. 4.1 with more precise spectral fits, they are displayed by the larger points, with the smaller points corresponding to poorer measurements. We set the threshold for a "good-quality" fit as a median spectral signal-to-noise ratio larger than five, and a geometric mean abundance, defined as (log[Ca/He]+log[Mg/He]+log[Fe/He])/3, of at least −8.7 dex.

The most extreme systems found towards the corners of Fig. 4.1 exhibit atmospheric compositions that are Ca-rich (red), Mg-rich (blue), and Fe-rich (green). As mentioned above, these three elements are convenient proxies for crust-like, mantle-like and core-like material respectively. We therefore also indicate with coloured crosses the abundance ratios of Earth's continental-crust, mantle, and core. The interior region bounded by these three points represents Ca/Mg/Fe values that can be decomposed into crust/mantle/core fractions assuming Earth-like compositions for each structural layer.

It is apparent from the diagram that such a decomposition is impossible for almost half of the DZ white dwarfs in our sample as they lie exterior to the triangle formed by the Earth's crust/mantle/core points. However, it is crucial to notice that most of these are clustered towards the Mg-rich corner (particular for values of $\mathrm{Fe}/[15\mathrm{Ca} + \mathrm{Mg} + \mathrm{Fe}] < 0.3$). We take this as evidence for Mg enhancement related to relative diffusion as discussed in Section 4.1.

It is therefore clear that for most DZ white dwarfs, the effects of relative diffusion have to be considered when discussing the parent body compositions. The exception to this rule is when the Mg fraction is particularly low, i.e. the extremely Ca-rich and Fe-rich systems highlighted in red and green respectively in Fig. 4.1.

Ignoring Mg for a moment, we are able to make some statements about the distribution of exoplanetesimal compositions by considering only the Fe to Ca ratio. As described in Section 4.1, our envelope calculations show Ca and Fe to have similar diffusion time-scales. Therefore over the few (no more than about 10) diffusion time-scales that the material can remain visible, the ratio of Fe to Ca changes only by a small amount compared to our measurement errors.

The distribution of log[Fe/Ca] spans two orders of magnitude (Fig. 4.2), and is approximately Gaussian in shape, although with a possible excess of systems in the low Fe/Ca wing. The mean and standard deviation of the distribution are found to be 1.03 ± 0.02 dex and 0.29 ± 0.02 dex respectively, where the errors are estimated from bootstrapping the data.

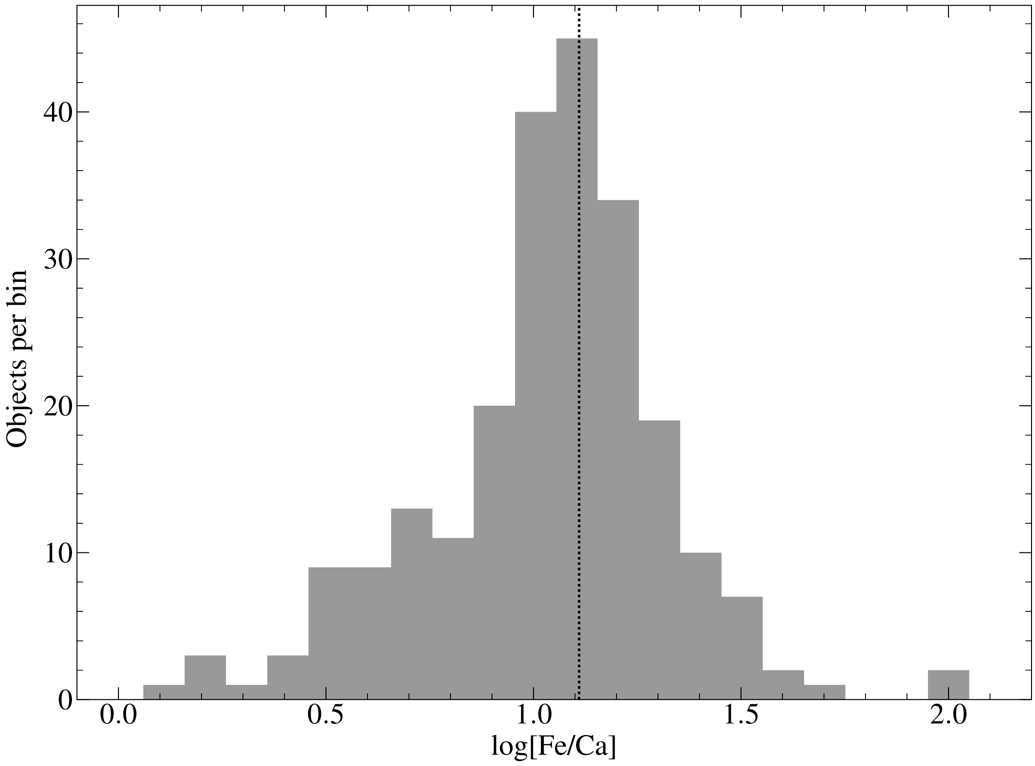

Figure 4.2: The distribution of log[Fa/Ca] for our DZ sample, with the bulk Earth value indicated by the vertical dashed line.

While it is tempting to interpret this distribution as directly representative of exoplanetesimal compositions, this is unlikely to be true. The wings of the distribution, where the Fe/Ca ratio is most extreme, indicate white dwarfs which have almost certainly accreted material from a single large parent body with an extreme composition. The atmospheric Fe/Ca ratios of white dwarfs located near the centre of the distribution can be explained through several different accretion histories. While accretion of single large asteroids with log[Fe/Ca] ≈ 1.1 dex could be true for some of the stars, other possibilities include accretion of multiple smaller asteroids with a bulk Earth composition, or even multiple planetesimals with wildly different compositions which average to a near bulk Earth Fe/Ca value. This means that our observed distribution must be narrower than the true distribution of planetesimal compositions. How much narrower depends not only on the underlying log[Fe/Ca] distribution but also on the planetesimal mass distribution (which may itself be a function of log[Fe/Ca]), which will determine how the averaging of compositions from multiple planetesimals is statistically weighted. Nevertheless, the distribution we derive is likely to have a mean close to that of the underlying log[Fe/Ca] distribution, which Fig. 4.2 suggests is close to the bulk Earth ratio. Furthermore, the distribution in Fig. 4.2 highlights the sample size required to detect systems with log[Fe/Ca] ratios of ± 1 dex from the mean.

4.3 Structural analysis and comparison with other white dwarf studies

In Fig. 4.1, we have highlighted several systems with atypically Ca- and Fe-rich compositions, which we have qualitatively described as being crust- and core-like, respectively. These descriptions are justified by the proximity to the locations of the Earth's crust and core within Fig. 4.1. In Fig. 4.2 these same objects are found in the bins at both ends of the distribution, spanning two orders of magnitude in their Fe to Ca ratios.

Here we demonstrate that we can be far more quantitative in assessing the crust- and core-like nature of these Ca- and Fe-rich systems if we make the assumptions that (1) rocky planetesimals can generally be described as a mixture, i.e. linear combination, of crust, mantle and core, and (2) the abundances of the Earth's crust/mantle/core are typical for differentiated planet(esimals). The first assumption is not strictly true if applied to primitive planetesimals, i.e. chondrites, which are homogenous in their composition, lacking the distinct geological layers that result from differentiation. Instead we can consider chondrites as a linear combination of potential crust/mantle/core had they undergone differentiation. The second assumption appears to be justified as none of the systems we analysed are more Ca-rich than the Earth's crust nor more Fe-rich than the Earth's core (Fig. 4.1).

To apply the above reasoning to the systems in our sample, we first consider an exoplanetesimal whose total mass is the linear sum of its crust, mantle, and core components, denoted as M_{Cru}, M_{Man}, and M_{Cor}, respectively (assumption 1). Applying assumption 2, that the atomic compositions of these three geological components are identical to those of the Earth, we then know each of their mass-fractions of Ca, Mg, and Fe. For instance 5.2 % of Earth's crust is comprised of Fe, which can be written as a matrix element $\mathrm{Cru}_{\mathrm{Fe}} = 0.052$. Thus the elemental masses M_{Ca}, M_{Mg}, and M_{Fe} for the entire asteroid are calculated via

$$\begin{pmatrix} M_{\mathrm{Ca}} \\ M_{\mathrm{Mg}} \\ M_{\mathrm{Fe}} \end{pmatrix} = \begin{pmatrix} \mathrm{Cru}_{\mathrm{Ca}} & \mathrm{Man}_{\mathrm{Ca}} & \mathrm{Cor}_{\mathrm{Ca}} \\ \mathrm{Cru}_{\mathrm{Mg}} & \mathrm{Man}_{\mathrm{Mg}} & \mathrm{Cor}_{\mathrm{Mg}} \\ \mathrm{Cru}_{\mathrm{Fe}} & \mathrm{Man}_{\mathrm{Fe}} & \mathrm{Cor}_{\mathrm{Fe}} \end{pmatrix} \times \begin{pmatrix} M_{\mathrm{Cru}} \\ M_{\mathrm{Man}} \\ M_{\mathrm{Cor}} \end{pmatrix}, \tag{4.4}$$

where, using values obtained from Rudnick & Gao (2003), Palme & O'Neill (2003), and McDonough (2000) for the the Earth's bulk continental crust, mantle, and core respectively, the complete set of matrix elements are

$$\begin{pmatrix} \mathrm{Cru}_{\mathrm{Ca}} & \mathrm{Man}_{\mathrm{Ca}} & \mathrm{Cor}_{\mathrm{Ca}} \\ \mathrm{Cru}_{\mathrm{Mg}} & \mathrm{Man}_{\mathrm{Mg}} & \mathrm{Cor}_{\mathrm{Mg}} \\ \mathrm{Cru}_{\mathrm{Fe}} & \mathrm{Man}_{\mathrm{Fe}} & \mathrm{Cor}_{\mathrm{Fe}} \end{pmatrix} = \begin{pmatrix} 0.046 & 0.026 & 0 \\ 0.028 & 0.222 & 0 \\ 0.052 & 0.063 & 0.85 \end{pmatrix}. \tag{4.5}$$

For the interpretation of the debris abundances determined from the spectroscopic analysis of our white dwarf sample, we approach the problem from the opposite direction, i.e. having measured Ca, Mg, and Fe abundances but wishing to determine the relative contributions of the three structural components. Since (4.5) is a non-degenerate square matrix, this is easily achieved through inversion of equation (4.4). Note that while equation (4.4) is defined in terms of masses, mass accretion rates (which are commonly found in the literature for systems assumed to be in accretion/diffusion equilibrium) can equally be used in their place. Since our goal is to determine structural component *fractions*, this simply means normalising such that they sum to one, and so no specific normalisation of Ca/Mg/Fe is required beforehand. A point worth mentioning is that so far we have been referring to atomic abundances, which is the standard convention in atomic spectroscopy. Here we require mass abundances, and so each of the Ca/Mg/Fe atomic abundances requires rescaling by its atomic mass.

Table 4.1: Estimated crust/mantle/core mass-fractions for the objects shown in Fig. 4.3, and calculated according to equation (4.4). The first set of systems are the Ca-rich and Fe-rich DZs from our sample. This is compared below with objects from the literature where accretion rates for Ca, Mg, and Fe are available.

Name	Crust	Mantle	Core	Ref.
SDSS J0741+3146	0.080	0.043	0.877	1
SDSS J0744+4649	0.798	0.158	0.044	1
SDSS J0823+0546	0.067	0.091	0.843	1
SDSS J1033+1809	0.897	−0.058	0.161	1
SDSS J1043+3516	0.102	0.179	0.719	1
SDSS J1055+3725	0.881	0.001	0.118	1
SDSS J1351+2645	0.897	−0.058	0.161	1
GD 16	0.273	0.420	0.307	2
GD 17	0.302	0.415	0.283	2
GD 40	0.770	0.132	0.098	3,4
GD 61	0.384	0.584	0.032	5
SDSS J0738+1835	−0.169	0.829	0.340	6
NLTT 19868	0.777	0.248	−0.025	7
SDSS J0845+2257	0.004	0.497	0.499	8
PG 1015+161	0.309	0.325	0.366	9
SDSS J1043+0855	0.618	0.383	−0.001	10
NLTT 25792	0.183	0.600	0.218	11
WD 1145+017	0.188	0.355	0.457	12
PG 1225−079	0.763	0.047	0.190	4
SDSS J1228+1040	0.480	0.369	0.150	9
SDSS J1242+5226	0.307	0.570	0.123	13
G 149−28	0.356	0.444	0.200	14
WD 1536+520	−0.016	0.782	0.234	15
NLTT 43806	0.579	0.380	0.042	14
GD 362	0.850	−0.022	0.172	4
GALEX J1931+0117	−0.191	0.578	0.613	16,17
G 241−6	0.520	0.384	0.096	3,4
HS 2253+8023	0.374	0.327	0.299	18
G 29−38	0.448	0.376	0.175	19

References: (1) This work/Hollands et al. (2017), (2) Gentile Fusillo et al. (2017), (3) Jura et al. (2012), (4) Xu et al. (2013), (5) Farihi et al. (2013a), (6) Dufour et al. (2012), (7) Kawka & Vennes (2016), (8) Wilson et al. (2015), (9) Gänsicke et al. (2012), (10) Melis & Dufour (2017), (11) Vennes & Kawka (2013), (12) Xu et al. (2016), (13) Raddi et al. (2015), (14) Zuckerman et al. (2011), (15) Farihi et al. (2016), (16) Vennes et al. (2011), (17) Melis et al. (2011), (18) Klein et al. (2011), (19) Xu et al. (2014).

Because of the effects of relative diffusion on Mg abundances (Section 4.1), we restrict our application of this approach to the seven Ca- and Fe-rich systems in our sample (Fig. 4.1) where the calculated crust/mantle/core values are largely insensitive to the low Mg fractions. For the other systems that are strongly affected by relative diffusion, application of equation (4.4) yields nonsensical negative crust fractions and/or and mantle fractions exceeding 100 %. We instead complement these seven Ca- and Fe-rich DZ white dwarfs with detailed abundance studies of 22 warmer and younger debris-polluted white dwarfs which are often assumed to be in accretion-diffusion equilibrium. This means their atmospheric abundances can be corrected for the different sinking times of the individual elements and hence the bulk compositions of the parent bodies from the accretion rate of each element. We present the results of our structural decomposition in Table 4.1 and graphically in Fig. 4.3. The additional systems were all selected with the requirement that all of Ca, Mg, and Fe had spectroscopic detections with calculated accretion rates. Therefore potentially interesting systems such as PG 0843+225 (Gänsicke et al., 2012), and GD 133 (Xu et al., 2014) could not be included at this time, as one of Ca/Mg/Fe had only an upper limit available. We also exclude WD 1425+540 (Xu et al., 2017) as it would be senseless to try and explain cometary material in terms of rocky geology[3].

For eight systems, application of equation (4.4) resulted in a negative value for one structural component. For display purposes, we set the negative values to 0, and renormalised the other two components such that they appear on the boundary of Fig. 4.3. For six of these the effect is only minor (only a few 0.01 or less), but for SDSS J0738+1835 and GALEX J1931+0117 the calculated crust values are $\simeq -0.2$ (displayed in grey in Fig. 4.3). This issue can be resolved if the parent body mantles were relatively Ca-poor compared to the Earth's, suggesting our second assumption (above) is not universally applicable. We find that reducing $\mathrm{Man}_{\mathrm{Ca}}$ in equation (4.5) by a factor of 2.5 is sufficient to move both SDSS J0738+183 and GALEX J1931+0117 within the bounds of Fig. 4.3, and thus with compositions consistent with combinations of mantle and core material. Additionally, it is suggested by Dufour et al. (2012) for SDSS J0738+183 and Melis et al. (2011) for GALEX J1931+0117, that their compositions may be indicative of stripping of their outer layers, including part of its mantle for GALEX J1931+0117.

---

[3] While WD 1425+540 is excluded from Table 4.1/Fig. 4.3 the values of (Crust/Mantle/Core) are derived here for completeness. Xu et al. (2017) determined two sets of accretion rates for WD1425+540, dependent on whether on the hydrogen abundance was measured from the Balmer lines or Lyα. For the two models we find (Crust/Mantle/Core) values of (0.204/0.418/0.378) and (0.095/0.410/0.495) respectively.

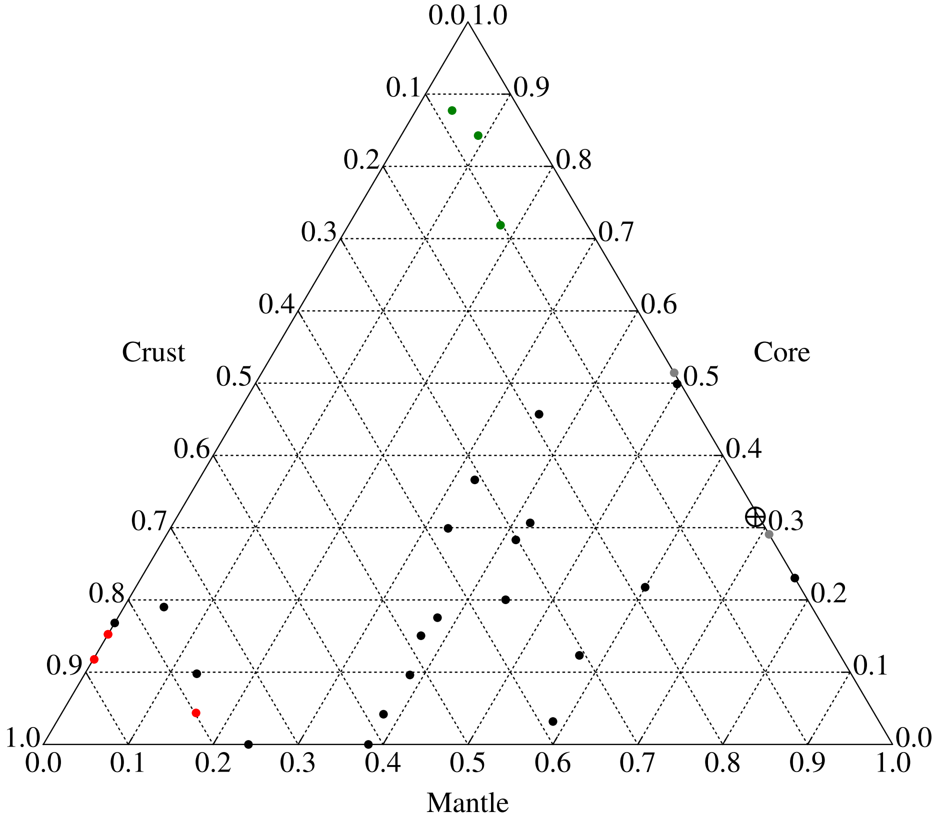

Figure 4.3: Ternary diagram illustrating the mass fraction of accreted planetary debris in terms of crust, mantle, and core material. The outliers in our sample are shown in red/green for Ca/Fe rich systems respectively (discussed at length in Section 4.4). Systems from other published abundance studies are shown in black (Table 4.1), and in grey in for two cases where the calculated crust value is $\simeq -0.2$ and so significant clipping was required to move these points to the boundary of the diagram. The bulk Earth is indicated by the $\oplus$ symbol.

We find the majority of systems from published analyses (black points in Fig. 4.3) are consistent with crust-like material or a mixture of crust and mantle rather than the bulk Earth (although, we note that WD 1536+520 is only $\simeq 0.1$ fractional plot units away). For instance the accreted material at NLTT 43806 is described as being in best agreement with "a mixture of terrestrial crust and upper mantle material" by Zuckerman et al. (2011), whose analysis also included the detection of Al accretion. The crust/mantle/core mass fractions we calculated (Table 4.1) corroborate this assertion. Similarly, we find that among the previously published systems (Table 4.1), SDSS J0845+2257 has the highest core mass fraction, in good agreement with the more detailed study of Wilson et al. (2015) who detected large abundances of Fe and Ni. Furthermore, Wilson et al. (2015) argued for a mantle/core mixture, but mantle depleted with respect to the Earth. We reach the same conclusion from our analysis, where we find a mantle/core mixture of 50/50 for SDSS J0845+2257 versus 70/30 for the Earth. These comparisons demonstrate the effectiveness of our relatively simple approach to classifying exoplanetesimal compositions, which only requires abundance measurements of Ca, Mg, and Fe.

The overall banana-shaped distribution in Fig. 4.3 may initially come as a surprise, however it is simple to see that this is indeed the expected distribution of crust, mantle, core combinations. The dearth of points along the right edge of the plot corresponds to the absence of parent bodies made of a crust+core mixture but lacking a mantle, which is consistent with the expectation that planetary objects undergoing differentiation will form with a significant mantle component, in addition to their core and crust. Finally there are no points in Fig. 4.3 corresponding to more than 80 % mantle, whereas multiple objects are seen with more than 80 % crust or core compositions. While it may be possible to create mantle-dominated asteroids via stripping of a larger body, the absence of points in this region potentially indicates that such a process rarely occurs.

The distribution of points in Fig. 4.3 makes it clear that rocky material accreted by white dwarfs often originates from highly differentiated parent bodies. In particular, the prevalence of crust-dominated and crust+mantle points suggests parent bodies originating from collisional fragments of the upper layers of (minor-)planets as proposed by Zuckerman et al. (2011) for NLTT 43806. This argument becomes especially appealing on consideration that the Earth's crust contributes less than 1 % of its mass, yet for most of the objects in Fig. 4.3/Table 4.1 this fraction is in range 15–90 %.

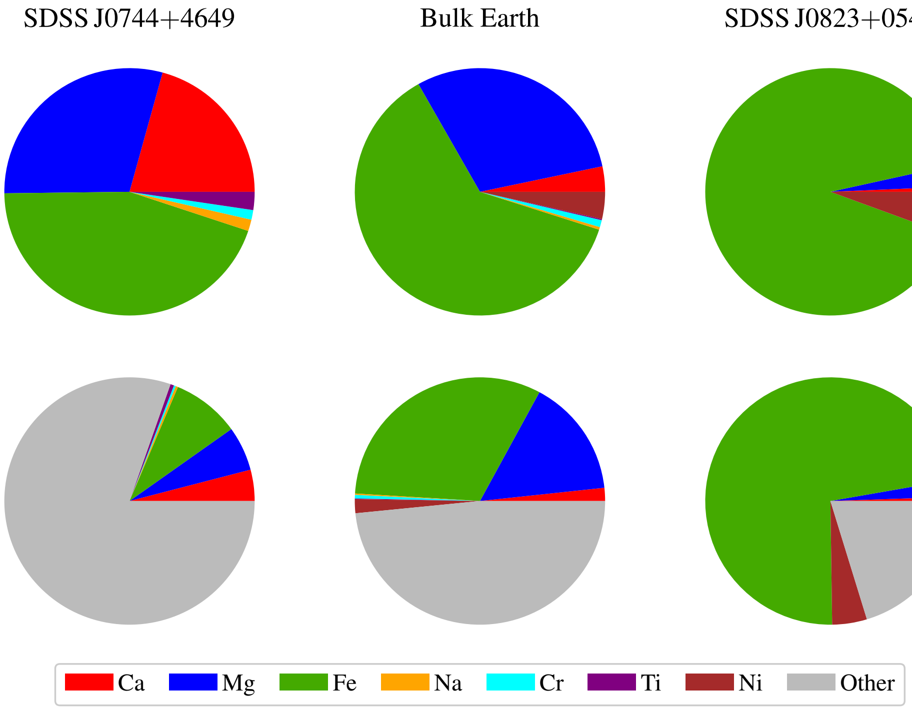

SDSS J0744+4649

Bulk Earth

SDSS J0823+0546

Figure 4.4: The mass fractions of the accreted material for two of the most extreme DZ white dwarfs in our sample compared with the bulk Earth. The top row includes only the elements we detected in the observed spectra. In the bottom row, we use equation (4.4) to estimate the fraction of undetected material (which is likely to be dominated by O and Si), which we simply label as "other". The material accreted by SDSS J0744+4649 has a composition consistent with pure crust, whereas core material is implied for the parent body accreted by SDSS J0823+0546.

4.4 Extreme abundance ratios

Instantaneous accretion can not be assumed for DZ white dwarfs due to the long time-scales for metals to diffuse out of the base of their CVZs (Section 4.1). Therefore in the general case, it is not possible to establish whether the observed metal contamination arises from the accretion of a single large object, or from multiple accretion episodes involving smaller parent bodies. However several systems in our sample show compositions consistent with the accretion of highly differentiated parent bodies in particular those that are rich in Ca or Fe as discussed in Sections 4.2 and 4.3. These white dwarfs have very likely accreted single large parent bodies because subsequent accretion episodes of many small planetesimals (that were not previously part of a single larger object) are expected to average out to a less extreme abundance pattern, e.g. more similar to the bulk Earth.

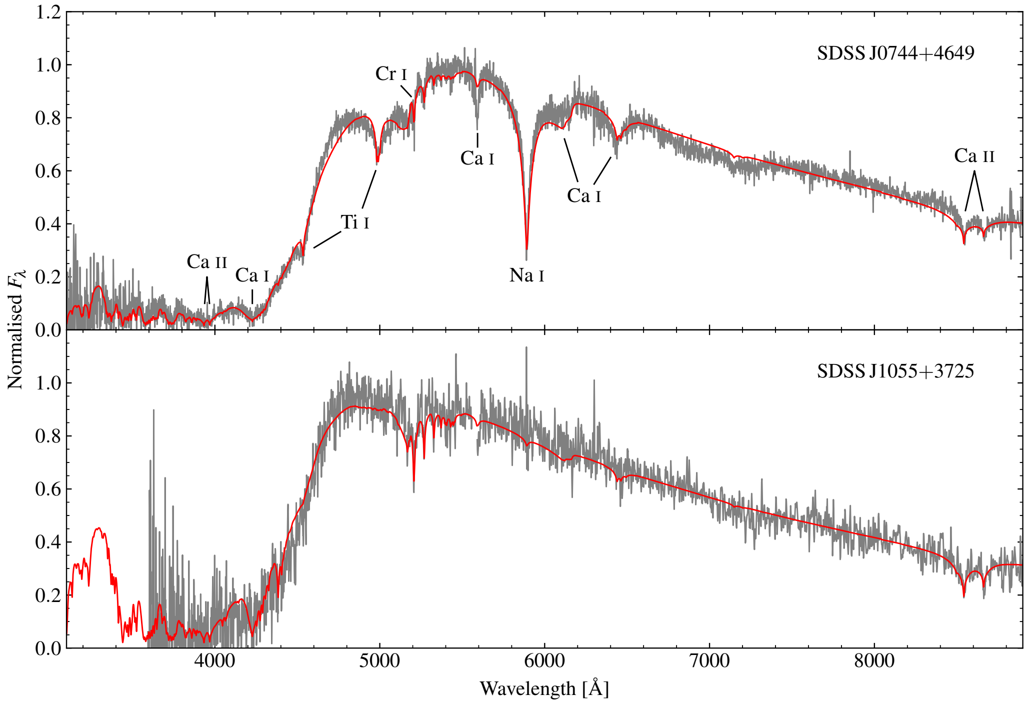

Figure 4.5: Two DZs that have accreted Ca-rich parent bodies. The two other Ca-rich DZs (SDSS J1033+1809 and SDSS J1351+2645) are spectroscopically similar to SDSS J1055+3725, and are thus not shown here.

4.4.1 Ca-rich objects

The four Ca-rich DZs we have identified are SDSS J0744+4649, SDSS J1033+1809, SDSS J1055+3725, and SDSS J1351+2645,[4] which are shown by the red points in Fig. 4.1/4.3. These are contenders for the most crust-like in nature with similar values to GD 40 (Jura et al., 2012; Xu et al., 2013), NLTT 19868 (Kawka & Vennes, 2016), PG 1225−079 (Xu et al., 2013), and GD 362 (Xu et al., 2013). The most striking spectral feature of these DZs (Fig. 4.5) is their huge increase in opacity bluewards of ≃ 4500 Å, resulting in the suppression of flux at shorter wavelengths. This arises from the extremely pressure-broadened wings of the Ca II H+K lines.

The most noteworthy of the Ca-rich systems is SDSS J0744+4649. The spectrum of this white dwarf is unique with no similar looking stars known. Compared to calcium, both magnesium and iron are depleted with Fe/Ca and Mg/Ca ratios ≃ 0.9 dex lower than those of the bulk Earth. The spectrum of this star also exhibits strong lines of Ti and Na which are typically not seen for other

---

[4] SDSS J1033+1809 and SDSS J1351+2645, have degenerate crust/mantle/core values and so are indistinguishable in Fig. 4.3.

DZs with $T_{\mathrm{eff}} \simeq 5000\,\mathrm{K}$. The abundance ratios are log[Ti/Ca]$= -1.02$ dex and log[Na/Ca]$= -0.90$ dex, where the respective abundances are -1.4 and -0.7 dex for the bulk Earth (McDonough, 2000), and -1.1 and -0.1 dex for the Earth's crust (Rudnick & Gao, 2003). The Ti/Ca ratio for SDSS J0744+4649 is much closer to the Earth's crust value than the bulk Earth ratio, and as both elements are refractory lithophiles, this reinforces the crust-like interpretation of the accreted planetesimal. On the other hand, the Na/Ca ratio is more similar to the bulk Earth ratio. However we note that while Na is a lithophile, it is also a volatile element and so is not expected to condense at the same temperature as Ca or Ti. Like Ca and Ti, Al is also a refractory lithophile and thus is likely to be present at an abundance of log[Al/Ca] $\simeq +0.4$ dex (Rudnick & Gao, 2003). However, the only strong optical Al I transitions are located at 3944 Å and 3961 Å, between the already saturated Ca H+K lines. As there is so little emergent flux in this wavelength region (Fig. 4.5) detecting Al at SDSS J0744+4649 would be extremely challenging even with improved instrumentation. We also detect the moderately refractory lithophile Cr at relative abundance of log[Cr/Ca] $= -1.3$ dex, much higher than the trace -2.6 dex for the Earth's crust (Rudnick & Gao, 2003). The mass fractions for each element including presumed unseen elements are demonstrated by the left-hand pie charts in Fig. 4.4. If the material accreted by SDSS J0744+4649 is indeed lithospheric, then Fig. 4.4 indicates that the unseen elements make up 80 % of the total mass of the parent body, with most of this comprised of O, followed by Si and then Al (Rudnick & Gao, 2003). Note that the optical transitions of O and Si become extremely weak for the T_{eff} range of our sample, thus prohibiting their detection in DZ white dwarfs.

For the other three Ca-rich objects, we are not able to offer an analysis as detailed as for SDSS J0744+4649, however they are worthy of discussion none the less. All three stars have qualitatively similar spectra, with SDSS J1055+3725 shown in Fig. 4.5. As their SDSS spectra are of much lower in quality than that of SDSS J0744+4649, Ti is only detected for SDSS J1351+2645 at a relative abundance of log[Ti/Ca] $\simeq -0.6$ dex, again supporting a crust-like interpretation of the accreted parent body. At both SDSS J1055+3725 and SDSS J1351+2645 we also detect Cr at relative abundances of -1.0 and -1.2 dex respectively. In all three detections of Cr (including SDSS J0744+4649), the Cr/Ca ratios are found to be greatly enhanced relative to the Earth's crust (-2.6 dex), with potential implications for their planetary formation conditions. McDonough (2000) notes that while regarded as a lithophile, under high pressure, Cr exhibits siderophile behaviour, and thus for the Earth is concentrated into the core (Moynier et al., 2011), where the bulk Earth value is log[Cr/Ca] $= -0.7$ dex. Therefore the parent bodies accreted by

SDSS J0744+4649, SDSS J1055+3725, and SDSS J1351+2645 were likely of much lower mass than the Earth and thus formed under lower pressure conditions where Cr exhibits lithophile behaviour.

4.4.2 Fe-rich objects

The inferred compositions for the material accreted by both SDSS J0741+3146 and SDSS J0823+0546 are extremely Fe-rich with with log[Fe/Ca] > 1.9 dex, the highest ratio known for any metal polluted white dwarfs (see Gänsicke et al. (2012), Kawka & Vennes (2016) and Wilson et al. (2015) for additional Fe-rich systems). The spectra of both stars are quite similar (Fig. 4.6) showing a dense forest of blended Fe I lines in the range 3400–3900 Å. Other notable Fe features include the strong $^3F \rightarrow {}^5G$ triplet near 4400 Å, and the $^5F \rightarrow {}^5D$ multiplet between 5250–5500 Å which provide additional constraints on the Fe abundance and $T_{\rm eff}$. While Fe is the dominant contaminant in the atmospheres of these two stars, the intrinsic strengths of the Ca H+K resonance lines result in the low Ca abundances remaining well constrained. SDSS J1043+3516, is the next most Fe-rich in our sample with log[Fe/Ca] $= 1.68$ dex. Its spectrum is qualitatively similar to those of SDSS J0741+3146 and SDSS J0823+0546, however the Fe lines are slightly weaker and H+K lines slightly stronger.

From our structural analysis in Section 4.3, it is clear that SDSS J0741+3146 and SDSS J0823+0546 are the most core dominated exoplanetesimals discovered to date. We note that the Fe-rich system NLTT 888 comes close with log[Fe/Ca] of 1.76 dex (Kawka & Vennes, 2014, 2016), however the lack of firm Mg measurement precludes it from being placed on Fig. 4.3, i.e. using either the quoted upper limit or precisely 0 for the Mg abundance yield wildly different results for the crust/mantle/core decomposition. Using the upper limit of log[Mg/He] < -8.7 dex leads to a negative crust-value, however by setting log[Mg/He] to -9.6 dex places NLTT 888 at the edge of Fig. 4.3 with a mantle fraction of 30 % and core fraction of 70 %.

For all three Fe-rich systems we obtained spectra using the *Intermediate dispersion Spectrograph and Imaging System* (ISIS) on the William Herschel Telescope (WHT). For SDSS J0823+0546, which we identified as a DZ candidate from its SDSS colours and its relatively high proper motion, this is the only available spectrum. Because the WHT spectra extend as far blue as 3100 Å, we are also able to constrain Ni abundances for all three stars using a set of Ni I lines at $\simeq 3390$ Å, and measure log[Fe/Ni] as 1.59, 1.23, and 1.35 dex for SDSS J0741+3146, SDSS J0823+0546, and

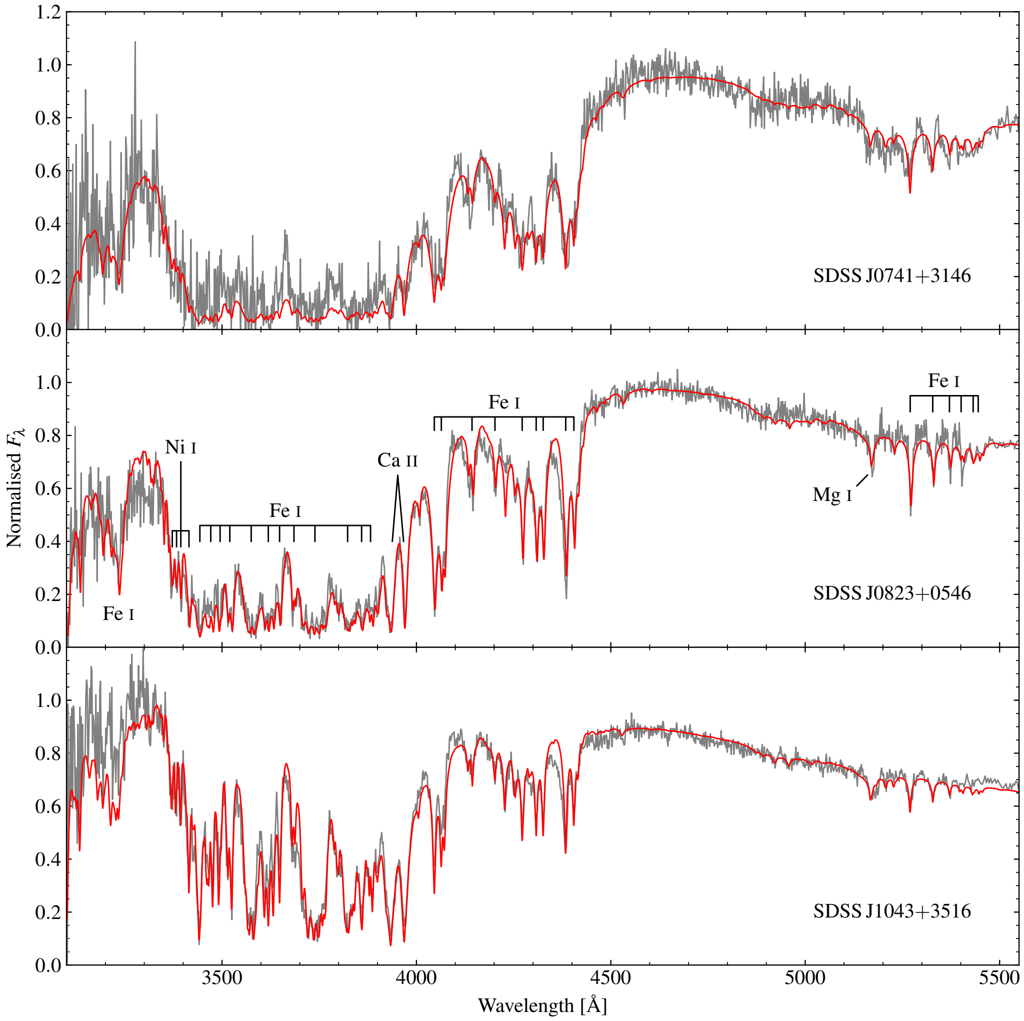

Figure 4.6: WHT spectra for the three objects which have accreted Fe-rich material. Because the WHT spectra extend as far blue as 3100 Å, we are able to constrain Ni abundances from the blend of lines at 3390 Å. The labelled spectrum of SDSS J0823+0546 shows that almost all absorption in these spectra comes from Fe I transitions, especially in the 3400–3900 range.

SDSS J1043+3516 respectively.[5] For the bulk Earth and the Earth's core, log[Fe/Ni] is about 1.24 and 1.20 dex respectively (McDonough, 2000) which is particularly close to the 1.23 dex measured for SDSS J0823+0546 – the most precisely analysed Fe-rich object in our sample due to the exceptional quality of the WHT spectrum (Fig. 4.6). We note that these Fe/Ni ratios are consistent with the metallic alloy kamacite which is predominantly Fe with a few percent Ni, and is found in metallic meteorites. In contrast, for the material accreted by Ton 345 Wilson et al. (2015) find a much higher Ni content consistent with taenite or a taenite/kamacite mixture.

Our structural decomposition of these systems combined with the Fe/Ni ratios leave little ambiguity that the accreted planetesimals underwent differentiation during their formation. The differentiated bodies must then have undergone stripping of their crust and mantle, resulting in exoplanetesimals comprised primarily of core material, which were subsequently accreted on to these white dwarfs.

For both SDSS J0741+3146 and SDSS J1043+3516 Cr is also detected via the 5207 Å Cr I line, but is notably absent from the spectrum of SDSS J0823+0546 (despite the high signal-to-noise ratio of the spectrum). Recalling that Cr is generally regarded a lithophile but exhibits siderophile behaviour at high pressure (McDonough, 2000), this may also suggest different formation environments for the core material observed across these systems. For SDSS J0741+3146 and SDSS J1043+3516 the atomic Cr/Fe ratio is measured to be −1.7 and −2.1 dex respectively, where McDonough (2000) quote a value of −2.0 dex for the Earth's core. Therefore we speculate that the parent bodies accreted by SDSS J0741+3146 and SDSS J1043+3516 may have originated from planetary mass objects, whereas for SDSS J0823+0546 the accreted planetesimal formed within a lower mass body such as a minor planet.

Under the hypothesis that the Fe currently residing in the CVZ originates from a single accretion episode, we can deduce a lower limit on the mass of the parent body. In the following, we assume $M_{\mathrm{wd}} = 0.6\,\mathrm{M}_{\odot}$, as the mass of the CVZ depends on the white dwarf mass. This results in $M_{\mathrm{Fe}} \simeq 2 \times 10^{21}$ g and $M_{\mathrm{Fe}} \simeq 3 \times 10^{21}$ g for SDSS J0741+3146 and SDSS J0823+0546, respectively.[6] These are, in fact, conservative lower limits, as the planetary cores are not purely composed of Fe, and as the debris composition suggests that the planetesimals were not entirely made up of core-material. Furthermore some of the Fe/Ni may have already sunk out of the base of convection zone depending on how long ago the accretion events occurred. It

---

[5] Note that for SDSS J0741+3146, the relative flux errors around 3400 Å are quite large and a weak magnetic field of 0.48 ± 0.05 MG appears to be present. Therefore, the Ni abundance of SDSS J0741+3146 is probably not as well constrained as the other two systems.

[6] Many other white dwarfs in our sample exhibit larger CVZ masses of Fe, but their unremarkable compositions are consistent with the accumulation of material from multiple accretion episodes or single large bodies with Earth-like compositions.

should also be noted these CVZ masses are based on the canonical white dwarf mass of $0.6\,\mathrm{M}_{\odot}$, and do not include systematic uncertainties in CVZ sizes. Application of equation (4.4) on the crust/mantle/core fractions (Table 4.1) implies Fe alone comprised $\simeq 72\,\%$ of the total parent body mass at SDSS J0823+0546. If we consider Ni as well as Fe, then these two core elements account for $\simeq 77\,\%$ of the total accreted mass. Because the columns in equation 4.5 do not sum to one, the implication is that most of the remaining mass includes undetected elements, such as O and Si (Fig. 4.4, bottom right). The measured compositions for SDSS J0823+0546 and those implied by equation 4 are illustrated in the right-hand pie charts of Fig. 4.4. At a maximum density of $7.9\,\mathrm{g\,cm^{-3}}$ (a pure Fe/Ni composition with no porosity), we arrive to minimum geometric-mean radii of 39 and 45 km for the planetesimals accreted by SDSS J0741+3146 and SDSS J0823+0546, respectively.

The above analysis assumes that the present CVZ metal masses correspond to the total accreted masses. While these estimated masses are comparable to moderately large Solar system asteroids, some of the material has presumably already sunk out of the bases of their CVZs since the accretion events occurred, and thus the parent bodies must have been larger. However, intuition tells us that the accreted planetesimals can not have been much more massive, as there ought to be fewer available bodies at higher mass-intervals. Consequently the accretion episodes ought to have occurred within only a few τ_{Fe} ago. For example, if the material at SDSS J0823+0546 was deposited $t = 10\tau_{\mathrm{Fe}}$ ago, the implied parent body mass would be similar to that of the Moon. While this is by no means impossible, a mass closer to that observed now in the CVZ seems far more reasonable, thus implying a more recent accretion history. We show here that this intuition can be translated directly into statistics, providing median values and 95th percentile upper-limits to the asteroid masses, and hence times since the accretion episodes.

The most massive planetesimals in the Solar asteroid belt have a power-law mass-distribution with an exponent $k \simeq 1.8$ (Kresak, 1977). We therefore assume that the large metallic exoplanetesimals accreted by SDSS J0741+3146 and SDSS J0823+0546 have masses, M, drawn from a similar distribution, $P(M)$, with the mass of material in the white dwarf CVZ, M_{cvz} as a lower bound. $P(M)$ can then be written as

$$P(M) = \frac{k-1}{M_{\mathrm{cvz}}}\left(\frac{M}{M_{\mathrm{cvz}}}\right)^{-k} \quad \text{for } M \geq M_{\mathrm{cvz}}, \quad k > 1. \tag{4.6}$$

Integrating (4.6) up to a mass $M_{\rm ast}$, yields the corresponding quantile q, i.e.

$$q = \int_{M_{\rm cvz}}^{M_{\rm ast}} P(M)\,\mathrm{d}M = 1 - \left(\frac{M_{\rm ast}}{M_{\rm cvz}}\right)^{1-k}. \tag{4.7}$$

Rearranging equation (4.7) to express the $M_{\rm ast}/M_{\rm cvz}$ ratio in terms of q,

$$M_{\rm ast}/M_{\rm cvz} = (1-q)^{1/1-k}, \tag{4.8}$$

it then becomes simple to calculate the median and 95th percentile upper-limit of $M_{\rm ast}/M_{\rm cvz}$, for a given value of the power-law exponent, k. Using $k = 1.8$ as above we find $M_{\rm ast}/M_{\rm cvz}$ has a median value of 2.4 and 95th-percentile upper-limit of 42. In other words, the initial planetesimal masses were probably only a few times larger than what currently remains within the CVZs, and is unlikely to be more than a few ten times larger. Given our calculated values of $Mcvz$, these upper limits correspond to $\sim 10^{23}$ g or about one tenth the mass of Ceres, for the metallic objects accreted by SDSS J0741+3146 and SDSS J0823+0546. Naturally, in an absolute sense, the quantiles of $M_{\rm ast}$ are subject to any systematic error in the calculation of $M_{\rm cvz}$ (although the ratio $M_{\rm ast}/M_{\rm cvz}$ is not).

Continuing this line of reasoning, we can place similar constraints on how long ago these planetesimals were accreted. Because their composition is dominated by Fe and Ni (which both have similar diffusion time-scales), we are justified in considering the time-evolution of material in the white dwarf CVZ as

$$M_{\rm cvz}(t) = M_{\rm ast}\mathrm{e}^{-t/\tau_{\rm Fe}}. \tag{4.9}$$

In the general case where the mass has components from elements with different sinking time-scales, (4.9) becomes a sum of exponentials, which cannot be analytically solved for t. Combining equations (4.8) and (4.9), we can then write the time since accretion in terms of q and k as

$$t = \tau_{\rm Fe}\frac{\ln(1-q)}{1-k}. \tag{4.10}$$

Using again $k = 1.8$, we find the median and 95-percentile upper-limits for t are $0.87\,\tau_{\rm Fe}$ and $3.74\,\tau_{\rm Fe}$ respectively.

To place these systems in context, there are several comparable Solar system objects that are worth consideration. This includes the main-belt asteroid, 16-Psyche, which is the largest M-type asteroid in the Solar system. Radar observations show that Psyche has a mostly metallic composition (Ostro, 1985) consistent with exposed core material. At a mass of $2.72 \pm 0.75 \times 10^{22}$ g. (Carry, 2012), it is only one order of magnitude larger than the estimated Fe mass currently residing in the CVZ of SDSS J0823+0546. While Psyche is thought to be chiefly comprised of Fe and Ni (Matter et al., 2013), NIR observations indicate that its surface composition also includes pyroxenes (Hardersen et al., 2005). As pyroxenes can include Ca and Mg it is possible that these elements we see in these Fe-rich white dwarfs could also arise from such compounds on the surface of the metallic asteroids.

The metallic (as opposed to rocky) nature of these exoplanetesimals offers the opportunity to investigate the process of the accretion on to the white dwarf surface which we show to be violently destructive, and not necessarily leading to the existence of a debris disc. Typically, planetesimals arriving at white dwarfs are assumed to be loose rubble piles held together through self-gravitation. Disruption occurs when tidal forces overcome self-gravity. In the case of loose rubble piles, the distance from the white dwarf at which this occurs (the Roche radius) depends only on the white dwarf mass and planetesimal density, and is typically in the range 1–2 $\mathrm{R}_\odot$. For Fe-rich asteroids, the mechanical strength of the material cannot be ignored, and a different treatment is required. The effect of mechanical stresses on planetesimals has previously been examined by some authors (e.g. Slyuta & Voropaev, 1997; Davidsson, 1999), with Brown et al. (2017) recently considering the disruption of high mechanical-strength planetesimals in the context of white dwarf accretion. They show that for an asteroid with density ρ, size a_0, and tensile strength S, a simple relation for the tidal disruption radius R_{td} is given by

$$R_{\mathrm{td}}^3 = \frac{G M_{\mathrm{wd}} \rho a_0^2}{2S}, \tag{4.11}$$

where G is the gravitational constant and M_{wd} is the white dwarf mass.

The small amount of literature available on the mechanical properties of metallic Solar system bodies indicates their characteristics can vary dramatically. For the meteorite samples that have been studied, tensile strengths have been found ranging from 40 MPa (Slyuta, 2013) up to 800 MPa (Opik, 1958), and exceeding 1 GPa for some cast Fe-Ni alloys (Petrovic, 2001). To explore an extreme example, we take $S = 800\,\mathrm{MPa}$. Assuming the density for meteoritic-iron of $7.9\,\mathrm{g\,cm^{-3}}$, we estimated above minimum radii of 39 km for SDSS J0741+3146 and 45 km for SDSS J0823+0546, respectively.[7] Setting M_{wd} to the canonical $0.6\mathrm{M}_\odot$, equation (4.11) implies similar tidal disruption distances for both systems at $R_{\mathrm{td}} \simeq$

---

[7] The radii were likely larger than this for two reasons. Firstly, as our above analysis shows, the masses could be somewhat larger, and secondly if the asteroids had any significant porosity, their effective densities would be lowered.

$0.17\,\mathrm{R}_\odot = 13\,R_\mathrm{wd}$, much closer than the $\simeq 1\,\mathrm{R}_\odot$ for a strengthless rubble pile. Of course, if any faults are present within the asteroid, this will allow for disintegration at greater distances from the white dwarf, but with the resulting smaller fragments more resilient to tidal effects.

Because these asteroids are presumably composed of largely ductile metal, it is interesting to consider the process of breakup itself. Before catastrophic mechanical failure when the asteroid reaches the tensile limit, it will first reach the yield limit. At this point additional stress causes plastic deformation, leaving the planetesimal shape permanently altered even if tensile forces are relaxed. Therefore breakup of metallic asteroids will result in deformation before mechanical failure (Slyuta, 2013). Knox (1970) found yield strengths of 400 MPa to be typical, with Petrovic (2001) showing that at room temperature, the ratio of tensile and yield strengths is typically 1.5–2. This act of deformation may hasten the breakup process, as the stretching will result in tidal heating, further weakening the metal. Additional heating/weakening could be provided by flux from the central star, but this strongly depends on whether the asteroid remains in the vicinity of the white dwarf long enough for it to thermally respond. While a temperature dependent reduction in mechanical strength will cause the planetsimal to disintegrate further away from the white dwarf, the ratio of tensile to yield strength will increase (Petrovic, 2001) allowing for a greater degree of deformation before fragmentation.

Although rather simplified, the size dependence of equation (4.11) indicates that the resulting fragments are more resistant to tidal forces, and so must move closer to the central white dwarf before further breakup can occur. This logically implies continuous fragmentation down to the surface of the white dwarf, with some final size for the accreted pieces. Setting the left hand side of equation (4.11) to R_wd, this implies km-sized fragments reaching the white dwarf surface, as also indicated by Brown et al. (2017) in their analysis of granite. In reality this minimum size will be smaller than 1 km due to the temperature dependence of the tensile strength and whether any significant melting/ablation of the fragments occurs on their final descent. That being said, even if we reduce the tensile strength by a factor of one hundred, this only reduces the final fragment size by a factor ten, i.e. fragments on the order of 100 m arriving at the white dwarf surface. In other words it is quite possible that the metal-rich material we see at SDSS J0741+3146 and SDSS J0823+0546 did not accrete on to their respective white dwarfs entirely in the gas phase, but rather impacted the stellar photosphere as millions of solid fragments. The prospect of solid debris surviving to the white dwarf surface, ultimately depends on how long the infalling body spends within the vicinity of the white dwarf, which in turn depends on the orbital eccentricity.

Because these impacts would occur at orbital speeds of several $1000\,\mathrm{km\,s^{-1}}$, the expected impact energy would be very large – a 100 m diameter iron sphere would impact a canonical $0.6\,\mathrm{M}_{\odot}$, $0.013\,\mathrm{R}_{\odot}$ white dwarf with a free-fall energy of $\sim 10^{30}$ erg. Because the scale-heights for cool white dwarfs with helium dominated atmospheres are on the order of 10 m, the energy release will take place on μs time-scales and thus lead to a short short-lived, but luminous burst. Brown et al. (2017) also considered this situation, with comparison to Solar impactors, with their analysis suggesting energies direct collisions of km-sized planetesimal fragments on to white dwarfs could be observable as transient sources. While we have conservatively assumed smaller fragments than Brown et al. (2017), the specific energy of 100 keV per nucleon is independent of the planetesimal mass.[8] Therefore the systems discussed in this section motivate future searches into high energy transients from direct impacts of solid bodies on to nearby accreting white dwarfs.

4.4.3 Mg-rich objects

SDSS J0956+5912 and SDSS J1158+1845 both stand out in Fig. 4.1 as Mg-rich (SDSS J1158+1845 is the right-most of the two blue points) and exhibit strong Mg I lines in their spectra (Fig. 4.7), They are are even more Mg-rich than the Earth's mantle (blue cross), however it is not clear whether these abundances reflect atypical planetesimal compositions, for example pure magnesium silicate, or the result of relative diffusion. As outlined in Section 4.1, we find that for the stars in our sample, the Mg diffusion time-scales are typically 2.8 times longer than those of Ca or Fe. Therefore any given point in Fig. 4.1 (with the exception of the left-edge, which implies zero initial Mg) will move towards the bottom right corner over time, as Ca and Fe diffuse out of the white dwarf CVZ faster than Mg.

Inspection of Fig. 4.1 shows that a line drawn between the bulk Earth composition and the bottom right corner passes close to both SDSS J0956+5912 and SDSS J1158+1845. Therefore, it is perhaps possible that these white dwarfs may have accreted Earth-like material several Myr ago which is now severely Mg enhanced. In units of Ca diffusion-time-scales, τ_{Ca}, an initial composition resembling the bulk Earth will arrive at the present position of SDSS J0956+5912 in approximately $2.5\,\tau_{\mathrm{Ca}}$ ($\simeq 3.2$ Myr), and about $3\,\tau_{\mathrm{Ca}}$ ($\simeq 3.7$ Myr) for SDSS J1158+1845. For SDSS J1158+1845 this corresponds to an initial Ca abundance close to -6.5 dex.

---

[8] Brown et al. (2017) quote a specific energy of 10 MeV per nucleon implying emission up to gamma-ray energies. However, this is in error and should be 100 keV per nucleon, and thus maximum emission energies of hard X-rays (J. Brown, priv. comm., 2017).

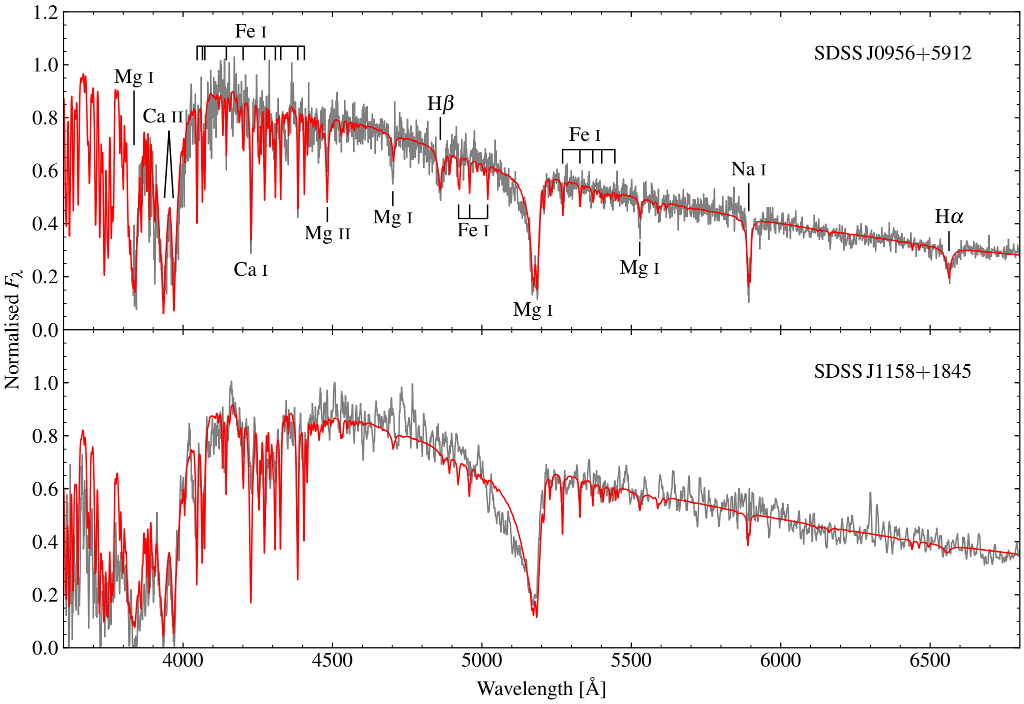

Figure 4.7: The two objects classed as Mg-rich show strong absorption from the Mg I-b triplet located at 5171 Å. While SDSS J0956+5912 exhibits Balmer lines, the atmosphere is in fact helium dominated, with hydrogen as a trace element.

This slightly surpasses SDSS J1340+2702 which has the highest observed Ca abundance in our sample at -6.98 dex. Assuming a 0.6 $M_\odot$ white dwarf, the total accreted mass (scaling from bulk Earth abundances), would have been roughly that of Ceres. For SDSS J0956+5912 the situation is even more extreme. Despite the very high Mg/Ca ratio, the absolute Ca-abundance is the second highest in our sample. For an accretion episode occurring $2.5\,\tau_{\rm Ca}$ ago, the original Ca abundance would have been about -6.1 dex, corresponding to total accreted metals of about 3×10^{24} g or 3 Ceres masses (again assuming a 0.6 $M_\odot$white dwarf).

As very few objects within the Solar system have masses in this range and above, on this basis alone, it would seem unlikely that we observe two systems having accreted such extremely large planetesimals. An alternative hypothesis is that increased dynamical activity at these systems several Myr ago led to the accretion of a large number of lower mass planetesimals totalling a Ceres mass or more. For instance tidal interactions of passing stars could provide such short lived dynamic instabilities (Bonsor & Veras, 2015; Hamers & Portegies Zwart, 2016; Veras et al., 2017b). Several Myr later after this intense accretion episode has ceased, these white dwarfs show Mg-rich material due to relative diffusion.

Finally we consider the possibility that the parent bodies that were accreted by SDSS J0956+5912 and SDSS J1158+1845 were intrinsically Mg-rich, far from our assumption that planetesimals follow the core/mantle/crust compositions of the Earth. For instance, the observations can be considered consistent with parent body masses of $\sim 10^{23}$ g accreted much more recently, but with substantially higher Mg/Ca and Mg/Fe ratios than even the Earth's mantle, e.g. predominantly enstatite, forsterite, or a mixture of the two.

Chapter 5

Evolution of remnant planetary systems

$T_{\rm eff}$ and atmospheric abundances are determined directly from spectral fitting, and so it is common practice to plot the abundance of one of the metals (usually Ca, as this is most easily detected) against $T_{\rm eff}$. While this is a useful way to illustrate variations in abundances across the full range of known white dwarfs, the non-linear relationship between $T_{\rm eff}$ and age does not provide the best handle on the evolution of the oldest systems. For instance Fig. 8 of Koester et al. (2014) shows that the highest observed accretion rates ($10^9\,{\rm g\,s^{-1}}$) of rocky debris on to DA white dwarfs remain constant over a large range in $T_{\rm eff}$, however most of the sample discussed in that paper spans only the first Gyr of white dwarf cooling. Several dynamical studies suggest that a decrease in scattering (and subsequent accretion) events ought to occur (Debes et al., 2012; Mustill et al., 2014; Veras et al., 2013, 2016a). In this chapter we provide evidence for a decline in maximum observed accretion rate, but over time-scales of many Gyr, which we are able to probe for the first time with our sample of cool DZ white dwarfs.

5.1 Evolution of remnant planetary systems

Since white dwarfs cool predictably after departing the AGB, we were able to estimate cooling ages for our DZ sample (Chapter 3/Table B.4). White dwarf ages depend not only on the white dwarf $T_{\rm eff}$, but also the white dwarf mass. As it is not possible to determine these spectroscopically for DZs, we used the SDSS white dwarf mass distribution (Kepler et al., 2015) as a prior. Propagating the measured $T_{\rm eff}$ values and mass prior through the Montreal DB cooling tracks (Fontaine et al., 2001; Bergeron et al., 2001; Holberg & Bergeron, 2006; Kowalski & Saumon, 2006; Bergeron et al., 2011), we thus were able to determine cooling ages and their associated uncertainties. The effect of factoring in the unknown masses into these calculations, is that the relative uncertainty on age is somewhat larger (typically 10–20 %) than the relative error on $T_{\rm eff}$ (usually only a few percent)

The oldest system in our sample is SDSS J1636+1619 at $7.7^{+0.3}_{-0.9}$ Gyr, which is unsurprising considering it also has the reddest $g-r$ colour at 1.10 ± 0.03 (Table B.1). Because the typical white dwarf progenitor is a $\simeq 2\,{\rm M}_\odot$ A-type star (Catalán et al., 2008) with a main-seqence life time of ~ 1 Gyr, the total system age is $\simeq 9$ Gyr. Therefore, our analysis indicates this object is nearly as old as the Galactic disc (Oswalt et al., 1996; del Peloso et al., 2005; Haywood et al., 2013), yet still shows the signs of a planetary system, long after departing the main-sequence.

In Fig. 5.1 we show log[Ca/He] versus the estimated cooling ages. The distribution is approximately triangular in shape, however only one of the edges has a physical significance. The left and lower edges (young and less polluted systems) merely result from our white dwarf identification method, which by design is insensitive to hot/young systems or white dwarfs with very low metal-abundances. In contrast, the upper edge is an apparently real boundary of the DZ white dwarf distribution, representing a decrease in the maximum-encountered Ca abundance of ≈ 2.5 dex across the full age-range of our sample.

Selection-bias can be easily ruled out as hypothetical objects within the upper-right corner (cool and extremely metal-rich), would have highly distinctive spectra, and would look unlike any main sequence star or quasar. Such model spectra were calculated for the DZ grid used in Chapter 3, with the most extreme example at $T_{\rm eff} = 4400$ K and $\log[{\rm Ca/He}] = -7$ dex shown in Fig. 5.4. Therefore, we are confident that we would have identified any such system. The absence of objects with $\log[{\rm Ca/He}] \simeq -7$ dex at old ages indicates they must be extremely rare.[1]

A physical interpretation for the decrease of log[Ca/He] must account for the 2.5 dex change we see in Fig. 5.1. We show here that neither variations in the size of the white dwarf CVZ, nor elemental diffusion time-scales are significant enough to explain the magnitude of this decrease, and thus we are unable to explain the abundance decrease as the result of evolving white dwarf properties.

For each white dwarf in our sample, we performed envelope calculations to determine the masses of their outer CVZs as well as the diffusion time-scales for each element (Table B.3). These properties change with white dwarf cooling, and so we

---

[1] A clear exception is SDSS J0916+2540 with $\log[{\rm Ca/He}] = -7.5$ dex and cooling age of $5.3^{+0.6}_{-1.2}$ Gyr, which we discuss in Section 5.2.

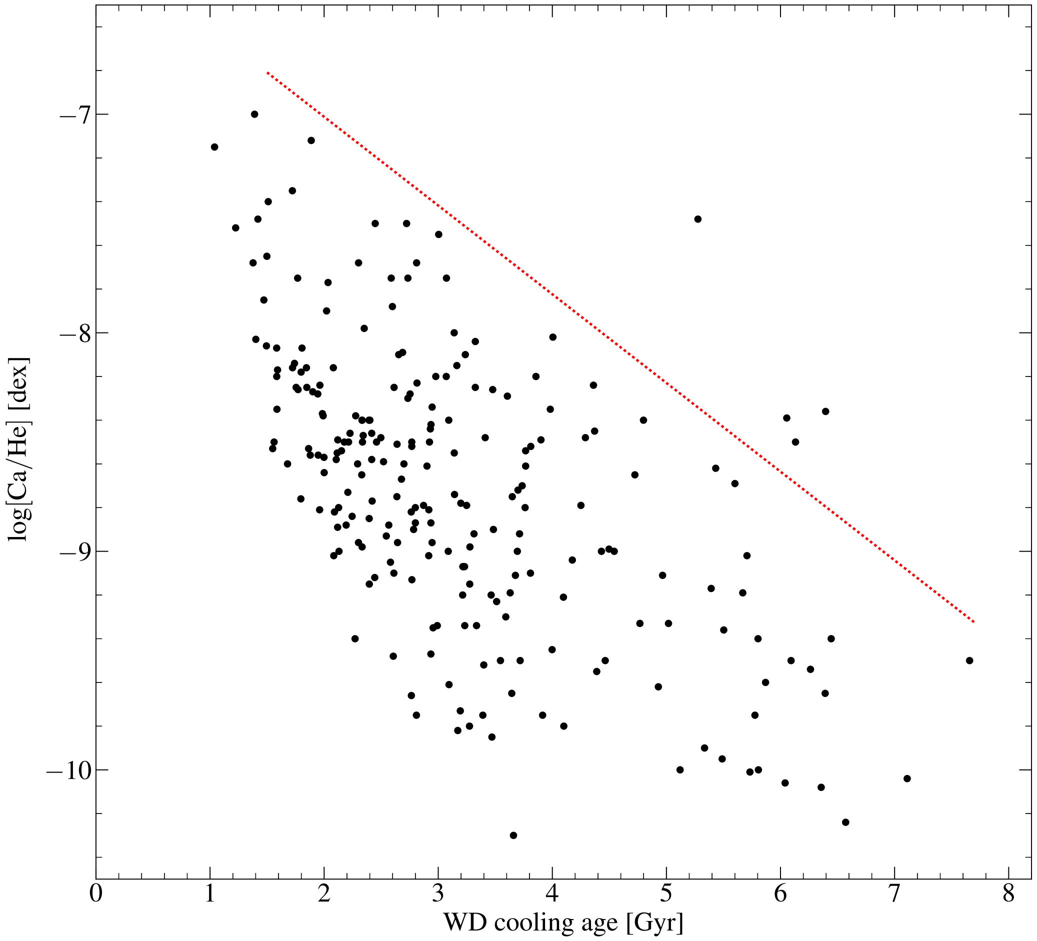

Figure 5.1: Atmospheric Ca abundances against white dwarf age. The dotted line indicates our inferred upper bound to the distribution with the exception of a few outliers (which are discussed in section 5.2).

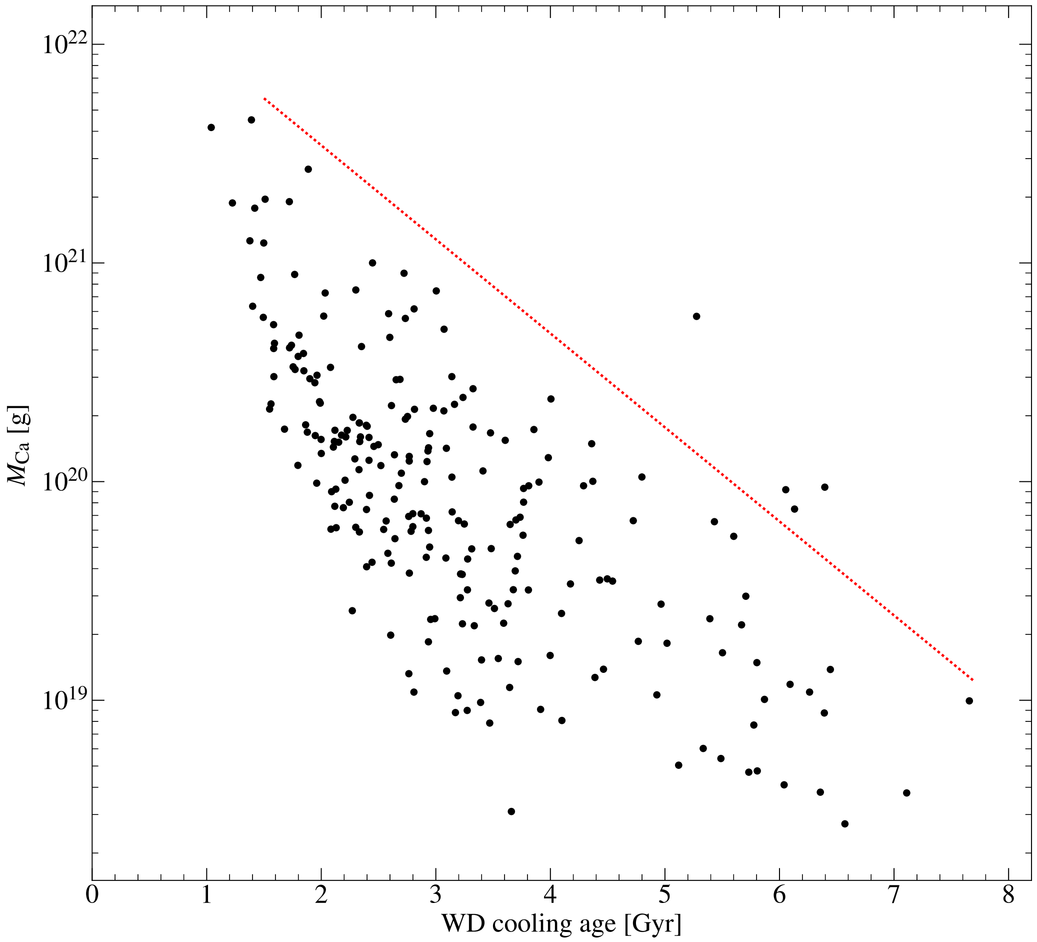

Figure 5.2: The Ca abundances from Fig. 5.1 have been rescaled by the CVZ masses, yielding the mass of Ca in the white dwarf CVZs. The slope of the dotted line is adjusted accordingly.

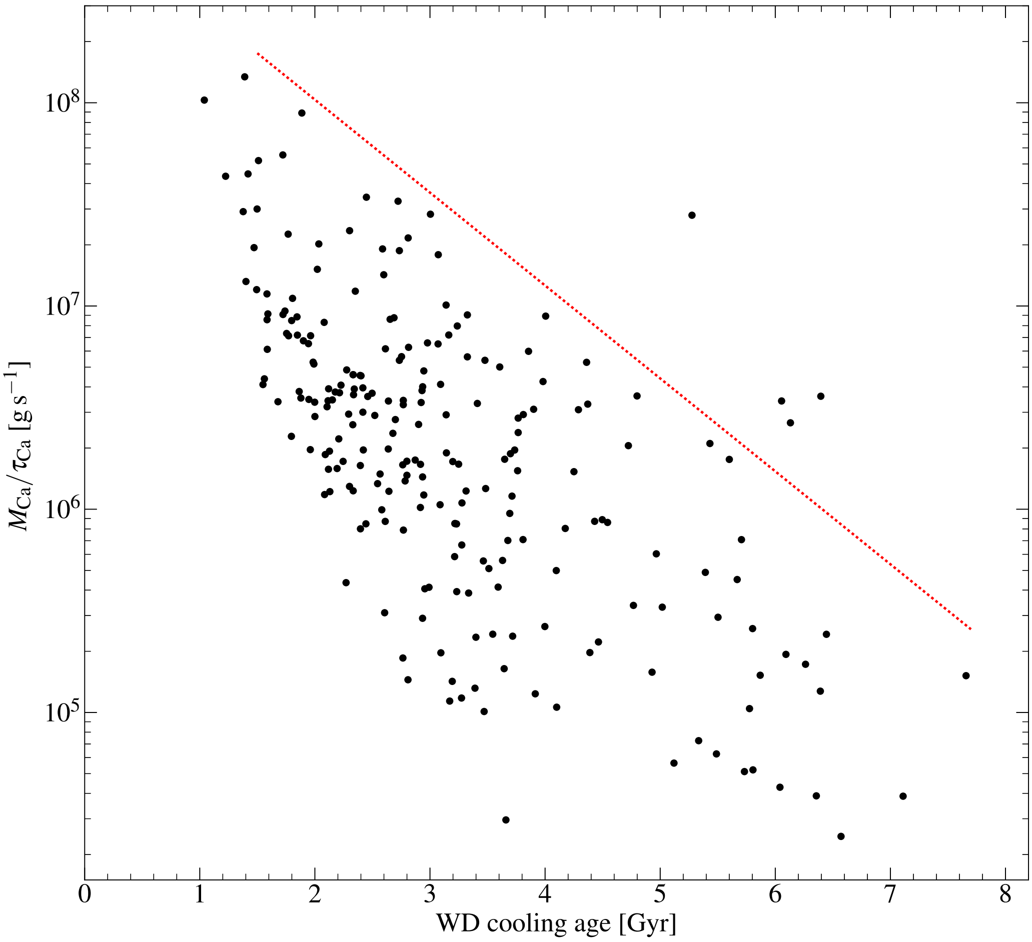

Figure 5.3: Ca masses from Fig. 5.2 are divided by the time-scales for Ca to diffuse out of the bottom of the CVZs. This can be interpreted as a diffusion flux or mean accretion rate. Again, the slope of the dotted line is updated.

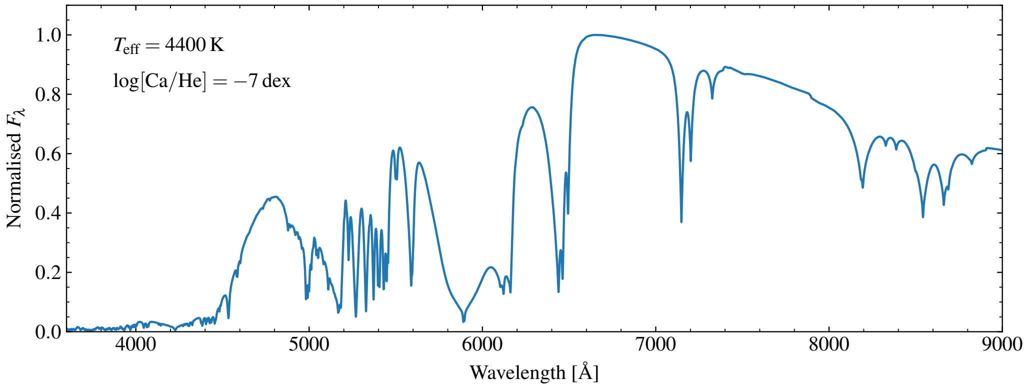

Figure 5.4: The coolest and most metal rich model spectrum from our DZ grid shows an intensely line blanketed spectrum. SDSS J1636+1619 is the most metal rich of the few DZ in our sample with a comparable $T_{\rm eff}$, yet has abundances 2.5 dex lower than this model.

investigated whether these could account for the trend seen in Fig. 5.1. We firstly scaled Ca abundances by the masses of the white dwarfs CVZs, which determines the mass of Ca mixed throughout the white dwarf envelopes. This had little effect on the trend, which remained at a $\simeq 2.5$ dex decrease across the age range of our sample (Fig. 5.2). We then rescaled these masses by each white dwarf's Ca diffusion time-scale, which determines the mass fluxes through the base of their CVZs, or in other words, the average accretion rates of Ca on to the stars. Rather than causing the trend to subside, we instead found it to steepen to $\simeq 3$ dex (Fig. 5.3)

The downwards trend is indicated by the dashed lines in all three figures and corresponds to an exponential decrease in the accretion rate upper bound with white dwarf age (for now ignoring four outliers above the lines, discussed separately below). The slope of the line in Fig. 5.3 corresponds to an e-folding time-scale of 0.95 Gyr. We found that this could not be varied much more than 0.1 Gyr before appearing incompatible with the data, and thus we argue that 0.95 ± 0.10 Gyr is the time-scale on which the accretion rate upper limit decays for our DZ sample. Since this decrease of white dwarf pollution with age does not appear to arise from either selection bias nor a change in white dwarf properties, it likely relates to the properties of the planetary systems at these white dwarfs.

We find the most reasonable explanation is that the number of planetesimals remaining in old remnant planetary systems, available to be scattered towards the white dwarf, decreases with time. Since the occurrence rate that white dwarfs accrete planetesimals will be proportional to the number available to be scattered inwards, then an exponential decrease in the largest objects is to be expected. Dynamical simulations have previously suggested that the occurrence rate of white dwarf pollution should be expected to decrease on Gyr time-scales (Debes et al., 2012; Mustill et al., 2014; Veras et al., 2013, 2016a) We therefore suggest that our observations may show the first evidence of this process occurring.

Our results in Chapter 3 provide one caveat to this interpretation. In Fig. 3.12, we compared our DZs with the DZ sample of Dufour et al. (2007) and the DBZ sample of Koester & Kepler (2015). There we noted an abrupt 2 dex increase in log[Ca/He] occurring at about 10 000 K (corresponding to a cooling age of 0.7 Gyr for a $0.6\,\mathrm{M}_\odot$ white dwarf), and speculated that this may indicate an incomplete understanding of white dwarf CVZ formation. It is therefore prudent to remain cautious of the 3 dex decrease we see here in Fig. 5.3. On the other hand, our envelope calculations currently suggest that the combined effect of variations in CVZ sizes and diffusion time-scales across our sample act to amplify the decline between Figs. 5.1 and 5.3, although only by about 0.5 dex. Therefore a change in our understanding of white dwarf CVZs would need to imply a three order of magnitude change in the opposite direction to remove the trend seen in Fig. 5.3.

Within Section 3.5, we also considered the alternative hypothesis that the 2 dex Ca abundance increase in Fig. 3.12 results from a dynamical instability that typically occurs after $\simeq 0.7$ Gyr of white dwarf cooling. Thus the changes in maximum abundance seen in Fig. 3.12 and Fig. 5.1 could both be related to the evolution of their planetary systems.

5.2 Metal rich outliers

We note that four systems in our sample (SDSS J0736+4118, SDSS J0744+4649, SDSS J0807+4930, and SDSS J0916+2540) are located above the upper envelope for all of Figs. 5.1, 5.2, and 5.3. Naturally these outliers are worthy of discussion in regards to their unusually high Ca-abundances/accretion rates for their ages. The spectra of SDSS J0736+4118, SDSS J0807+4930, and SDSS J0916+2540 are displayed in Fig. 5.5 – the spectrum of SDSS J0744+4649 can be found in Fig. 4.5.

SDSS J0744+4649

This system has already been discussed in detail in Section 4.4.1, due to the Ca-rich nature of the accreted material which, combined with the moderate total-metal-abundance for this star, leads to a particularly high location in Fig. 5.1. In terms of log[Mg/He] or log[Fe/He], this star is located within the distribution of our sample (although only just).

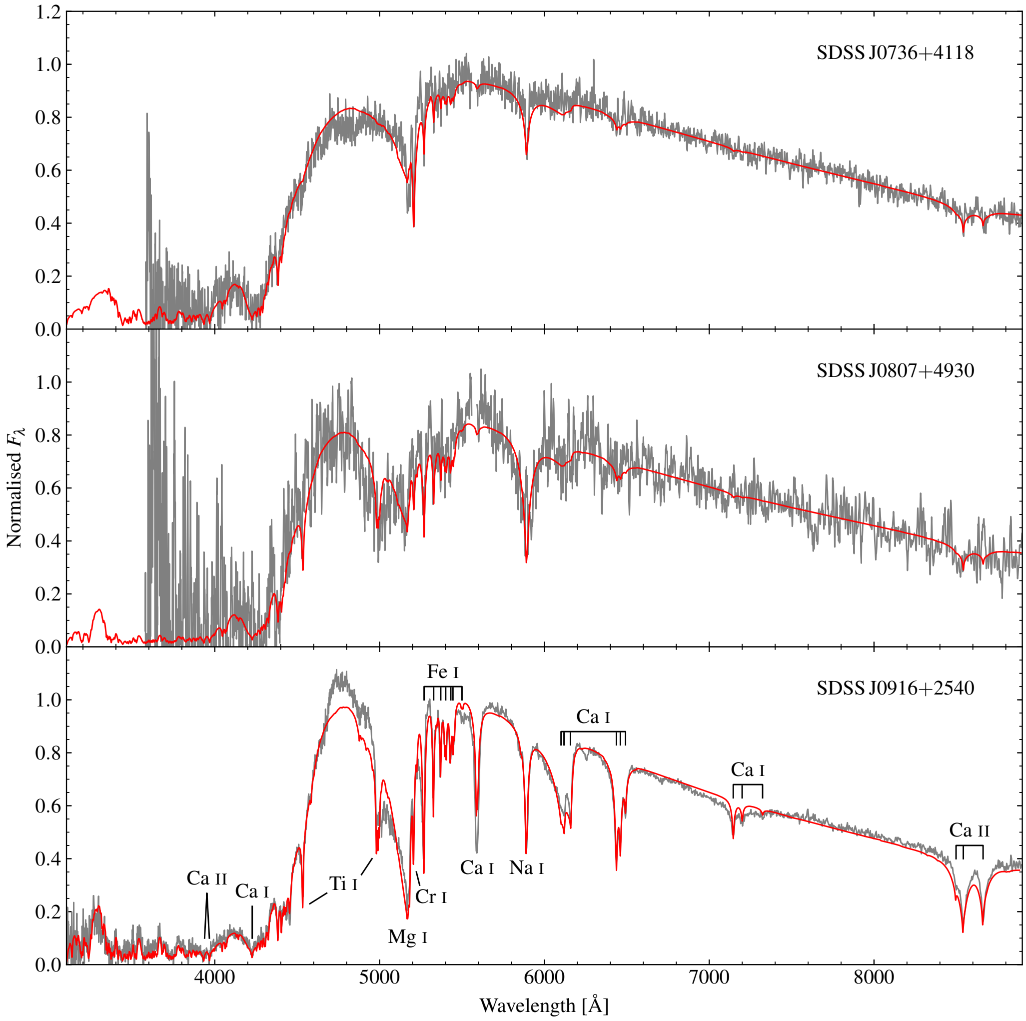

Figure 5.5: Spectra for three of the four outliers in Fig. 5.1 are shown with their best fitting atmospheric models. The remaining system, SDSS J0744+4649 is already shown in Fig. 4.5. The unique spectrum of SDSS J0916+2540 exhibits many deep, broad absorption features with some of the shallower lines observed only in this DZ.

SDSS J0916+2540

This extremely metal-rich DZ shows a spectrum quite unlike any other white dwarf, with extreme photospheric absorption by a large number of elements across the entire optical range. This system was first analysed by KGGD11[2] in their sample of 26 DZ stars. As our DZ sample is nine times larger than that of Koester et al. (2011), one might expect to find several more similar objects, however SDSS J0916+2540 remains unique among our 230 objects. No doubt such an usual spectrum could be recognised even in low quality data (but with reduced scope for spectral analysis), and so we are lucky that this intrinsically faint star is so nearby ($d = 43.4 \pm 5.4$ pc) that its spectrum can be studied in exquisite detail.

Within Fig. 5.1, SDSS J0916+2540 is an order of magnitude more abundant in Ca, compared to other white dwarfs of similar temperature/age, suggesting some rare phenomenon results in its extremely metal-rich photosphere. The answer, we believe, lies approximately 40 arcseconds to the South-East in the form of a K-star common-proper-motion companion (J. Farihi, priv. comm., 2013). At the estimated distance of 43.4 ± 5.4 pc (Table B.4), the projected separation between the two stars is 1900 ± 200 AU.

Several recent theoretical studies suggest that wide binary companions can cause secular instabilities in white dwarf planetary systems, even at large ages, resulting in an increased influx of planetesimals. Bonsor & Veras (2015) considered the effect of Galactic tides on wide binary systems, and found that secular variations in the orbital elements, can lead to a close approach several Gyr after the primary has entered the white dwarf cooling track, thus turning a previously stable planetary system into a dynamically active one.

In contrast, Petrovich & Muñoz (2017) considered systems where a belt of exoplanetesimals is initially located between an inner planetary system and a, potentially stellar, inclined outer companion. During the main-sequence, they argued that the inner planetary system dynamically shields planetesimals against perturbations from the outer companion. However if the inner system is engulfed during stellar evolution to the white dwarf stage, then the planetesimal belt that may have been dynamically stable throughout the main-sequence can now be affected by the outer perturber via the Kozai-Lidov mechanism. Under this mechanism, an orbiting companion inclined with the plane of the planetary system causes planetesimals on previously circular orbits to exchange eccentricity with their own inclination. This can result in planetesimals on highly eccentric orbits, with pericentres within the

---

[2] SDSS J0916+2540 was also independently identified by members of the Galaxy Zoo community from its SDSS spectrum, who also correctly classified it as an unusual white dwarf (`http://www.galaxyzooforum.org/index.php?topic=276688.15`).

white dwarf tidal-disruption radius. According to Petrovich & Muñoz (2017), this mechanism also has the advantage that it is always active, and so could explain the extreme abundances at SDSS J0916+2540, despite the present binary separation of several thousand AU.

SDSS J0807+4930

We note that qualitatively, the spectrum of this white dwarf resembles that of SDSS J0916+2540, but far less extreme (an "0916-lite"), motivating us to check this system for binarity. Due to the faintness of this white dwarf ($r = 20.5$), no published proper-motion is available, however we were able to calculate a moderate proper-motion of $\vec{\mu} = (\mu_\alpha \cos\delta, \mu_\delta) = (-113.9 \pm 3.3, -54.0 \pm 3.1)\,\mathrm{mas\,yr^{-1}}$using two imaging epochs from SDSS (2000.3154 and 2003.8123), and one from Pan-STARRS (2013.5689). Searching nearby stars for binary membership revealed an obvious companion 27 arcseconds to the North-West. Based on its colours, the companion is a mid-to-late M-type star ($r = 20.1$) with proper-motion $\vec{\mu} = (-112.6 \pm 5.6, -51.1 \pm 5.6)\,\mathrm{mas\,yr^{-1}}$. At an estimated distance of 156 ± 20 pc (Table B.4), this implies a projected separation of 4200 ± 500 AU.

While 70 % of the DZs in our sample have proper motion measurements, we find no evidence for wide companions to any of the white dwarfs further to SDSS J0807+4930 and SDSS J0916+2540. Therefore these two systems provide a strong case that binarity is correlated with higher than average accretion rates. We also note that WD 1425+540, recently analysed by Xu et al. (2017), is also a member of wide binary, where the companion is speculated to have provided the perturbations leading to the accretion of a Kuiper-belt-like object by the white dwarf.

SDSS J0736+4118

Of the four outliers, SDSS J0736+4118 is the only system with no obvious property naturally explaining its high Ca abundance in Fig. 5.1. However of the four objects, it is also the least extreme ($t_\mathrm{cool} = 6.1$ Gyr, $\log[\mathrm{Ca/He}] = -8.50$ dex). Therefore it may simply be the case that SDSS J0736+4118 has accreted its atmospheric metals much more recently than other systems in our sample or even that accretion is still ongoing.

Chapter 6

Magnetism of DZ white dwarfs

For cool white dwarfs with pure hydrogen/helium atmospheres, their intensity spectra will lack absorption features needed to detect magnetic fields. However, for cool white dwarfs that have accreted exoplanetary material, the presence of Zeeman split metal lines in their spectra becomes a powerful tool for determining their magnetic properties.

Prior to the embarking upon of this project, only six white dwarfs were known to display both metals combined with the effects of magnetism, which included three DZHs and three DAZHs. The three DZHs are LHS 2534 (Reid et al., 2001), WD 0155+003 (Schmidt et al., 2003), and G 165−7 (Dufour et al., 2006), with respective surface averaged field strengths, B_S, of 1.9, 3.5, and 0.6 MG. All three have SDSS spectra and appear in our sample and so we refer to these using the SDSS Jhhmm±ddmm naming format (SDSS J1214−0234, SDSS J0157+0033, and SDSS J1330+3029 respectively) for consistency with our convention used throughout the rest of this thesis. The three DAZH, G 77−50 (Farihi et al., 2011a), NLTT 43806 (Zuckerman et al., 2011) and NLTT 10480 (Kawka & Vennes, 2011) have fields of 0.12 MG, 0.07 MG and 0.5 MG respectively. During the early stages of this project, Kawka & Vennes (2014) also identified an additional DAZH, NLTT 53908 with a field strength of and 0.33 MG.

In our sample we found 33 magnetic DZ white dwarfs including the previously identified DZHs SDSS J1214−0234, SDSS J0157+0033, and SDSS J1330+3029. In the initial stages of this project when the DZ sample amounted to only 79 objects (SDSS DR10 data) we identified 10 magnetic systems (Hollands et al., 2015). With the full sample of 231 DR12 objects, 23 additional magnetic systems have been identified, and so in this chapter we present an expanded set of results, including follow-up observations of some of the most interesting systems.

6.1 Measuring white dwarf magnetic fields

Measuring the surface-averaged magnetic fields of white dwarfs (B_{S}), can be remarkably precise. Unlike many quantities encountered in astrophysics, the Zeeman effect often allows B_{S} to be measured to better than 1 % precision. Additionally, the methods used to measure white dwarf magnetism are often quite simple, but this depends on which field-strength regime the star falls into.

Within our sample we find that most of the magnetic objects fall into the Paschen-Back regime, where absorption lines are are split into three components, whose energy spacing is directly proportional to the magnitude of the magnetic field. We find this regime is generally applicable for objects with B_{S} in the range 1–10 MG. For lower field strengths, measurement is in fact *more* complicated due to the non-negligible spin-orbit effect. We find 10 of the 33 magnetic systems fall into this low-field regime. Finally we find a single system with a field of $\simeq 30$ MG where the quadratic Zeeman effect appears to dominate and thus requires its own approach to field measurement. The field strengths are summarised within Table 6.1, with the visibly split transitions listed for each object.

6.1.1 Paschen-Back regime

In the spectra of 22 objects, we are able to identify transitions from metallic species that are Zeeman split into three components. In most cases these transitions are from Mg I at 5171 Å and/or Na I at 5893 Å. In the zero-field case, the Mg feature is actually already a triplet, and the Na feature is a doublet, due to the spin-orbit effect. For both of these elements, at fields beyond $\simeq 1$ MG, the Zeeman effect becomes the dominant perturbation and so spin and orbital angular momenta decouple. Thus we observe the Mg and Na atoms in the Paschen-Back regime where the Zeeman splitting profile results from only the contribution of orbital angular momentum. In Fig. 6.1 we show four examples of white dwarfs where Mg and Na are observed in the Paschen-Back regime.

To precisely measure the field strengths we fitted the spectra with a 7-parameter model. The continuum flux in the vicinity of the triplet was modelled as a second-order polynomial. A linear approximation would not suffice, particularly for the wings of the broad Mg feature. We then modelled the triplet as the sum of three Gaussian profiles with equal width, depth (in continuum normalised flux) and separation in wavenumber, $1/\lambda$. The wavenumber of the π-component of the triplet was also included as a free parameter to account for small shifts. In most cases, we found the π-components are blueshifted from their rest wavelengths, and

Table 6.1: Magnetic objects in our sample with the measured average field strengths and their detected Zeeman split lines.

SDSS J	B_S [MG]	Split lines	Note	Ref.
0037−0525	7.09 ± 0.04	Mg I, Na I		1,2
0107+2650	3.37 ± 0.07	Mg I, Na I		1,2
0157+0033	3.49 ± 0.05	Mg I,		3
0200+1646	10.71 ± 0.07	Mg I, Na I		1
0735+2057	6.12 ± 0.06	Mg I, Na I		4
0741+3146	0.48 ± 0.05	Fe I,		
0806+4058	0.80 ± 0.03	Fe I, Na I, Ca II		1
0832+4109	2.35 ± 0.11	Na I		4
0902+3625	1.92 ± 0.05	Na I		4
0927+4931	2.10 ± 0.09	Mg I		1
1003−0031	4.37 ± 0.05	Mg I, Na I		4
1040+2407	0.35 ± 0.03	Fe I,		
1105+5006	4.13 ± 0.11	Mg I, Na I		1
1106+6737	3.50 ± 0.09	Mg I, Ca I		1,2
1113+2751	3.18 ± 0.09	Mg I		1,2
1143+6615	30 ± 3		a	1,2
1150+4533	2.01 ± 0.20	Mg I, Na I		1
1152+1605	2.72 ± 0.04	Mg I, Na I		4
1214−0234	2.11 ± 0.02	Mg I, Na I, Ca I		5
1249+6514	2.15 ± 0.05	Mg I		1
1330+3029	0.58 ± 0.02	Fe I, Na I, Ca II		6
1336+3547	0.32 ± 0.04	Fe I		
1345+1153	0.25 ± 0.03	Fe I		
1347+1415	0.51 ± 0.04	Fe I		
1412+2836	1.99 ± 0.10	Na I		1
1536+4205	9.59 ± 0.04	Mg I, Na I		4,7
1546+3009	0.85 ± 0.02	Fe I		1
1616+3303	0.40 ± 0.02	Fe I, Ca II		
1649+2238	0.44 ± 0.04	Fe I, Ca II		
1651+4249	3.12 ± 0.28	Mg I, Na I	b	1
2254+3031	2.53 ± 0.03	Mg I, Na I		1,2
2325+0448	6.56 ± 0.09	Mg I		4
2330+2956	3.40 ± 0.04	Mg I, Na I		1,2

References: (1) Hollands et al. (2017), (2) Kepler et al. (2016), (3) Schmidt et al. (2003), (4) Hollands et al. (2015), (5) Reid et al. (2001), (6) Dufour et al. (2006), (7) Kepler et al. (2015).

Notes: (a) Mg I and Na I lines are seen but splitting is not apparent. Rather they show quadratic Zeeman shifts of a few 1000 $\mathrm{km\,s^{-1}}$, indicating a very high surface field. (b) Lines are broadened rather than completely split, however the SDSS subspectra suggest this white dwarf has a roughly 0.5 hr rotation period leading to smeared Zeeman lines in the coadded spectrum.

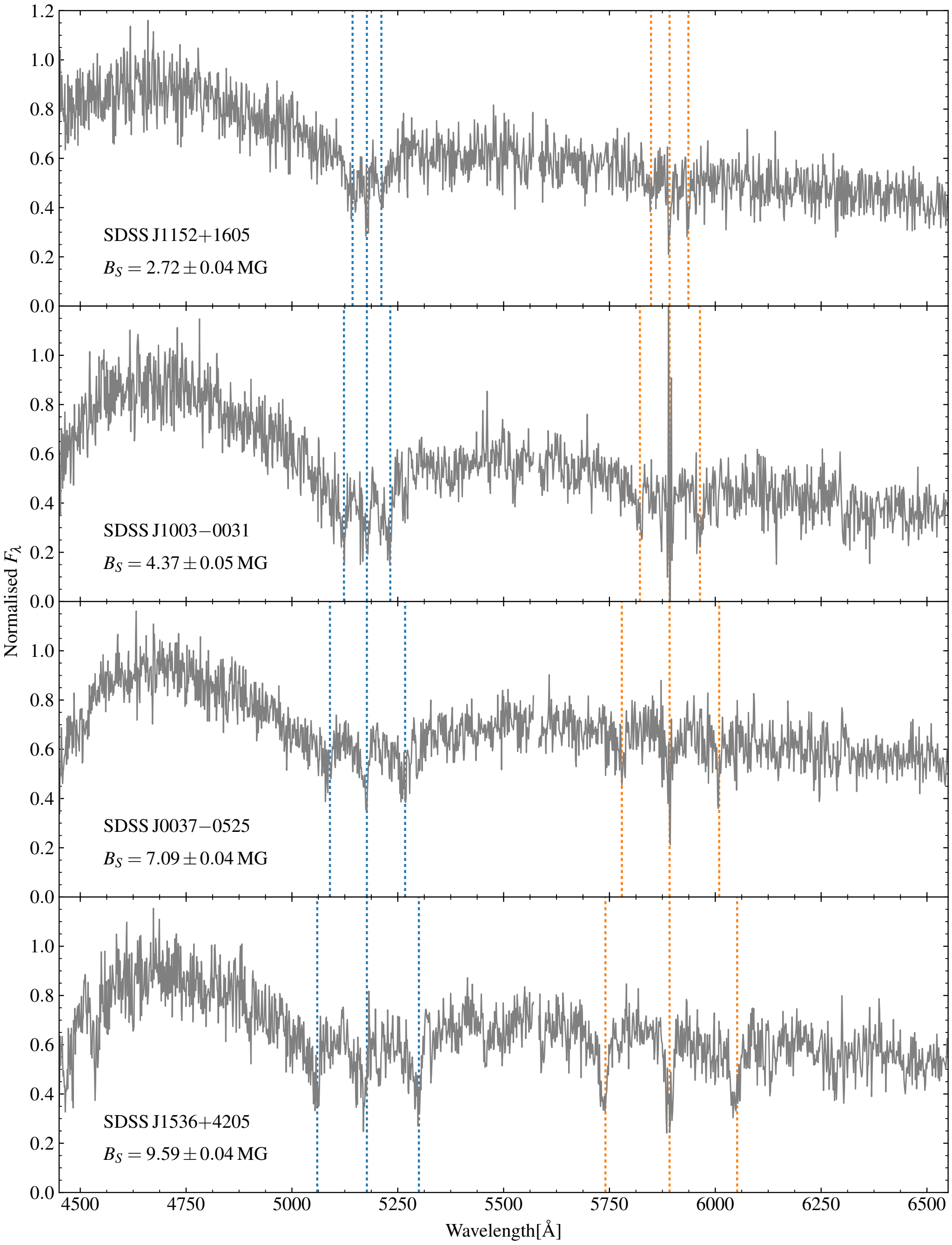

Figure 6.1: All four DZHs shown here have $B_{\mathrm{S}} > 1\,\mathrm{MG}$ and thus Mg and Na lines are observed as simple Zeeman triplets. The Paschen-Back effect causes equal splitting in wavenumber/energy for all elements, and thus in terms wavelength the degree of splitting for Na is $\simeq 30\,\%$ larger than for Mg.

generally increasing with field strength, suggesting this is predominantly caused by the quadratic Zeeman effect, with only minor contributions from gravitational and Doppler shifts. The maximum blueshift of the π-component is found to be 5 Å for the Na triplet of SDSS J1536+4205. The small (few percent) measurement error this may have on our field measurements does not affect our discussion on magnetic incidence.

We used least-squares minimisation via the Levenberg-Marquardt algorithm to optimise these parameters. Where possible we fitted both the Mg and Na lines, however, this could not always be achieved for a variety of reasons: One of the lines may be significantly less deep than the other; the Mg line in some cases is very broad and asymmetric, such that the 3 components cannot be distinguished; or poor subtraction of sky emission distorts the flux near the π component of the Na triplet, making a fit to this line less reliable than for the Mg triplet.

The average surface magnetic field strength, B_{S}, was subsequently calculated from

$$B_{\mathrm{S}}/\mathrm{MG} = \frac{\Delta(1/\lambda)}{46.686}, \tag{6.1}$$

where $\Delta(1/\lambda)$ is the inverse wavelength separation in cm^{-1} between the components of a triplet (Reid et al., 2001). As an example, the fit to SDSS J1536+4205 is shown in Fig. 6.2 with a measured field strength of $B_{\mathrm{S}} = 9.59 \pm 0.04\,\mathrm{MG}$.

6.1.2 Low fields

As described in Section 1.6, for sufficiently low magnetic fields where spin-orbit angular momenta remain coupled, the Zeeman splitting pattern can be much more complex than the simple Zeeman triplets observed in the Paschen-Back regime.

We initially began to explore this low field regime in more depth when confronted with the magnetic DZ white dwarf SDSS J0806+4058. Naively assuming Paschen-Back Zeeman splitting, the Na-D line indicated a field of 0.78 ± 0.05 MG, yet a clearly split Fe I line at 4384 Å suggested an average field strength of 1.01 ± 0.04 MG (under the assumption of normal Zeeman splitting).

Our initial hypothesis was that these metals could be non-uniformly distributed on the stellar surface. For instance, if Na accreted as a neutral gas, the accretion geometry would be unaffected by the magnetic field. If Fe were in its ionised form, it would accrete onto the magnetic poles and so the absorption lines would preferentially sample the higher fields at those locations. This argument suffered from two major flaws. Firstly, the ionisation potential of Na is much lower

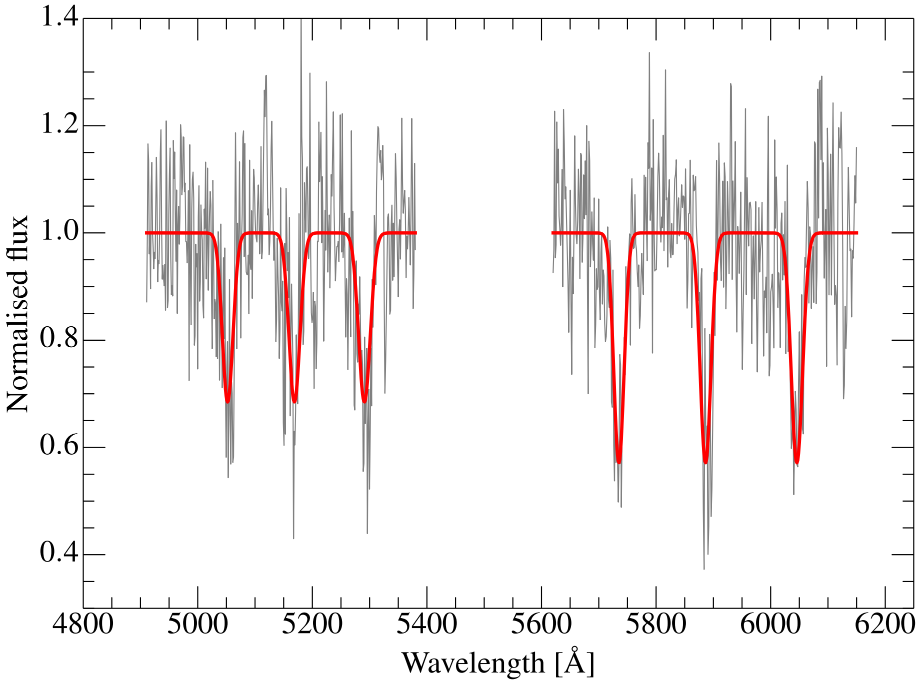

Figure 6.2: Fits to the Mg and Na splittings for SDSS J1536+4205. Transitions are fit with three Gaussians with equal $1/\lambda$ separations from the central π components.

than for Fe, and so would more readily be accreted as ions. Secondly, if the white dwarf is presumed to be convective (which the observation of surface metals suggests to be the case), then convection would rapidly redistribute metals across the entire stellar surface, on timescales far shorter than the sinking timescales for the metals.

This conundrum was readily solved upon realisation that the spin and orbit angular momenta remained coupled for the energy levels associated with the observed Fe transitions. For the Na transitions, the corresponding energy levels had already transitioned to the Paschen-Back regime. We therefore developed a model suited to measuring magnetism from transitions in the low-field regime, which we describe below.

Firstly, we defined the characteristics of an energy level as consisting of four quantities, the rest energy, $k0$ (in cm^{-1} as is conventional in spectroscopy), and the three angular momentum quantum numbers J, L, and S. From this the Lande-g factor could be calculated according to

$$g_J = 1 + \frac{J(J+1) + S(S+1) - L(L+1)}{2J(J+1)}. \tag{6.2}$$

Recall from Section 1.6 that in this regime the level consists of $2J + 1$ degenerate states, each with quantum number m_J running from $-J$ to J in integer steps. Upon application of a small magnetic field, the degeneracy of these states is lifted, shifting their energies to

$$k = k_0 + 46.686\, g_J\, m_J\, B. \tag{6.3}$$

Because of the spin-orbit effect for transitions where this approach is necessary, transitions do not occur between only two levels, but sets of both upper and lower levels with J running from $|L - S|$ and $L + S$ in integer steps. Thus, transitions then occur between a set of lower levels and a set of upper levels. For the Fe multiplet of interest in the spectrum of SDSS J0806+4058, its lower levels have quantum numbers $L = 3$, $S = 1$, and thus $J = 2, 3, 4$, with $L = 4$, $S = 2$, and $J = 2, \ldots, 6$ for the upper levels. Considering all the possible combinations of m_J, there are then 21 lower states and 45 upper states (from the three lower and five upper levels). Electric dipole transitions then occur between lower and upper states according to the selection rules $\Delta J = 0, \pm 1$ and $\Delta m_J = 0, \pm 1$. Note that the first rule prohibits any transition between the lower states and the states in the $J = 6$ level. With the k_0, J, L, and S information for all relevant levels as well as the selection rules in hand, it is then not too much effort to determine which transitions occur and what wavelengths.

To generate model spectra we simply construct a sum of Voigt-profiles at the location of each line. The strengths of the lines are weighted by their gf values, multiplied by an arbitrary scaling parameter, and divided by the number of lines contributing to each zero-field transition. We then take the negative exponential to produce the absorption spectrum with a continuum of 1. This can the be multiplied by a polynomial to scale the model spectrum to data. The free parameters in this model are the line strength scaling parameter, Lorentzian line width,[1] field strength, redshift, and any polynomial coefficients used to rescale the continuum.

An example of this model is shown in Fig. 6.3 demonstrating that the 4400 Å Fe I line appears as a normal Zeeman triplet due to the low resolution of typical data, but in fact additional fine-structure splitting is also seen when this model is calculated for very narrow line profiles. Fitting this model to SDSS J0806+4058 revealed a magnetic field of 0.82 ± 0.03 MG – within 1-σ agreement of the field measured from the Na line. The fit to the data is shown in Fig. 6.4.

The success of this model in explaining the field measurement discrepancy of SDSS J0806+4058 motivated investigation of other DZ white dwarfs and applying the models to other transitions. In the range $B \lesssim 1$ MG, other transitions of interest include the infrared Ca II triplet and the Fe I $^5F \leftrightarrow {}^5D$ around 5300 Å. In principle, the low field approximation remains valid for the Ca H+K lines up to about 1.5 MG, however these lines are usually saturated in cool DZ spectra, and at this field strength, other lines (such as Na) can be much more easily used to detect and measure a magnetic field.

We then sought to search through our sample for any other DZ white dwarfs with weak fields that we may have previously missed. In total we identified seven additional magnetic objects, and for three previously known low-field systems we were able to determine improved field measurements. The results are listed in Table 6.2, with the corresponding fits displayed in Fig. 6.5.

It is clear from Fig. 6.5 that the Fe I multiplet near 5300 Å is the most sensitive transition for detecting weak magnetic fields. This is in part due to the high g-factors associated with these transitions, allowing better sensitivity at the same spectral resolution compared with lines in the Paschen-Back regime where $g = 1$. This is best demonstrated by SDSS J1345+1153, which to our knowledge has the lowest detected field for any white dwarf using SDSS spectroscopy. Despite the low signal-to-noise of the spectrum, it is clear from both the figure and the small, 0.03 MG error in Table 6.2, that the data is inconsistent with a non-magnetic object. It could be argued that rotation would also produce a similarly good fit, however we

---

[1] We fix the Gaussian component of the Voigt profile to the instrumental resolution of the data.

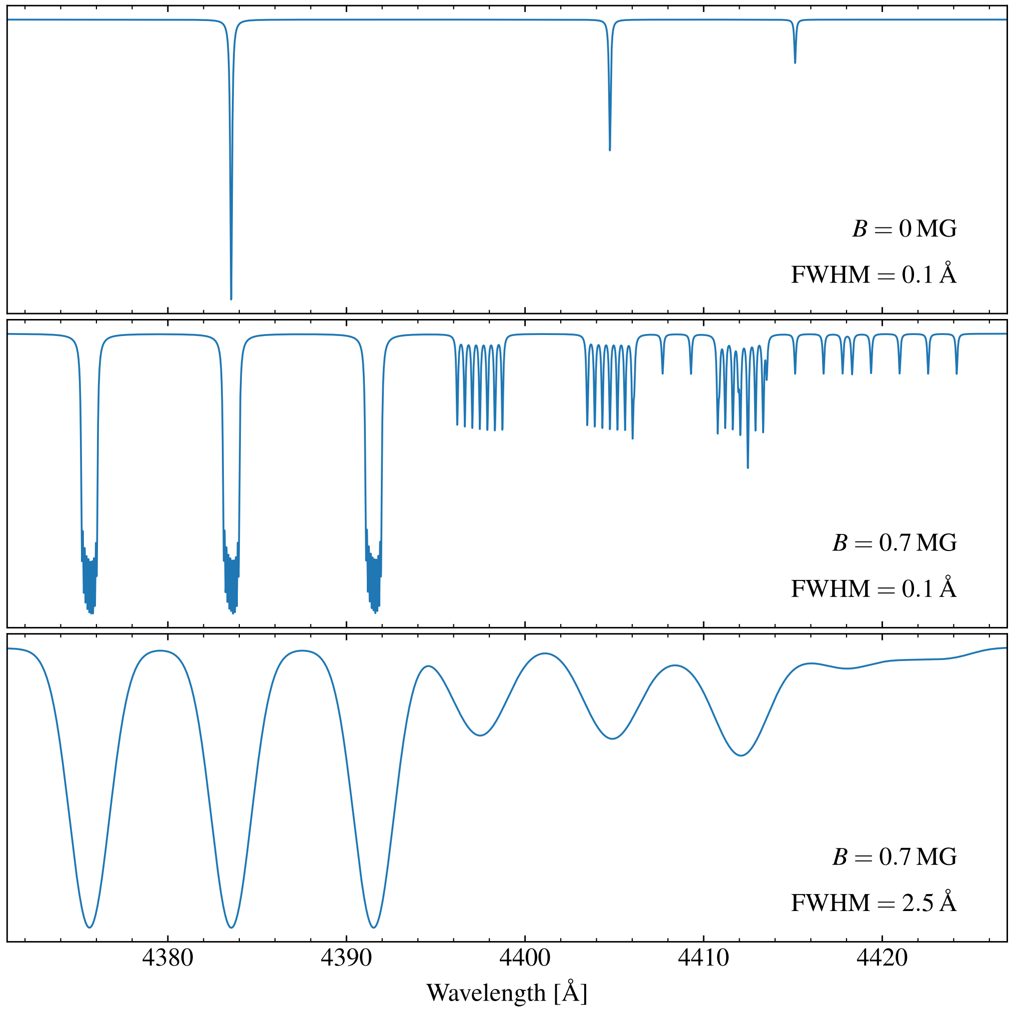

Figure 6.3: Magnetic model applied to the Fe I $^3F \leftrightarrow {}^5G$ multiplet. The top and middle rows show the multiplet computed at high resolution with applied field strengths of 0 and 0.7 MG respectively. The bottom panel is also calculated with $B = 0.7$ MG but convolved to the resolution typical of SDSS spectra. In the middle panel it is clear that the spin-orbit effect results in a large number of transitions, but the lower resolution of the spectra used in this work (bottom panel) completely washes out the fine structure, and so only triplets are apparent. Because of the variety of line-broadening mechanisms present in cool helium atmospheres, even high resolution spectra are unlikely to reveal the fine structure in DZs.

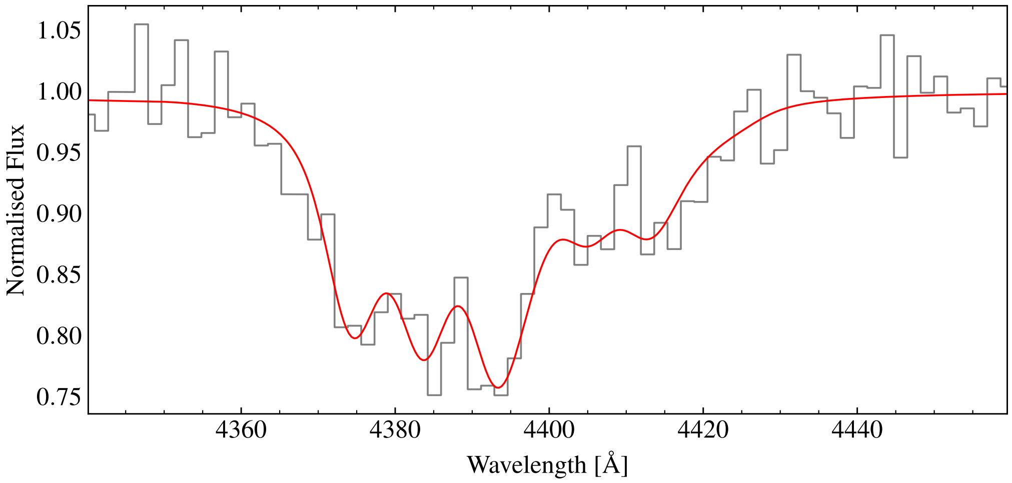

Figure 6.4: Low field model fitted to the WHT data of SDSS J0806+4058. At the 4 Å resolution of our WHT spectrum, the fine structure of the Zeeman splitting is not detected. However the large g-factors associated with the lines resolve the discrepancy when compared with the field measurement from the Na-D line.

Table 6.2: Magnetic fields below 1 MG as measured from three different multiplets. Errors are the 1-σ errors determined from the covariance matrices of the fits.

	B_S [MG]		
J2000	Fe I (4400 Å)	Fe I (5300 Å)	Ca II (8500 Å)
0741+3146	0.49 ± 0.05	0.47 ± 0.07	-
0806+4058	0.82 ± 0.03	-	0.78 ± 0.03
1040+2407	-	0.35 ± 0.03	-
1330+3029	0.57 ± 0.02	0.52 ± 0.01	0.59 ± 0.01
1336+3547	0.35 ± 0.04	0.28 ± 0.06	-
1345+1153	-	0.25 ± 0.03	-
1347+1415	0.56 ± 0.04	0.46 ± 0.05	-
1546+3009	0.87 ± 0.02	0.75 ± 0.04	-
1616+3303	0.41 ± 0.02	0.37 ± 0.02	0.42 ± 0.03
1649+2238	-	0.44 ± 0.04	0.42 ± 0.13

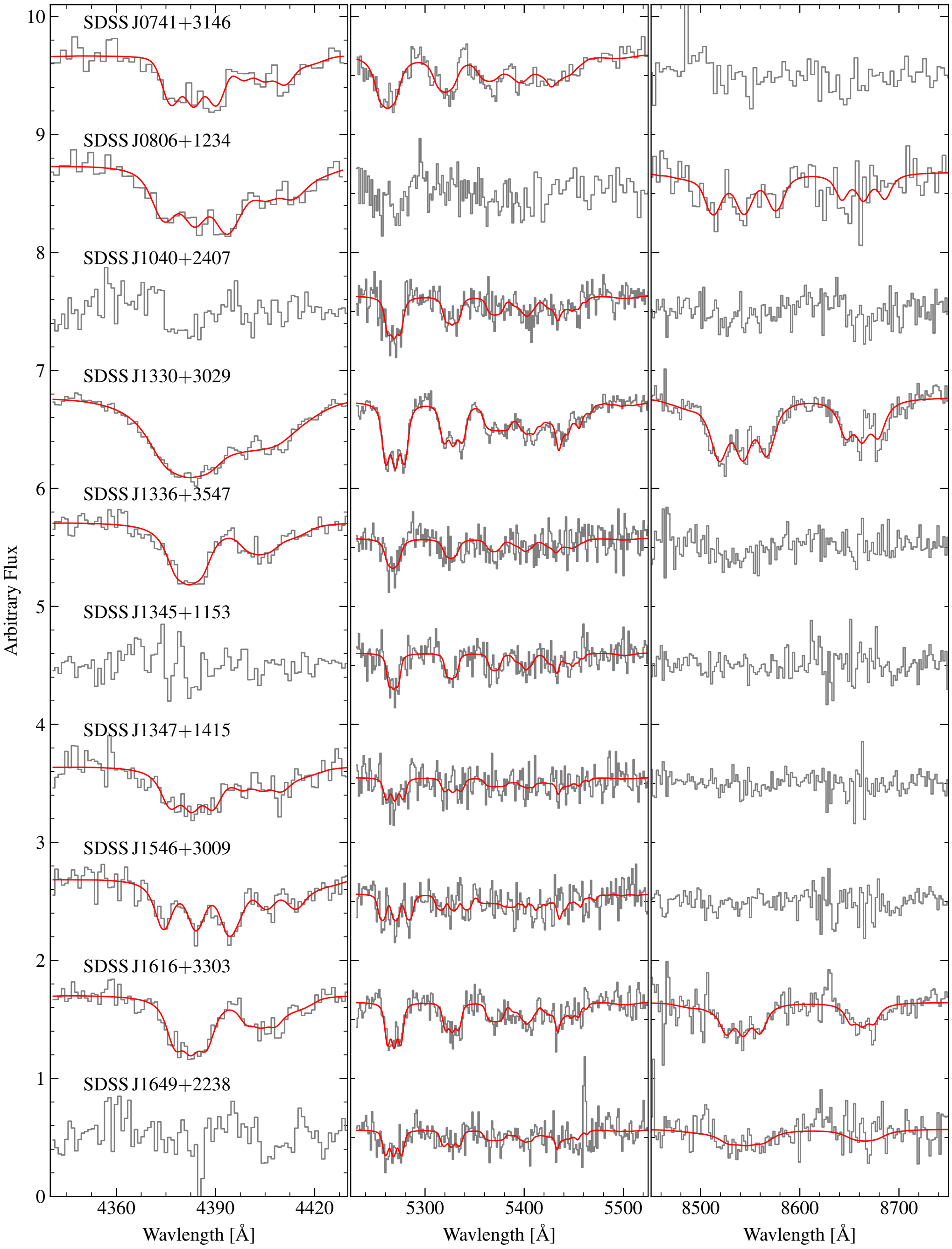

Figure 6.5: Low field Zeeman splitting of Fe lines (left) and the Ca triplet (right), with their best fitting models shown by the red curves. The flux scaling was chosen on a per spectrum basis as the depth of the lines vary significantly.

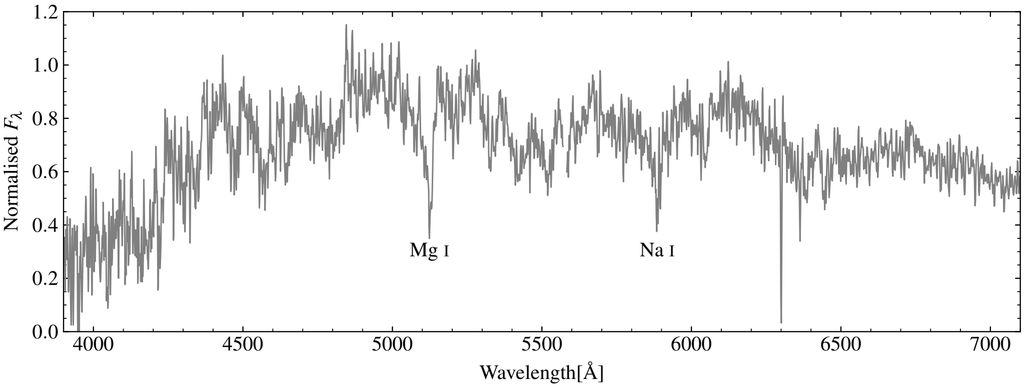

Figure 6.6: The SDSS spectrum of SDSS J1143+6615 is almost unrecognisable compared with the other DZs in our sample. The only lines we were able to identify were of Mg and Na. All other spectral features are unknown in origin.

estimate from the data that a $v \sin i$ of approximately 350 km s^{-1} would be needed to provide the necessary rotational broadening. For a 0.013 $R_\odot$ white dwarf observed edge on, this would imply an extremely short rotation period of only a few minutes. Since rotation periods are usually in the region of a few hours to a few days, a weak magnetic field seems like a far more plausible explanation for the broad Fe lines of SDSS J1345+1153.

For SDSS J1330+3029, where the data quality is very high, some departure of the model is seen around 5400 Å. This is because at field strengths of > 0.4 MG, Zeeman splitting of the states from the upper levels of the red-most transitions in the multiplet become close together. While our model presumes that these states continue to linearly change in energy with increasing magnetic field strength, in reality mixing of states from other levels occurs, as spin and orbital angular momentum decouple, and the Fe atoms enter the Paschen-Back regime.

A second limitation of this basic model is seen, again for SDSS J1330+3029, but in the 4400 Å Fe I multiplet. Because of the very broad line wings, the line cores are not resolved in our model as they are in the data. This fit could be improved using a 2-component model, where each line is now represented by two Lorentzian profiles of different width and depth. The poor fit may also be exacerbated by assuming only a single field-strength, neglecting the variable field geometry over the surface of the star.

6.1.3 SDSS J1143+6615

We first identified SDSS J1143+6615 as a peculiar white dwarf from SDSS DR12. Its spectrum is unlike any other known stellar object (Fig. 6.6), but appears to be a cool object with its flux peaking around 5000 Å. Additionally its reduced proper-motion is comparable to other cool white dwarfs. Furthermore, the unmistakeable asymmetric Mg-b line is detected, as is the Na-D line, and thus we concluded this star must be some kind of unusual DZ.

In addition to Mg and Na, multiple broad absorption features are seen across Fig. 6.6. We give some speculation to their origin at the end of this section. Features near 4600 Å and 5400 Å appear similar to Zeeman triplets which led Kepler et al. (2016) to classify this object as a peculiar DZH with $B_{\mathrm{S}} \simeq 6\,\mathrm{MG}$. We agree that this star is indeed a peculiar DZH, although we have reason to believe the magnetic field is substantially higher.

Firstly, we identified several DZHs with field strengths that are comparable or even larger in magnitude, all of which were recognised with ease. Secondly, of the DZHs with field strengths of a few MG, Zeeman splitting is only found for the Mg and Na lines, yet both of these transitions are present for SDSS J1143+6615, but without the σ-components expected for Zeeman splitting. The final, and most important clue for a large field comes from wavelengths of the Mg and Na features which on close inspection are found to be highly blueshifted.

For the Mg line, the blueshift is found to be about 48 Å ($2800\,\mathrm{km\,s^{-1}}$), and 8 Å ($400\,\mathrm{km\,s^{-1}}$) for the Na line. The conflicting measurements indicate that stellar motion can not be the cause of the line shifts (moreover $2800\,\mathrm{km\,s^{-1}}$ is faster than any known Milky Way stellar object, Geier et al. 2015). Recall from Section 6.1.1 that field strength dependent blueshifts were also measured for the Mg I lines of other DZHs, and was postulated to arise from the quadratic Zeeman effect.

To estimate the field of SDSS J1143+6615 we assumed its Mg line is the π-component of a Zeeman triplet (where the σ components are severely broadened, and thus not seen). From Section 6.1.1 we had measured the field strengths and central wavelengths of other DZHs with Zeeman split Mg lines. In Fig. 6.7 (top) we show the corresponding central wavenumber versus the measured field strength. For the wavenumber uncertainties we add in quadrature contributions of $50\,\mathrm{km\,s^{-1}}$radial velocity and $20\,\mathrm{km\,s^{-1}}$gravitational redshift as systematic errors. We then fitted the data with a parabola centred on $B = 0$ (only the intercept and B^2 coefficient as free parameters). The best fit is shown by the red line, and the 1σ and 2σ errors on the fit shown by the grey regions. The Mg line of SDSS J1143+6615 is itself quite broad, and so we constrain it to a wavenumber of $19502 \pm 18\,\mathrm{cm^{-1}}$. Extrapolating

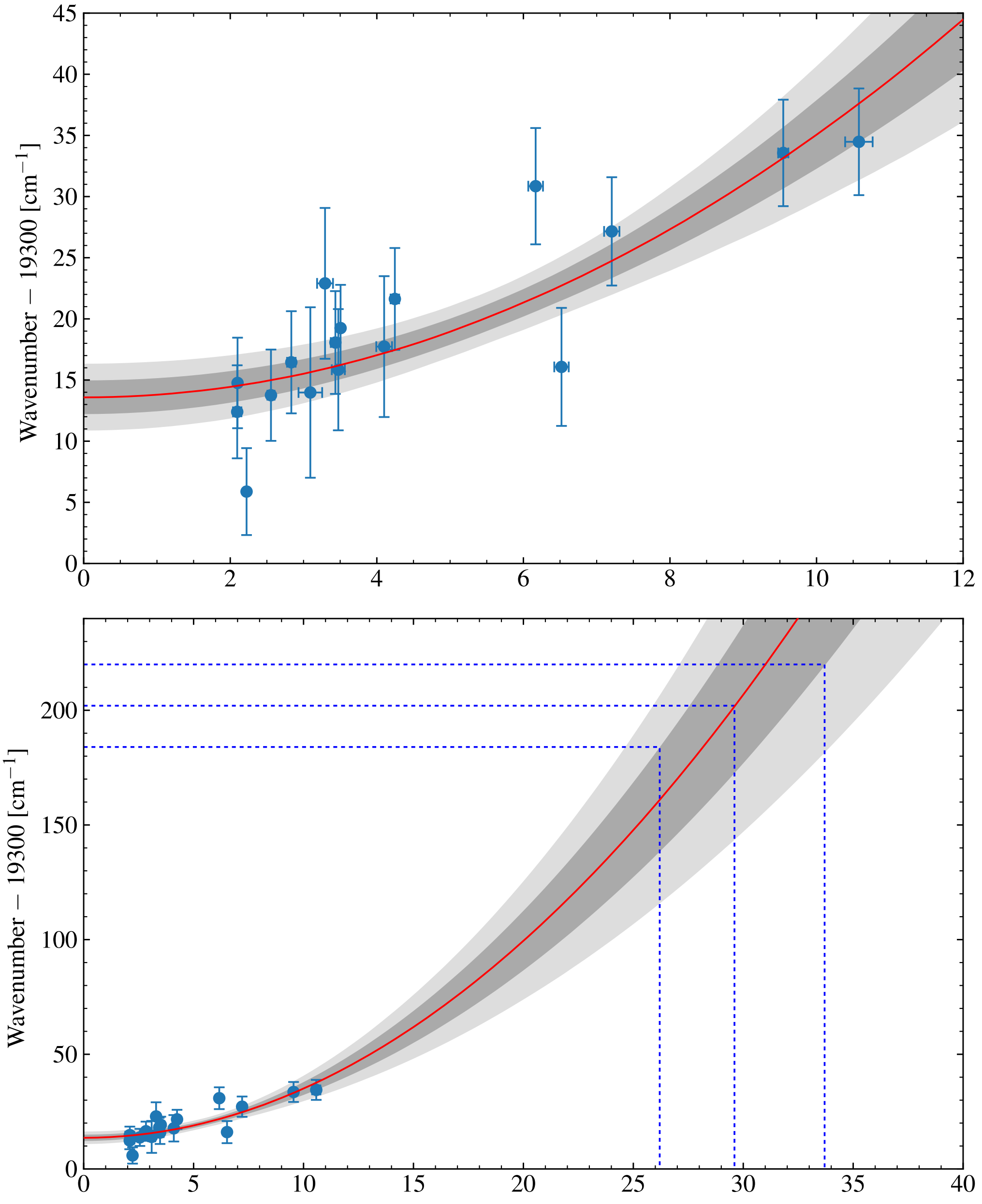

Figure 6.7: (Top): The central position of the Mg line was fitted for all DZH in the Paschen-Back regime. Wavenumber is found to generally increase with magnetic field strength, which we fit with a parabola centred on $B = 0$. The 1σ and 2σ errors on the fit are shown by the grey regions. (Bottom): Interpreting the Mg-line of SDSS J1143+6615 as a blueshifted Zeeman π-component is consistent with a 30 ± 4 MG field.

the quadratic fit (Fig. 6.7) to this wavenumber, we infer a field of 30 ± 4 MG for SDSS J1143+6615.

If this interpretation is correct, then we can estimate the locations of the σ-components for both Mg and Na. For Mg, the σ-components are expected at 4780 ± 40 Å and 5520 ± 60Å. For Na the corresponding locations are 5440 ± 60 Å and 6420 ± 80 Å. In all four cases, otherwise unexplained absorption features are present at these locations in Fig. 6.6, suggesting our estimate of 30 ± 4 MG is correct. This may also imply one or more of the broad features near 4500 Å is the σ^+ component to the 4227 Å Ca I line, where the π-component is tenuously present in Fig 6.6.

6.1.4 Cumulative field distribution

Having measured average surface fields for all 33 magnetic objects in our sample (Table 6.1/6.2), we show their cumulative distribution in Fig. 6.8. Below 0.25 MG no further magnetic objects were found, which is enforced by the 2.5 Å resolution of SDSS. Beyond about 10 MG the distribution flattens out as only SDSS J1143+6615 is found. Broadly speaking, for $0.25 < B_{\mathrm{S}} < 10$ MG the cumulative distribution is seen to be linear in the logarithm of B_{S}, consistent with the distribution seen in other white dwarf samples (Kawka et al., 2007). A minor deviation from linear is apparent between 1 and 2 MG. This is almost certainly due to the challenge of identifying magnetism within this range. For fields $\gtrsim 1$ MG the Fe and Ca lines used to detect low fields in Section 6.1.2 begin to transition to the Paschen-Back regime, where we then no longer detect their presence (in any of the systems with $B_{\mathrm{S}} > 2$ MG). For the Mg and Na lines used to detect higher fields in Section 6.1.1, their intrinsic widths prohibit detection of Zeeman splitting for $B_{\mathrm{S}} \lesssim 2$ MG. It is therefore possible that some DZs in our sample have fields in this range which have evaded detection.

6.2 Magnetic field topology

For a magnetic white dwarf with the simplest possible field structure, a centred magnetic dipole, the magnetic field across the star varies with magnetic latitude, resulting in a field twice as strong at the poles compared to the magnetic equator (Achilleos et al., 1992). A spectrum taken of a magnetic white dwarf integrates over its entire visible hemisphere, and therefore over the range in field strengths, resulting in magnetic broadening of the σ components in a given Zeeman triplet. This effect is often observed for magnetic white dwarfs and can be used to constrain the line-of-sight inclination to the magnetic axis to some degree (e.g. Bergeron et al.,

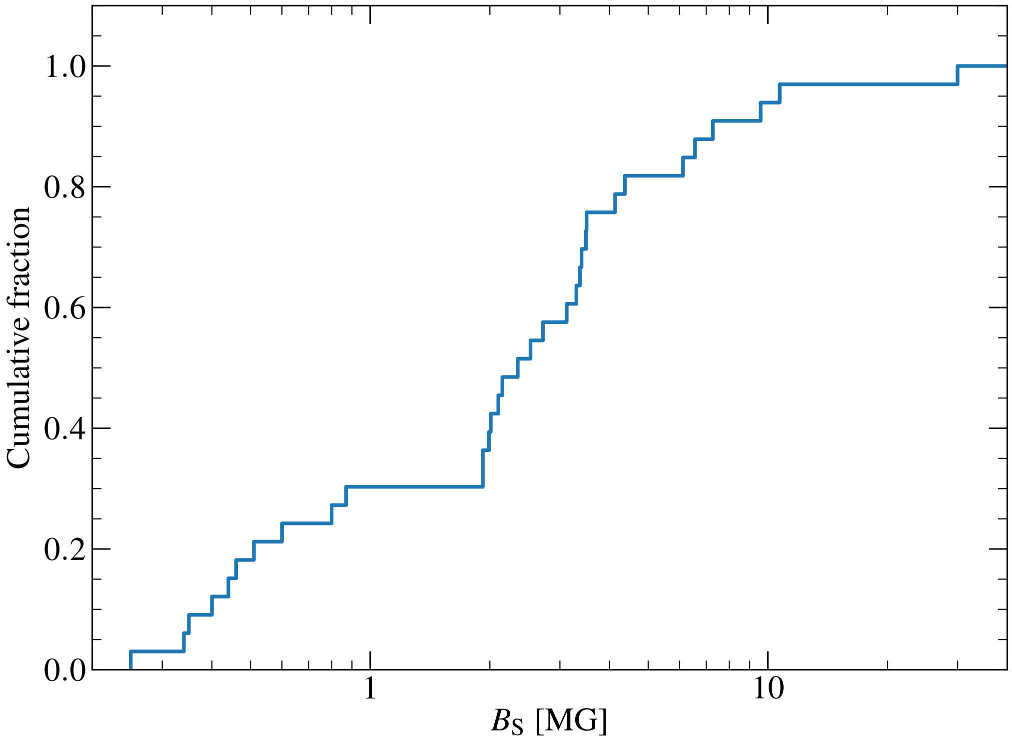

Figure 6.8: Cumulative distribution of surface fields from our sample. The increase is seen to be approximately linear in $log B_\mathrm{S}$ between 0.25 MG and 10 MG.

1992).

In Fig. 6.9 we show Zeeman profiles for Na which we have calculated with a polar field (B_d) of 10 MG, and viewed from three different inclinations. Fig. 6.1 shows that for many of these objects, no inclination to the magnetic axis can reproduce the data. In particular SDSS J1536+4205 (also Fig. 6.2) shows the three components are similar in width and depth for both Mg and Na.

This suggests that these white dwarfs may have more complex field topologies. We show that a dipole offset from the star's centre can reproduce the observed Zeeman line profiles, at the cost of only one additional free parameter. In principle this offset, a, can be in any direction relative to the unshifted magnetic field axis (Achilleos & Wickramasinghe, 1989), however, here we consider only displacement along the magnetic dipole axis (which we define to be in the z-direction), i.e. $a_x = a_y = 0$ as in Achilleos et al. (1992).

For an arbitrary point on the surface of the white dwarf with coordinates (x, y, z) in units of R_{wd}, the strength of the field, $B(x, y, z)$, is given by (Achilleos et al., 1992)

$$B(x,y,z) = B_d \left[r^2 + 3(z - a_z)^2\right]^{1/2} / 2r^4, \tag{6.4}$$

where a_z is the dipole offset, B_d is the dipolar field strength,[2] and

$$r^2 = x^2 + y^2 + (z - a_z)^2. \tag{6.5}$$

These equations can be used to compute synthetic Zeeman line profiles for given B_d, a_z, and inclination, i.

In our model, we first generated a set of 10^5 points randomly distributed over the visible disc of the star. At each point, the magnetic field strength was evaluated using equation (6.4), accounting for the inclination to the magnetic axis. Additionally we determined limb darkening coefficients appropriate for a 6000 K, $\log g = 8$ white dwarf from Gianninas et al. (2013), adopting the logarithmic limb darkening law described therein. For performance reasons, these 10^5 points were then histogramed into 100 field strength bins (weighted by limb darkening factors). For each bin, Zeeman-split line profiles were generated according to

$$\exp\left(-A\left[L_- + L_0 + L_+\right]\right) \tag{6.6}$$

---

[2] B_d is defined in such a way that the magnetic field has this strength at $z = a_z \pm 1$ white dwarf radii along the magnetic axis.

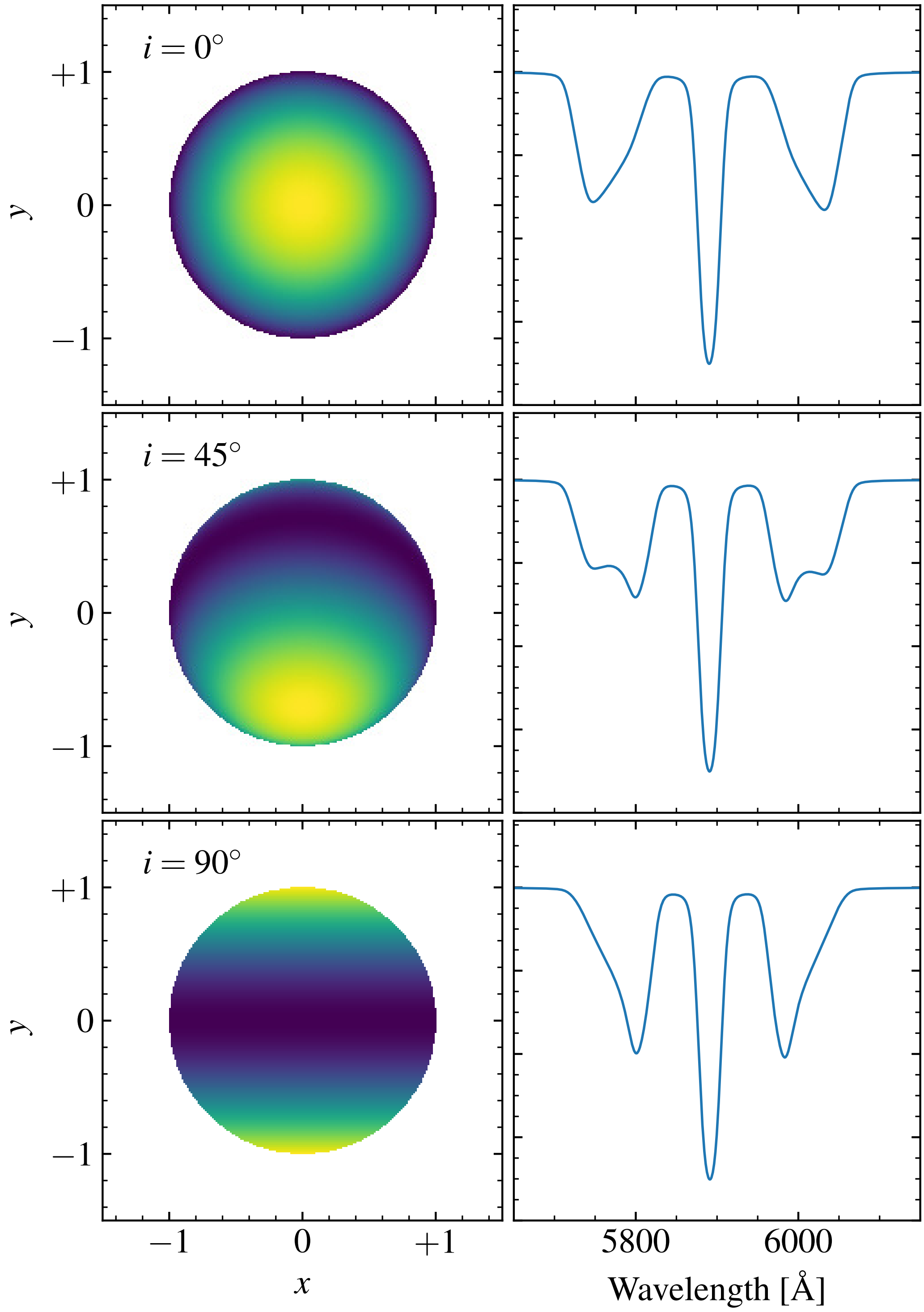

Figure 6.9: Centred dipole magnetic field geometries observed from different inclinations between the line-of-sight and magnetic axis affect the Zeeman splitting profile. Here we show the effect of observing Na from three different inclinations with a 10 MG polar field.

where the L are unit height Lorentzian profiles for each Zeeman component, and A is a free parameter for the line intensity. The Lorentzian width was also left as a free (nuisance) parameter. We then computed a weighted average of these 100 spectra with weights from the field strength histogram. Finally the spectrum was convolved with a Gaussian to the spectral resolution of the data, and multiplied by a second-order polynomial to account for the continuum.

We fitted the above model to the Zeeman lines in SDSS J1536+4205 using the affine invariant MCMC sampler, EMCEE. Replacing B_S from before with B_d and including the inclination and dipole offset, increased the number of free parameters in the fit (compared with Section 6.1.1) to nine. For this case, the three parameters of interest, B_d, i and a_z, can all be assigned well-reasoned priors. For surface fields in the range 10^3–10^9 G the distribution of their strengths is found to be uniform in its logarithm (Kawka et al., 2007). Thus for the $\sim 10^7$ G field of SDSS J1536+4205, we are justified in using this distribution as a prior. Since B_d (rather than $\log(B_d)$ is our free parameter, the corresponding prior is $B_d \propto 1/B_d$.[3] For the inclination i, the prior can be found through a geometric argument. A random point on on a sphere is more likely to be near its equator than the poles, as there is simply more solid angle in this region. It is thus simple to show that the correct prior is $P(i) = \sin(i)$, where $0 \geq i \geq \pi/2$. Some freedom exists in our choice of prior for a_z, but we argue that some restrictions can be made. Firstly the prior must be equal to zero for $|a_z| > 1$. Secondly it must be an even function of a_z. Finally we might expect the prior probability to drop to zero as a_z approaches ± 1. For these reasons we use $P(a_z) \propto 1 - a_z^2$ for $|a_z| < 1$, and 0 elsewhere. Clearly other possibilities satisfy these conditions such as $P(a_z) \propto \cos(\pi a_z/2)$, however we expect the likelihood be bigger constraint on a_z than subtle differences in prior.

Since SDSS J1536+4205 shows distinctly split lines of both Mg and Na, both were fitted independently. The results for B_d, i, and a_z are listed in Table 6.3, with the corresponding fits to the spectra shown in Fig. 6.10. While the line profiles appear similar to the simple model shown in Fig. 6.2, it should be recalled that we have now fitted a physical model capable of reproducing the observed narrow Zeeman lines rather than the assumption of unbroadened lines used in Section 6.1.1.

The fit to the Mg triplet has a slightly worse reduced χ^2 than that of the Na triplet. This is the result of the Mg I line having an intrinsically asymmetric profile as described in Section 3.3.1. Therefore the use of symmetric profiles limits the quality of our fit. Nevertheless, the resulting parameters from the Mg and Na

---

[3] Note that the prior on B_d is an improper prior as its integral over all finite values diverges. In reality, the true distribution must to drop to zero at both extremes of $\log(B)$. As none of the objects in this work are found at such extremes, we are justified in using this improper prior.

Table 6.3: Results from our MCMC fits to SDSS J1536+4205 assuming an offset dipole field structure. Quoted values and uncertainties are, respectively, the 50th, 15.9/84.1th percentiles of the posterior probability distributions. Reduced χ^2 values are calculated using the median for each parameter. Note that the prior on inclination, i is in radians.

Parameter	Prior	Mg	Na
B_d [MG]	$\propto 1/B_d$	$18.3^{+2.3}_{-0.8}$	$19.6^{+1.7}_{-1.3}$
i [deg]	$\propto \sin(i)$	31 ± 14	35^{+17}_{-14}
a_z [$R_{\rm wd}$]	$\propto 1 - a_z^2$	$-22.8^{+3.0}_{-7.7}$	$-27.4^{+4.9}_{-5.1}$
$\chi^2_{\rm red}$		1.26	1.05

fits are in agreement within their (similarly large) uncertainties. The values of a_z we find are well within the range of those found for SDSS DA white dwarfs (Külebi et al., 2009).

While the inclination uncertainties permit a wide range of values within the allowed parameter space (0–90 °), the results for B_d and a_z strongly suggest an offset dipole. However, it is worth noting that corner plots for these parameters (Fig. 6.11 shown for Na) indicate there are two viable solutions for both B_d and a_z, which together are seen to be strongly anti-correlated. The main solution is centred on $B_d \simeq 18.3$ MG and $a_z \simeq -0.23$, with the second solution at $B_d \simeq 21.0$ MG and $a_z \simeq -0.31$. The posterior distribution of Mg also shows both solutions but weighted more strongly to the 18.3 MG solution (as also shown by Table 6.3). We will show in Section 6.7.1, that former solution is indeed the correct one.

Regardless of which mode is used, the fit values of B_d, i, and a_z indicate SDSS J1536+4205 has a dipole offset away from the Earth with an almost uniform field of $\simeq 9.59$ MG on the visible hemisphere resulting in sharp σ-components of the Zeeman triplets. It follows from this model that the opposite, invisible hemisphere of the star exhibits a large gradient in field strengths with a strongly magnetic spot ($\simeq$ 50 MG) emerging at the pole. Since only a small amount of the higher field hemisphere enters the limb of the star, the σ components of the Zeeman triplets are only slightly broadened with their depths reduced by a few percent. If the sign of a_z was reversed, the strong gradient in the field across the now visible hemisphere would have a major observational consequence. The σ components in the Mg and Na triplets would be magnetically broadened to the extent of reducing their depth to only $\simeq 15$ % of the π component. Therefore, identifying the magnetic nature of the star would require a S/N ratio of at least 40 (for a 3σ detection).

An alternative explanation for narrow Zeeman components is a non-uniform

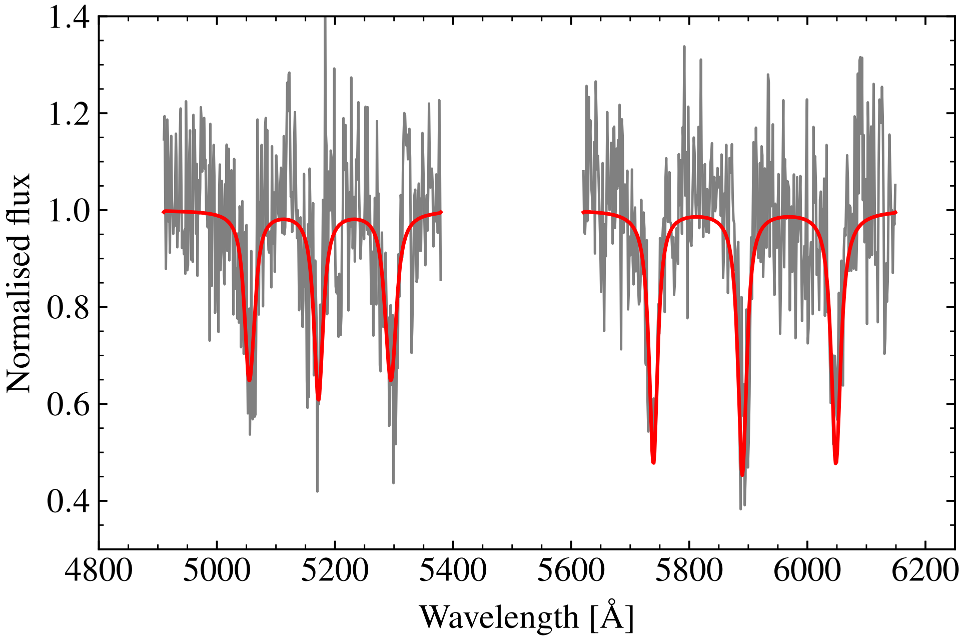

Figure 6.10: Similar to Fig. 6.2, but fitted with an offset dipole model. The adopted values of B_d, i, and a_z are given in Table 6.3, i.e. the two triplets are shown with their individual fits. The σ components are now slightly less deep than the respective π components, as seen in the data.

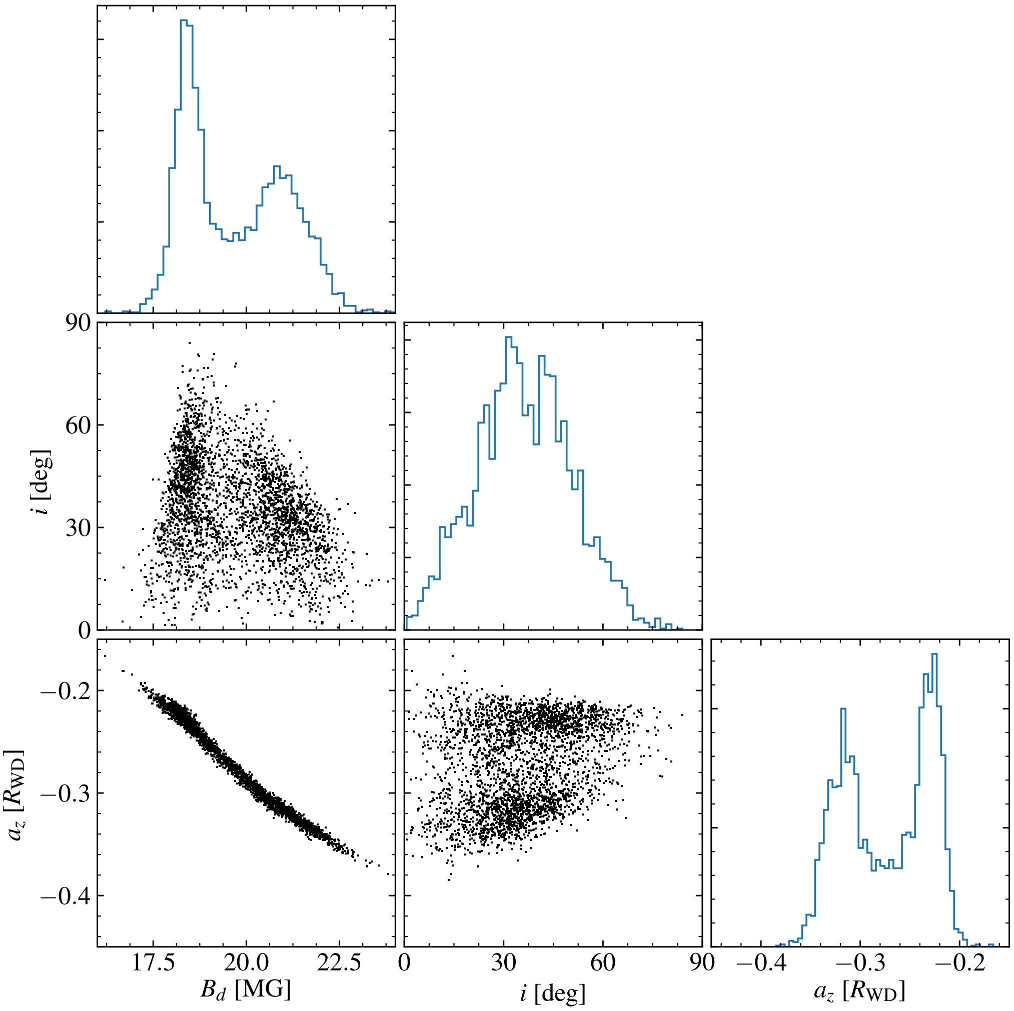

Figure 6.11: Corner plot for the posterior distribution of the fit to Na. The B_d vs. a_z plane shows these two parameters to be highly correlated and with two nearby solutions able to reproduce the data. While the marginalised posterior distribution shows inclination is not so well constrained, values > 70 degrees are effectively ruled out (which a-priori are most likely).

distribution of metals across the surface of the white dwarf. If for instance the accreted material accumulated at the poles, the resulting spectrum would exhibit splitting consistent with only the polar field strength. However, to reproduce the minimal magnetic broadening we observe, the metals would have to be constrained to such a small region that the resulting Zeeman triplets would have negligible depths. Alternatively, metals confined to the magnetic equator would also produce a spectrum showing a small range of field strengths, but would be able cover a much greater portion of the visible surface without significant magnetic broadening. However, equatorial accretion would necessitate at least a quadrapolar field.

Metzger et al. (2012) considered accretion of metals onto a magnetic white dwarf. If the sublimation radius of the white dwarf is smaller than the Alfvén radius (true for our magnetic white dwarf sample), then material is expected to accrete along the magnetic field lines as soon as it enters an ionised state. However, Metzger et al. (2012) also discuss a potential caveat to this scenario. The presence of dust grains mixed within the gaseous disc may inhibit the ionisation of the gas component, and so even a strong magnetic field may have little influence over the accretion flow of rocky debris.

6.3 Magnetic incidence

If we wish to determine the underlying magnetic incidence fraction f for cool white dwarfs, it is sensible to treat our sample (total size N), with M magnetic objects as the result of a binomial process where f is the rate parameter. Thus we may naively choose to calculate the expectation value of f as $E(f) = M/N$, and the variance as $V(f) = f(1-f)/N$, as per binomial statistics.[4] However, we show this common approach is incorrect for two reasons.

Firstly, the value of f will be biased downwards *if* we cannot tell whether some members of the sample are magnetic or not. There this approach only provides a minimum fraction – which has its place as a lower bound – but does not tell the whole story. If there are U unknown systems then $M/(N-U)$ provides a less biased estimator for f, although with a greater variance.

The second problem is perhaps less obvious, but is apparent in the limit of $M = 0$ or $M = N$. Consider a sample of two white dwarfs ($N = 2$), where neither are magnetic ($M = 0$). Our expectation value for f with the above approach is simply zero. However, when we calculate the variance, we also arrive at zero. Intuitively a

---

[4] For small samples, the N in the denominator of the variance should be replaced by $N-1$ to account for statistical bias.

low, but non-zero incidence, ought to occasionally result in zero out of two magnetic objects. Thus binomial statistics "taken neat" appears to be inadequate to calculate something as simple as a fraction.

The solution becomes apparent when explicitly writing down the expression for the binomial distribution. In general, the binomial distribution gives the *discrete* probability distribution for a certain number of events k, out of n trials, given a rate parameter r, i.e.

$$P(k|r,n) = \binom{n}{k} r^k (1-r)^{n-k}. \tag{6.7}$$

Ostensibly, what we desire is not $P(k|r,n)$, but rather $P(r|k,n)$, the continuous distribution on r where *both* k and n are fixed. This is resolvable using Bayes theorem given by equation (2.3), and hence

$$P(r|k,n) = \frac{P(k|r,n)\,P(r)}{P(k,n)}. \tag{6.8}$$

$P(k,n)$ is a constant since for fixed k and n, and so equation(6.8) can be written as

$$P(r|k,n) \propto P(r) \times r^k (1-r)^{n-k}. \tag{6.9}$$

Now all that remains is to choose a suitable prior on r. The most tempting choice is simply a uniform distribution between 0 and 1. However, better choices of prior are available. The "conjugate prior" to the binomial distribution is the beta-distribution given by

$$P(x;\alpha,\beta) = \frac{x^{\alpha-1}(1-x)^{\beta-1}}{B(\alpha,\beta)}, \tag{6.10}$$

where α and β are shape parameters, and $B(\alpha,\beta)$ is a normalisation term. For $\alpha = \beta = 1$, this reduces to the uniform distribution, however in the field of Bayesian inference, a more common choice is Jeffrey's prior. Jeffrey's priors have the property that they are invariant under reparametrisations of x (Koch, 2007), and for the beta distribution, simply amounts to $\alpha = \beta = 1/2$. Thus with

$$P(r) \propto r^{-1/2}(1-r)^{-1/2}, \tag{6.11}$$

we arrive at

$$P(r|k,n) \propto r^{k-1/2}(1-r)^{n-k-1/2}, \tag{6.12}$$

which is itself a beta distribution with $\alpha = k+1/2$ and $\beta = n-k+1/2$. In calculating magnetic incidence we simply make the substitutions $r \to f$, $k \to M$, and $n \to N$. From our earlier example of $N = 2$ and $M = 0$, we arrive at a distribution that peaks at $f = 0$, has zero probability density at $f = 1$, and is finite at all intermediate values. For such small number statistics, the distribution is one-sided and so, rather than a mean and uncertainty on f, we can claim a 95 % upper limit of 0.57.

In our sample of 231 cool DZs, we identify 33 of these to be magnetic above 0.2 MG (Table 6.1). Applying equation (6.12) leads to an *observed* incidence of 14.4 ± 2.3 %. Inspecting all of the SDSS spectra carefully, we estimate that for 77 of these objects, their data were not of sufficient quality to assess the presence of a field either way. I.e. while they exhibited a few broad features sufficient for approximate measurements of Ca/Mg/Fe abundances, none of the moderately sharp metal lines we had relied on for detecting magnetic fields were present. Using the remaining 154 systems, we arrive at a less precise, but more accurate magnetic incidence of 21.6 ± 3.3 %. While we believe this estimate is significantly less biased than when including all systems, this is not to say that the reduced sample of 154 objects is free from biases. On the contrary, various selection effects, which we discuss here, suggest that the true magnetic incidence may be higher still.

If the offset dipole model presented in Section 6.2 the correct interpretation for the narrow Zeeman lines of SDSS J1546+4205, this indicates additional bias in our DZ magnetic incidence. As discussed in that section, many of the magnetic white dwarfs in our sample all have Zeeman triplets that could arguably be explained by a dipole offset away from the Earth. If cool magnetic white dwarfs have a tendency for their dipoles to be offset, then statistically this implies that several of the other white dwarfs within our sample should have dipoles offset *towards* the Earth. The σ components of their Zeeman lines would be broadened to the point that they cannot be distinguished at the low S/N of the SDSS spectra, and so they would not been identified as magnetic. Thus, if true, the offset dipole scenario increases the selection bias against identifying magnetic white dwarfs.

6.4 Magnetic field origin and evolution

While the true incidence of magnetism among white dwarfs on the whole is still widely debated, estimates between 5–20 % are common for isolated degenerate objects (Wickramasinghe & Ferrario, 2000; Liebert et al., 2003; Sion et al., 2014). It has been suggested that older (cooler) white dwarfs exhibit a higher incidence of magnetism (Kawka & Vennes, 2014; Liebert et al., 2003), which at face value is supported by the large fraction of cool magnetic white dwarfs in our sample. However, we can at present not exclude that the high incidence of magnetism is linked to the presence of metals in the atmospheres of the cool DZ, e.g. through (merger) interaction with planets.

In addition, the origin of magnetic fields among white dwarfs remains under discussion with the most plausible mechanisms proposed being:

1. From the initial-to-final mass relation (Catalán et al., 2008) and main sequence lifetime as a function of stellar mass, most of the known white dwarfs are thought to have evolved from A and B type stars. These stars are known to exhibit magnetic fields (Angel et al., 1981; Wickramasinghe & Ferrario, 2000; Neiner et al., 2014), with the peculiar Ap and Bp stars having comparatively higher fields. As the star evolves off of the main sequence it is expected that the magnetic flux of the progenitor star is conserved and so the change in stellar radius amplifies the surface field, i.e. $B_{\mathrm{wd}}/B_{\mathrm{ms}} = (R_{\mathrm{ms}}/R_{\mathrm{wd}})^2$. This is known as the fossil field hypothesis, and can produce white dwarfs with field strengths in the observed range (Woltjer, 1964; Angel & Landstreet, 1970; Angel et al., 1981; Wickramasinghe & Ferrario, 2000).

   Ohmic decay is expected to cause magnetic fields to decrease in strength with time. However, the timescale for this is expected to be of the order 10^{10} yr due to the high electrical conductivity in the degenerate cores of white dwarfs (Wendell et al., 1987). Therefore the fossil field hypothesis is not unreasonable for describing the field origin in the old white dwarfs we identify in this work.

   However, recent estimates of magnetic incidence exceeding 10 % (Liebert et al., 2003; Kawka et al., 2007; Sion et al., 2014), challenge the fossil field hypothesis. The space density of Ap/Bp stars is insufficient to account for all the known magnetic white dwarfs with $B_{\mathrm{S}} \gtrsim 1\,\mathrm{MG}$ (Kawka & Vennes, 2004), and so at least one other evolution channel is required for producing magnetic white dwarfs.

2. Tout et al. (2008) suggested that white dwarfs with $B_{\mathrm{S}} > 1\,\mathrm{MG}$ are the products of an initial binary origin. Stellar evolution of one of the binary components can lead to a common envelope (CE) stage. It is during this phase that a magnetic dynamo may be generated within the CE. The resulting field then

persists beyond the lifetime of the CE, within the now close binary or merged single object. For a close binary, a merger may take place later.

The binary origin of these highly magnetised white dwarfs naturally leads to higher masses than the canonical $0.6\,\mathrm{M}_\odot$ for non-magnetic white dwarfs, compatible with the observation that magnetic white dwarfs are typically more massive than non-magnetics (Liebert, 1988; Liebert et al., 2003).

However, a binary origin would in our case raise questions about how these white dwarfs come to be polluted by material from a remnant planetary system. This model need not be constrained only to stellar binaries. Nordhaus et al. (2011) suggested that the engulfment of gaseous planets or brown dwarf companions during the asymptotic giant branch (AGB) phase could also lead to magnetic dynamo generation and eventually a high field magnetic white dwarf. In this scenario, magnetic white dwarfs would not be expected to have higher masses than non-magnetics, but it would allow for evolved planetary systems which later pollute the white dwarf with metals. Farihi et al. (2011a) identified a cool ($T_{\rm eff}$= 5310 k) magnetic ($B \simeq 120\,\mathrm{kG}$) DAZ white dwarf, and speculate on that basis that the white dwarf underwent a CE with a closely orbiting gas giant planet during the progenitor star's AGB phase, leading to the emergence of a magnetic field. If this is indeed the mechanism from which magnetic fields are produced in DZ, it may explain the particularly high magnetic incidence found in our sample.

Unlike the fossil field hypothesis, the giant planet CE scenario would be correlated with the presence of metals in the atmospheres of white dwarfs, where the metal lines are an indicator of an evolved planetary system. Therefore, if DC white dwarfs, which originate from the same stellar population as DZ (Farihi et al., 2010a), have a significantly different distribution of magnetic fields, then this could present a compelling case for the CE hypothesis, although this would depend on the effect of magnetism on diffusion timescales.

3. An alternative origin for magnetism among white dwarfs is $\alpha\omega$ dynamo generation. For a differentially rotating white dwarf with a convective envelope, a magnetic dynamo may be generated at the base of the convection zone (Markiel et al., 1994). However this would be unlikely to produce fields on the order of 1 MG (Thomas et al., 1995), and would lead to magnetic fields strongly aligned with the white dwarf rotation axis which is in general not observed (Latter et al., 1987; Burleigh et al., 1999; Euchner et al., 2005).

4. A last, more recently hypothesis for white dwarf magnetism is dynamo gen-

eration in the cores of giant stars resulting in magnetic objects at the white dwarf stage. Asteroseismology of giant stars with Kepler has revealed that often their cores are highly spun up with respect to the outer layers (Beck et al., 2012; Mosser et al., 2012) due to decoupling of the radiative core and convective envelope (Cantiello et al., 2014). This has led some authors to consider the evolution of the internal magnetic fields of giant branch stars (Fuller et al., 2015; Kissin & Thompson, 2015a,b).

Kissin & Thompson (2015a) investigated the transportortaion of angular-momentum throughout the giant branches and the potential for magnetic dynamo generation within the giant core. They established that angular momentum pumping inwards, could generate a magnetic dynamo at the boundary of the radiative core and convective envelope, as the core is grown (Kissin & Thompson, 2015b), depositing magnetic helicity at its surface which would eventually result in a long-lived magnetic field at the white dwarf stage.

Such a dynamo would only be established if a rotational threshold (Charbonneau, 2014) is reached, which could be aided increase by the engulfment of a giant planet and the subsequent addition of angular momentum (Kissin & Thompson, 2015b). Furthermore, rapid mass loss during the giant-branches can cause this threshold to no longer be met, and thus the dynamo to switch off while the carbon-oxygen core is still growing. Kissin & Thompson (2015b) speculate on the observational consequences this would have for white dwarfs. Firstly, they predict fields reaching up to $\sim 10^7$G which is approximately the upper limit for fields observed in our sample. Additionally, they consider that depending on when during stellar evolution that dynamo activity ceases, the layer of magnetised material can be buried by a layer of non-magnetised matter. This would result in an initially non-magnetic white, where the field emerges on Gyr timescales due to ohmic diffusion, thus providing a mechanism for an age dependence of white dwarf magnetism. Because this field generation mechanism is aided by the engulfment of giant planets, this scenario suggests that white dwarf magnetism could be correlated with the sizes of their planetary systems.

6.5 The apparent lack of magnetism in warm DZs

The largest sample of white dwarfs identified in SDSS was presented by Kleinman et al. (2013), using SDSS DR7 spectroscopy. In total they identified 257 DZ, most of which are hotter than the sample we present here ($T_{\rm eff} > 8000\,$K), in which case Ca H+K are usually the only metal lines detected, such as in the hotter DZ example in Fig. 1.4. Unlike for cool DZs where the broad wings of the H+K lines absorb most of the flux below 4000 Å, for warmer DZs, our model from Section 6.1.2 indicates the H+K lines could allow detection of fields as low as $\gtrsim 0.3\,\mathrm{MG}$ using SDSS spectra. Additionally, because of the larger sample size and higher T_{eff}, there is are an abundance of these spectra where the H+K lines have good S/N ratios. We find 64 spectra with $\mathrm{S/N} > 10$ (25 %), and 27 with $\mathrm{S/N} > 15$ (10 %).

Inspecting the Ca H+K lines of all 257 DZ did not reveal magnetic splitting for a single object. This is in stark contrast to our fraction of $21.6 \pm 3.3\,\%$. One object, SDSS J080131.15+532900.8, has what appear to be broadened Ca H+K lines which could indicate a magnetic field. However the SDSS images reveal this white dwarf to be situated ∼7 arcsec away from a bright ($r = 13.6$) M-type star, which likely caused flux contamination in the DZ spectrum (obtained through a 3 arcsec fibre).

We performed an independent check by inspecting the 118 warm DZ identified from SDSS DR10 by Gentile Fusillo et al. (2015). They selected candidate white dwarfs from a colour-cut in the $(u - g)$ vs. $(g - r)$ plane situated above the main sequence compared to our cut in Fig. 3.5, and making use of proper-motions. All spectroscopic objects with $g < 19$ bounded by this cut were visually inspected and classified into the various white dwarf subclasses. We inspected the H+K lines of all objects classed as DZ for splitting. Again, we did not find a single star that can be convincingly claimed to be magnetic. Since the Gentile Fusillo et al. (2015) sample was only selected by colour and proper-motion, they are not biased against finding magnetic DZ as Kleinman et al. (2013) might be.

Kepler et al. (2015) have published a list of new white dwarfs from SDSS DR10 spectra including 397 objects classified as DZ (where most have $T_{\mathrm{eff}} > 10\,000\,\mathrm{K}$). Inspecting these 397 spectra reveals Kepler et al. (2015) have independently discovered 4 of the white dwarfs that we have shown are magnetic (SDSS J0735+2057, SDSS J0832+4109, SDSS J1003−0031, and SDSS J1536+4205), however, beyond these, we found no further magnetic objects.

The dearth of magnetic white dwarfs with $T_{\mathrm{eff}} > 8000\,\mathrm{K}$ in the above three samples suggests that magnetic incidence strongly increases with white dwarf cooling age, at least for white dwarfs with remnant planetary systems. If this is truly the case, then this places some constraints on the origin of white dwarf magnetic fields. These observations are perhaps most consistent with interior field generation during stellar evolution (Section 6.4, hypothesis 4). Recall that Kissin & Thompson (2015a) found that magnetic fields could form buried below the white dwarf photosphere, only emerging at the surface after ohmic diffusion on Gyr timescales. This hypothesis is therefore consistent with the apparent lack of young DZH. Furthermore this scenario naturally explains why some cool DZs have fields of several MG while most appear to have none at all. Since a threshold must be exceeded for dynamo generation at the boundary of the giant star core, generation of a permanent magnetic field is dependent on sufficient angular momentum being transferred inwards, i.e. through engulfment of giant planet.

6.6 Comparison with magnetic DAZ

For cool DZ we arrive at a magnetic incidence of $21.6 \pm 3.3\,\%$. Yet if we compare this against DAZ white dwarfs, the result is very different. In fact very few magnetic DAZs are known at all, and their magnetic fields are not nearly as strong as found among the DZs in this study.

Kawka et al. (2007) list all magnetic white dwarfs known up to June 2006. Among these are the three previously known magnetic DZs (SDSS J0157+0033, SDSS J1214−0234, SDSS J1330+3029). However, not a single magnetic DAZ was known at that time.

Since then, four DAZHs *have* been identified, all with $T_{\mathrm{eff}} < 7000\,\mathrm{K}$ (Farihi et al., 2011a; Zuckerman et al., 2011; Kawka & Vennes, 2011, 2014), and with the most magnetic (NLTT 10480) possessing a field of only 0.5 MG (Kawka & Vennes, 2011). As with DZs (Section 6.5) all known magnetic DAZ have $T_{\mathrm{eff}} < 8000\,\mathrm{K}$, again suggesting field generation/emergence late on the white dwarf cooling track.

Additionally, the fact that cool DAZHs are not found with the same regime of magnetic field strengths as DZHs is somewhat surprising as they will have similar cooling ages, and so the magnetic field distribution would be expected to be the same, assuming similar progenitors. However, magnetic fields should strongly impede convective mixing (Tremblay et al., 2015; Gentile Fusillo et al., 2018) in white dwarf envelopes, reducing diffusion timescales of heavy elements. Due to the difference in pressure/density in the outer layers of hydrogen versus helium dominated atmospheres, the effect of magnetism will likely also differ as a function of composition, potentially increasing the selection bias against MG-field DAZH versus DZH white dwarfs. Another possible explanation is that because metal lines in DAZs appear weaker for a given metal abundance compared with DZs, magnetic splitting of these lines will reduce the overall strength of the Zeeman components, potentially to the point of non-detection. Therefore strongly magnetised DAZHs would instead be classified as DAHs (where the magnetic field can still be inferred from the Balmer series). Higher S/N spectra may reveal known DAH white dwarfs to also be metal polluted.

It is also worth noting that, to date, there are no known magnetic DBZ. However, this remains consistent with the observation that no metal polluted white dwarfs are known to be magnetic for $T_{\mathrm{eff}} > 8000\,\mathrm{K}$.

6.7 Follow-up observations of DZH white dwarfs

6.7.1 SDSS J1536+4205

Search for rotation

In Section 6.2 we showed that the sets of three sharp Zeeman components observed for SDSS J1536+4205 could be explained via an offset dipole model. This allowed for a relatively uniform field on the visible hemisphere, but required a strong gradient of fields on the opposite side to exclude a monopole configuration.

Brinkworth et al. (2013) showed that isolated magnetic white dwarfs have typical rotation periods of hours to days. Many of the white dwarfs they observed have T_{eff} falling into the range we study here. In general the magnetic axes of magnetic white dwarfs are not aligned with the rotation axes (Latter et al., 1987; Burleigh et al., 1999; Euchner et al., 2005), therefore by taking spectra at multiple epochs, one can expect to see modulation in the Zeeman line profiles of these stars.

To investigate the field configuration of SDSS J1536+4205 further, we obtained GTC spectra of this star on four occasions using the OSIRIS instrument, with our goal to detect rotation through Zeeman line variation. If the star was seen to rotate, we would be able to constrain the field over the surface of the star, potentially distinguishing between an offset dipole or a more complex field structure. Should SDSS J1536+4205 not rotate, we would instead be able to form a high quality coadded spectrum, potentially allowing the identification of further Zeeman split metal lines in a 10 MG field. Furthermore, an emission line at 8440 Å appeared to be present in the SDSS spectrum, which also warranted investigation.

The four service-mode observations were obtained during April–June 2015. We opted to use the R1000R grating with a 0.6-arcsec slit (dispersion of 2.62 Å per 2×2 binned pixel) which allowed us to observe both the Na Zeeman triplet (5600–6200 Å) and the potential 8440 Å emission line simultaneously. Each epoch was separated by approximately three weeks from the previous one with some deliberate variation to minimise the chance of observing on a rotational alias.

For each night, we obtained two back-to-back integrations of 900 s each.

Table 6.4: Information for each OSIRIS observation. The quoted MJD refers to that at the start of the night. Airmass is the average of the two integrations.

OB	MJD	Airmass	Flux standard
1	57126	1.06	Hilt 600
2	57140	1.31	GD 153
3	57159	1.17	GD 153
4	57180	1.03	Ross 640

Standard calibration frames, i.e. biases, flat-fields, arc spectra, and flux standard spectra were taken each night. The observing log is given in Table 6.4. Standard spectral reduction techniques were used, as described in Chapter 2 and Section 3.2. All of the reduced spectra (as well as the SDSS spectrum for comparison) are shown in Fig. 6.12. The coadded GTC spectrum is shown in Fig. 6.13.

Inspection of Fig. 6.12 does not show clear signs of rotation. However, with the new GTC data and an improved model of the Na Zeeman line profile, we proceeded to fit the data to confirm this finding.

Our fit to the Na Zeeman triplet had 14 free parameters – 9 free parameters shared across all five epochs (which are assumed to be constant in time), and an inclination for each spectrum of the SDSS and GTC spectra. The 9 parameters fixed across observations are: the dipole field strength B_{d}, the dipole offset a_z, the Lorentzian line width, the stellar redshift, a coefficient for the quadratic Zeeman shift, a line depth parameter, and 2nd order polynomial for the continuum flux.

In Section 6.2, we set the wavelength of the π-component as a free parameter to account for shifts from the rest wavelength of 5893 Å. Here, we instead adopt a free-parameter for the quadratic Zeeman effect. This is because for $l = 0 \to 1$ transitions, the quadratic Zeeman shift is proportional to $1+m_l^2$ (Preston, 1970). In other words, the σ-components are blue-shifted twice as much as the π-component. We therefore include this strength, Q, in our expression for energy splitting,

$$\Delta(1/\lambda) = 46.686\,\Delta m_l B + Q(1+\Delta m_l^2)B^2. \tag{6.13}$$

Apart from these minor changes and the inclusion of additional inclination free-parameters, our model was otherwise the same as that used in Section 6.2. Similarly, we used EMCEE to perform an MCMC fit to the data using the same priors as before, although with an inclination prior for each observation. The resulting fits to each spectrum are shown in Fig. 6.15, with the posterior distribution of B_d a_z and all five inclination measurements (with their tabulated values) in Fig. 6.14. Evidently, no change in the observer inclination to the magnetic axis is detected.

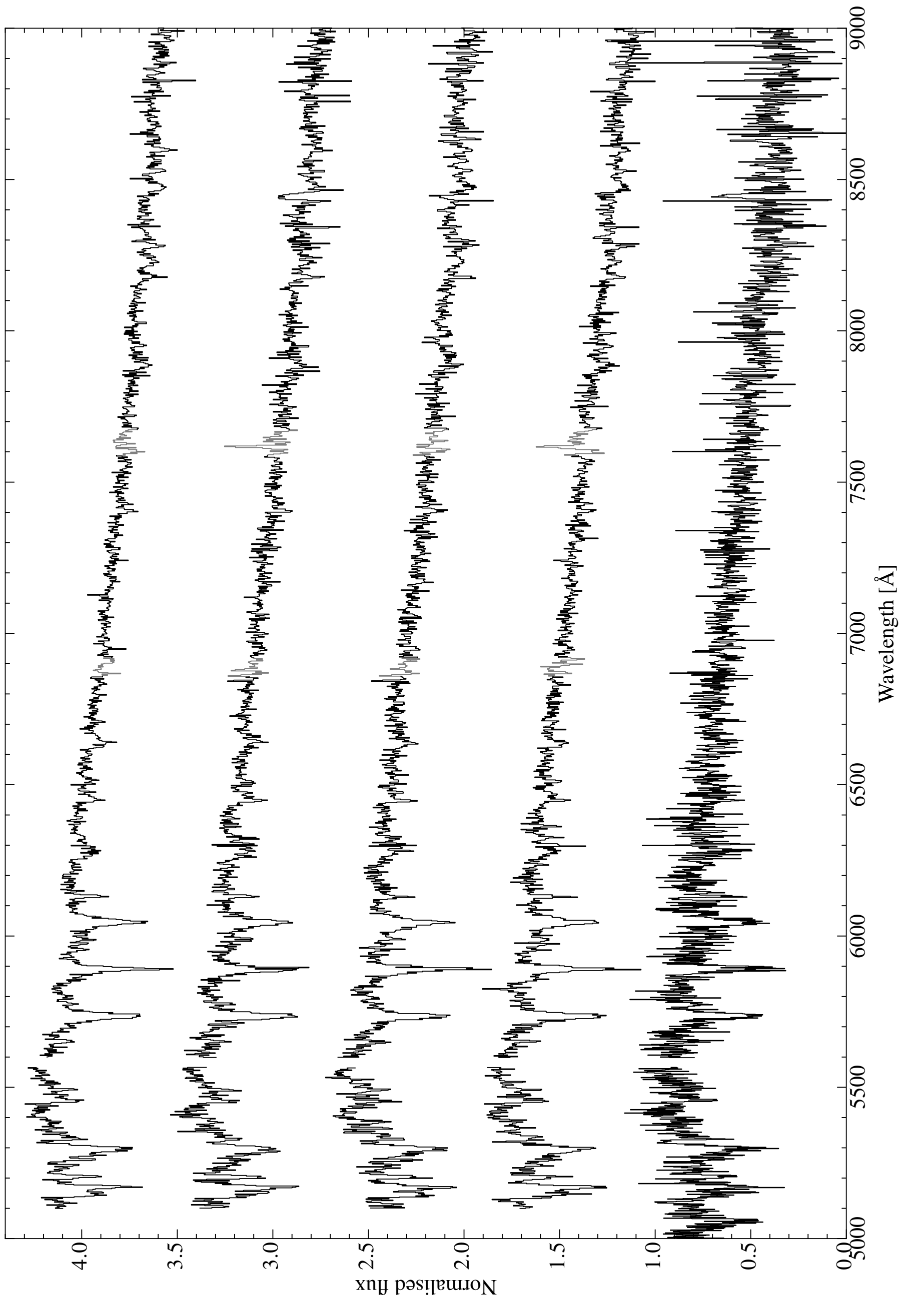

Figure 6.12: Optical spectra of SDSS J1536+4205. All spectra are normalised to peak at unity and are offset from one another by 0.8. The SDSS discovery spectrum is shown at the bottom and covers the full Mg I Zeeman triplet (centred at 5172 Å). The GTC spectra are shown with observation date increasing upwards. A small region around 5550 Å containing a strong sky emission line tends to subtract poorly, and is thus masked. Regions of the GTC spectra where significant telluric correction has been applied are drawn in grey.

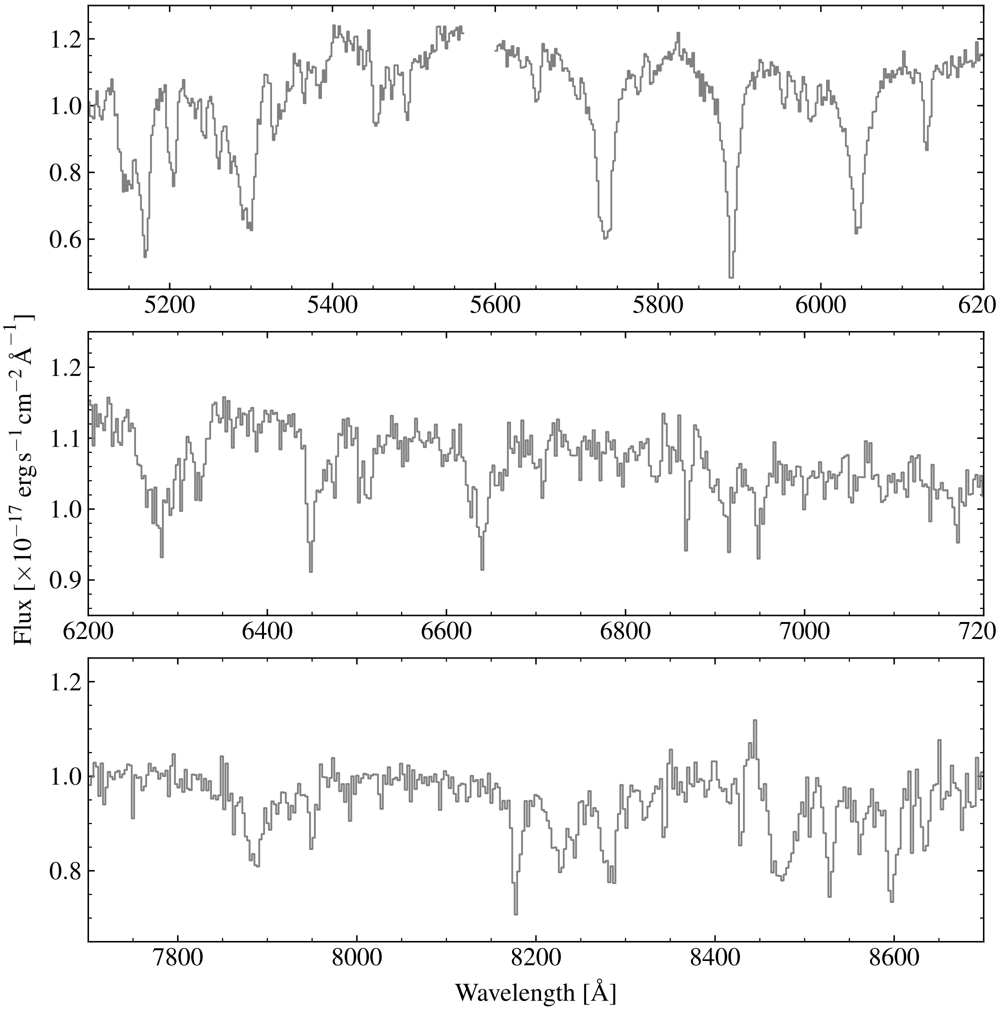

Figure 6.13: Coadded spectrum of SDSS J1536+4205 combining GTC spectra from all 4 nights. The feature at $\simeq 6900$ Å is telluric in nature and should not be mistaken for photospheric transitions.

The most significant change between any two epochs (accounting for parameter covariances) is found for observations 3 and 4, with a difference of 11.6 ± 5.5 degrees, or $2.1\,\sigma$ – for five measurements, a deviation of this magnitude has a p-value of 0.2, and thus can not be considered significant. However, the result of fitting to all spectra simultaneously produces tight constraints on both the dipole field strength B_{d}, and the dipole offset a_z (Fig. 6.14).

The lack of observed rotation within these data may arise from any of three different possibilities. Firstly, the star may well be a slow rotator. Indeed, it is known that some isolated magnetic white dwarfs have rotation periods possibly up to a century (Brinkworth et al., 2013). Secondly, the white dwarf may rotate with a period of a few days or less, but if the magnetic axis and rotation axis happen to be strongly aligned, no change in inclination will be seen by the observer. Finally, the white dwarf may rotate, but if the rotation axis is within a few degrees of the line of sight, then observer inclination to the magnetic axis will appear constant.

The high quality fits in Fig. 6.15 continue to support an offset-dipole field geometry, however without rotationally resolved spectra we cannot rule a more complicated field structure, e.g. offset-dipole + quadrapole (e.g. Euchner et al., 2005). Regardless of the exact field structure the far side must have have a strong gradient of fields. Under the assumption of an offset-dipole, our fit parameters imply a field strength of 40.3 ± 0.6 MG for the far magnetic pole of SDSS J1536+4205.

Additional transitions

The substantial improvement in signal-to-noise of the GTC spectra when compared to the SDSS data permits identification of additional Zeeman split lines. These are clearest in the coadded GTC spectrum in Fig. 6.13.

The most obvious of these is the asymmetric Ca I feature centred at around 6500 Å. Thanks to the uniform field, the σ-components take on the same asymmetric profile as the π-component making identification of this transition quite simple, considering the relatively shallower line depth. Due to the large Ca-abundances required, this feature is only visible in a few other (non-magnetic) DZs such as SDSS J0744+4649 (Fig. 4.5) and SDSS J0916+2540 (Fig. 5.5). Slightly to the red of the Mg I lines (π-component located at 5171 Å), are two other lines. We interpret these to be π and σ^+ components of the Cr I nominally located at 5207 Å.

A few other features in the coadded spectrum lack clear identifications. A sharp line at 6130 Å is seen in Fig. 6.13. The wavelength of this line also coincides with a common Ca I line seen in the spectra of cool DZ white dwarfs. However, that transition ought to be asymmetric much like the 6500 Å feature. At 5967 Å, a small

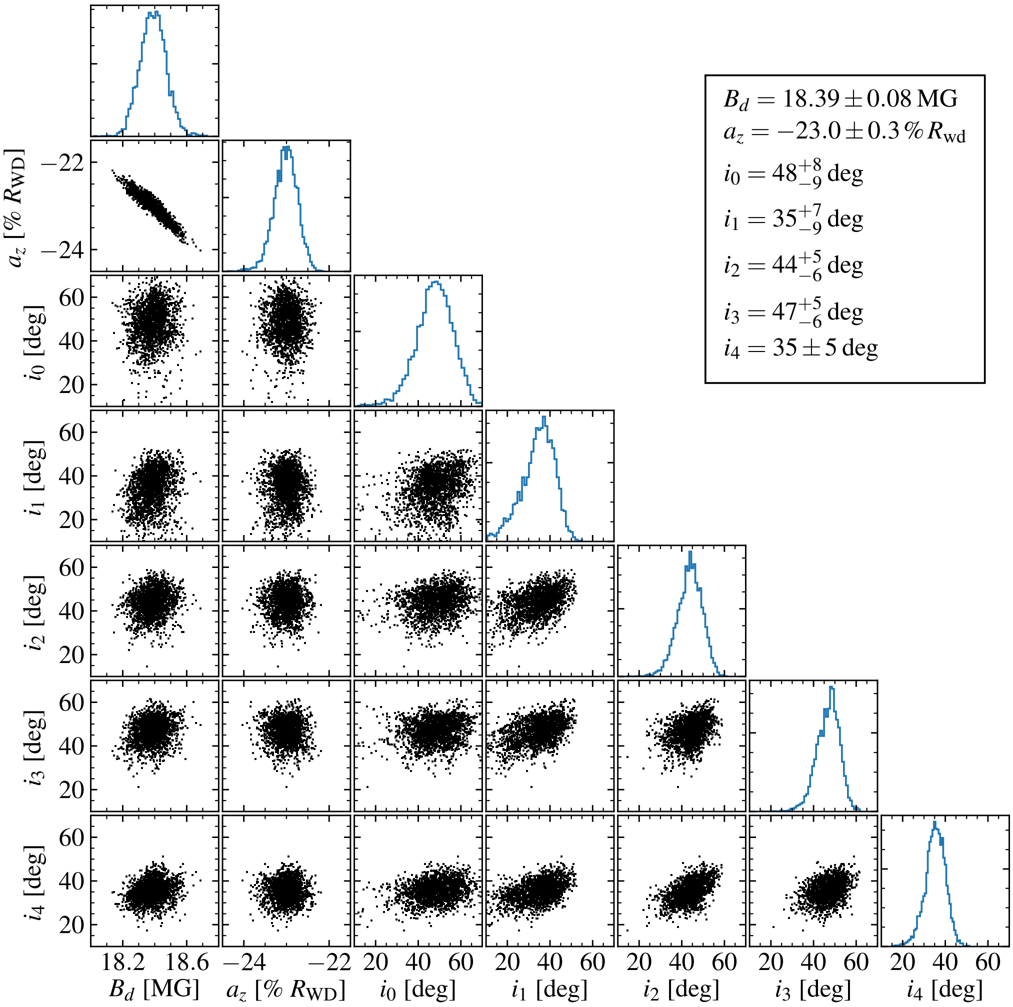

Figure 6.14: Corner plot for our combined fit to the Na triplet for all five epochs. Once again the B_d vs. a_z plane exhibits high degree of covariance, but with much tighter constraints on both parameters compared with fitting only the SDSS data. Here, i_0 refers to the SDSS data, whereas i_1 to i_4 refer to the GTC spectra in order of observation. In the table, we use the 50th and 15.9/84.1th percentiles of the marginalised distributions for the quoted values and uncertainties.

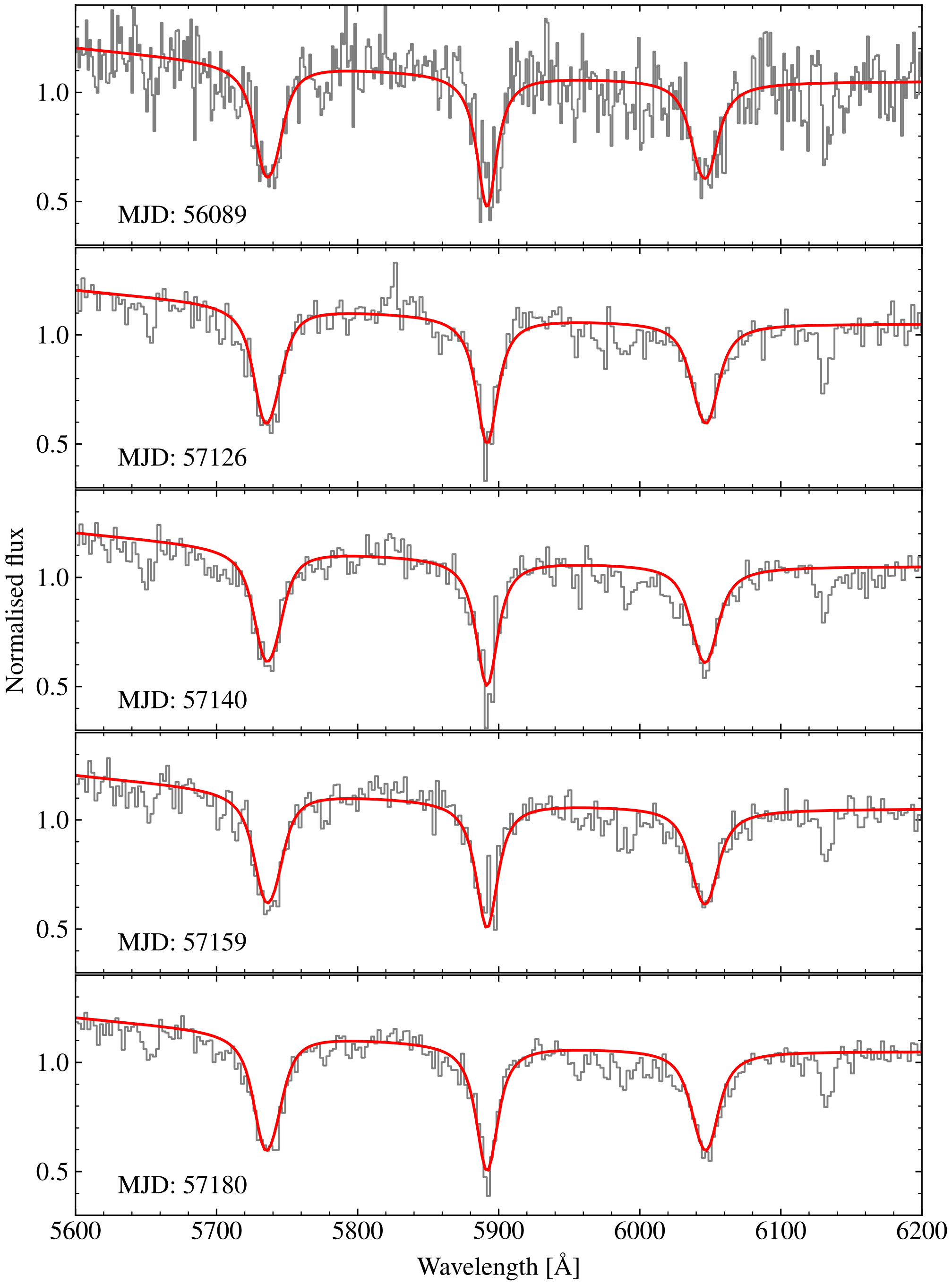

Figure 6.15: MCMC fits to the SDSS and GTC spectra of SDSS J1535+4205. Small absorption lines either side of the Na triplet are masked during the fitting procedure.

multiplet of lines is seen. While we have no way of identifying this feature ourselves, upcoming magnetic model atmospheres codes are seen to be able to reproduce this (Dufour et al., 2015; Hardy et al., 2017). Between the Mg I and Na I Zeeman triplets, several transitions are observed. These do not trivially correspond to a feature seen in other DZ white dwarfs. However for zero-field DZ stars, this region often contains a multiplet of Fe lines, which may be responsible for the transitions seen in Fig. 6.13.

Finally, an emission line is seen at 8440 Å in some of the spectra in Fig. 6.12, and also averaged into Fig. 6.13. While the red end of optical contains numerous sky-emission lines, the observed line, is not located close to any of them, and thus cannot be the result of poor sky-subtraction. Particularly curious is the variability of this feature, as it is seen in the SDSS spectrum and half of the GTC spectra. While certainly astrophysical in nature, we were eventually able to conclude that this otherwise mysterious feature is not associated with SDSS J1536+4205. Inspection of the raw GTC frames showed the emission to be offset from the stellar trace by $\simeq 0.5$ arcsec in the spatial direction. The line is instead attributed to O III emission from a faint, almost overlapping background quasar (A. Levan, priv. comm., 2016), which is visible *only* via this single transition. The variability of the line, it turns out, was dependent on the slit rotation angle on the sky. While we concluded this feature is of little physical relevance to this work, it serves as important lesson in meticulous assessment of data before finalising conclusions.

Quadratic Zeeman splitting

One other set of transitions warrants its own section. Between 7900 and 8600 Å (Fig. 6.13) three absorption features are seen, each comprised of multiple components. While not so clear when plotted against wavelength, if the spectrum is displayed with a wavenumber scale, the spacing between the three groups of splittings is seen to be the same as those of the Mg I, Na I, and Ca I triplets. Essentially these three groups of splittings are themselves a single Zeeman triplet. The fine structure within each group results from the quadratic Zeeman effect which lifts the degeneracy between transitions of the same Δm_l, but different overall m_l quantum number. This therefore marks the first detection of quadratic splitting for a metal in any astrophysical context.

To investigate this feature further, we obtained four additional GTC observations in 2016, instead opting for the higher resolution R2500I grating, which has its maximum throughput between 7700 and 8600 Å (for R1000R wavelengths > 8000 Å extend into the tail of its throughput curve). Coadding all GTC spectra (including the 2015 observations), produced a very high quality spectrum (Fig. 6.16) with a

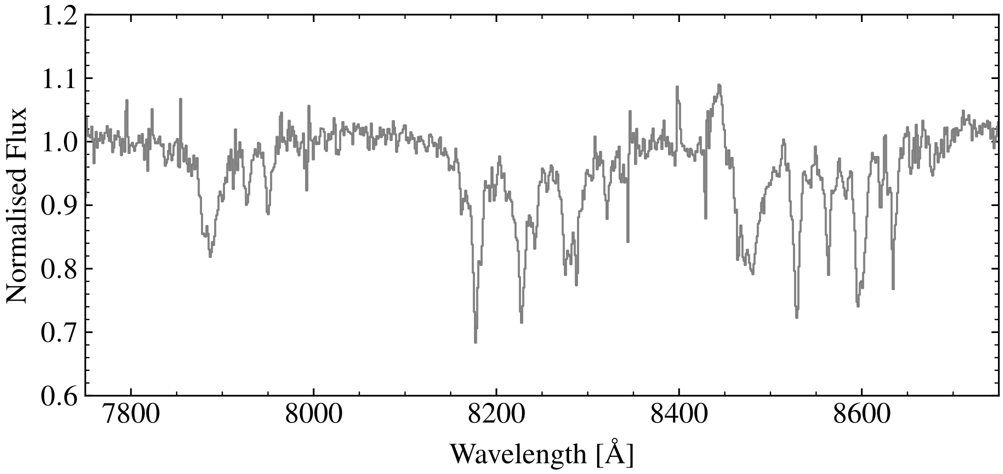

Figure 6.16: The coadded spectrum of all GTC observations of SDSS J1536+4205 zoomed in to the near IR Zeeman triplet. Each Zeeman component is itself composed of multiple narrow lines which in a smaller field would normally be degenerate.

median signal-to-noise ratio of 60.

Identifying the ion responsible for these these splittings is not trivial, although we have narrowed this down to either Na I or Ca II. As seen in Section 6.1.3, the quadratic Zeeman effect can result in large line shifts. However, the magnitude of the shift is highly dependent on the ionic species, thus the wavelength of the π-component cannot be simply compared with tabulated tables of transitions. For a given ion, the quadratic Zeeman shift is proportional to the radial quantum number of the upper level to the fourth power, n_{up}^4 (Wickramasinghe & Ferrario, 2000). Therefore in laboratory settings with field strengths of $\sim 10^5$ G, the quadratic effect is only observable by pumping atoms into high n_{up}. Any direct solution to the origin of this group of transitions is best suited to a computational approach.

Even in the absence of such numerical calculations, we can still speculate on the most likely transitions. The two closest lines found in any other DZs come from the Ca II triplet and the 8190 Å Na I doublet. The Ca abundance is already established to be high due to the presence of the usually undetectable 6500 Å Ca I feature. However if the transitions are from Ca II, then this necessitates a huge $\simeq 380$ Å quadratic shift (the Ca II transition is calculated to correspond to 8581 Å if the spin-orbit effect is excluded Kramida et al. 2016).

Alternatively the line may originate from the 8190 Å Na I doublet. This transition peaks in strength at low temperatures, and is thus prominent in the spectra of M-type stars. The only DZ in our sample where we unambiguously detect this transition is SDSS J1214−0234 (LHS 2534), which is also magnetic with a 2.1 MG field.[5] We marginally detect this feature in the spectra of the cool, but Na-rich SDSS J1014+2827, SDSS J1102+2827, and SDSS J1430−0151.

Regardless of whether the transitions in Fig. 6.16 come from Ca II, Na I or another ion, we hope these observations motivate new atomic physics calculations for metals in $> 10^7$ G magnetic fields that we observe in our sample.

6.7.2 SDSS J1143+6615

In March 2016, we obtained high signal-to-noise Gemini spectra of SDSS J1143+6615 (Section 6.1.3). These observations were motivated by the tentative detection of modulation of the Mg and Na lines between the SDSS subspectra. Thus we sought to confirm and potentially measure rotation of this metal-rich and highly magnetic white dwarf. In particular the Mg I line was shown to be quite sensitive to field strength (Section 6.1.3/Fig. 6.7). Thus, any change in the average field strength (B_{S}) on the visible hemisphere should result in a $\simeq 1.7$ Å line shift per MG (recalling the estimated field strength to be $B_{\mathrm{S}} = 30 \pm 4$ MG).

For these observations we obtained 17 back-to-back GMOS spectra with an exposure time of 630 s for each, allowing us to monitor SDSS J1143+6615 for approximately 3 hours. The GMOS instrument contains three CCDs covering the optical, each separated by small gap in terms of wavelength. We took care to choose the central wavelength such that the detector gaps fell in regions where no absorption had been previously detected in the SDSS spectrum. As with all previously described observations, standard calibration images were taken, with spectral reduction performed using STARLINK software.

The Mg and Na lines both fell onto the central CCD. All 17 spectra are shown in Fig. 6.17. These higher quality spectra do not reveal any obvious signs of rotation. As with SDSS J1536+4205 the three explanations consistent with this result are, slow rotation that over the span of our observations; rotation occurs, but the star is viewed down the rotation axis; or rotation occurs, but the magnetic axis (for a largely dipolar field topology) is close to aligned with the rotation axis.

While we once again failed to detect rotation, the data were still useful. The coadded spectrum is shown in Fig. 6.18, demonstrating both sharp and broad absorption features. The much more precise wavelength/wavenumber measurement further constrains the field to $B_{\mathrm{S}} = 30 \pm 3$ MG – the remaining uncertainty in this

---

[5] Interestingly, our measurements of the Mg, Ca, Na lines in our WHT spectrum tightly constrain the field of SDSS J1214−0234 to $B_{\mathrm{S}} = 2.11 \pm 0.02$ MG, about 10 % larger than the field measured for the SDSS spectrum and that of Reid et al. (2001) (1.92 MG). This likely indicates the star has rotated in the sixteen years between those observations, resulting in different measurements.

value is dominated by the fit in Fig. 6.7. The higher quality spectra reveal that the previously tenuous line near 4227 Å is a genuine feature, which is most likely to be the π-component of the Ca I resonance line, seen in many DZ spectra. If we assume this identification is correct, then the σ^+-component ought be located at 4490±30 Å. Indeed a moderately sharp feature is seen at 4475 Å, which if interpreted correctly, implies a revised field strength of $B_\mathrm{S} = 28.0 \pm 0.6\,\mathrm{MG}$ (where the error is estimated from the width of the supposed σ^+-component).

Many mysteries still remain for SDSS J1143+6615. In particular the broadest absorption features lack clear identifications, and the origin of the large magnetic field for a white dwarf apparently possessing a planetary system. A full interpretation of our spectra will only be achievable once atmospheres codes capable of modelling the physics of metals at high strengths become widely available.

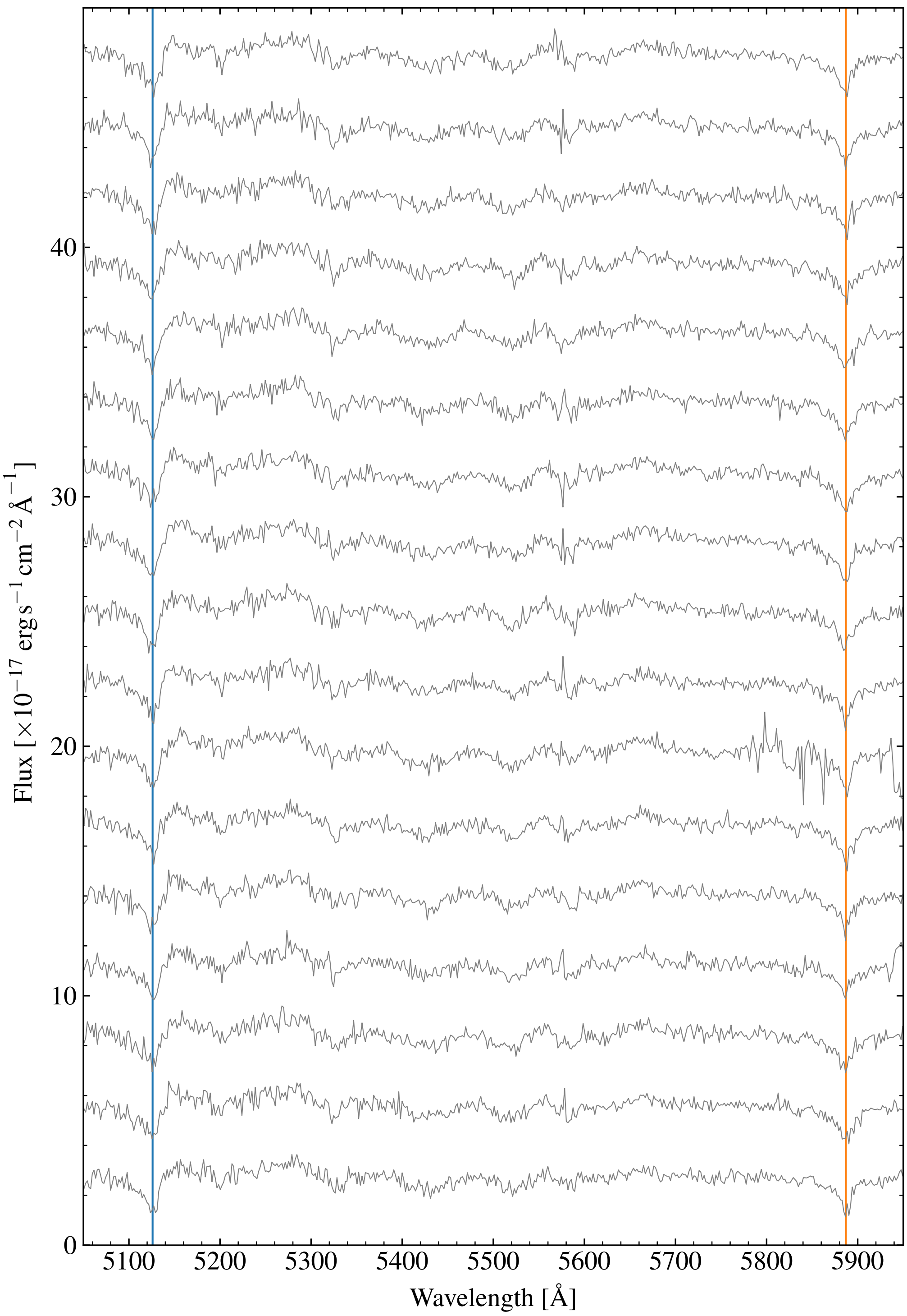

Figure 6.17: Gemini GMOS spectra of SDSS J1143+6615. The spectra are offset from one another by $2.8 \times 10^{-17}\,\mathrm{erg\,cm^{-2}\,s^{-1}\,\AA^{-1}}$. The blue and orange lines are fiducial markers for the Mg and Na lines respectively.

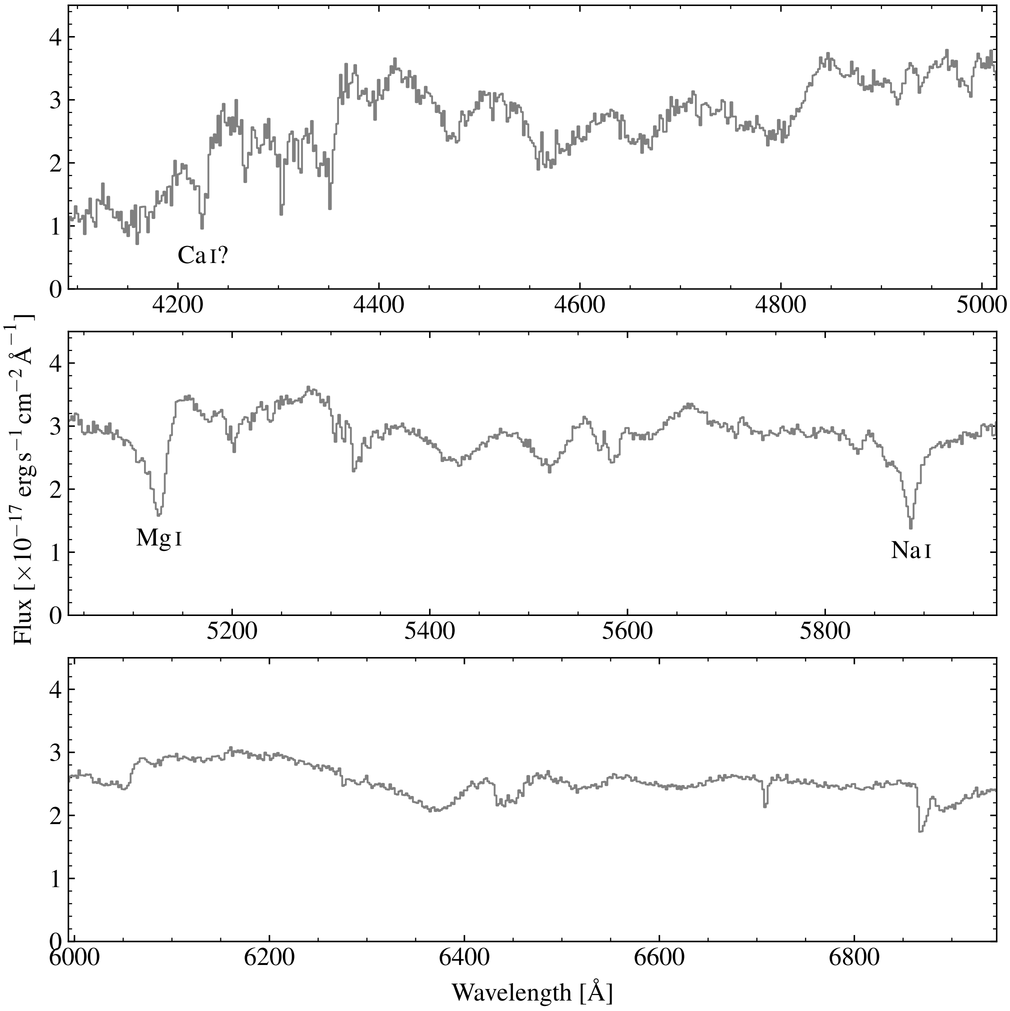

Figure 6.18: The coadded spectra of SDSS J1143+6615 are shown for the three GMOS chips. The Mg and Na lines are labelled in the central chip, with the potential detection of the Ca I resonance line marked on the bluest chip. The features redder than 6700 Å are all telluric in nature.

Chapter 7

Conclusions and future perspectives

7.1 Conclusions

In this thesis I have identified a large sample of 231 cool DZ white dwarfs using spectroscopy from the Sloan Digital Sky Survey. These stars exhibit strong metal absorption features in their spectra, indicating recent accretion from their planetary systems. Using state of the art model atmosphere codes, I fitted the spectrum of each star determining the effective temperature and atmospheric abundances of Ca, Mg, Fe, Na, Cr, Ti, and Ni – rock forming elements from accreted exoplanetesimals.

Relative abundances for the accreted metals were used to investigate the distribution of planetesimal compositions. In all systems I was able to estimate abundances of Ca, Mg, and Fe. Na, Cr, Ti, and Ni were typically found in only trace amounts, and thus not always detected. While attempting to use Ca, Mg, and Fe as a primary set of elements, I found that the slower diffusion rate of Mg (by about a factor three) made interpretation of Ca/Mg/Fe distribution subject to uncertainty for DZ stars. However the similarity in Ca and Fe sinking timescales did not pose this problem, where I found that the Fe/Ca ratio varying by two orders of magnitude across my sample.

The systems with the highest Ca and Fe fractions in the accreted material qualitatively implied parent bodies with crust-like and core-like compositions respectively. To quantify this assessment, I developed a simple method to reinterpret Ca, Mg, and Fe abundances/accretion rates in terms of crust, mantle, and core material. For the most extreme systems in terms of Ca and Fe (where relative diffusion of Mg could be safely ignored), I compared their crust/mantle/core fractions to accreting systems analysed elsewhere. The combined distribution spanned from high in crust to Earth-like to rich in core material, but as expected systems composed of core and crust material but lacking a mantle were found to absent. I also conclude that two of the systems in my sample, SDSS J0741+3146 and SDSS J0823+0546, have accreted the most core-like exoplanetesimals discovered to date.

This sample of cool white dwarfs also spans a wide range in cooling ages from 1 to almost 8 Gyr. I have shown that the diminishing amount of metal pollution with increasing age may provide evidence for the slow decay in the sizes of remnant planetary systems as the largest planetesimals are scattered away. This occurs on an e-folding time-scale of about 0.95 ± 0.10 Gyr, an effect that previously escaped notice due to selection bias towards younger systems that do not sufficiently sample changes on this time-scale. A few outliers appear to go against this trend showing large metal abundances at ages > 5 Gyr. I found that two of these were members of wide binaries, a property not exhibited by any other DZs in my sample. This provides convincing evidence that white dwarfs in binary systems experience higher than average accretion rates of exoplanetesimals, as a result of dynamical instabilities that have been previously argued for theoretically.

Finally, I found that within my sample of 231 cool DZs *at least* 33 possess magnetic fields in the range 0.2–30 MG. This implies a minimum magnetic incidence of 14 ± 2 percent which is substantially higher than for young hot DAs. Furthermore, by excluding systems where it is not possible to tell either way, I found a more likely value of 22 ± 3 percent. The narrowness of the Zeeman split lines in several of these objects suggested complex magnetic field topologies, which by modelling of the Zeeman line profiles, I found to be consistent with an offset dipole. For two systems with fields $\gtrsim 9$ MG, I also identified both additional line splitting and shifts attributed to the quadratic Zeeman effect. Hitherto, this effect has not been observed for metals in an astrophysical context, and thus motivates new atomic theory calculations.

7.2 Future perspectives

While I was able study many of the properties DZ white dwarfs and planetary systems from my sample, their scientific potential is far from exhausted. This includes both observational and theoretical aspects. New surveys and follow-up observations will lead to even larger sample of white dwarfs for statistical analysis, and improvements in to the input physics of white dwarf models will result in an enhanced understanding of the continuing data.

7.2.1 HST data

In order to check the consistency of our models when extrapolating into the near-UV (NUV), I obtained additional data of three DZs with the Hubble Space Telescope (HST) between April and August 2016. The observations consisted of low resolution spectra ($R = 500$) spanning 1500–3000 Å, using the Space Telescope Imaging Spectrograph (STIS).

The three white dwarfs in question are SDSS J0956+5912, SDSS J1038−0036, and SDSS J1535+1247. These stars were chosen for two reasons. Firstly, they are among the brightest stars in our sample, where all have NUV photometry from the GALEX space-mission. Secondly, these three white dwarfs span 5800–8800 K in $T_{\rm eff}$ from our fits in Chapter 3, and so allow us to investigate our models across most of the $T_{\rm eff}$-range in our sample.

Preliminary fits indicate that our models are generally accurate over this wavelength range. By-eye, the previous models for white dwarfs SDSS J1038−0036 and SDSS J1535+1247 appear satisfactory when compared with the data, with only minor adjustments in $T_{\rm eff}$/abundances possible for additional improvement. On the other hand, we have found more drastic changes are needed for SDSS J0956+5912, with a $T_{\rm eff} \simeq 8000$ K required to fit the optical and NUV simultaneously (a change of −800 K).

However further inspection reveals SDSS J0956+5912 to exhibit a unique abundance pattern. A secondary goal of these observations was to obtain Si abundances for the above three white dwarfs. However, following these preliminary fits, we noted the strongest Si-constraint of SDSS J0956+5912 in fact comes from an *optical* Si I line at 3906 Å. This transition is plainly visible in the SDSS spectrum, yet is absent for all 230 of the other DZs in our sample.

In hindsight, the large Si abundance is not surprising. The most common Si-bearing mineral in the Earth is $MgSiO_3$ (McDonough, 2000). Recalling from Section 4.4.3, that SDSS J0956+5912 is particularly rich in Mg, we should expect a similarly large Si abundance (which appears to be the case). The attentive reader will notice that assuming $MgSiO_3$ as the dominant source of metals at SDSS J0956+5912 implies an O-abundance three times higher (+0.5 dex) than for Mg and Si. Even so, the expected abundance would be insufficient to produce any appreciable absorption features at this $T_{\rm eff}$.

Fortunately, we thought it worthwhile to check the data regardless of our expectations. At 7774 Å, we found a small absorption feature, which we have since confirmed with GTC spectroscopy. The implied abundance is about 1 dex higher than anticipated for $MgSiO_3$. Since trace hydrogen is also present at this object, the implication is that SDSS J0956+5912 accreted a planetesimal with a large water fraction similarly to GD 61 (Farihi et al., 2013a) and SDSS J124231.07+522626.6 (Raddi et al., 2015). Investigation into other possible compositions are still ongoing, and requires consideration of elemental diffusion as a source of O-enhancement.

7.2.2 Convection and diffusion

Within this thesis, two important physical considerations are the presence of convection zones, and diffusion of heavy elements throughout these zones. However, the understanding of these topics still has room for improvement.

In Section 3.5, I noted an unexpected trend in the upper-bound of log[Ca/He] as a function of T_{eff} (Fig. 3.12), particularly between temperatures of 10 000–12 000 K. From DA white dwarfs in this temperature range, no such trend is inferred from the measured accretion rates (Koester et al., 2014). Since the accretion rates should not be statistically different onto helium versus hydrogen dominated atmospheres, it is likely the trend is related to large systematic uncertainties in the onset of convection zone formation (which simultaneously affects diffusion rates of heavy elements). Thus, a better understanding of convection zone physics is needed to fully understand the metal accretion onto helium-rich white dwarf atmospheres over all T_{eff} ranges.

Furthermore, as discussed throughout Chapter 6, a moderate fraction of the white dwarfs in our sample possess magnetic fields. Theory and recent observations indicate that even magnetic fields much weaker than those studied here should be sufficient to impede convection (Gentile Fusillo et al., 2018). Without deep convection zones, diffusion timescales of heavy elements should be dramatically reduced, restricting the amount of time that metals can be detected at magnetic objects, and consequently lowering the measured magnetic incidence. The high magnetic fraction of our sample appears to defy this expectation, suggesting that convection is still present even in the MG-regime. Thus, our results motivate investigation of the interaction between magnetic fields and metal-rich convective envelopes.

7.2.3 Gaia

Gaia is an ongoing space-mission measuring astrometry for ~ 1 billion sources to high precision. The second Gaia data release, DR2, will occur during April 2018, with most sources expected to have five-parameter astrometric solutions (position at a given epoch, proper-motion, and parallax).

Over the full mission (including later data releases), Gaia is expected to measure the parallaxes for, and thus identify, several 10^5 white dwarfs (Gänsicke et al., 2016a). The combination of Gaia parallaxes and optical photometry/spectroscopy (e.g. SDSS), will naturally lead to the discovery of thousands more cool DZ stars, for which the analysis demonstrated throughout this thesis can be extended.

Results from Gaia will not only be limited to new identifications, but also to an improved understanding of white dwarf physics. The primary parameter that Gaia will make accessible for cool white dwarfs is the stellar mass. While we have shown we can make accurate measurements of T_{eff}, the surface gravities of the white dwarfs in our work were fixed to $\log g = 8$, due to their otherwise unknown masses. With parallaxes, the integrated stellar flux can be determined, and thus the stellar radius can be calculated via the Stefan-Boltzmann law. Finally the stellar mass can be determined via the white dwarf mass-radius relation.

With the masses in hand, it will become possible to improve our previous work in a variety of ways. With measured values of $\log g$, we will be able to refit our spectra without the caveat of degeneracy between abundances and surface gravity. Furthermore, revised calculations of convection zone masses and diffusion timescales will improve the estimates of average accretion rates onto the white dwarfs in our sample. Finally, precise white dwarf masses also lead to higher precision cooling-ages, which will be important for further investigations into the evolution of remnant planetary systems.

Precision white dwarf masses are also expected to shed light on open questions regarding magnetic white dwarfs. As discussed in Chapter 6, one such question relates to the mass distribution of magnetic white dwarfs, specifically whether isolated magnetic white dwarfs tend to be more massive than non-magnetics. While, Gaia will lead us closer to answering this question, it will be challenging due to difficulties in measuring T_{eff} for magnetic objects. With increased numbers of magnetic white dwarfs discovered (and potentially more accurate cooling ages), we will also be possible to reexamine the observation that magnetic incidence increases for the oldest magnetic white dwarfs, and whether this holds true for larger samples.

Appendix A

DZ sample spectra

- Fig. A.1: SDSS J0002+3209 – SDSS J0143+0113
- Fig. A.2: SDSS J0144+1920 – SDSS J0744+4408
- Fig. A.3: SDSS J0744+2701 – SDSS J0902+1004
- Fig. A.4: SDSS J0906+1141 – SDSS J1014+2827
- Fig. A.5: SDSS J1017+3447 – SDSS J1105+0228
- Fig. A.6: SDSS J1106+6737 – SDSS J1205+3536
- Fig. A.7: SDSS J1211+2326 – SDSS J1308+0258
- Fig. A.8: SDSS J1314+3748 – SDSS J1405+1549
- Fig. A.9: SDSS J1411+3410 – SDSS J1542+4650
- Fig. A.10: SDSS J1543+2024 – SDSS J2123+0016
- Fig. A.11: SDSS J2157+1206 – SDSS J2357+2348

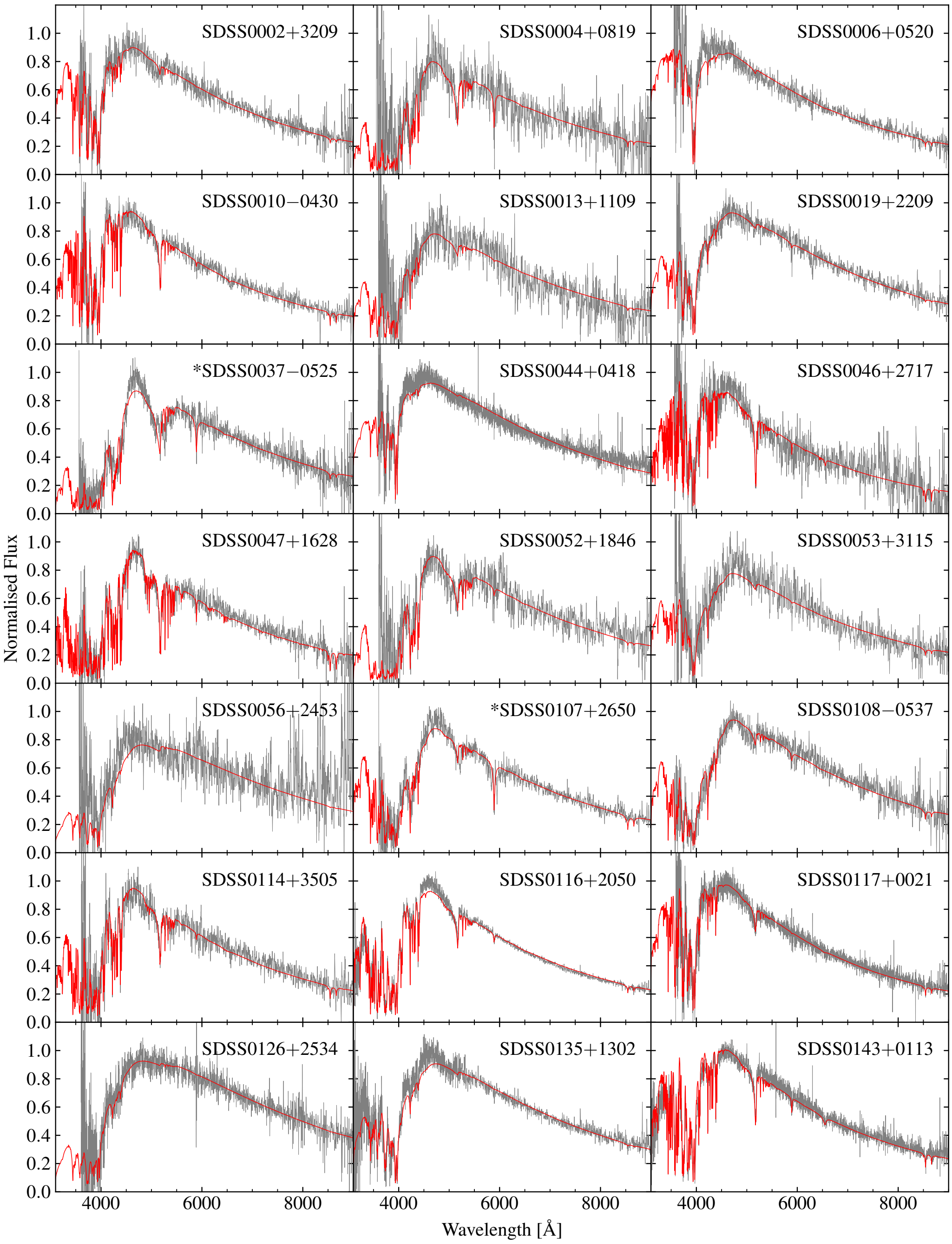

Figure A.1: DZ spectra with best fitting models. Asterisks precede the name of magnetic systems with $B_S > 1\,\mathrm{MG}$.

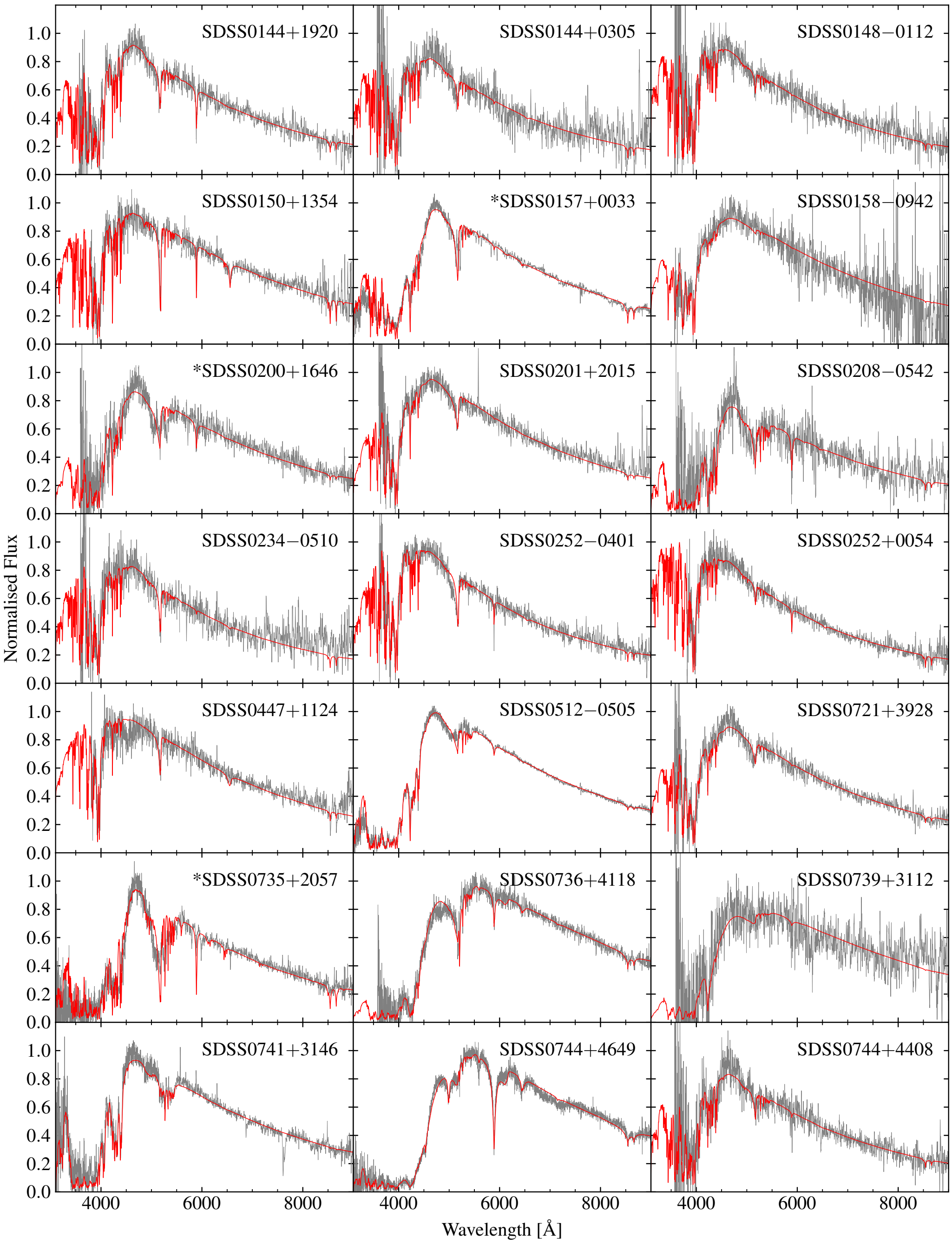

Figure A.2: Figure A.1 continued.

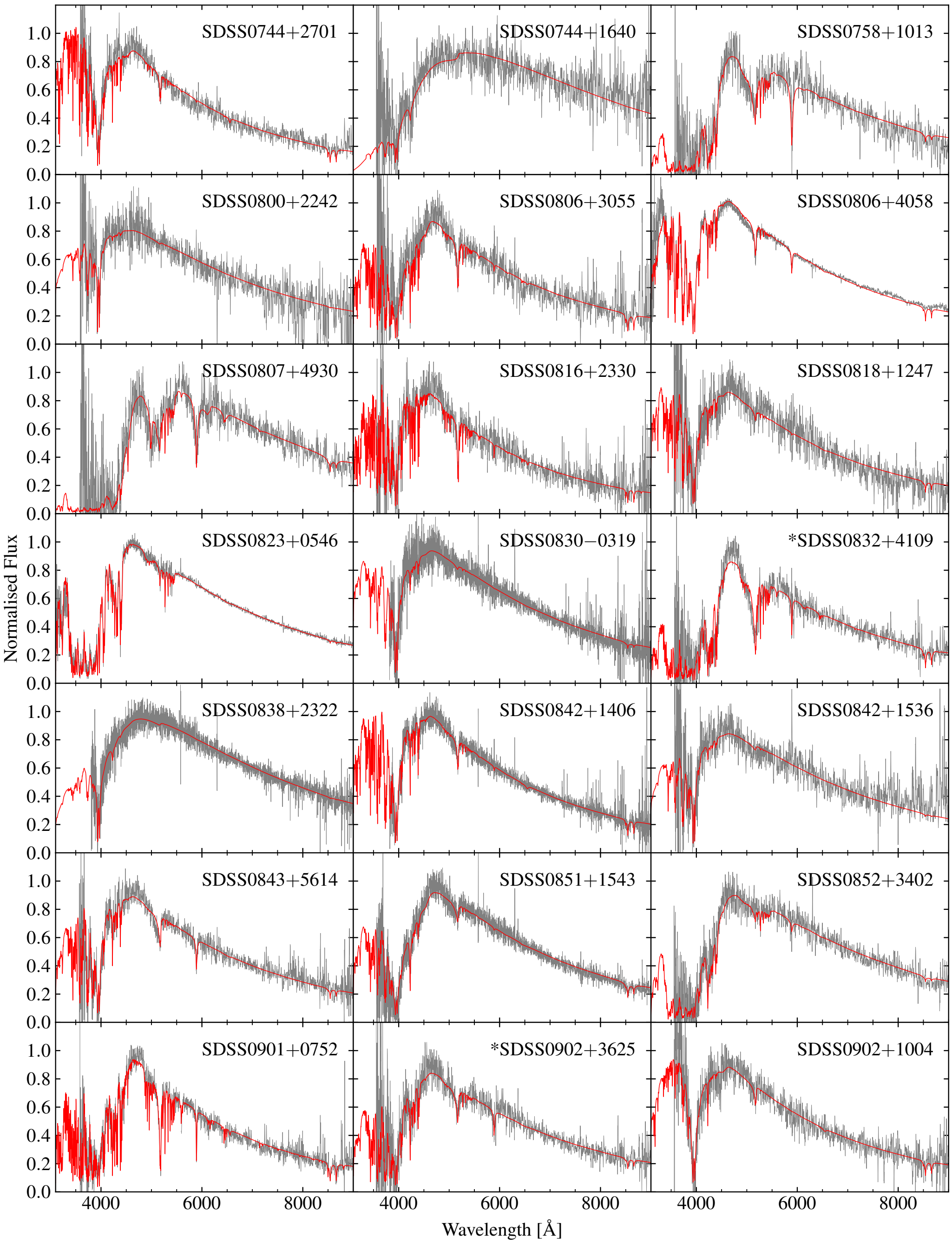

Figure A.3: Figure A.1 continued.

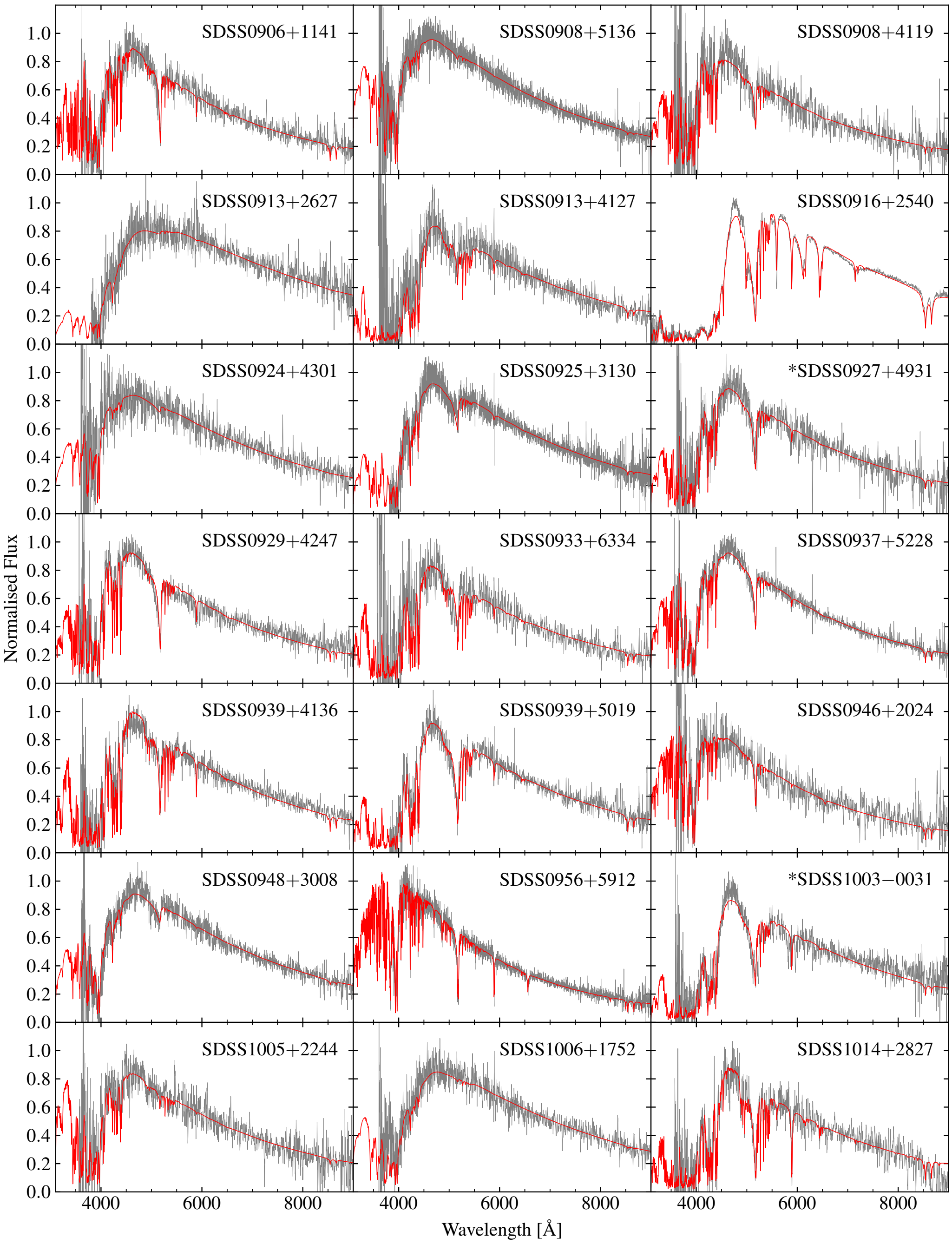

Figure A.4: Figure A.1 continued.

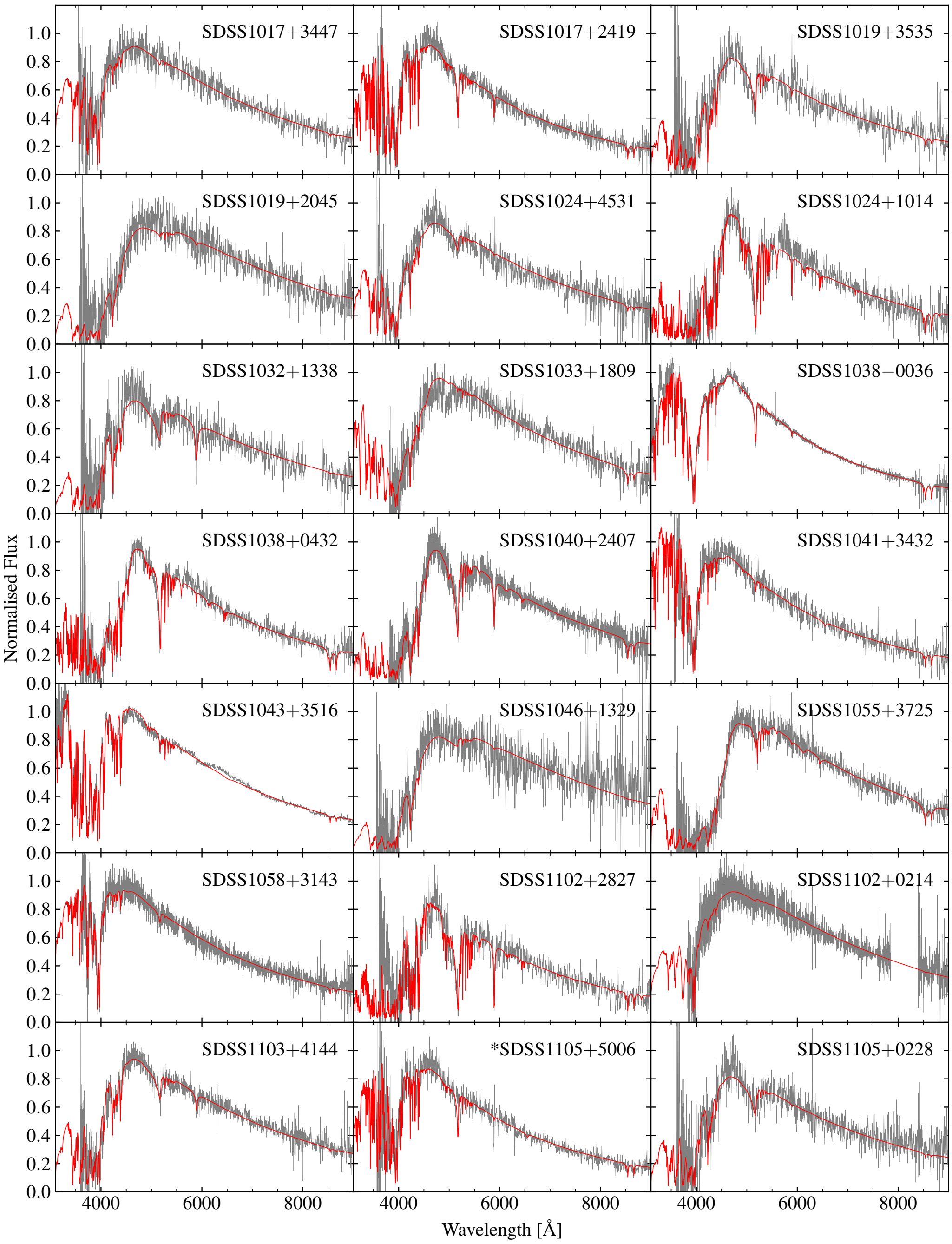

Figure A.5: Figure A.1 continued.

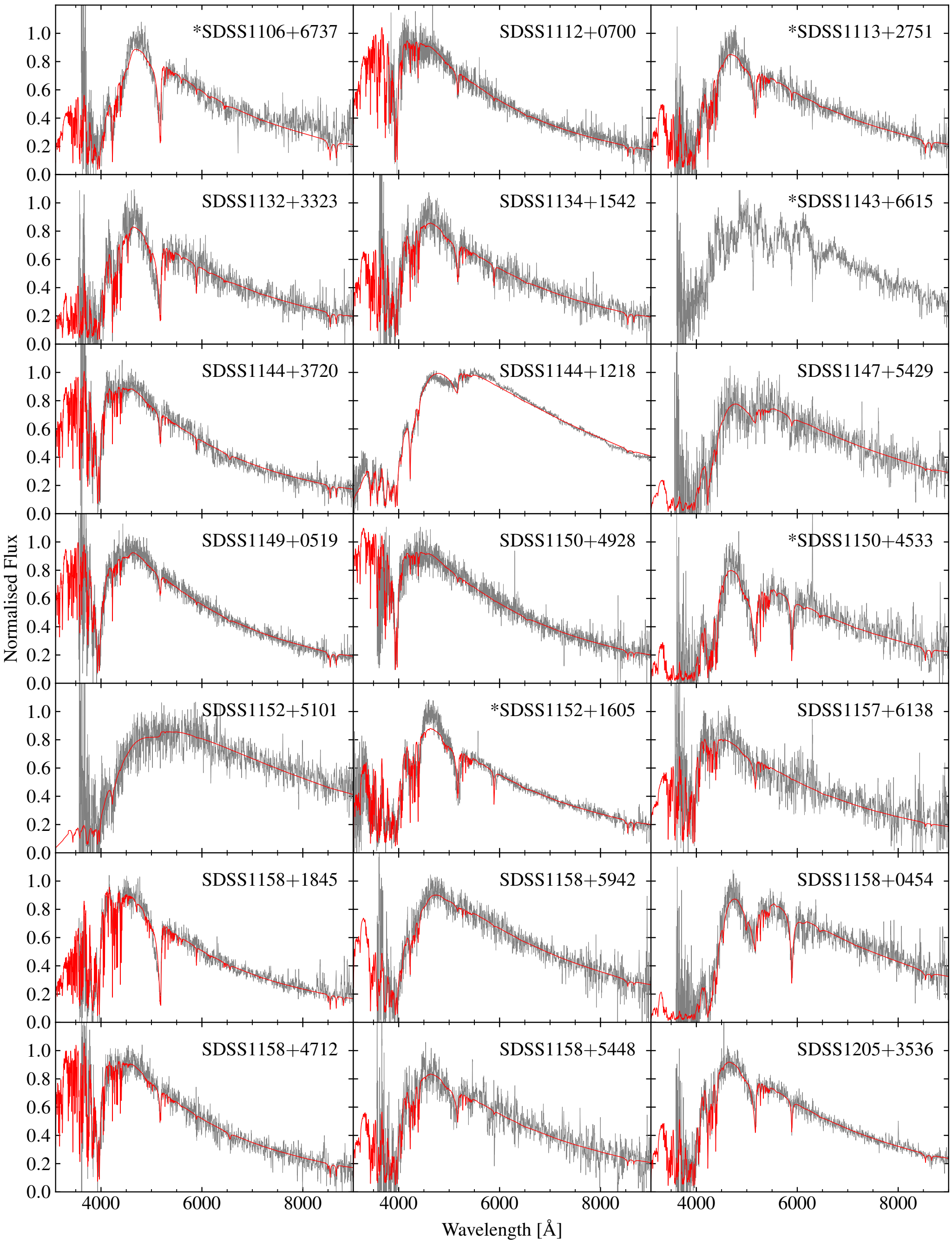

Figure A.6: Figure A.1 continued.

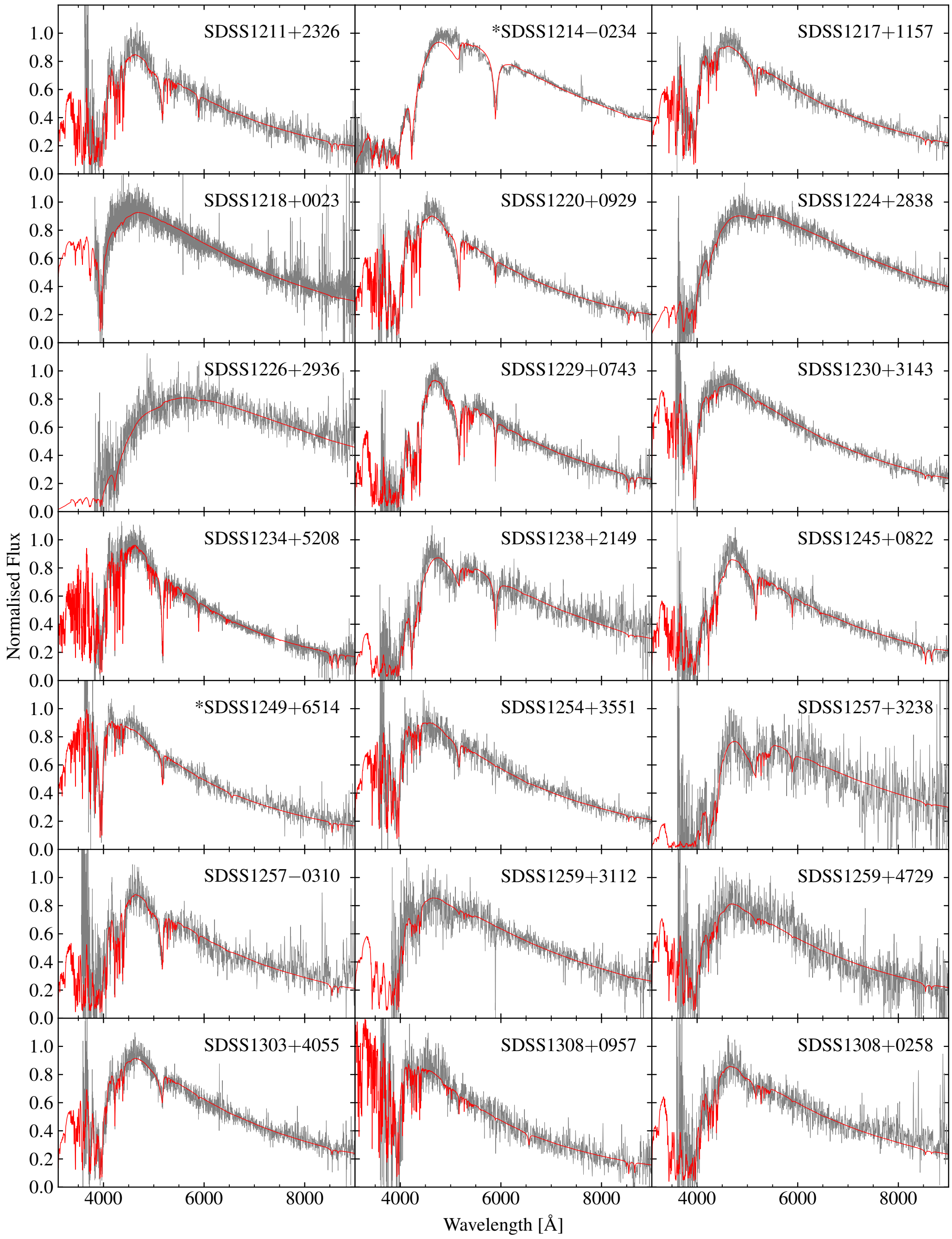

Figure A.7: Figure A.1 continued.

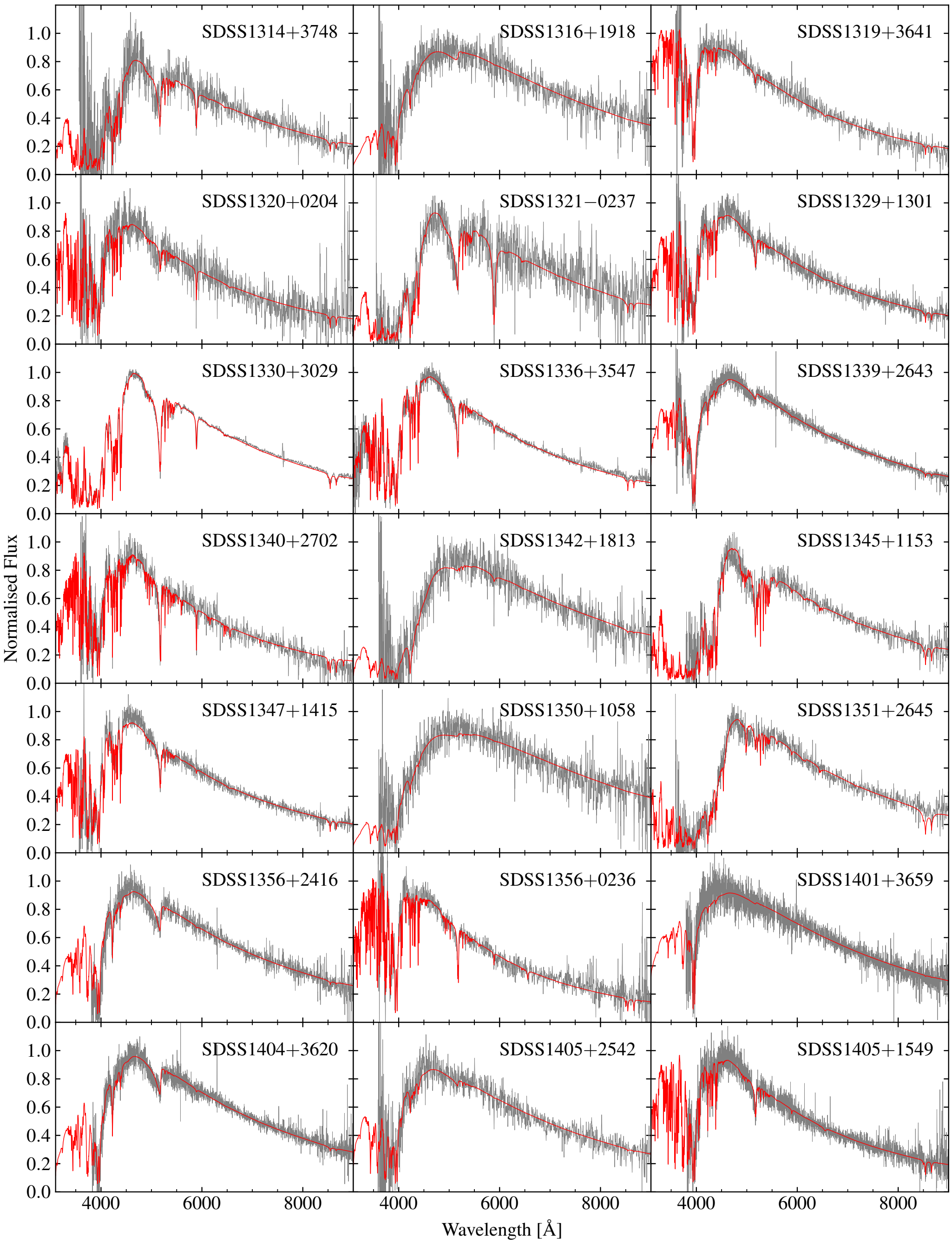

Figure A.8: Figure A.1 continued.

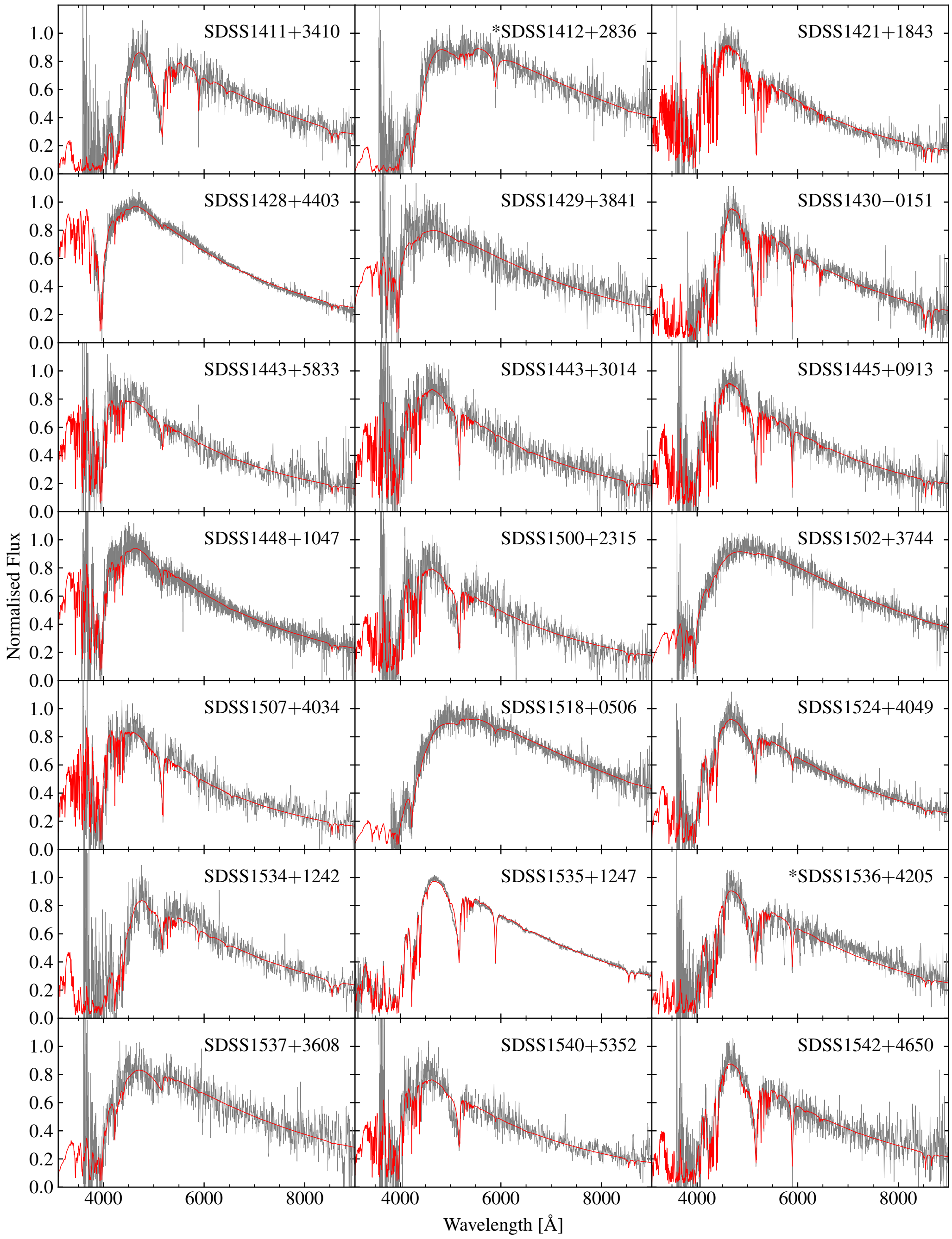

Figure A.9: Figure A.1 continued.

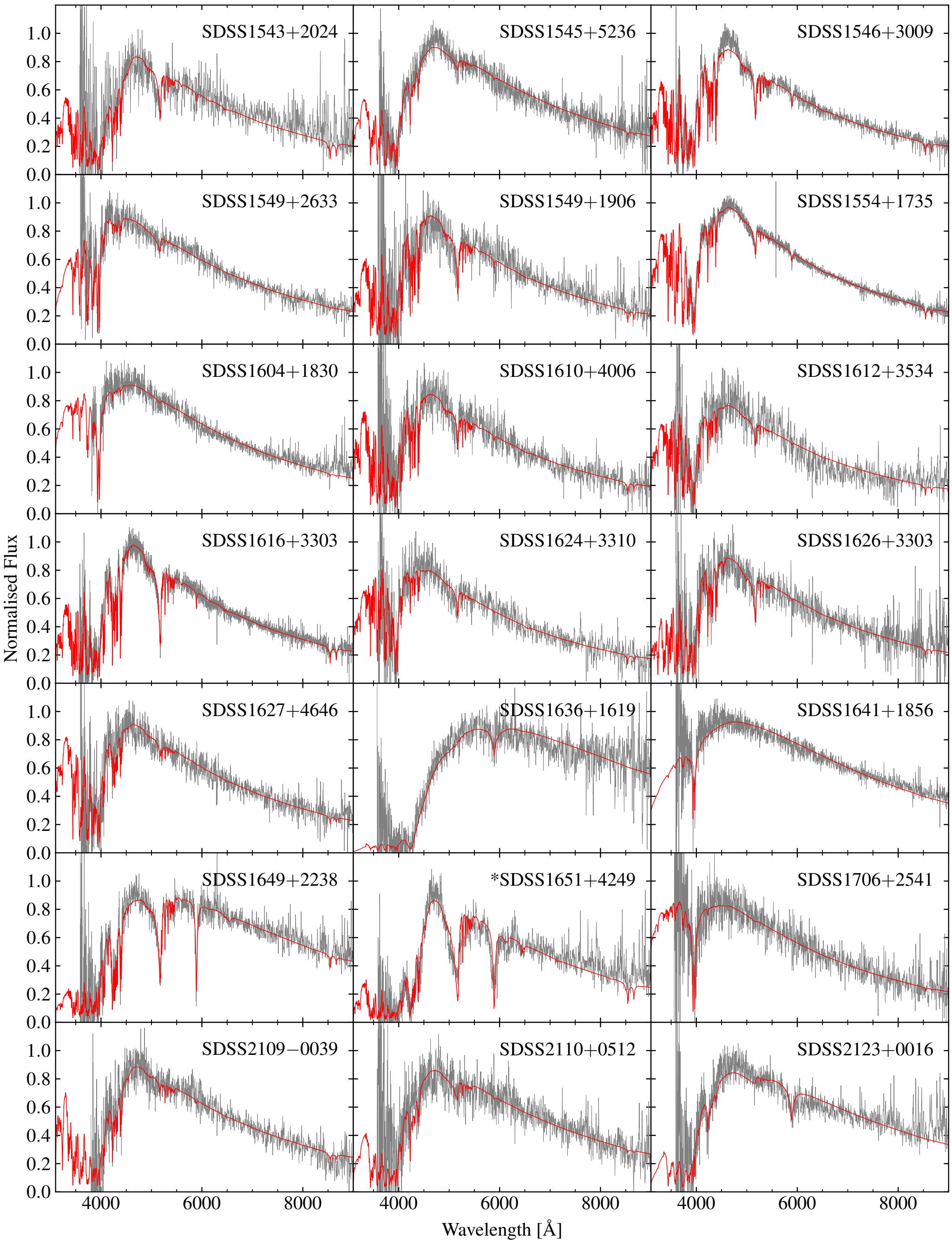

Figure A.10: Figure A.1 continued.

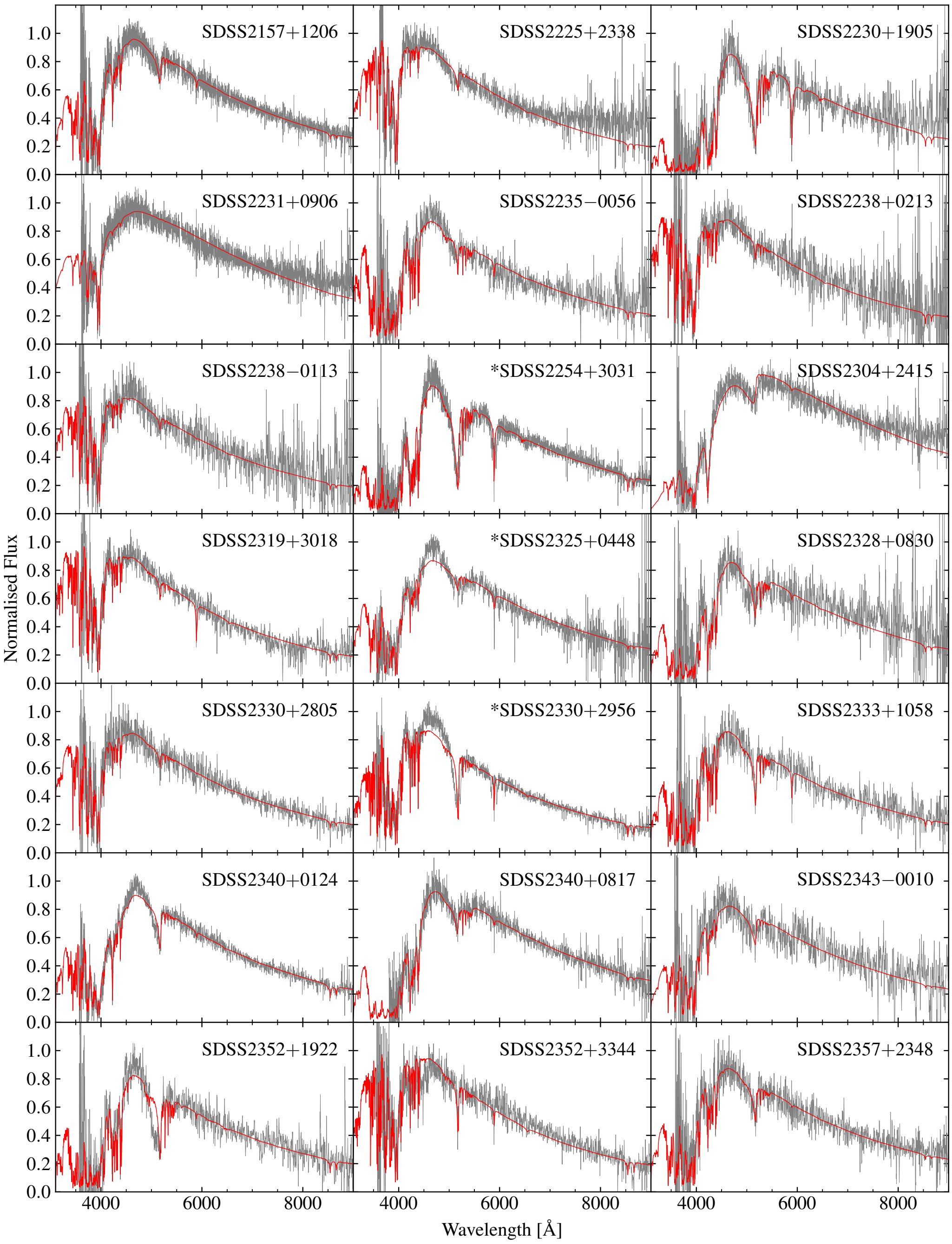

Figure A.11: Figure A.1 continued.

Appendix B

DZ sample tables

- B.1: DZ photometry
- B.2: $T_{\rm eff}$ and abundances from spectroscopic fits
- B.3: Convection zone sizes and diffusion timescales
- B.4: Distances, proper-motions, and tangential velocities

Table B.1: SDSS PSF photometry for all white dwarfs in our sample. Plate-MJD-fib indicates the SDSS spectrum we used for fitting. N_{SDSS} is the number of SDSS spectra available per object.

SDSS J	Plate-MJD-Fib	N_{SDSS}	u [mag]	g [mag]	r [mag]	i [mag]	z [mag]
000215.64+320914.1	7144-56564-126	2	21.83 ± 0.12	20.53 ± 0.02	20.35 ± 0.02	20.38 ± 0.03	20.33 ± 0.11
000418.68+081929.9	4534-55863-333	1	24.87 ± 0.70	22.33 ± 0.07	21.65 ± 0.06	21.76 ± 0.09	21.70 ± 0.30
000614.53+052039.0	4415-55831-160	1	22.14 ± 0.26	20.51 ± 0.03	20.24 ± 0.04	20.15 ± 0.05	20.28 ± 0.20
001052.56−043014.3	7035-56568-898	1	21.55 ± 0.14	20.32 ± 0.03	20.11 ± 0.03	20.22 ± 0.04	20.28 ± 0.12
001309.43+110949.0	5648-55923-842	1	23.40 ± 0.49	21.61 ± 0.05	21.26 ± 0.05	21.37 ± 0.10	21.54 ± 0.34
001949.25+220926.5	6175-56265-833	1	21.95 ± 0.22	20.39 ± 0.04	19.96 ± 0.03	20.04 ± 0.04	20.14 ± 0.20
003708.41−052532.7	7039-56572-140	2	22.93 ± 0.39	20.09 ± 0.03	19.63 ± 0.02	19.68 ± 0.02	19.78 ± 0.07
004451.68+041819.2	4305-55509-609	1	19.90 ± 0.04	18.77 ± 0.02	18.49 ± 0.02	18.46 ± 0.02	18.56 ± 0.03
004634.22+271737.6	6253-56574-458	1	21.14 ± 0.11	20.37 ± 0.03	20.26 ± 0.03	20.41 ± 0.05	20.78 ± 0.29
004757.06+162836.5	6204-56220-386	1	25.13 ± 0.79	20.87 ± 0.04	20.39 ± 0.03	20.52 ± 0.04	20.38 ± 0.14
005247.16+184649.5	5702-56221-615	1	25.92 ± 0.72	21.57 ± 0.07	21.12 ± 0.06	21.06 ± 0.07	20.75 ± 0.17
005304.14+311555.8	6872-56540-171	1	22.70 ± 0.51	21.30 ± 0.05	21.06 ± 0.05	21.10 ± 0.08	21.14 ± 0.30
005649.27+245335.4	6278-56266-122	1	24.80 ± 0.85	21.54 ± 0.05	21.01 ± 0.04	20.95 ± 0.06	21.43 ± 0.34
010728.47+265019.9	6255-56240-896	1	23.27 ± 0.64	19.36 ± 0.02	18.83 ± 0.01	18.67 ± 0.02	18.78 ± 0.05
010825.79−053755.6	7045-56577-456	2	22.05 ± 0.21	20.39 ± 0.03	20.12 ± 0.02	20.02 ± 0.05	20.36 ± 0.11
011421.17+350547.1	6598-56574-832	1	23.25 ± 0.58	20.96 ± 0.03	20.60 ± 0.03	20.66 ± 0.05	20.39 ± 0.14
011646.10+205001.9	5134-55868-352	1	19.88 ± 0.03	18.21 ± 0.02	17.99 ± 0.01	18.08 ± 0.01	18.19 ± 0.03
011759.83+002138.3	4227-55481-937	2	20.19 ± 0.05	19.32 ± 0.03	19.12 ± 0.02	19.17 ± 0.02	19.37 ± 0.06
012620.47+253433.6	5694-56213-606	1	22.65 ± 0.53	20.64 ± 0.04	20.20 ± 0.04	20.10 ± 0.04	20.31 ± 0.16
013504.11+130240.4	4661-55614-318	2	20.84 ± 0.07	19.31 ± 0.02	19.00 ± 0.02	18.93 ± 0.02	18.99 ± 0.05
014300.52+011356.8	4231-55444-824	4	20.31 ± 0.05	19.41 ± 0.03	19.22 ± 0.03	19.24 ± 0.02	19.40 ± 0.06
014415.12+192021.4	5121-55856-186	1	24.29 ± 1.60	20.69 ± 0.05	20.40 ± 0.04	20.34 ± 0.06	20.36 ± 0.18
014441.64+030536.2	4272-55509-246	1	22.81 ± 0.30	21.30 ± 0.04	21.17 ± 0.05	21.22 ± 0.07	21.38 ± 0.30

SDSS J	Plate-MJD-Fib	N_{SDSS}	u [mag]	g [mag]	r [mag]	i [mag]	z [mag]
014834.00−011235.9	4232-55447-294	2	21.81 ± 0.12	20.75 ± 0.03	20.61 ± 0.03	20.64 ± 0.04	20.68 ± 0.13
015008.55+135433.9	1899-53262-118	1	21.03 ± 0.08	20.15 ± 0.03	19.92 ± 0.03	19.89 ± 0.03	19.85 ± 0.10
015748.14+003315.0	0700-52199-627	1	21.30 ± 0.07	19.59 ± 0.02	19.19 ± 0.02	19.21 ± 0.02	19.36 ± 0.05
015849.02−094225.3	7184-56629-144	1	21.66 ± 0.17	20.41 ± 0.03	20.20 ± 0.03	20.20 ± 0.04	20.47 ± 0.17
020018.74+164631.0	5119-55836-838	1	22.59 ± 0.26	20.89 ± 0.03	20.39 ± 0.03	20.49 ± 0.05	20.49 ± 0.15
020128.66+201521.8	5110-55913-721	1	21.71 ± 0.24	20.39 ± 0.03	20.04 ± 0.03	20.18 ± 0.07	20.32 ± 0.18
020809.93−054258.3	4398-55946-982	1	23.64 ± 0.77	21.18 ± 0.06	20.79 ± 0.04	20.74 ± 0.05	20.84 ± 0.19
023407.46−051028.1	4399-55811-626	1	22.61 ± 0.30	21.10 ± 0.04	20.89 ± 0.04	20.98 ± 0.07	21.01 ± 0.26
025206.06−040130.3	7054-56575-682	1	21.42 ± 0.12	20.28 ± 0.03	20.10 ± 0.02	20.21 ± 0.03	20.42 ± 0.13
025253.19+005439.4	0708-52175-411	1	20.64 ± 0.06	19.86 ± 0.03	19.78 ± 0.02	19.83 ± 0.02	19.95 ± 0.08
044751.20+112403.7	2673-54096-587	1	21.23 ± 0.09	20.36 ± 0.02	20.07 ± 0.02	19.98 ± 0.03	20.12 ± 0.11
051212.78−050503.4		0	20.72 ± 0.16	17.91 ± 0.02	17.44 ± 0.02	17.42 ± 0.02	17.49 ± 0.02
072144.23+392843.3	3655-55240-286	1	22.77 ± 0.43	20.55 ± 0.03	20.28 ± 0.04	20.38 ± 0.05	20.34 ± 0.16
073549.19+205720.9	4480-55591-432	1	23.08 ± 0.34	20.53 ± 0.02	19.98 ± 0.02	19.92 ± 0.02	20.09 ± 0.09
073635.22+411828.1	3664-55245-628	1	25.47 ± 0.60	20.32 ± 0.02	19.42 ± 0.03	19.27 ± 0.05	19.31 ± 0.06
073953.46+311204.2	4448-55538-588	1	23.83 ± 0.61	21.38 ± 0.04	20.78 ± 0.04	20.65 ± 0.04	20.44 ± 0.17
074153.45+314620.4	4443-55539-251	1	22.58 ± 0.23	20.50 ± 0.03	20.12 ± 0.02	20.12 ± 0.03	20.19 ± 0.08
074414.66+464912.5	3665-55247-106	2	23.02 ± 0.34	19.47 ± 0.03	18.52 ± 0.01	18.32 ± 0.02	18.26 ± 0.03
074444.03+440845.6	3671-55483-294	1	22.61 ± 0.29	21.18 ± 0.04	21.01 ± 0.05	20.98 ± 0.07	21.21 ± 0.35
074450.24+270132.6	4462-55600-836	1	20.98 ± 0.08	20.28 ± 0.03	20.18 ± 0.03	20.41 ± 0.04	20.49 ± 0.17
074456.21+164041.8	4492-55565-292	1	24.64 ± 0.90	20.88 ± 0.03	20.19 ± 0.02	20.03 ± 0.02	20.07 ± 0.08
075853.46+101347.4	4510-55559-490	1	23.82 ± 0.73	21.42 ± 0.04	20.71 ± 0.03	20.75 ± 0.04	20.96 ± 0.20
080003.90+224210.1	4471-55617-740	1	22.32 ± 0.22	20.71 ± 0.03	20.59 ± 0.04	20.56 ± 0.04	20.74 ± 0.19
080626.70+305555.7	3755-55504-120	1	22.00 ± 0.15	20.67 ± 0.03	20.50 ± 0.03	20.60 ± 0.04	20.63 ± 0.11
080643.94+405837.7	3803-55513-734	1	20.56 ± 0.06	19.08 ± 0.02	18.77 ± 0.02	18.77 ± 0.02	18.86 ± 0.04
080740.69+493059.7	3684-55246-924	1	25.31 ± 0.99	21.31 ± 0.05	20.52 ± 0.04	20.33 ± 0.04	20.19 ± 0.14

SDSS J	Plate-MJD-Fib	N_{SDSS}	u [mag]	g [mag]	r [mag]	i [mag]	z [mag]
081606.19+233030.1	4468-55894-462	1	22.02 ± 0.23	20.96 ± 0.03	20.82 ± 0.03	21.07 ± 0.06	20.87 ± 0.18
081828.12+124717.2	4504-55571-200	1	22.06 ± 0.20	21.00 ± 0.03	20.85 ± 0.04	21.02 ± 0.06	21.23 ± 0.28
082303.82+054656.1		0	19.53 ± 0.03	17.50 ± 0.01	17.16 ± 0.01	17.18 ± 0.02	17.26 ± 0.02
083033.65−031911.0	2828-54438-401	1	20.79 ± 0.08	19.69 ± 0.02	19.49 ± 0.02	19.56 ± 0.03	19.68 ± 0.11
083200.38+410937.9	3808-55513-148	1	23.62 ± 0.79	21.32 ± 0.05	20.63 ± 0.03	20.70 ± 0.05	20.75 ± 0.14
083858.56+232252.9	3373-54940-462	2	20.19 ± 0.05	19.21 ± 0.02	18.86 ± 0.02	18.82 ± 0.02	18.83 ± 0.04
084223.14+140615.9	2427-53815-040	2	19.29 ± 0.03	18.31 ± 0.02	18.17 ± 0.03	18.27 ± 0.02	18.44 ± 0.03
084239.85+153628.8	5286-56225-336	1	22.02 ± 0.14	20.76 ± 0.04	20.48 ± 0.04	20.45 ± 0.05	20.36 ± 0.13
084300.22+561452.8	5153-56577-159	1	21.82 ± 0.19	20.52 ± 0.04	20.31 ± 0.03	20.38 ± 0.05	20.41 ± 0.19
085100.23+154301.6	5292-55926-402	2	20.28 ± 0.05	19.03 ± 0.01	18.73 ± 0.02	18.79 ± 0.03	18.84 ± 0.05
085217.60+340211.3	4602-55644-366	2	23.72 ± 0.56	21.25 ± 0.04	20.44 ± 0.03	20.43 ± 0.04	20.12 ± 0.09
090146.86+075206.8	4868-55895-702	1	21.54 ± 0.12	20.01 ± 0.02	19.80 ± 0.02	19.90 ± 0.03	20.05 ± 0.13
090222.98+362539.6	4645-55623-596	2	22.58 ± 0.32	20.75 ± 0.03	20.46 ± 0.04	20.36 ± 0.06	20.50 ± 0.22
090244.75+100459.6	5296-55922-260	1	21.33 ± 0.09	20.70 ± 0.03	20.62 ± 0.03	20.65 ± 0.05	20.65 ± 0.15
090652.19+114149.9	5296-55922-944	1	22.86 ± 0.27	20.96 ± 0.03	20.79 ± 0.04	20.82 ± 0.04	20.99 ± 0.16
090803.35+513633.1	5729-56598-406	2	20.84 ± 0.06	19.48 ± 0.02	19.25 ± 0.02	19.27 ± 0.02	19.40 ± 0.06
090814.52+411918.3	4603-55999-334	1	22.28 ± 0.18	21.15 ± 0.03	20.92 ± 0.04	20.99 ± 0.05	21.14 ± 0.20
091322.38+262752.0	5779-56338-164	2	22.79 ± 0.25	20.28 ± 0.04	19.79 ± 0.02	19.72 ± 0.03	19.62 ± 0.06
091356.05+412728.6	4641-55947-678	1	23.90 ± 0.53	21.07 ± 0.03	20.63 ± 0.03	20.74 ± 0.04	20.75 ± 0.13
091621.36+254028.4	2087-53415-166	1	21.26 ± 0.09	18.35 ± 0.01	17.47 ± 0.02	17.39 ± 0.02	17.53 ± 0.02
092450.03+430136.4	4639-55944-860	1	23.63 ± 0.35	21.11 ± 0.03	20.89 ± 0.03	20.82 ± 0.05	20.70 ± 0.14
092523.09+313019.0	1938-53379-608	2	21.03 ± 0.09	18.96 ± 0.02	18.61 ± 0.01	18.63 ± 0.02	18.75 ± 0.04
092713.34+493109.3	5731-56363-684	1	22.53 ± 0.20	21.10 ± 0.03	20.74 ± 0.03	20.88 ± 0.04	20.84 ± 0.15
092932.49+424757.9	4639-55944-034	2	21.62 ± 0.08	20.18 ± 0.03	19.91 ± 0.02	19.96 ± 0.03	20.19 ± 0.10
093320.01+633441.2	7447-56746-366	1	23.40 ± 0.35	21.11 ± 0.04	20.82 ± 0.05	20.91 ± 0.06	21.00 ± 0.28
093719.14+522802.2	2404-53764-197	3	20.73 ± 0.07	19.44 ± 0.02	19.17 ± 0.02	19.24 ± 0.03	19.45 ± 0.08

SDSS J	Plate-MJD-Fib	N_{SDSS}	u [mag]	g [mag]	r [mag]	i [mag]	z [mag]
093916.03+413612.9	4571-55629-621	1	23.03 ± 0.34	20.57 ± 0.03	20.18 ± 0.03	20.21 ± 0.03	20.31 ± 0.12
093944.58+501917.6	0901-52641-584	1	22.92 ± 0.29	19.94 ± 0.02	19.48 ± 0.02	19.51 ± 0.02	19.66 ± 0.06
094648.94+202423.2	5783-56017-824	2	21.59 ± 0.10	20.82 ± 0.03	20.63 ± 0.03	20.85 ± 0.04	20.63 ± 0.14
094813.73+300851.2	5801-56328-728	1	21.61 ± 0.15	20.27 ± 0.03	20.03 ± 0.02	20.10 ± 0.03	20.13 ± 0.09
095645.14+591240.6	0453-51915-621	1	18.94 ± 0.03	18.39 ± 0.02	18.41 ± 0.01	18.56 ± 0.02	18.75 ± 0.04
100346.66−003123.1	3783-55246-902	1	22.91 ± 0.33	20.61 ± 0.03	20.06 ± 0.02	20.00 ± 0.03	20.20 ± 0.11
100537.43+224403.1	6459-56273-144	1	23.05 ± 0.33	21.36 ± 0.04	21.12 ± 0.04	21.27 ± 1.08	21.20 ± 0.22
100609.15+175221.3	5332-55981-544	1	22.40 ± 0.19	20.66 ± 0.04	20.18 ± 0.03	20.16 ± 0.04	20.12 ± 0.11
101451.15+282701.6	6462-56326-444	1	23.45 ± 0.52	21.25 ± 0.04	20.70 ± 0.05	20.82 ± 0.06	21.15 ± 0.28
101711.53+344710.5	4568-55600-124	2	21.64 ± 0.12	20.45 ± 0.03	20.25 ± 0.03	20.23 ± 0.04	20.14 ± 0.11
101750.24+241911.6	6465-56279-332	1	21.22 ± 0.08	19.89 ± 0.03	19.77 ± 0.02	19.81 ± 0.03	19.84 ± 0.09
101924.73+353527.6	4564-55570-466	2	22.92 ± 0.41	21.21 ± 0.04	20.89 ± 0.04	21.02 ± 0.06	21.08 ± 0.21
101959.51+204553.4	5872-56027-268	1	23.41 ± 0.43	21.05 ± 0.04	20.58 ± 0.03	20.55 ± 0.04	20.36 ± 0.10
102414.83+453109.9	6659-56607-412	1	21.74 ± 0.16	20.32 ± 0.03	20.04 ± 0.03	20.01 ± 0.03	20.19 ± 0.11
102438.05+101410.5	1598-53033-081	1	23.06 ± 0.38	20.59 ± 0.03	20.03 ± 0.03	20.13 ± 0.05	20.19 ± 0.13
103205.15+133833.4	5343-55999-834	1	24.86 ± 0.78	21.20 ± 0.04	20.78 ± 0.04	20.62 ± 0.05	21.32 ± 0.35
103352.89+180935.3	2593-54175-225	1	21.47 ± 0.11	19.81 ± 0.02	19.45 ± 0.02	19.46 ± 0.03	19.72 ± 0.10
103809.19−003622.4	0274-51913-265	1	17.71 ± 0.01	17.01 ± 0.02	16.94 ± 0.01	17.08 ± 0.01	17.31 ± 0.02
103839.00+043223.8	4773-55648-618	1	22.43 ± 0.24	20.67 ± 0.03	20.30 ± 0.03	20.30 ± 0.03	20.44 ± 0.14
104046.48+240759.5	3250-54883-505	2	21.52 ± 0.10	19.33 ± 0.02	18.83 ± 0.02	18.83 ± 0.02	19.00 ± 0.04
104130.65+343240.7	4635-55615-408	2	21.36 ± 0.11	20.63 ± 0.04	20.59 ± 0.04	20.64 ± 0.05	20.63 ± 0.21
104319.84+351641.6	2025-53431-328	2	20.65 ± 0.07	18.96 ± 0.02	18.65 ± 0.02	18.61 ± 0.02	18.67 ± 0.03
104658.12+132911.3	5350-56009-118	2	23.92 ± 0.63	20.70 ± 0.03	20.07 ± 0.03	20.00 ± 0.03	19.89 ± 0.08
105533.73+372542.7	4630-55623-900	1	22.76 ± 0.28	20.33 ± 0.03	19.75 ± 0.02	19.82 ± 0.03	19.96 ± 0.08
105826.60+314358.3	6445-56366-988	2	19.81 ± 0.04	19.09 ± 0.02	18.95 ± 0.02	19.01 ± 0.02	19.18 ± 0.06
110216.09+282730.7	6435-56341-510	1	23.45 ± 0.51	21.29 ± 0.05	20.87 ± 0.04	20.95 ± 0.07	20.87 ± 0.21

SDSS J	Plate-MJD-Fib	N_{SDSS}	u [mag]	g [mag]	r [mag]	i [mag]	z [mag]
110234.21+021459.2	3243-54910-298	2	21.22 ± 0.08	19.53 ± 0.02	19.20 ± 0.02	19.17 ± 0.02	19.30 ± 0.06
110304.15+414434.9	4620-55652-506	2	21.68 ± 0.16	19.75 ± 0.02	19.40 ± 0.02	19.39 ± 0.02	19.42 ± 0.06
110513.62+500652.6	6700-56384-146	1	21.13 ± 0.10	20.25 ± 0.03	20.19 ± 0.02	20.31 ± 0.05	20.16 ± 0.14
110556.17+022849.0	4741-55704-652	1	22.06 ± 0.21	20.55 ± 0.03	20.17 ± 0.03	20.13 ± 0.04	19.89 ± 0.14
110644.27+673708.6	7111-56741-676	1	22.31 ± 0.26	20.11 ± 0.03	19.67 ± 0.02	19.73 ± 0.03	19.82 ± 0.10
111215.05+070052.3	1004-52723-111	1	20.18 ± 0.05	19.27 ± 0.02	19.24 ± 0.02	19.35 ± 0.02	19.41 ± 0.06
111330.26+275131.4	6435-56341-036	1	22.26 ± 0.17	20.75 ± 0.03	20.42 ± 0.03	20.50 ± 0.05	20.35 ± 0.14
113209.59+332353.0	4619-55599-069	2	24.58 ± 0.91	21.12 ± 0.04	20.76 ± 0.04	20.85 ± 0.06	21.04 ± 0.23
113410.85+154245.9	5373-56010-938	1	22.53 ± 0.22	21.13 ± 0.03	20.98 ± 0.04	21.03 ± 0.07	20.71 ± 0.21
114333.46+661532.0	7114-56748-973	1	22.39 ± 0.23	20.56 ± 0.03	20.01 ± 0.03	19.95 ± 0.04	20.13 ± 0.12
114408.04+372007.8	4653-55622-700	1	21.08 ± 0.08	20.29 ± 0.02	20.19 ± 0.03	20.29 ± 0.04	20.26 ± 0.13
114441.92+121829.2	1608-53138-515	1	20.71 ± 0.08	18.42 ± 0.02	17.85 ± 0.02	17.76 ± 0.02	17.76 ± 0.02
114709.09+542940.8	6697-56419-035	1	25.84 ± 0.54	21.55 ± 0.05	21.03 ± 0.05	20.92 ± 0.06	20.95 ± 0.26
114944.94+051947.7	4848-55955-088	1	20.50 ± 0.05	19.60 ± 0.02	19.48 ± 0.02	19.64 ± 0.02	19.74 ± 0.07
115015.73+492843.7	6684-56412-006	1	20.50 ± 0.07	19.96 ± 0.03	19.89 ± 0.03	19.93 ± 0.03	19.97 ± 0.11
115029.52+453314.0	6642-56396-549	2	24.28 ± 0.93	21.66 ± 0.06	21.07 ± 0.06	21.02 ± 0.07	20.98 ± 0.20
115207.15+510126.2	6683-56416-348	1	24.86 ± 0.81	21.44 ± 0.05	20.85 ± 0.04	20.70 ± 0.05	20.67 ± 0.16
115224.51+160546.7	5383-56013-772	2	21.73 ± 0.12	20.18 ± 0.03	19.95 ± 0.02	20.02 ± 0.03	20.08 ± 0.09
115748.34+613845.9	7106-56663-173	1	22.47 ± 0.39	21.42 ± 0.06	21.27 ± 0.06	21.24 ± 0.12	21.19 ± 0.42
115809.38+184557.3	5881-56038-014	1	21.55 ± 0.12	20.04 ± 0.03	19.88 ± 0.03	19.95 ± 0.03	20.11 ± 0.09
115809.88+594210.3	7098-56661-152	1	22.14 ± 0.19	20.59 ± 0.02	20.30 ± 0.02	20.29 ± 0.03	20.09 ± 0.11
115818.76+045447.5	4747-55652-590	1	23.09 ± 0.32	20.96 ± 0.04	20.25 ± 0.03	20.13 ± 0.03	20.27 ± 0.09
115822.31+471214.9	6644-56384-812	1	21.31 ± 0.09	20.67 ± 0.03	20.62 ± 0.04	20.72 ± 0.06	20.81 ± 0.22
115844.35+544837.5	6839-56425-090	1	22.78 ± 0.35	21.02 ± 0.04	20.77 ± 0.04	20.80 ± 0.06	20.77 ± 0.24
120548.97+353642.4	4610-55621-722	2	24.07 ± 1.09	20.39 ± 0.03	20.09 ± 0.04	20.11 ± 0.05	20.40 ± 0.14
121106.42+232623.0	5974-56314-668	1	22.28 ± 0.29	20.80 ± 0.03	20.52 ± 0.04	20.56 ± 0.06	20.49 ± 0.14

SDSS J	Plate-MJD-Fib	N_{SDSS}	u [mag]	g [mag]	r [mag]	i [mag]	z [mag]
121456.39−023402.7	0333-52313-399	1	20.87 ± 0.06	18.32 ± 0.02	17.75 ± 0.01	17.56 ± 0.01	17.51 ± 0.02
121731.31+115715.9	5394-56001-974	2	22.03 ± 0.24	20.26 ± 0.04	20.07 ± 0.04	20.11 ± 0.04	20.27 ± 0.12
121837.12+002303.7	2568-54153-352	3	20.42 ± 0.05	19.52 ± 0.02	19.35 ± 0.02	19.32 ± 0.02	19.46 ± 0.06
122035.75+092948.1	5396-55947-158	1	22.11 ± 0.26	20.89 ± 0.04	20.64 ± 0.04	20.71 ± 0.05	20.79 ± 0.18
122437.07+283853.0	5976-56356-818	2	22.40 ± 0.26	19.77 ± 0.02	19.22 ± 0.03	19.08 ± 0.03	19.01 ± 0.05
122656.39+293643.9	2234-53823-273	2	23.09 ± 0.47	20.55 ± 0.03	19.74 ± 0.02	19.60 ± 0.03	19.63 ± 0.09
122943.92+074311.8	5402-55927-698	2	23.31 ± 0.58	20.42 ± 0.04	20.07 ± 0.03	20.07 ± 0.03	20.33 ± 0.15
123024.03+314339.7	6479-56364-318	1	21.56 ± 0.14	20.37 ± 0.02	20.18 ± 0.03	20.21 ± 0.04	20.20 ± 0.12
123415.21+520808.1	0885-52379-269	1	19.54 ± 0.04	18.42 ± 0.03	18.30 ± 0.02	18.42 ± 0.01	18.68 ± 0.03
123826.92+214937.7	5985-56089-738	2	24.21 ± 0.67	20.80 ± 0.04	20.32 ± 0.03	20.21 ± 0.03	20.16 ± 0.09
124547.10+082231.4	5407-55926-966	1	22.56 ± 0.28	20.94 ± 0.03	20.52 ± 0.03	20.50 ± 0.04	20.97 ± 0.23
124937.50+651407.6	6963-56724-634	1	21.16 ± 0.10	20.44 ± 0.03	20.39 ± 0.03	20.46 ± 0.04	21.02 ± 0.27
125454.93+355145.7	3975-55321-364	1	21.81 ± 0.17	20.60 ± 0.03	20.45 ± 0.03	20.41 ± 0.04	20.51 ± 0.13
125710.13+323848.5	6485-56342-980	1	24.02 ± 0.87	21.61 ± 0.05	20.96 ± 0.05	20.90 ± 0.08	20.95 ± 0.23
125720.87−031025.1	3794-55241-204	1	22.17 ± 0.22	20.64 ± 0.04	20.28 ± 0.03	20.35 ± 0.04	20.74 ± 0.22
125922.03+311215.2	1994-53845-010	1	21.50 ± 0.11	19.78 ± 0.02	19.44 ± 0.02	19.42 ± 0.02	19.50 ± 0.06
125945.32+472953.6	6618-56401-742	1	23.54 ± 0.80	20.85 ± 0.05	20.58 ± 0.04	20.71 ± 0.08	20.81 ± 0.32
130328.06+405545.5	4706-55705-506	1	20.93 ± 0.10	19.73 ± 0.04	19.54 ± 0.06	19.51 ± 0.03	19.62 ± 0.09
130826.36+095724.0	5421-55980-840	1	21.69 ± 0.15	21.05 ± 0.04	20.99 ± 0.04	21.08 ± 0.07	21.13 ± 0.27
130830.03+025844.5	4007-55327-584	1	22.52 ± 0.26	20.83 ± 0.03	20.50 ± 0.04	20.42 ± 0.05	20.54 ± 0.17
131420.49+374806.5	3978-55330-030	1	22.74 ± 0.30	20.83 ± 0.04	20.48 ± 0.03	20.44 ± 0.03	20.52 ± 0.11
131612.86+191806.5	5867-56034-712	2	23.89 ± 0.58	21.02 ± 0.04	20.55 ± 0.03	20.51 ± 0.04	20.43 ± 0.11
131900.18+364149.8	3979-55597-929	1	20.95 ± 0.07	20.20 ± 0.03	20.15 ± 0.02	20.26 ± 0.03	20.47 ± 0.15
132005.53+020419.0	4006-55328-686	1	21.95 ± 0.19	21.04 ± 0.04	20.90 ± 0.05	21.10 ± 0.08	21.35 ± 0.39
132144.04−023751.4	4049-55591-276	1	22.50 ± 0.27	20.73 ± 0.03	20.13 ± 0.03	20.04 ± 0.04	19.99 ± 0.12
132941.79+130131.9	5432-56008-689	1	21.13 ± 0.11	19.95 ± 0.03	19.83 ± 0.02	19.89 ± 0.03	20.12 ± 0.10

SDSS J	Plate-MJD-Fib	N_{SDSS}	u [mag]	g [mag]	r [mag]	i [mag]	z [mag]
133059.26+302953.2	2110-53467-148	1	18.28 ± 0.02	16.32 ± 0.02	15.89 ± 0.01	15.91 ± 0.02	16.09 ± 0.03
133624.26+354751.2	2101-53858-254	1	19.48 ± 0.03	17.85 ± 0.02	17.64 ± 0.01	17.71 ± 0.03	17.83 ± 0.02
133905.97+264322.9	6002-56104-590	1	20.00 ± 0.03	18.98 ± 0.02	18.77 ± 0.01	18.82 ± 0.02	18.95 ± 0.04
134050.31+270219.0	6002-56104-622	1	21.52 ± 0.12	20.86 ± 0.03	20.81 ± 0.04	20.89 ± 0.06	20.98 ± 0.22
134203.60+181332.8	5439-56045-828	1	23.61 ± 0.52	21.13 ± 0.04	20.61 ± 0.04	20.53 ± 0.04	20.67 ± 0.14
134520.99+115357.6	1701-53142-440	1	22.64 ± 0.30	19.92 ± 0.02	19.39 ± 0.02	19.45 ± 0.02	19.54 ± 0.06
134711.47+141528.0	5441-56017-258	1	21.20 ± 0.07	19.70 ± 0.01	19.50 ± 0.02	19.51 ± 0.02	19.53 ± 0.06
135054.01+105808.0	5440-55983-996	1	24.40 ± 0.94	20.97 ± 0.04	20.37 ± 0.03	20.31 ± 0.03	20.34 ± 0.11
135123.86+264546.5	6006-56105-212	2	22.99 ± 0.40	20.38 ± 0.02	19.87 ± 0.02	19.86 ± 0.03	19.86 ± 0.11
135632.62+241606.0	2119-53792-216	1	20.38 ± 0.05	19.05 ± 0.02	18.73 ± 0.02	18.78 ± 0.02	18.87 ± 0.04
135654.01+023641.5	4036-55330-762	1	20.44 ± 0.06	19.53 ± 0.02	19.50 ± 0.02	19.61 ± 0.03	19.47 ± 0.09
140137.31+365909.9	1642-53115-198	1	19.94 ± 0.03	18.81 ± 0.02	18.53 ± 0.02	18.52 ± 0.02	18.55 ± 0.03
140410.72+362056.8	2931-54590-302	2	20.01 ± 0.04	18.83 ± 0.03	18.46 ± 0.02	18.51 ± 0.02	18.70 ± 0.03
140525.20+254212.4	6008-56093-808	1	23.29 ± 0.41	20.96 ± 0.03	20.72 ± 0.03	20.72 ± 0.05	20.78 ± 0.19
140557.09+154940.5	2744-54272-586	2	20.00 ± 0.04	18.93 ± 0.02	18.78 ± 0.02	18.91 ± 0.02	19.11 ± 0.04
141140.27+341039.4	3863-55280-502	1	24.96 ± 0.82	20.79 ± 0.03	20.08 ± 0.02	20.02 ± 0.03	19.84 ± 0.11
141211.53+283618.7	6497-56329-380	1	25.00 ± 0.90	21.39 ± 0.05	20.59 ± 0.03	20.52 ± 0.05	20.29 ± 0.13
142120.11+184351.6	5897-56042-460	2	22.06 ± 0.14	20.35 ± 0.03	20.08 ± 0.02	20.19 ± 0.04	20.34 ± 0.11
142833.77+440346.1	2907-54580-126	1	17.90 ± 0.02	17.05 ± 0.02	16.88 ± 0.02	16.94 ± 0.02	17.05 ± 0.02
142939.38+384113.2	4713-56044-876	1	22.26 ± 0.16	20.64 ± 0.03	20.40 ± 0.03	20.33 ± 0.03	20.38 ± 0.10
143007.15−015129.5	0919-52409-358	1	21.48 ± 0.12	19.48 ± 0.02	19.03 ± 0.02	18.99 ± 0.02	19.10 ± 0.06
144301.55+583301.6	6806-56419-314	1	22.50 ± 0.29	21.35 ± 0.04	21.26 ± 0.06	21.34 ± 0.10	22.08 ± 0.73
144354.13+301413.3	3874-55280-732	1	22.67 ± 0.25	21.48 ± 0.05	21.27 ± 0.05	21.40 ± 0.08	21.36 ± 0.25
144535.03+091340.4	5472-55976-842	1	22.54 ± 0.37	21.31 ± 0.05	21.03 ± 0.05	21.20 ± 0.07	21.49 ± 0.36
144804.49+104709.0	5475-56011-394	2	20.18 ± 0.04	18.81 ± 0.02	18.65 ± 0.02	18.67 ± 0.02	18.75 ± 0.03
150028.02+231554.0	6020-56087-828	1	24.10 ± 0.88	21.60 ± 0.05	21.38 ± 0.06	21.46 ± 0.10	21.82 ± 0.56

SDSS J	Plate-MJD-Fib	N_{SDSS}	u [mag]	g [mag]	r [mag]	i [mag]	z [mag]
150228.70+374452.9	5168-56035-732	2	21.58 ± 0.09	19.79 ± 0.02	19.45 ± 0.02	19.42 ± 0.03	19.51 ± 0.05
150739.03+403408.9	6054-56089-176	1	22.15 ± 0.20	21.08 ± 0.04	20.94 ± 0.05	21.08 ± 0.09	21.43 ± 0.39
151835.63+050627.4	1834-54562-231	1	21.94 ± 0.17	19.45 ± 0.02	18.86 ± 0.02	18.79 ± 0.02	18.77 ± 0.04
152449.58+404938.1	2936-54626-537	4	21.79 ± 0.11	20.15 ± 0.02	19.76 ± 0.02	19.80 ± 0.03	19.92 ± 0.09
153407.58+124254.4	4891-55736-812	1	23.18 ± 0.54	21.59 ± 0.06	21.15 ± 0.05	21.10 ± 0.07	20.99 ± 0.26
153505.75+124744.2	2754-54240-570	1	18.04 ± 0.02	15.98 ± 0.02	15.50 ± 0.02	15.45 ± 0.02	15.50 ± 0.01
153642.53+420519.2	6050-56089-620	1	23.32 ± 0.65	20.84 ± 0.04	20.30 ± 0.03	20.17 ± 0.04	20.33 ± 0.16
153745.52+360818.6	4974-56038-738	1	23.36 ± 0.42	21.11 ± 0.03	20.67 ± 0.03	20.66 ± 0.04	20.85 ± 0.14
154022.79+535239.8	6708-56452-298	1	22.89 ± 0.28	21.16 ± 0.04	20.95 ± 0.04	20.99 ± 0.05	21.25 ± 0.24
154201.75+465020.2	6032-56067-716	1	23.01 ± 0.53	20.85 ± 0.04	20.42 ± 0.03	20.42 ± 0.04	20.70 ± 0.19
154349.79+202442.9	3943-55336-100	1	23.08 ± 0.44	21.47 ± 0.04	21.09 ± 0.05	21.21 ± 0.08	21.22 ± 0.34
154510.31+523618.4	6715-56449-768	1	21.59 ± 0.10	20.05 ± 0.03	19.70 ± 0.02	19.71 ± 0.02	19.80 ± 0.07
154625.33+300946.2	4726-55712-632	2	21.43 ± 0.08	19.80 ± 0.02	19.53 ± 0.02	19.64 ± 0.02	19.80 ± 0.06
154913.45+263301.1	3946-55659-698	1	21.45 ± 0.10	20.59 ± 0.03	20.55 ± 0.04	20.41 ± 0.04	20.59 ± 0.19
154933.23+190646.7	3931-55350-572	1	22.63 ± 0.33	21.32 ± 0.05	20.95 ± 0.05	20.97 ± 0.07	20.85 ± 0.26
155429.00+173545.9	2170-53875-154	1	18.67 ± 0.02	17.59 ± 0.02	17.42 ± 0.01	17.47 ± 0.01	17.65 ± 0.02
160429.80+183035.4	3289-54910-379	1	20.70 ± 0.06	19.70 ± 0.02	19.55 ± 0.02	19.61 ± 0.02	19.76 ± 0.09
161026.10+400619.7	6052-56092-036	1	22.58 ± 0.21	21.00 ± 0.03	20.75 ± 0.03	20.92 ± 0.05	21.09 ± 0.24
161248.17+353434.8	4964-55749-238	1	22.38 ± 0.21	21.31 ± 0.04	21.30 ± 0.05	21.31 ± 0.07	21.26 ± 0.97
161603.00+330301.3	4960-55747-224	2	21.02 ± 0.08	19.25 ± 0.02	18.98 ± 0.02	19.07 ± 0.02	19.15 ± 0.05
162408.57+331019.0	4955-55750-650	1	22.26 ± 0.18	21.12 ± 0.03	20.96 ± 0.04	21.06 ± 0.06	20.76 ± 0.15
162612.73+330308.2	4955-55750-774	1	22.13 ± 0.25	20.99 ± 0.04	20.79 ± 0.04	20.88 ± 0.06	20.50 ± 0.15
162703.34+464658.2	6029-56099-975	2	22.01 ± 0.15	20.42 ± 0.02	20.13 ± 0.02	20.15 ± 0.03	20.34 ± 0.11
163601.33+161907.1	4063-55364-316	2	23.43 ± 0.51	20.64 ± 0.03	19.53 ± 0.02	19.29 ± 0.02	19.30 ± 0.05
164104.94+185602.1	4062-55383-728	1	21.83 ± 0.13	20.22 ± 0.02	19.85 ± 0.02	19.75 ± 0.02	19.81 ± 0.07
164939.22+223807.2	4182-55446-900	1	23.67 ± 0.46	21.00 ± 0.03	20.35 ± 0.02	20.14 ± 0.03	20.16 ± 0.09

SDSS J	Plate-MJD-Fib	N_{SDSS}	u [mag]	g [mag]	r [mag]	i [mag]	z [mag]
165101.72+424955.5	6031-56091-046	1	22.51 ± 0.23	19.80 ± 0.02	19.20 ± 0.01	19.02 ± 0.01	19.12 ± 0.05
170638.11+254111.7	5014-55717-420	1	25.15 ± 1.59	20.98 ± 0.04	20.91 ± 0.06	20.96 ± 0.09	20.54 ± 0.24
210916.51−003921.6	0985-52431-104	1	21.86 ± 0.15	20.06 ± 0.02	19.76 ± 0.02	19.76 ± 0.02	19.67 ± 0.07
211045.34+051214.8	4078-55358-358	1	23.32 ± 0.39	21.53 ± 0.04	21.15 ± 0.04	21.07 ± 0.05	21.10 ± 0.21
212312.20+001653.5	4192-55469-974	3	22.40 ± 0.18	20.32 ± 0.02	19.90 ± 0.02	19.76 ± 0.03	19.62 ± 0.07
215752.30+120603.1	5063-55831-628	1	21.26 ± 0.10	19.74 ± 0.02	19.41 ± 0.02	19.35 ± 0.02	19.38 ± 0.05
222503.70+233855.1	6299-56478-666	1	21.19 ± 0.16	19.49 ± 0.02	19.27 ± 0.02	19.27 ± 0.03	19.54 ± 0.12
223014.70+190514.4	5025-55836-498	1	23.21 ± 0.56	20.87 ± 0.04	20.26 ± 0.03	20.17 ± 0.04	20.27 ± 0.15
223101.11+090635.1	5057-56209-944	2	20.70 ± 0.09	19.29 ± 0.02	18.94 ± 0.01	18.84 ± 0.01	18.78 ± 0.04
223507.65−005607.7	4203-55447-092	1	22.27 ± 0.22	20.49 ± 0.03	20.21 ± 0.02	20.30 ± 0.04	20.42 ± 0.15
223811.10+021352.9	4295-55858-413	1	21.57 ± 0.14	20.73 ± 0.03	20.54 ± 0.03	20.55 ± 0.04	20.32 ± 0.12
223815.97−011336.9	4204-55470-321	1	22.38 ± 0.26	20.78 ± 0.04	20.59 ± 0.04	20.62 ± 0.05	20.68 ± 0.17
225448.83+303107.1	6507-56478-276	1	22.46 ± 0.28	19.86 ± 0.02	19.33 ± 0.02	19.24 ± 0.02	19.30 ± 0.06
230414.48+241554.0	6589-56536-655	1	22.02 ± 0.16	19.85 ± 0.02	19.17 ± 0.02	19.04 ± 0.02	18.96 ± 0.05
231937.39+301848.4	6583-56566-754	2	21.67 ± 0.14	20.87 ± 0.03	20.81 ± 0.04	20.86 ± 0.06	20.71 ± 0.18
232538.93+044813.1	4408-55888-256	1	21.44 ± 0.15	19.88 ± 0.02	19.58 ± 0.03	19.68 ± 0.04	19.69 ± 0.11
232833.31+083028.4	6164-56181-140	1	23.21 ± 0.56	21.59 ± 0.05	21.01 ± 0.05	21.04 ± 0.10	21.08 ± 0.30
233054.31+280517.4	6514-56487-489	1	22.08 ± 0.26	20.77 ± 0.03	20.56 ± 0.04	20.53 ± 0.06	20.35 ± 0.19
233056.81+295652.6	6501-56563-406	1	21.34 ± 0.09	19.84 ± 0.02	19.64 ± 0.02	19.71 ± 0.02	19.95 ± 0.10
233320.38+105830.2	6157-56238-852	1	23.40 ± 0.88	21.46 ± 0.04	21.18 ± 0.04	21.27 ± 0.07	21.31 ± 0.27
234034.61+012416.6	4280-55503-444	1	21.10 ± 0.08	19.40 ± 0.02	19.08 ± 0.02	19.15 ± 0.02	19.20 ± 0.04
234048.74+081753.3	2628-54326-108	3	22.68 ± 1.03	20.25 ± 0.02	19.81 ± 0.02	19.86 ± 0.03	19.93 ± 0.07
234307.67−001016.3	4214-55451-438	1	22.11 ± 0.17	20.46 ± 0.03	20.07 ± 0.02	20.11 ± 0.03	20.08 ± 0.10
235224.26+192247.3	6127-56274-424	1	24.80 ± 1.33	21.35 ± 0.05	20.91 ± 0.05	20.99 ± 0.07	21.48 ± 0.92
235249.13+334439.2	7143-56572-070	1	21.74 ± 0.11	20.95 ± 0.03	20.75 ± 0.03	20.82 ± 0.04	20.71 ± 0.17
235715.03+234848.9	6513-56543-314	1	23.00 ± 0.55	21.26 ± 0.05	20.91 ± 0.05	20.92 ± 0.07	21.20 ± 0.32

Table B.2: Derived parameters from atmospheric modelling of the SDSS and WHT spectra. Abundances are relative to He in units of dex.

SDSS J	$T_{\rm eff}$ [K]	Ca	Mg	Fe	Na	Cr	Ti	Ni	H
0002+3209	6410 ± 180	−9.05	−8.14	−7.84	-	-	-	-	-
0004+0819	5820 ± 380	−8.72	−7.51	−7.51	−8.80	-	-	-	-
0006+0520	6790 ± 170	−9.00	−8.09	−8.39	-	-	-	-	-
0010−0430	6960 ± 160	−8.38	−6.92	−7.12	-	-	-	-	-
0013+1109	5830 ± 320	−9.11	−8.20	−8.10	-	-	-	-	-
0019+2209	5970 ± 150	−9.34	−8.53	−8.58	−9.42	-	-	-	-
0037−0525	5630 ± 120	−8.79	−7.58	−7.68	−9.07	-	-	-	-
0044+0418	6050 ± 70	−9.82	−8.81	−8.71	-	-	-	-	-
0046+2717	7640 ± 290	−7.65	−6.19	−6.84	-	−7.80	-	-	-
0047+1628	6620 ± 180	−7.68	−6.77	−6.47	−8.66	−8.53	-	-	-
0052+1846	5660 ± 290	−9.04	−7.83	−7.53	-	−9.59	-	-	-
0053+3115	6180 ± 320	−8.87	−8.26	−8.66	-	-	-	-	-
0056+2453	5440 ± 310	−9.62	−8.61	−8.71	-	-	-	-	-
0107+2650	6190 ± 140	−8.44	−7.93	−7.73	−8.22	-	-	-	-
0108−0537	6010 ± 130	−8.79	−8.18	−8.08	−9.27	-	-	-	-
0114+3505	6370 ± 210	−8.51	−7.30	−7.20	-	−9.06	-	-	-
0116+2050	6207 ± 80	−8.81	−7.65	−7.60	−9.29	-	−9.74	−8.76	-
0117+0021	6800 ± 80	−8.80	−7.50	−7.60	-	−9.48	-	-	-
0126+2534	5320 ± 120	−9.95	−8.94	−8.64	-	-	-	-	-
0135+1302	5800 ± 100	−9.50	−8.70	−8.69	-	-	-	-	-
0143+0113	6700 ± 80	−8.50	−7.10	−7.30	−8.68	-	-	-	−3.1
0144+1920	6500 ± 190	−8.50	−7.34	−7.39	−8.18	-	-	-	-
0144+0305	6950 ± 330	−8.37	−7.21	−7.26	-	-	-	-	-

SDSS J	T_{eff} [K]	Ca	Mg	Fe	Na	Cr	Ti	Ni	H
0148−0112	6830 ± 210	−8.82	−7.56	−7.31	-	-	-	-	-
0150+1354	6310 ± 160	−7.75	−6.54	−7.24	−8.03	−10.10	-	-	−1.7
0157+0033	6110 ± 140	−8.20	−7.39	−7.69	-	-	-	-	-
0158−0942	5940 ± 170	−9.52	−8.61	−8.41	-	-	-	-	-
0200+1646	5810 ± 180	−8.92	−7.61	−7.91	−9.00	-	-	-	-
0201+2015	6180 ± 140	−8.96	−7.65	−8.25	-	-	-	-	-
0208−0542	5800 ± 350	−8.54	−7.53	−7.33	−8.82	-	-	-	-
0234−0510	7050 ± 340	−8.27	−6.91	−7.21	-	-	-	-	-
0252−0401	6950 ± 160	−8.57	−6.96	−7.46	−8.25	−8.62	-	-	-
0252+0054	7500 ± 190	−8.35	−7.24	−7.14	−7.83	-	-	-	≤−4.3
0447+1124	6530 ± 190	−8.77	−7.26	−8.06	-	-	-	-	−2.5
0512−0505	5563 ± 60	−8.99	−8.05	−7.79	−9.65	−10.09	-	-	-
0721+3928	6280 ± 150	−8.90	−7.79	−8.09	-	-	-	-	-
0735+2057	6110 ± 180	−7.75	−6.74	−6.84	−8.33	-	-	-	-
0736+4118	5100 ± 100	−8.50	−7.69	−7.69	−9.68	−8.95	-	-	−3.0
0739+3112	5080 ± 320	−9.50	−8.29	−8.39	-	-	-	-	-
0741+3146	5592 ± 140	−9.55	−8.94	−7.50	-	−9.60	−10.06	−9.09	-
0744+4649	5028 ± 70	−8.36	−7.99	−8.17	−9.26	−9.69	−9.38	-	-
0744+4408	6370 ± 230	−8.75	−7.64	−7.54	−9.23	-	-	-	-
0744+2701	7890 ± 210	−7.68	−6.92	−6.87	-	-	-	-	≤−4.3
0744+1640	4940 ± 190	−10.24	−8.63	−9.33	-	-	-	-	-
0758+1013	5500 ± 290	−8.65	−7.54	−7.34	−8.73	−9.20	-	-	-
0800+2242	6260 ± 260	−9.75	−8.69	−8.69	-	-	-	-	-
0806+3055	6900 ± 250	−7.77	−7.01	−7.16	-	−8.47	-	-	-
0806+4058	6808 ± 80	−8.49	−7.38	−7.49	−8.33	−9.11	-	−9.00	-
0807+4930	5100 ± 250	−8.39	−7.58	−7.28	−9.27	−9.34	−9.06	-	-

SDSS J	T_{eff} [K]	Ca	Mg	Fe	Na	Cr	Ti	Ni	H
0816+2330	7790 ± 300	−7.48	−6.27	−6.37	-	−7.68	−8.65	-	≤−4.5
0818+1247	6810 ± 270	−8.58	−7.87	−7.77	-	-	-	-	-
0823+0546	6019 ± 60	−9.34	−8.51	−7.36	-	-	−9.90	−8.59	-
0830−0319	6400 ± 110	−9.10	−8.49	−8.29	-	-	-	-	-
0832+4109	6070 ± 190	−8.00	−7.04	−7.04	−8.73	−8.80	-	-	-
0838+2322	5670 ± 80	−9.80	−8.89	−9.30	-	-	-	-	-
0842+1406	7160 ± 90	−8.16	−7.20	−7.30	-	-	-	-	-
0842+1536	6180 ± 220	−9.47	−8.46	−8.46	-	-	-	-	-
0843+5614	6600 ± 170	−8.65	−7.44	−7.74	−8.23	-	-	-	-
0851+1543	6300 ± 90	−8.50	−7.89	−8.20	-	-	-	-	-
0852+3402	5580 ± 180	−9.00	−8.39	−7.79	−9.58	−9.75	-	-	-
0901+0752	7100 ± 120	−7.12	−6.21	−6.21	−7.70	−8.07	−8.79	-	-
0902+3625	6330 ± 210	−8.60	−7.54	−7.64	−8.53	-	-	-	-
0902+1004	7250 ± 250	−8.25	−7.29	−8.19	-	-	-	-	-
0906+1141	6910 ± 270	−7.90	−6.64	−6.94	−8.43	-	−8.62	-	-
0908+5136	6180 ± 90	−9.35	−8.50	−8.24	-	-	-	-	-
0908+4119	6700 ± 300	−8.73	−7.07	−7.12	-	-	-	-	-
0913+2627	5210 ± 180	−9.75	−8.74	−8.64	-	-	-	-	-
0913+4127	5780 ± 290	−8.52	−7.86	−7.16	-	−9.42	−9.04	-	-
0916+2540	5378 ± 70	−7.48	−6.83	−7.09	−9.32	−8.90	−8.75	-	-
0924+4301	5950 ± 240	−9.75	−8.44	−8.54	-	-	-	-	-
0925+3130	5810 ± 90	−9.00	−7.79	−7.99	−9.68	-	-	-	-
0927+4931	6200 ± 230	−8.61	−7.20	−7.50	−9.09	-	-	-	-
0929+4247	6530 ± 160	−8.46	−6.85	−7.15	−8.64	−9.01	-	-	-
0933+6334	6290 ± 370	−8.28	−7.17	−6.77	-	−8.83	-	-	-
0937+5228	6600 ± 100	−8.40	−7.09	−7.50	−8.98	−9.25	-	-	-

SDSS J	T_{eff} [K]	Ca	Mg	Fe	Na	Cr	Ti	Ni	H
0939+4136	6310 ± 180	−8.30	−7.09	−6.79	−8.58	−8.55	-	-	-
0939+5019	5980 ± 190	−8.25	−7.04	−7.14	−9.23	−8.70	-	-	-
0946+2024	7490 ± 390	−8.07	−6.66	−7.06	-	-	-	-	-
0948+3008	6000 ± 130	−9.15	−8.04	−8.44	-	-	-	-	-
0956+5912	8800 ± 110	−7.15	−5.30	−6.14	−6.60	−7.50	-	-	−3.6
1003−0031	5740 ± 140	−8.49	−7.28	−7.28	−8.97	-	-	-	-
1005+2244	6360 ± 320	−8.96	−8.10	−7.40	-	-	-	-	-
1006+1752	5710 ± 190	−9.45	−8.94	−8.34	-	-	-	-	-
1014+2827	6250 ± 330	−7.68	−6.47	−6.47	−7.86	−8.43	−9.05	-	-
1017+3447	6150 ± 190	−9.34	−8.43	−8.33	-	-	-	-	-
1017+2419	7200 ± 150	−8.07	−6.86	−6.96	−8.15	-	-	-	≤−4.3
1019+3535	5840 ± 270	−8.75	−7.64	−7.74	-	-	-	-	-
1019+2045	5300 ± 220	−9.36	−8.65	−8.25	-	-	-	-	-
1024+4531	5980 ± 160	−8.92	−8.06	−8.11	-	-	-	-	-
1024+1014	6310 ± 280	−7.50	−6.54	−6.64	−8.63	−8.40	−8.52	-	-
1032+1338	5490 ± 240	−9.33	−7.82	−8.02	−9.01	-	-	-	-
1033+1809	6070 ± 230	−8.55	−8.84	−8.04	-	-	-	-	-
1038−0036	7700 ± 60	−7.85	−6.80	−7.40	−8.60	-	−9.60	-	≤−4.8
1038+0432	6510 ± 170	−7.50	−6.84	−6.99	−9.13	−8.70	-	-	-
1040+2407	5750 ± 90	−8.20	−7.29	−7.59	−8.88	−9.35	−9.27	-	-
1041+3432	7500 ± 220	−8.20	−7.49	−7.29	-	-	-	-	-
1043+3516	6720 ± 120	−8.88	−8.00	−7.20	-	−8.92	−10.54	−8.55	-
1046+1329	5170 ± 230	−9.60	−8.39	−8.29	-	-	-	-	-
1055+3725	5600 ± 120	−8.24	−8.23	−7.83	-	−9.19	-	-	-
1058+3143	6850 ± 100	−9.02	−7.81	−8.01	-	-	-	-	-
1102+2827	6400 ± 380	−7.75	−6.24	−6.44	−7.73	−8.30	-	-	-

SDSS J	T_{eff} [K]	Ca	Mg	Fe	Na	Cr	Ti	Ni	H
1102+0214	5730 ± 90	−9.75	−8.84	−8.74	-	-	-	-	-
1103+4144	5850 ± 100	−9.30	−7.94	−8.04	−9.13	-	-	-	-
1105+5006	7280 ± 190	−8.14	−6.83	−6.93	-	-	-	-	-
1105+0228	5780 ± 260	−9.10	−7.84	−8.14	-	-	-	-	-
1106+6737	6400 ± 170	−7.88	−6.87	−7.67	−9.36	-	-	-	-
1112+0700	7560 ± 170	−8.53	−7.12	−7.37	−8.76	-	-	-	≤−4.6
1113+2751	6180 ± 210	−8.42	−7.41	−7.51	−9.20	-	-	-	-
1132+3323	6250 ± 270	−8.23	−6.82	−7.32	−8.71	−8.88	−8.70	-	-
1134+1542	6680 ± 250	−8.46	−7.25	−7.35	−8.44	-	-	-	-
1144+3720	7490 ± 190	−8.17	−6.96	−7.16	−8.25	-	-	-	-
1144+1218	5434 ± 100	−9.33	−8.13	−8.37	-	−10.22	-	−10.13	−3.3
1147+5429	5320 ± 340	−9.17	−8.16	−8.06	−9.85	-	-	-	-
1149+0519	7310 ± 140	−8.16	−7.30	−7.60	-	-	-	-	≤−4.3
1150+4928	7210 ± 160	−8.76	−7.95	−7.65	-	-	-	-	-
1150+4533	5720 ± 320	−8.35	−7.14	−7.14	−8.53	-	-	-	-
1152+5101	5000 ± 240	−10.08	−8.67	−8.97	-	-	-	-	-
1152+1605	6550 ± 160	−8.40	−7.19	−7.19	−8.28	-	-	-	-
1157+6138	6540 ± 380	−9.15	−7.44	−7.64	-	-	-	-	-
1158+1845	7250 ± 170	−7.75	−5.74	−6.84	-	-	-	-	-
1158+5942	6000 ± 170	−8.98	−8.72	−8.02	-	-	-	-	-
1158+0454	5270 ± 180	−8.69	−7.68	−7.58	−8.97	−9.34	−9.46	-	-
1158+4712	7650 ± 210	−8.06	−6.90	−6.85	-	-	-	-	-
1158+5448	6280 ± 340	−8.82	−7.61	−7.61	-	-	-	-	-
1205+3536	6070 ± 150	−8.74	−7.43	−7.63	−8.72	-	-	-	-
1211+2326	6450 ± 230	−8.59	−7.28	−7.28	−8.57	-	-	-	-
1214−0234	5210 ± 100	−9.40	−8.19	−8.49	−8.98	-	-	-	-

SDSS J	$T_{\rm eff}$ [K]	Ca	Mg	Fe	Na	Cr	Ti	Ni	H
1217+1157	6440 ± 150	−8.93	−7.52	−7.92	-	-	-	-	-
1218+0023	6100 ± 90	−9.61	−9.20	−8.90	-	-	-	-	-
1220+0929	6640 ± 150	−8.38	−7.07	−7.37	−8.46	−8.93	-	-	-
1224+2838	5210 ± 110	−10.00	−8.69	−8.89	-	-	-	-	-
1226+2936	4680 ± 240	−10.04	−8.63	−8.93	-	-	-	-	-
1229+0743	6160 ± 130	−8.20	−7.29	−7.09	−8.48	−8.85	−9.87	-	-
1230+3143	6510 ± 160	−9.12	−8.41	−8.21	-	-	-	-	-
1234+5208	7630 ± 100	−7.40	−6.00	−6.39	−7.90	−7.95	−8.87	-	≤ -4.9
1238+2149	5440 ± 190	−9.11	−8.10	−8.00	−8.89	-	-	-	-
1245+0822	6360 ± 190	−8.10	−7.34	−7.59	−8.68	-	-	-	-
1249+6514	7540 ± 170	−8.50	−6.89	−7.49	-	-	-	-	-
1254+3551	6620 ± 210	−8.96	−7.55	−7.75	-	-	-	-	-
1257+3238	5210 ± 340	−9.02	−7.81	−7.61	−9.70	-	-	-	-
1257−0310	6280 ± 230	−8.52	−7.26	−7.31	-	-	-	-	-
1259+3112	5840 ± 240	−9.65	−8.74	−8.14	-	-	-	-	-
1259+4729	6260 ± 290	−8.80	−8.29	−7.99	-	-	-	-	-
1303+4055	6200 ± 120	−9.02	−7.71	−8.11	-	-	-	-	-
1308+0957	7830 ± 320	−8.03	−7.52	−6.62	-	-	-	-	−3.6
1308+0258	6030 ± 210	−9.07	−8.16	−7.66	-	-	-	-	-
1314+3748	5940 ± 320	−8.48	−7.42	−7.52	−8.71	-	-	-	-
1316+1918	5350 ± 190	−9.90	−8.49	−8.99	-	-	-	-	-
1319+3641	7360 ± 190	−8.60	−7.59	−7.49	-	-	-	-	-
1320+0204	7000 ± 310	−8.28	−7.37	−7.17	−7.96	-	-	-	-
1321−0237	5620 ± 240	−8.48	−7.47	−7.47	−8.36	−9.33	-	-	-
1329+1301	6810 ± 150	−8.55	−7.34	−7.44	−9.23	-	-	-	-
1330+3029	6100 ± 60	−8.40	−7.15	−7.30	−8.80	−9.00	−9.70	−8.66	-

SDSS J	$T_{\rm eff}$ [K]	Ca	Mg	Fe	Na	Cr	Ti	Ni	H
1336+3547	6600 ± 70	−8.50	−7.10	−7.39	−9.00	−9.40	-	-	-
1339+2643	6300 ± 70	−9.13	−8.30	−8.60	-	-	-	-	-
1340+2702	7855 ± 260	−6.98	−5.73	−6.27	−7.41	-	-	-	-
1342+1813	5240 ± 220	−9.19	−8.68	−8.58	-	-	-	-	-
1345+1153	6020 ± 200	−8.10	−7.49	−6.89	-	−8.70	−9.07	-	-
1347+1415	6740 ± 120	−8.50	−7.19	−7.29	-	−8.75	-	-	-
1350+1058	5120 ± 170	−10.06	−8.85	−8.75	-	-	-	-	-
1351+2645	5980 ± 160	−8.04	−8.33	−7.53	−9.72	−9.19	−8.61	-	-
1356+2416	6030 ± 120	−9.20	−7.84	−8.54	-	-	-	-	-
1356+0236	8260 ± 180	−7.52	−6.21	−6.41	−8.00	-	-	-	≤ -4.2
1401+3659	6000 ± 110	−9.80	−8.84	−8.94	-	-	-	-	-
1404+3620	5900 ± 70	−9.20	−7.90	−8.50	-	-	-	-	-
1405+2542	5880 ± 190	−9.50	−8.49	−8.39	-	-	-	-	-
1405+1549	7150 ± 110	−8.25	−7.14	−7.14	−8.93	-	-	-	-
1411+3410	5480 ± 210	−8.40	−7.24	−7.39	−9.28	−9.15	-	-	-
1412+2836	4990 ± 160	−9.40	−8.39	−7.99	−9.58	-	-	-	-
1421+1843	7300 ± 210	−7.35	−5.89	−6.19	-	-	-	-	-
1428+4403	6600 ± 60	−8.98	−8.20	−8.40	-	-	-	-	-
1429+3841	6040 ± 270	−9.73	−8.72	−8.72	-	-	-	-	-
1430−0151	6150 ± 160	−7.55	−6.54	−6.99	−8.13	−8.50	−8.80	-	-
1443+5833	7080 ± 340	−8.56	−7.15	−7.25	-	-	-	-	-
1443+3014	6840 ± 300	−8.16	−6.90	−7.15	-	-	-	-	-
1445+0913	6580 ± 230	−7.98	−6.77	−6.77	−7.81	−8.58	-	-	-
1448+1047	6550 ± 100	−8.85	−7.77	−7.80	-	-	-	-	-
1500+2315	6530 ± 430	−8.40	−6.89	−7.19	-	-	-	-	-
1502+3744	5410 ± 100	−10.00	−8.99	−8.99	-	-	-	-	-

SDSS J	T_{eff} [K]	Ca	Mg	Fe	Na	Cr	Ti	Ni	H
1507+4034	7180 ± 330	-8.18	-6.57	-7.17	-	-	-	-	-
1518+0506	5020 ± 100	-9.65	-8.64	-8.74	-10.03	-	-	-	-
1524+4049	5900 ± 120	-8.90	-7.69	-7.79	-9.18	-9.65	-	-	-
1534+1242	5860 ± 340	-8.29	-7.78	-7.48	-	-	-	-	-
1535+1247	5773 ± 50	-8.61	-7.36	-7.57	-8.72	-9.25	-9.62	-8.90	≤ -3.0
1536+4205	5800 ± 140	-8.70	-7.49	-7.59	-8.78	-8.90	-8.90	-	-
1537+3608	5570 ± 270	-9.50	-8.19	-8.49	-	-	-	-	-
1540+5352	6520 ± 360	-8.58	-7.07	-7.47	-	-	-	-	-
1542+4650	6060 ± 220	-8.15	-6.94	-7.04	-8.18	-8.70	-	-	-
1543+2024	6330 ± 360	-8.09	-7.33	-7.38	-	-	-	-	-
1545+5236	5840 ± 120	-9.19	-8.28	-8.18	-	-	-	-	-
1546+3009	6600 ± 120	-8.40	-7.19	-7.19	-8.78	-8.65	-	-	-
1549+2633	6290 ± 180	-9.66	-7.95	-8.25	-	-	-	-	-
1549+1906	6460 ± 290	-8.48	-7.17	-7.22	-9.11	-8.78	-	-	-
1554+1735	6630 ± 70	-8.60	-7.54	-7.64	-8.90	-	-	-	-
1604+1830	6400 ± 120	-9.48	-8.47	-8.57	-	-	-	-	-
1610+4006	6580 ± 280	-8.47	-7.46	-7.11	-	-	-	-	-
1612+3534	6750 ± 400	-8.54	-7.43	-7.53	-	-	-	-	-
1616+3303	6400 ± 80	-8.25	-6.95	-7.14	-8.93	-8.80	-9.62	-	-
1624+3310	6930 ± 340	-8.64	-7.28	-7.53	-	-	-	-	-
1626+3303	6260 ± 250	-8.87	-7.41	-7.61	-	-	-9.04	-	-
1627+4646	6420 ± 200	-8.88	-8.07	-7.62	-	-8.73	-	-	-
1636+1619	4410 ± 150	-9.50	-8.29	-8.79	-10.18	-	-	-	-
1641+1856	5820 ± 100	-10.30	-9.49	-9.59	-	-	-	-	-
1649+2238	5332 ± 160	-8.62	-6.89	-7.21	-8.29	-8.83	-	-	-1.8
1651+4249	5710 ± 200	-8.02	-6.91	-7.31	-8.20	-	-	-	-

SDSS J	T_{eff} [K]	Ca	Mg	Fe	Na	Cr	Ti	Ni	H
1706+2541	6640 ± 260	-9.40	-8.49	-8.89	-	-	-	-	-
2109−0039	6040 ± 240	-8.78	-8.42	-7.67	-	-	-	-	-
2110+0512	5680 ± 260	-9.21	-8.10	-8.00	-	-	-	-	-
2123+0016	5230 ± 140	-10.01	-8.50	-8.50	-9.19	-	-	-	-
2157+1206	6100 ± 100	-9.00	-7.79	-8.09	-9.18	-	-	-	-
2225+2338	7000 ± 130	-8.81	-7.40	-7.80	-	-	-	-	-
2230+1905	5600 ± 250	-8.45	-7.14	-7.24	-8.73	-8.90	-	-	-
2231+0906	5900 ± 90	-9.85	-9.24	-8.84	-	-	-	-	-
2235−0056	6340 ± 200	-8.67	-7.66	-7.26	-8.85	-	-	-	-
2238+0213	7000 ± 250	-8.56	-7.55	-7.30	-	-	-	-	-
2238−0113	6800 ± 260	-8.89	-7.73	-7.78	-	-	-	-	-
2254+3031	5900 ± 90	-8.26	-6.95	-7.25	-8.54	-9.01	-	-	-
2304+2415	5060 ± 100	-9.54	-7.98	-8.93	-	-	-	-	-
2319+3018	7120 ± 200	-8.53	-7.42	-7.37	-7.71	-	-	-	-
2325+0448	6020 ± 100	-9.07	-8.06	-8.06	-8.95	-	-	-	-
2328+0830	5800 ± 330	-8.80	-7.69	-7.59	-	-	-	-	-
2330+2805	6670 ± 210	-8.84	-7.73	-7.63	-	-	-	-	-
2330+2956	7000 ± 110	-8.24	-6.63	-7.13	-8.02	-	-	-	-
2333+1058	6220 ± 300	-8.79	-7.28	-7.38	-8.67	-	-	-	-
2340+0124	6200 ± 100	-8.50	-7.54	-7.90	-	-	-	-	-
2340+0817	5550 ± 120	-9.00	-7.99	-7.69	-	-	-	-	-
2343−0010	5900 ± 290	-9.23	-7.82	-8.22	-	-	-	-	-
2352+1922	6170 ± 310	-8.34	-7.13	-7.03	-	-	-	-	-
2352+3344	7230 ± 220	-8.26	-6.85	-7.05	-8.34	-	-	-	-
2357+2348	6030 ± 240	-9.07	-7.66	-7.76	-	-	-	-	-

Table B.3: The mass fraction of the convection zone, q, and logarithm of the diffusion timescales in years for each element.

SDSS J	$\log(q)$	Ca	Mg	Fe	Na	Cr	Ti	Ni
0002+3209	−5.34	6.18	6.62	6.17	6.57	6.15	6.13	6.21
0004+0819	−5.51	6.05	6.51	6.05	6.46	6.03	6.01	6.09
0006+0520	−5.27	6.20	6.65	6.21	6.60	6.19	6.16	6.25
0010−0430	−5.32	6.15	6.58	6.16	6.53	6.13	6.11	6.19
0013+1109	−5.44	6.16	6.58	6.11	6.53	6.09	6.07	6.15
0019+2209	−5.38	6.25	6.63	6.16	6.58	6.14	6.12	6.19
0037−0525	−5.54	6.05	6.51	6.04	6.46	6.02	6.00	6.08
0044+0418	−5.30	6.39	6.71	6.23	6.66	6.20	6.18	6.26
0046+2717	−5.32	6.11	6.54	6.14	6.49	6.11	6.09	6.17
0047+1628	−5.51	6.01	6.43	6.02	6.39	6.00	5.97	6.06
0052+1846	−5.49	6.13	6.56	6.08	6.51	6.06	6.04	6.12
0053+3115	−5.41	6.12	6.58	6.12	6.53	6.10	6.08	6.16
0056+2453	−5.41	6.33	6.65	6.15	6.60	6.13	6.11	6.19
0107+2650	−5.48	6.06	6.51	6.06	6.46	6.04	6.02	6.10
0108−0537	−5.46	6.09	6.54	6.09	6.49	6.06	6.04	6.12
0114+3505	−5.43	6.09	6.54	6.10	6.49	6.08	6.05	6.13
0116+2050	−5.42	6.11	6.57	6.12	6.52	6.09	6.07	6.15
0117+0021	−5.30	6.18	6.63	6.19	6.58	6.17	6.14	6.22
0126+2534	−5.37	6.44	6.70	6.19	6.65	6.17	6.17	6.22
0135+1302	−5.38	6.30	6.65	6.16	6.60	6.14	6.12	6.20
0143+0113	−5.36	6.13	6.57	6.14	6.53	6.12	6.09	6.18
0144+1920	−5.40	6.11	6.55	6.12	6.50	6.09	6.07	6.15
0144+0305	−5.33	6.14	6.58	6.16	6.53	6.13	6.11	6.19
0148−0112	−5.29	6.19	6.63	6.19	6.58	6.17	6.15	6.23
0150+1354	−5.56	5.97	6.41	5.99	6.36	5.97	5.94	6.02
0157+0033	−5.54	6.01	6.45	6.02	6.41	6.00	5.97	6.05
0158−0942	−5.35	6.32	6.66	6.18	6.61	6.16	6.14	6.21
0200+1646	−5.48	6.09	6.55	6.08	6.50	6.06	6.04	6.12
0201+2015	−5.40	6.13	6.59	6.13	6.54	6.11	6.09	6.17
0208−0542	−5.55	6.02	6.48	6.02	6.43	6.00	5.98	6.06
0234−0510	−5.32	6.14	6.58	6.16	6.53	6.13	6.11	6.19
0252−0401	−5.30	6.17	6.60	6.18	6.56	6.16	6.13	6.21
0252+0054	−5.23	6.19	6.62	6.21	6.58	6.19	6.16	6.25
0447+1124	−5.35	6.15	6.59	6.15	6.55	6.13	6.11	6.19
0512−0505	−5.51	6.11	6.54	6.07	6.49	6.04	6.02	6.10
0721+3928	−5.39	6.13	6.59	6.14	6.54	6.12	6.09	6.17
0735+2057	−5.61	5.95	6.38	5.96	6.34	5.93	5.91	5.99
0736+4118	−5.68	5.95	6.42	5.95	6.37	5.92	5.90	5.98

SDSS J	log(q)	Ca	Mg	Fe	Na	Cr	Ti	Ni
0739+3112	−5.48	6.29	6.62	6.11	6.56	6.09	6.07	6.14
0741+3146	−5.40	6.31	6.65	6.15	6.59	6.13	6.11	6.19
0744+4649	−5.72	5.92	6.39	5.92	6.34	5.89	5.87	5.95
0744+4408	−5.39	6.12	6.57	6.13	6.53	6.11	6.08	6.16
0744+2701	−5.28	6.14	6.56	6.16	6.51	6.14	6.11	6.20
0744+1640	−5.38	6.55	6.73	6.19	6.67	6.18	6.23	6.23
0758+1013	−5.59	6.01	6.48	6.01	6.43	5.99	5.96	6.04
0800+2242	−5.27	6.38	6.71	6.24	6.66	6.21	6.19	6.27
0806+3055	−5.43	6.06	6.49	6.08	6.44	6.05	6.03	6.11
0806+4058	−5.34	6.14	6.58	6.15	6.53	6.13	6.11	6.19
0807+4930	−5.70	5.93	6.40	5.93	6.35	5.91	5.89	5.96
0816+2330	−5.33	6.10	6.52	6.13	6.47	6.10	6.07	6.16
0818+1247	−5.32	6.15	6.60	6.17	6.55	6.14	6.12	6.20
0823+0546	−5.37	6.26	6.64	6.16	6.59	6.14	6.12	6.20
0830−0319	−5.33	6.19	6.63	6.18	6.58	6.15	6.13	6.21
0832+4109	−5.58	5.98	6.42	5.99	6.37	5.96	5.94	6.02
0838+2322	−5.35	6.38	6.69	6.19	6.64	6.17	6.16	6.23
0842+1406	−5.32	6.14	6.57	6.16	6.53	6.13	6.11	6.19
0842+1536	−5.32	6.30	6.67	6.20	6.61	6.17	6.15	6.23
0843+5614	−5.36	6.14	6.59	6.15	6.54	6.12	6.10	6.18
0851+1543	−5.45	6.08	6.53	6.09	6.48	6.06	6.04	6.12
0852+3402	−5.51	6.11	6.54	6.07	6.49	6.05	6.03	6.10
0901+0752	−5.51	5.98	6.40	6.00	6.35	5.98	5.95	6.04
0902+3625	−5.42	6.10	6.55	6.10	6.50	6.08	6.06	6.14
0902+1004	−5.29	6.16	6.59	6.18	6.55	6.15	6.13	6.21
0906+1141	−5.41	6.08	6.51	6.09	6.46	6.07	6.04	6.13
0908+5136	−5.34	6.26	6.65	6.18	6.60	6.16	6.14	6.22
0908+4119	−5.33	6.16	6.61	6.17	6.56	6.15	6.12	6.20
0913+2627	−5.42	6.37	6.67	6.16	6.61	6.14	6.12	6.19
0913+4127	−5.56	6.02	6.47	6.02	6.42	6.00	5.97	6.05
0916+2540	−5.82	5.81	6.25	5.82	6.21	5.80	5.77	5.85
0924+4301	−5.32	6.37	6.70	6.21	6.64	6.19	6.17	6.24
0925+3130	−5.47	6.11	6.56	6.09	6.51	6.07	6.05	6.13
0927+4931	−5.45	6.08	6.53	6.09	6.49	6.07	6.04	6.12
0929+4247	−5.40	6.11	6.55	6.12	6.50	6.09	6.07	6.15
0933+6334	−5.48	6.05	6.49	6.06	6.44	6.03	6.01	6.09
0937+5228	−5.39	6.11	6.55	6.12	6.50	6.09	6.07	6.15
0939+4136	−5.48	6.05	6.50	6.06	6.45	6.04	6.02	6.10
0939+5019	−5.56	6.00	6.45	6.01	6.40	5.99	5.96	6.04
0946+2024	−5.27	6.16	6.59	6.18	6.54	6.15	6.13	6.21
0948+3008	−5.40	6.18	6.60	6.14	6.55	6.11	6.09	6.17

SDSS J	log(q)	Ca	Mg	Fe	Na	Cr	Ti	Ni
0956+5912	−5.30	6.11	6.51	6.14	6.47	6.11	6.08	6.18
1003−0031	−5.57	6.01	6.46	6.01	6.41	5.99	5.96	6.04
1005+2244	−5.36	6.15	6.61	6.15	6.56	6.13	6.11	6.19
1006+1752	−5.40	6.28	6.64	6.15	6.58	6.13	6.11	6.18
1014+2827	−5.59	5.96	6.39	5.97	6.34	5.95	5.92	6.01
1017+3447	−5.35	6.26	6.65	6.18	6.59	6.16	6.13	6.21
1017+2419	−5.32	6.13	6.56	6.15	6.52	6.13	6.10	6.19
1019+3535	−5.51	6.06	6.52	6.06	6.47	6.04	6.02	6.09
1019+2045	−5.48	6.25	6.60	6.10	6.55	6.08	6.06	6.14
1024+4531	−5.45	6.10	6.56	6.10	6.51	6.08	6.06	6.14
1024+1014	−5.61	5.94	6.37	5.96	6.32	5.93	5.91	5.99
1032+1338	−5.46	6.24	6.60	6.11	6.55	6.09	6.07	6.15
1033+1809	−5.49	6.06	6.51	6.06	6.46	6.04	6.02	6.10
1038−0036	−5.28	6.15	6.57	6.17	6.52	6.14	6.12	6.21
1038+0432	−5.56	5.97	6.39	5.98	6.35	5.96	5.93	6.02
1040+2407	−5.62	5.96	6.41	5.97	6.36	5.95	5.92	6.00
1041+3432	−5.25	6.18	6.61	6.20	6.56	6.17	6.14	6.23
1043+3516	−5.30	6.18	6.63	6.19	6.58	6.17	6.14	6.22
1046+1329	−5.45	6.32	6.64	6.13	6.59	6.11	6.09	6.16
1055+3725	−5.65	5.95	6.41	5.96	6.36	5.93	5.91	5.99
1058+3143	−5.26	6.21	6.66	6.22	6.61	6.20	6.17	6.25
1102+2827	−5.54	5.99	6.42	6.00	6.37	5.98	5.95	6.04
1102+0214	−5.35	6.37	6.69	6.19	6.63	6.17	6.15	6.23
1103+4144	−5.41	6.24	6.62	6.14	6.57	6.12	6.10	6.18
1105+5006	−5.30	6.15	6.58	6.17	6.53	6.14	6.12	6.20
1105+0228	−5.46	6.15	6.58	6.11	6.53	6.08	6.06	6.14
1106+6737	−5.52	6.01	6.44	6.02	6.40	6.00	5.97	6.06
1112+0700	−5.20	6.22	6.65	6.24	6.60	6.21	6.19	6.27
1113+2751	−5.49	6.05	6.50	6.06	6.45	6.04	6.01	6.09
1132+3323	−5.50	6.03	6.48	6.04	6.43	6.02	6.00	6.08
1134+1542	−5.37	6.12	6.57	6.14	6.52	6.11	6.09	6.17
1144+3720	−5.26	6.17	6.60	6.19	6.55	6.17	6.14	6.23
1144+1218	−5.47	6.24	6.60	6.11	6.55	6.09	6.07	6.14
1147+5429	−5.52	6.18	6.57	6.07	6.51	6.05	6.03	6.11
1149+0519	−5.29	6.15	6.58	6.17	6.54	6.15	6.12	6.21
1150+4928	−5.23	6.22	6.66	6.23	6.61	6.21	6.18	6.26
1150+4533	−5.60	5.98	6.44	5.99	6.39	5.96	5.94	6.02
1152+5101	−5.40	6.49	6.71	6.18	6.65	6.16	6.19	6.22
1152+1605	−5.40	6.10	6.54	6.11	6.50	6.09	6.06	6.15
1157+6138	−5.30	6.21	6.65	6.20	6.60	6.17	6.15	6.23
1158+1845	−5.36	6.09	6.52	6.12	6.47	6.09	6.06	6.15

SDSS J	log(q)	Ca	Mg	Fe	Na	Cr	Ti	Ni
1158+5942	−5.43	6.12	6.57	6.11	6.52	6.09	6.07	6.15
1158+0454	−5.62	6.01	6.47	5.99	6.42	5.97	5.95	6.03
1158+4712	−5.25	6.17	6.60	6.19	6.55	6.17	6.14	6.23
1158+5448	−5.40	6.12	6.58	6.13	6.53	6.10	6.08	6.16
1205+3536	−5.46	6.08	6.54	6.09	6.49	6.07	6.04	6.12
1211+2326	−5.40	6.11	6.56	6.12	6.51	6.10	6.07	6.16
1214−0234	−5.49	6.26	6.61	6.10	6.55	6.08	6.06	6.14
1217+1157	−5.35	6.16	6.61	6.16	6.56	6.14	6.11	6.19
1218+0023	−5.32	6.34	6.68	6.21	6.63	6.18	6.16	6.24
1220+0929	−5.39	6.11	6.55	6.12	6.50	6.10	6.07	6.16
1224+2838	−5.38	6.46	6.71	6.19	6.65	6.17	6.18	6.22
1226+2936	−5.44	6.49	6.70	6.16	6.64	6.14	6.18	6.19
1229+0743	−5.53	6.02	6.46	6.03	6.41	6.00	5.98	6.06
1230+3143	−5.31	6.20	6.64	6.19	6.59	6.17	6.15	6.23
1234+5208	−5.37	6.08	6.49	6.10	6.45	6.08	6.05	6.14
1238+2149	−5.51	6.16	6.56	6.07	6.51	6.05	6.03	6.11
1245+0822	−5.50	6.03	6.47	6.04	6.43	6.02	6.00	6.08
1249+6514	−5.21	6.21	6.65	6.23	6.60	6.21	6.18	6.27
1254+3551	−5.31	6.18	6.63	6.19	6.58	6.16	6.14	6.22
1257+3238	−5.56	6.13	6.53	6.04	6.48	6.02	6.00	6.07
1257−0310	−5.45	6.08	6.53	6.09	6.48	6.06	6.04	6.12
1259+3112	−5.35	6.34	6.67	6.19	6.62	6.17	6.15	6.22
1259+4729	−5.41	6.12	6.57	6.12	6.52	6.10	6.08	6.16
1303+4055	−5.39	6.15	6.60	6.14	6.55	6.12	6.10	6.18
1308+0957	−5.23	6.18	6.61	6.21	6.56	6.18	6.15	6.24
1308+0258	−5.41	6.15	6.59	6.13	6.54	6.11	6.08	6.16
1314+3748	−5.53	6.03	6.48	6.03	6.43	6.01	5.99	6.07
1316+1918	−5.38	6.42	6.70	6.18	6.64	6.16	6.16	6.22
1319+3641	−5.22	6.21	6.65	6.23	6.60	6.20	6.18	6.26
1320+0204	−5.33	6.14	6.57	6.15	6.53	6.13	6.10	6.19
1321−0237	−5.60	5.99	6.45	5.99	6.40	5.97	5.95	6.03
1329+1301	−5.33	6.15	6.59	6.16	6.54	6.14	6.11	6.20
1330+3029	−5.51	6.04	6.49	6.05	6.44	6.02	6.00	6.08
1336+3547	−5.38	6.12	6.56	6.13	6.52	6.11	6.08	6.17
1339+2643	−5.35	6.18	6.63	6.17	6.58	6.15	6.12	6.20
1340+2702	−5.43	6.03	6.44	6.06	6.39	6.03	6.00	6.09
1342+1813	−5.52	6.19	6.57	6.07	6.51	6.05	6.03	6.11
1345+1153	−5.58	5.98	6.43	5.99	6.38	5.97	5.95	6.03
1347+1415	−5.35	6.14	6.58	6.15	6.53	6.12	6.10	6.18
1350+1058	−5.38	6.48	6.71	6.19	6.66	6.17	6.19	6.22
1351+2645	−5.59	5.97	6.41	5.98	6.37	5.96	5.93	6.01

SDSS J	log(q)	Ca	Mg	Fe	Na	Cr	Ti	Ni
1356+2416	−5.39	6.20	6.61	6.15	6.56	6.13	6.10	6.18
1356+0236	−5.27	6.14	6.55	6.17	6.50	6.14	6.11	6.20
1401+3659	−5.31	6.38	6.70	6.22	6.65	6.20	6.18	6.25
1404+3620	−5.41	6.20	6.61	6.13	6.55	6.11	6.09	6.17
1405+2542	−5.37	6.31	6.65	6.17	6.60	6.15	6.13	6.21
1405+1549	−5.30	6.15	6.58	6.17	6.54	6.14	6.12	6.20
1411+3410	−5.64	5.96	6.43	5.97	6.38	5.94	5.92	6.00
1412+2836	−5.52	6.26	6.60	6.09	6.54	6.07	6.05	6.12
1421+1843	−5.43	6.04	6.46	6.06	6.41	6.04	6.01	6.10
1428+4403	−5.31	6.18	6.63	6.18	6.58	6.16	6.14	6.22
1429+3841	−5.31	6.37	6.70	6.21	6.64	6.19	6.17	6.25
1430−0151	−5.64	5.92	6.35	5.94	6.31	5.91	5.89	5.97
1443+5833	−5.28	6.18	6.62	6.19	6.57	6.17	6.14	6.23
1443+3014	−5.38	6.10	6.54	6.12	6.49	6.09	6.07	6.15
1445+0913	−5.46	6.05	6.48	6.06	6.43	6.04	6.01	6.09
1448+1047	−5.34	6.16	6.61	6.16	6.56	6.14	6.12	6.20
1500+2315	−5.41	6.10	6.54	6.11	6.49	6.08	6.06	6.14
1502+3744	−5.36	6.45	6.71	6.20	6.66	6.18	6.18	6.24
1507+4034	−5.31	6.15	6.58	6.16	6.53	6.14	6.11	6.20
1518+0506	−5.47	6.34	6.64	6.13	6.59	6.11	6.09	6.16
1524+4049	−5.47	6.09	6.55	6.09	6.50	6.07	6.05	6.12
1534+1242	−5.58	5.99	6.44	6.00	6.39	5.97	5.95	6.03
1535+1247	−5.54	6.03	6.49	6.03	6.44	6.01	5.99	6.07
1536+4205	−5.52	6.05	6.51	6.05	6.46	6.03	6.00	6.08
1537+3608	−5.42	6.30	6.64	6.15	6.58	6.12	6.11	6.18
1540+5352	−5.38	6.12	6.57	6.13	6.52	6.11	6.08	6.16
1542+4650	−5.56	6.00	6.44	6.01	6.39	5.98	5.96	6.04
1543+2024	−5.50	6.03	6.47	6.04	6.42	6.01	5.99	6.07
1545+5236	−5.43	6.19	6.60	6.13	6.55	6.10	6.08	6.16
1546+3009	−5.39	6.11	6.55	6.12	6.50	6.09	6.07	6.15
1549+2633	−5.28	6.35	6.70	6.23	6.65	6.21	6.19	6.26
1549+1906	−5.41	6.10	6.54	6.11	6.50	6.08	6.06	6.14
1554+1735	−5.36	6.14	6.58	6.15	6.53	6.12	6.10	6.18
1604+1830	−5.28	6.31	6.68	6.22	6.63	6.20	6.18	6.25
1610+4006	−5.39	6.11	6.56	6.12	6.51	6.10	6.08	6.16
1612+3534	−5.34	6.14	6.58	6.15	6.54	6.13	6.11	6.19
1616+3303	−5.46	6.06	6.50	6.07	6.46	6.05	6.02	6.11
1624+3310	−5.29	6.17	6.61	6.18	6.57	6.16	6.14	6.22
1626+3303	−5.40	6.13	6.58	6.13	6.53	6.11	6.09	6.17
1627+4646	−5.36	6.15	6.60	6.15	6.55	6.13	6.11	6.19
1636+1619	−5.56	6.32	6.61	6.07	6.56	6.05	6.05	6.10

SDSS J	$\log(q)$	Ca	Mg	Fe	Na	Cr	Ti	Ni
1641+1856	−5.27	6.52	6.76	6.26	6.71	6.24	6.24	6.29
1649+2238	−5.62	5.99	6.46	5.99	6.41	5.97	5.94	6.02
1651+4249	−5.66	5.93	6.37	5.94	6.33	5.91	5.89	5.97
1706+2541	−5.25	6.27	6.69	6.23	6.64	6.21	6.19	6.27
2109−0039	−5.46	6.09	6.54	6.09	6.49	6.07	6.04	6.12
2110+0512	−5.45	6.20	6.59	6.11	6.54	6.09	6.07	6.15
2123+0016	−5.38	6.46	6.71	6.19	6.65	6.17	6.18	6.22
2157+1206	−5.41	6.13	6.59	6.13	6.54	6.11	6.08	6.16
2225+2338	−5.26	6.20	6.64	6.21	6.59	6.19	6.16	6.25
2230+1905	−5.61	5.99	6.45	5.99	6.40	5.96	5.94	6.02
2231+0906	−5.31	6.39	6.71	6.22	6.65	6.20	6.18	6.25
2235−0056	−5.41	6.11	6.56	6.12	6.51	6.09	6.07	6.15
2238+0213	−5.29	6.17	6.61	6.18	6.56	6.16	6.13	6.22
2238−0113	−5.28	6.19	6.64	6.20	6.59	6.18	6.15	6.23
2254+3031	−5.58	5.99	6.44	6.00	6.39	5.97	5.95	6.03
2304+2415	−5.48	6.30	6.63	6.11	6.57	6.09	6.07	6.15
2319+3018	−5.27	6.18	6.62	6.20	6.57	6.17	6.15	6.23
2325+0448	−5.41	6.15	6.59	6.13	6.54	6.11	6.08	6.16
2328+0830	−5.50	6.07	6.52	6.06	6.47	6.04	6.02	6.10
2330+2805	−5.32	6.17	6.62	6.18	6.57	6.15	6.13	6.21
2330+2956	−5.33	6.13	6.57	6.15	6.52	6.12	6.10	6.18
2333+1058	−5.42	6.11	6.57	6.12	6.52	6.09	6.07	6.15
2340+0124	−5.47	6.07	6.52	6.07	6.47	6.05	6.03	6.11
2340+0817	−5.51	6.11	6.54	6.07	6.49	6.04	6.02	6.10
2343−0010	−5.41	6.21	6.61	6.14	6.56	6.12	6.09	6.17
2352+1922	−5.50	6.04	6.49	6.05	6.44	6.02	6.00	6.08
2352+3344	−5.29	6.16	6.59	6.18	6.55	6.15	6.13	6.21
2357+2348	−5.41	6.15	6.59	6.13	6.54	6.11	6.08	6.16

Table B.4: Distances d, proper-motions μ, transverse motions $v_\perp$, and white dwarf cooling ages for our DZ sample.

SDSS J	d [pc]	μ [mas yr^{-1}]	$v_\perp$ [km s^{-1}]	Age [Gyr]
0002+3209	210 ± 28	38.4 ± 5.3	38.5 ± 7.6	$2.6^{+0.8}_{-0.7}$
0004+0819	336 ± 46	-	-	$3.7^{+1.6}_{-1.2}$
0006+0520	216 ± 28	-	-	$2.1^{+0.6}_{-0.5}$
0010−0430	221 ± 30	66.7 ± 4.2	70 ± 11	$2.0^{+0.5}_{-0.4}$
0013+1109	277 ± 36	-	-	$3.7^{+1.4}_{-1.1}$
0019+2209	155 ± 20	45.4 ± 3.3	33.4 ± 5.0	$3.3^{+1.0}_{-0.9}$
0037−0525	125 ± 16	12.5 ± 3.5	7.4 ± 2.3	$4.3^{+1.0}_{-1.1}$
0044+0418	79 ± 10	63.1 ± 6.6	23.8 ± 4.0	$3.2^{+0.9}_{-0.8}$
0046+2717	272 ± 37	28.7 ± 4.6	37.2 ± 7.8	$1.5^{+0.4}_{-0.3}$
0047+1628	246 ± 32	-	-	$2.3^{+0.7}_{-0.5}$
0052+1846	250 ± 33	-	-	$4.2^{+1.4}_{-1.3}$
0053+3115	276 ± 37	-	-	$2.9^{+1.1}_{-0.8}$
0056+2453	214 ± 28	-	-	$4.9^{+1.2}_{-1.5}$
0107+2650	101 ± 13	262.5 ± 3.1	126 ± 17	$2.9^{+0.8}_{-0.8}$
0108−0537	173 ± 23	26.7 ± 3.4	22.1 ± 4.0	$3.2^{+0.9}_{-0.9}$
0114+3505	243 ± 32	-	-	$2.6^{+0.8}_{-0.7}$
0116+2050	68.3 ± 8.9	118.4 ± 2.8	38.5 ± 5.1	$2.9^{+0.8}_{-0.8}$
0117+0021	132 ± 18	501.8 ± 7.4	316 ± 42	$2.1^{+0.5}_{-0.5}$
0126+2534	140 ± 18	122.4 ± 4.7	81 ± 11	$5.5^{+0.6}_{-1.3}$
0135+1302	94 ± 12	105.5 ± 3.6	47.4 ± 6.2	$3.7^{+1.0}_{-1.0}$
0143+0113	137 ± 18	74.4 ± 3.8	48.6 ± 6.9	$2.2^{+0.6}_{-0.5}$
0144+1920	225 ± 30	31.9 ± 4.5	34.2 ± 6.7	$2.5^{+0.8}_{-0.6}$
0144+0305	356 ± 48	-	-	$2.0^{+0.7}_{-0.5}$
0148−0112	266 ± 36	13.4 ± 4.8	17.0 ± 6.5	$2.1^{+0.6}_{-0.5}$
0150+1354	167 ± 22	96.8 ± 3.8	77 ± 11	$2.7^{+0.8}_{-0.7}$
0157+0033	120 ± 16	31.5 ± 6.7	18.0 ± 4.5	$3.1^{+0.9}_{-0.8}$
0158−0942	171 ± 22	86.3 ± 5.0	70 ± 10	$3.4^{+1.0}_{-0.9}$
0200+1646	186 ± 24	52.0 ± 4.6	46.0 ± 7.3	$3.7^{+1.1}_{-1.0}$
0201+2015	174 ± 23	-	-	$2.9^{+0.8}_{-0.8}$
0208−0542	227 ± 30	-	-	$3.8^{+1.5}_{-1.2}$
0234−0510	321 ± 44	-	-	$1.9^{+0.7}_{-0.5}$
0252−0401	215 ± 29	66.7 ± 4.2	68 ± 10	$2.0^{+0.5}_{-0.4}$
0252+0054	206 ± 28	57.4 ± 4.7	56.5 ± 8.9	$1.6^{+0.4}_{-0.3}$
0447+1124	188 ± 25	32.7 ± 5.0	29.3 ± 5.9	$2.4^{+0.7}_{-0.6}$
0512−0505	55.5 ± 6.9	85.2 ± 3.1	22.5 ± 2.9	$4.5^{+0.8}_{-1.1}$
0721+3928	199 ± 26	-	-	$2.8^{+0.8}_{-0.7}$
0735+2057	176 ± 23	38.2 ± 5.5	32.1 ± 6.2	$3.1^{+0.9}_{-0.8}$
0736+4118	93 ± 12	141.7 ± 3.1	62.5 ± 7.9	$6.1^{+0.5}_{-1.1}$

SDSS J	d [pc]	μ [$\mathrm{mas\,yr^{-1}}$]	$v_\perp$ [$\mathrm{km\,s^{-1}}$]	Age [Gyr]
0739+3112	169 ± 21	-	-	$6.1^{+1.0}_{-1.6}$
0741+3146	153 ± 19	-	-	$4.4^{+1.0}_{-1.1}$
0744+4649	59.7 ± 7.3	69.4 ± 3.3	19.7 ± 2.6	$6.4^{+0.4}_{-1.1}$
0744+4408	289 ± 39	72.1 ± 4.9	99 ± 15	$2.6^{+0.9}_{-0.7}$
0744+2701	272 ± 37	23.9 ± 4.0	31.0 ± 6.8	$1.4^{+0.3}_{-0.3}$
0744+1640	118 ± 15	-	-	$6.6^{+0.5}_{-1.2}$
0758+1013	197 ± 26	-	-	$4.7^{+1.2}_{-1.4}$
0800+2242	220 ± 30	-	-	$2.8^{+1.0}_{-0.8}$
0806+3055	266 ± 36	-	-	$2.0^{+0.6}_{-0.5}$
0806+4058	114 ± 16	111 ± 11	60 ± 10	$2.1^{+0.5}_{-0.5}$
0807+4930	156 ± 20	-	-	$6.1^{+0.9}_{-1.4}$
0816+2330	369 ± 51	-	-	$1.4^{+0.4}_{-0.3}$
0818+1247	294 ± 41	-	-	$2.1^{+0.7}_{-0.5}$
0823+0546	52.2 ± 6.7	251.9 ± 2.7	62.6 ± 8.1	$3.2^{+0.9}_{-0.9}$
0830−0319	140 ± 19	51.9 ± 3.4	34.6 ± 5.2	$2.6^{+0.7}_{-0.7}$
0832+4109	234 ± 31	55.0 ± 5.4	61 ± 10	$3.1^{+1.0}_{-0.9}$
0838+2322	84 ± 10	41.9 ± 3.3	16.8 ± 2.5	$4.1^{+0.9}_{-1.0}$
0842+1406	93 ± 12	79.3 ± 4.8	35.3 ± 5.2	$1.8^{+0.4}_{-0.4}$
0842+1536	209 ± 28	36.3 ± 3.6	36.0 ± 6.0	$2.9^{+1.0}_{-0.8}$
0843+5614	218 ± 30	20.9 ± 4.1	21.7 ± 5.2	$2.3^{+0.7}_{-0.6}$
0851+1543	99 ± 13	76.4 ± 3.0	36.0 ± 5.0	$2.8^{+0.7}_{-0.7}$
0852+3402	176 ± 22	-	-	$4.4^{+1.1}_{-1.2}$
0901+0752	209 ± 28	44.7 ± 3.9	44.4 ± 7.0	$1.9^{+0.4}_{-0.4}$
0902+3625	222 ± 29	-	-	$2.7^{+0.9}_{-0.7}$
0902+1004	290 ± 40	-	-	$1.8^{+0.5}_{-0.4}$
0906+1141	306 ± 41	-	-	$2.0^{+0.6}_{-0.5}$
0908+5136	119 ± 15	43.8 ± 3.7	24.8 ± 3.9	$3.0^{+0.8}_{-0.8}$
0908+4119	303 ± 42	-	-	$2.2^{+0.8}_{-0.5}$
0913+2627	111 ± 14	72.1 ± 4.8	38.1 ± 5.4	$5.8^{+0.7}_{-1.3}$
0913+4127	212 ± 28	-	-	$3.8^{+1.3}_{-1.1}$
0916+2540	43.4 ± 5.4	237.8 ± 2.8	49.1 ± 6.2	$5.3^{+0.6}_{-1.2}$
0924+4301	236 ± 31	52.0 ± 4.8	58.3 ± 9.3	$3.4^{+1.1}_{-1.0}$
0925+3130	81 ± 10	137.0 ± 3.3	53.1 ± 6.9	$3.7^{+0.9}_{-1.0}$
0927+4931	248 ± 33	65.6 ± 5.5	78 ± 12	$2.9^{+1.0}_{-0.8}$
0929+4247	185 ± 25	15.0 ± 3.7	13.2 ± 3.7	$2.4^{+0.7}_{-0.6}$
0933+6334	269 ± 36	-	-	$2.8^{+1.2}_{-0.8}$
0937+5228	132 ± 18	69.0 ± 3.6	43.2 ± 6.2	$2.3^{+0.6}_{-0.6}$
0939+4136	202 ± 27	43.7 ± 5.4	42.0 ± 7.7	$2.7^{+0.8}_{-0.7}$
0939+5019	134 ± 17	81.6 ± 5.5	52.1 ± 7.6	$3.3^{+1.0}_{-0.9}$
0946+2024	311 ± 43	-	-	$1.6^{+0.5}_{-0.4}$
0948+3008	164 ± 21	70.0 ± 3.6	54.5 ± 7.4	$3.3^{+0.9}_{-0.9}$

SDSS J	d [pc]	μ [mas yr^{-1}]	$v_{\perp}$ [km s^{-1}]	Age [Gyr]
0956+5912	139 ± 19	125.8 ± 3.0	83 ± 12	$1.0^{+0.1}_{-0.2}$
1003−0031	161 ± 20	40.7 ± 5.8	31.2 ± 5.9	$3.9^{+1.0}_{-1.0}$
1005+2244	301 ± 41	50 ± 14	72 ± 22	$2.6^{+1.0}_{-0.7}$
1006+1752	159 ± 20	-	-	$4.0^{+1.1}_{-1.1}$
1014+2827	257 ± 35	-	-	$2.8^{+1.1}_{-0.8}$
1017+3447	186 ± 25	115.9 ± 3.6	103 ± 14	$3.0^{+0.9}_{-0.8}$
1017+2419	199 ± 27	77.4 ± 3.6	73 ± 11	$1.8^{+0.4}_{-0.4}$
1019+3535	239 ± 31	-	-	$3.6^{+1.3}_{-1.1}$
1019+2045	169 ± 22	84.5 ± 5.4	68.0 ± 9.7	$5.5^{+0.9}_{-1.5}$
1024+4531	166 ± 21	15.7 ± 5.4	12.3 ± 4.5	$3.3^{+1.0}_{-0.9}$
1024+1014	194 ± 26	51.3 ± 4.8	47.4 ± 7.6	$2.7^{+1.0}_{-0.7}$
1032+1338	198 ± 25	-	-	$4.8^{+1.1}_{-1.4}$
1033+1809	131 ± 17	225 ± 99	140 ± 66	$3.1^{+1.1}_{-0.9}$
1038−0036	58.9 ± 7.8	99.1 ± 2.9	27.8 ± 3.8	$1.5^{+0.2}_{-0.3}$
1038+0432	228 ± 30	-	-	$2.4^{+0.7}_{-0.6}$
1040+2407	91 ± 12	166.6 ± 3.4	72.5 ± 9.4	$3.9^{+0.9}_{-1.0}$
1041+3432	299 ± 41	-	-	$1.6^{+0.4}_{-0.3}$
1043+3516	105 ± 14	148.9 ± 3.2	75 ± 10	$2.2^{+0.6}_{-0.5}$
1046+1329	126 ± 16	-	-	$5.9^{+0.8}_{-1.4}$
1055+3725	134 ± 17	105.7 ± 5.1	67.5 ± 9.4	$4.4^{+1.0}_{-1.1}$
1058+3143	122 ± 16	38.8 ± 4.5	22.5 ± 4.0	$2.1^{+0.5}_{-0.5}$
1102+2827	288 ± 39	-	-	$2.6^{+1.1}_{-0.7}$
1102+0214	101 ± 13	96.5 ± 3.6	46.3 ± 6.2	$3.9^{+0.9}_{-1.0}$
1103+4144	117 ± 15	53.0 ± 3.8	29.6 ± 4.3	$3.6^{+1.0}_{-0.9}$
1105+5006	245 ± 33	35.8 ± 4.0	41.8 ± 7.4	$1.7^{+0.4}_{-0.4}$
1105+0228	166 ± 21	-	-	$3.8^{+1.3}_{-1.1}$
1106+6737	161 ± 22	62.1 ± 3.9	47.8 ± 7.1	$2.6^{+0.8}_{-0.7}$
1112+0700	163 ± 22	67.7 ± 3.9	52.4 ± 7.7	$1.5^{+0.3}_{-0.3}$
1113+2751	213 ± 28	22.4 ± 4.6	22.7 ± 5.5	$2.9^{+0.9}_{-0.8}$
1132+3323	257 ± 35	-	-	$2.8^{+1.0}_{-0.8}$
1134+1542	309 ± 41	-	-	$2.2^{+0.8}_{-0.5}$
1144+3720	252 ± 34	16.5 ± 4.7	19.8 ± 6.2	$1.6^{+0.4}_{-0.3}$
1144+1218	50.2 ± 6.2	617.1 ± 5.8	147 ± 18	$5.0^{+0.7}_{-1.2}$
1147+5429	212 ± 28	96.5 ± 5.2	97 ± 14	$5.4^{+1.2}_{-1.7}$
1149+0519	174 ± 23	40.1 ± 3.5	33.3 ± 5.3	$1.7^{+0.3}_{-0.4}$
1150+4928	202 ± 27	62.2 ± 3.9	59.7 ± 8.8	$1.8^{+0.4}_{-0.4}$
1150+4533	253 ± 33	-	-	$4.0^{+1.5}_{-1.2}$
1152+5101	165 ± 21	-	-	$6.4^{+0.7}_{-1.3}$
1152+1605	188 ± 26	48.7 ± 3.9	43.5 ± 6.9	$2.4^{+0.7}_{-0.6}$
1157+6138	335 ± 46	-	-	$2.4^{+1.0}_{-0.6}$
1158+1845	212 ± 28	68.5 ± 3.4	69.1 ± 9.7	$1.8^{+0.4}_{-0.4}$

SDSS J	d [pc]	μ [mas yr^{-1}]	$v_\perp$ [km s^{-1}]	Age [Gyr]
1158+5942	186 ± 24	16.3 ± 5.2	14.5 ± 5.0	$3.3^{+1.0}_{-0.9}$
1158+0454	146 ± 19	26.1 ± 5.0	18.2 ± 4.2	$5.6^{+0.8}_{-1.4}$
1158+4712	319 ± 44	60.1 ± 5.5	91 ± 15	$1.5^{+0.3}_{-0.3}$
1158+5448	254 ± 35	-	-	$2.8^{+1.1}_{-0.8}$
1205+3536	176 ± 23	-	-	$3.1^{+0.9}_{-0.8}$
1211+2326	238 ± 32	106.6 ± 4.8	121 ± 17	$2.5^{+0.8}_{-0.6}$
1214−0234	43.2 ± 5.3	550 ± 19	113 ± 14	$5.8^{+0.5}_{-1.2}$
1217+1157	188 ± 25	36.4 ± 5.2	32.6 ± 6.3	$2.5^{+0.7}_{-0.6}$
1218+0023	119 ± 16	59.8 ± 4.0	33.9 ± 5.0	$3.1^{+0.8}_{-0.8}$
1220+0929	263 ± 35	18.9 ± 4.9	23.6 ± 7.0	$2.3^{+0.7}_{-0.5}$
1224+2838	85 ± 11	99.9 ± 3.5	40.5 ± 5.2	$5.8^{+0.6}_{-1.2}$
1226+2936	85 ± 11	205.2 ± 5.1	83 ± 11	$7.1^{+0.5}_{-1.1}$
1229+0743	183 ± 24	18.9 ± 4.9	16.5 ± 4.8	$3.0^{+0.8}_{-0.8}$
1230+3143	198 ± 27	39.8 ± 4.7	37.5 ± 6.8	$2.4^{+0.7}_{-0.6}$
1234+5208	112 ± 15	94.1 ± 3.2	50.3 ± 7.1	$1.5^{+0.3}_{-0.3}$
1238+2149	157 ± 20	74.9 ± 4.9	55.9 ± 7.9	$5.0^{+0.9}_{-1.3}$
1245+0822	236 ± 31	-	-	$2.7^{+0.8}_{-0.7}$
1249+6514	275 ± 37	81.0 ± 7.8	106 ± 18	$1.6^{+0.3}_{-0.3}$
1254+3551	234 ± 32	107.6 ± 7.4	120 ± 18	$2.3^{+0.8}_{-0.6}$
1257+3238	198 ± 26	51.9 ± 4.8	49.0 ± 7.9	$5.7^{+1.1}_{-1.7}$
1257−0310	206 ± 28	-	-	$2.8^{+0.9}_{-0.7}$
1259+3112	118 ± 15	75.6 ± 3.8	42.5 ± 5.9	$3.6^{+1.2}_{-1.0}$
1259+4729	228 ± 31	66.7 ± 5.5	72 ± 12	$2.8^{+1.0}_{-0.8}$
1303+4055	139 ± 18	27.7 ± 3.4	18.3 ± 3.4	$2.9^{+0.8}_{-0.8}$
1308+0957	386 ± 54	-	-	$1.4^{+0.4}_{-0.3}$
1308+0258	208 ± 27	-	-	$3.2^{+1.0}_{-0.9}$
1314+3748	205 ± 28	54.3 ± 4.9	52.9 ± 8.6	$3.4^{+1.3}_{-1.0}$
1316+1918	166 ± 21	48.3 ± 3.5	38.0 ± 5.5	$5.3^{+0.8}_{-1.4}$
1319+3641	236 ± 32	22.4 ± 4.8	25.1 ± 6.4	$1.7^{+0.4}_{-0.4}$
1320+0204	317 ± 44	18.0 ± 6.0	27.1 ± 9.8	$1.9^{+0.6}_{-0.5}$
1321−0237	156 ± 20	-	-	$4.3^{+1.3}_{-1.3}$
1329+1301	186 ± 25	167.0 ± 7.6	148 ± 21	$2.1^{+0.6}_{-0.5}$
1330+3029	26.1 ± 3.4	487.0 ± 2.4	60.6 ± 7.8	$3.1^{+0.8}_{-0.8}$
1336+3547	65.6 ± 8.9	126.5 ± 2.6	39.5 ± 5.4	$2.3^{+0.6}_{-0.6}$
1339+2643	98 ± 13	64.3 ± 3.0	30.1 ± 4.3	$2.8^{+0.7}_{-0.7}$
1340+2702	373 ± 51	7.8 ± 3.8	13.8 ± 7.1	$1.4^{+0.3}_{-0.3}$
1342+1813	168 ± 21	74.3 ± 5.1	59.5 ± 8.6	$5.7^{+0.8}_{-1.4}$
1345+1153	131 ± 17	139.9 ± 3.8	87 ± 11	$3.2^{+1.0}_{-0.9}$
1347+1415	158 ± 21	14.0 ± 3.5	10.5 ± 3.0	$2.2^{+0.6}_{-0.5}$
1350+1058	139 ± 17	69.7 ± 5.0	46.1 ± 6.5	$6.0^{+0.7}_{-1.2}$
1351+2645	161 ± 20	55.4 ± 4.4	42.5 ± 6.4	$3.3^{+1.0}_{-0.9}$

SDSS J	d [pc]	μ [mas yr^{-1}]	$v_\perp$ [km s^{-1}]	Age [Gyr]
1356+2416	90 ± 12	112.2 ± 3.2	48.3 ± 6.3	$3.2^{+0.9}_{-0.8}$
1356+0236	214 ± 30	24.9 ± 5.2	25.4 ± 6.5	$1.2^{+0.2}_{-0.2}$
1401+3659	80 ± 10	59.8 ± 2.9	22.7 ± 3.1	$3.3^{+0.9}_{-0.9}$
1404+3620	77.0 ± 9.8	176.2 ± 3.0	64.6 ± 8.3	$3.5^{+0.9}_{-0.9}$
1405+2542	214 ± 28	21.1 ± 4.9	21.6 ± 5.8	$3.5^{+1.0}_{-1.0}$
1405+1549	124 ± 17	112.8 ± 3.1	66.4 ± 9.1	$1.8^{+0.4}_{-0.4}$
1411+3410	149 ± 19	70.3 ± 4.8	49.9 ± 7.1	$4.8^{+1.1}_{-1.3}$
1412+2836	148 ± 19	103.0 ± 3.6	72.8 ± 9.5	$6.4^{+0.5}_{-1.2}$
1421+1843	245 ± 34	36.4 ± 3.8	42.5 ± 7.3	$1.7^{+0.4}_{-0.4}$
1428+4403	44.1 ± 6.0	278.8 ± 2.5	58.5 ± 8.0	$2.3^{+0.6}_{-0.6}$
1429+3841	192 ± 25	34.7 ± 3.7	31.7 ± 5.3	$3.2^{+1.1}_{-0.9}$
1430−0151	115 ± 15	60.4 ± 3.7	33.1 ± 4.8	$3.0^{+0.9}_{-0.8}$
1443+5833	380 ± 53	209.9 ± 4.2	380 ± 53	$1.9^{+0.6}_{-0.4}$
1443+3014	370 ± 51	-	-	$2.1^{+0.7}_{-0.5}$
1445+0913	317 ± 43	-	-	$2.4^{+0.8}_{-0.6}$
1448+1047	100 ± 13	63.9 ± 3.2	30.6 ± 4.3	$2.4^{+0.6}_{-0.6}$
1500+2315	363 ± 52	-	-	$2.4^{+1.1}_{-0.7}$
1502+3744	102 ± 13	104.0 ± 3.8	50.3 ± 6.6	$5.1^{+0.7}_{-1.2}$
1507+4034	338 ± 46	-	-	$1.8^{+0.6}_{-0.4}$
1518+0506	67.4 ± 8.4	39.7 ± 3.8	12.7 ± 2.0	$6.4^{+0.5}_{-1.1}$
1524+4049	143 ± 19	26.2 ± 3.9	17.8 ± 3.6	$3.5^{+1.0}_{-0.9}$
1534+1242	276 ± 37	-	-	$3.6^{+1.4}_{-1.1}$
1535+1247	19.4 ± 2.4	247.8 ± 2.3	22.9 ± 2.9	$3.8^{+1.0}_{-0.9}$
1536+4205	181 ± 23	41.4 ± 5.6	35.7 ± 6.7	$3.7^{+1.0}_{-1.0}$
1537+3608	193 ± 24	-	-	$4.5^{+1.3}_{-1.3}$
1540+5352	294 ± 40	-	-	$2.4^{+1.0}_{-0.6}$
1542+4650	209 ± 27	50.5 ± 5.5	50.3 ± 8.5	$3.2^{+1.0}_{-0.9}$
1543+2024	306 ± 42	-	-	$2.7^{+1.1}_{-0.8}$
1545+5236	134 ± 18	47.2 ± 5.9	30.2 ± 5.4	$3.6^{+1.0}_{-1.0}$
1546+3009	157 ± 21	18.4 ± 3.4	13.7 ± 3.1	$2.3^{+0.6}_{-0.5}$
1549+2633	222 ± 30	51.3 ± 3.6	54.1 ± 8.2	$2.8^{+0.8}_{-0.7}$
1549+1906	292 ± 39	42.2 ± 4.9	59 ± 10	$2.5^{+0.9}_{-0.6}$
1554+1735	58.6 ± 7.7	147.5 ± 2.5	41.2 ± 5.4	$2.3^{+0.6}_{-0.5}$
1604+1830	142 ± 19	55.1 ± 3.1	37.4 ± 5.4	$2.6^{+0.7}_{-0.7}$
1610+4006	274 ± 38	-	-	$2.3^{+0.8}_{-0.6}$
1612+3534	362 ± 52	39.6 ± 5.5	68 ± 14	$2.2^{+0.9}_{-0.5}$
1616+3303	117 ± 15	52.0 ± 3.5	29.1 ± 4.3	$2.6^{+0.7}_{-0.7}$
1624+3310	319 ± 44	-	-	$2.0^{+0.7}_{-0.5}$
1626+3303	256 ± 34	17.9 ± 5.2	21.8 ± 7.0	$2.8^{+1.0}_{-0.8}$
1627+4646	193 ± 26	19.0 ± 4.0	17.5 ± 4.4	$2.6^{+0.8}_{-0.7}$
1636+1619	66.9 ± 8.0	87.0 ± 4.1	27.7 ± 3.6	$7.7^{+0.3}_{-0.9}$

SDSS J	d [pc]	μ [mas yr^{-1}]	$v_{\perp}$ [km s^{-1}]	Age [Gyr]
1641+1856	137 ± 17	53.9 ± 3.4	35.1 ± 5.0	$3.7^{+0.9}_{-0.9}$
1649+2238	147 ± 18	31.8 ± 4.0	22.2 ± 4.0	$5.4^{+0.7}_{-1.3}$
1651+4249	106 ± 14	80 ± 16	41 ± 10	$4.0^{+1.2}_{-1.1}$
1706+2541	281 ± 38	13.7 ± 5.2	18.4 ± 7.6	$2.3^{+0.8}_{-0.5}$
2109−0039	149 ± 19	42.8 ± 5.0	30.5 ± 5.4	$3.2^{+1.1}_{-0.9}$
2110+0512	252 ± 33	-	-	$4.1^{+1.3}_{-1.2}$
2123+0016	116 ± 14	109.5 ± 4.8	60.4 ± 8.0	$5.7^{+0.7}_{-1.3}$
2157+1206	127 ± 17	38.9 ± 3.6	23.5 ± 3.8	$3.1^{+0.8}_{-0.8}$
2225+2338	147 ± 20	43.2 ± 7.0	30.2 ± 6.3	$2.0^{+0.5}_{-0.4}$
2230+1905	168 ± 22	17.3 ± 3.1	13.8 ± 3.1	$4.4^{+1.2}_{-1.3}$
2231+0906	93 ± 12	218.4 ± 3.0	97 ± 13	$3.5^{+0.9}_{-0.9}$
2235−0056	200 ± 27	-	-	$2.7^{+0.8}_{-0.7}$
2238+0213	267 ± 36	-	-	$1.9^{+0.6}_{-0.4}$
2238−0113	258 ± 35	-	-	$2.1^{+0.7}_{-0.5}$
2254+3031	120 ± 15	49.4 ± 3.1	28.3 ± 4.0	$3.5^{+0.9}_{-0.9}$
2304+2415	79.1 ± 9.8	115.2 ± 3.6	43.4 ± 5.5	$6.3^{+0.5}_{-1.1}$
2319+3018	306 ± 41	-	-	$1.9^{+0.5}_{-0.4}$
2325+0448	134 ± 17	40.3 ± 3.2	25.8 ± 3.9	$3.2^{+0.9}_{-0.9}$
2328+0830	251 ± 34	-	-	$3.8^{+1.4}_{-1.2}$
2330+2805	249 ± 33	44.9 ± 4.5	53.3 ± 8.9	$2.2^{+0.7}_{-0.5}$
2330+2956	180 ± 24	36.2 ± 3.6	31.0 ± 5.1	$2.0^{+0.4}_{-0.4}$
2333+1058	302 ± 40	-	-	$2.9^{+1.1}_{-0.8}$
2340+0124	114 ± 15	115.1 ± 3.0	62.7 ± 8.4	$2.9^{+0.8}_{-0.8}$
2340+0817	132 ± 16	138.1 ± 3.6	86 ± 11	$4.5^{+1.0}_{-1.2}$
2343−0010	163 ± 22	59.1 ± 5.2	45.9 ± 7.2	$3.5^{+1.3}_{-1.0}$
2352+1922	272 ± 37	-	-	$2.9^{+1.1}_{-0.8}$
2352+3344	312 ± 42	20.6 ± 3.8	30.6 ± 7.0	$1.8^{+0.4}_{-0.4}$
2357+2348	251 ± 33	-	-	$3.2^{+1.1}_{-0.9}$

Bibliography

Aannestad P. A., Sion E. M., 1985, AJ, 90, 1832

Aannestad P. A., Kenyon S. J., Hammond G. L., Sion E. M., 1993, AJ, 105, 1033

Achilleos N., Wickramasinghe D. T., 1989, ApJ, 346, 444

Achilleos N., Wickramasinghe D. T., Liebert J., Saffer R. A., Grauer A. D., 1992, ApJ, 396, 273

Adams W. S., 1915, PASP, 27, 236

Allard N. F., Alekseev V. A., 2014, Adv. Space Res., 54, 1248

Allard N., Kielkopf J., 1982, Rev. Mod. Phys., 54, 1103

Allard N. F., Royer A., Kielkopf J. F., Feautrier N., 1999, Phys. Rev. A, 60, 1021

Allard N. F., Leininger T., Gadéa F. X., Brousseau-Couture V., Dufour P., 2016a, A&A, 588, A142

Allard N. F., Guillon G., Alekseev V. A., Kielkopf J. F., 2016b, A&A, 593, A13

Almlöf J., Taylor P. R., 1987, J. Chem. Phys., 86, 4070

Alonso R., Rappaport S., Deeg H. J., Palle E., 2016, A&A, 589, L6

Althaus L. G., Córsico A. H., Isern J., García-Berro E., 2010, A&AR, 18, 471

Angel J. R. P., Landstreet J. D., 1970, ApJ Lett., 160, L147

Angel J. R. P., Borra E. F., Landstreet J. D., 1981, ApJS, 45, 457

Aquilante F., et al., 2010, J. Comp. Chem., 31, 224

Barber S. D., Belardi C., Kilic M., Gianninas A., 2016, MNRAS, 459, 1415

Beck P. G., et al., 2012, Nat, 481, 55

Becklin E. E., Farihi J., Jura M., Song I., Weinberger A. J., Zuckerman B., 2005, ApJ Lett., 632, L119

Bergeron P., Ruiz M. T., Leggett S. K., 1992, ApJ, 400, 315

Bergeron P., Ruiz M. T., Leggett S. K., 1997, ApJS, 108, 339

Bergeron P., Leggett S. K., Ruiz M., 2001, ApJS, 133, 413

Bergeron P., et al., 2011, ApJ, 737, 28

Bergeron P., Rolland B., Limoges M.-M., Giammichele N., Séguin-Charbonneau L., Green E. M., 2015, in Dufour P., Bergeron P., Fontaine G., eds, Astronomical Society of the Pacific Conference Series Vol. 493, 19th European Workshop on White Dwarfs. p. 33

Bergfors C., Farihi J., Dufour P., Rocchetto M., 2014, MNRAS, 444, 2147

Bessel F. W., 1844, MNRAS, 6, 136

Böhm K.-H., 1968, Ap&SS, 2, 375

Böhm K. H., Cassinelli J. P., 1970, in Bulletin of the American Astronomical Society. p. 297

Bonsor A., Veras D., 2015, MNRAS, 454, 53

Bonsor A., Wyatt M. C., 2012, MNRAS, 420, 2990

Bonsor A., Mustill A. J., Wyatt M. C., 2011, MNRAS, 414, 930

Brandt B. L., Hannahs S., Schneider-Muntau H. J., Boebinger G., Sullivan N. S., 2001, Physica B Condensed Matter, 294, 505

Brinkworth C. S., Gänsicke B. T., Marsh T. R., Hoard D. W., Tappert C., 2009, ApJ, 696, 1402

Brinkworth C. S., Gänsicke B. T., Girven J. M., Hoard D. W., Marsh T. R., Parsons S. G., Koester D., 2012, ApJ, 750, 86

Brinkworth C. S., Burleigh M. R., Lawrie K., Marsh T. R., Knigge C., 2013, ApJ, 773, 47

Brown J. C., Veras D., Gänsicke B. T., 2017, MNRAS, 468, 1575

Burleigh M. R., Jordan S., Schweizer W., 1999, ApJ Lett., 510, L37

Cantiello M., Mankovich C., Bildsten L., Christensen-Dalsgaard J., Paxton B., 2014, ApJ, 788, 93

Carry B., 2012, Planet. Space Sci., 73, 98

Catalán S., Isern J., García-Berro E., Ribas I., 2008, MNRAS, 387, 1693

Chandrasekhar S., 1931a, ApJ, 74, 81

Chandrasekhar S., 1931b, MNRAS, 91, 456

Chandrasekhar S., 1935, MNRAS, 95, 207

Chandrasekhar S., 1939, An introduction to the study of stellar structure

Charbonneau P., 2014, A&AR, 52, 251

Charbonneau D., Brown T. M., Noyes R. W., Gilliland R. L., 2002, ApJ, 568, 377

Cottrell P. L., Bessell M. S., Wickramasinghe D. T., 1977, ApJ Lett., 218, L133

Cowles M. K., 2013, Applied Bayesian Statistics, 1 edn. Springer Texts in Statistics Vol. 89, Springer-Verlag, New York

Czuchaj E., Rebentrost F., Stoll H., Preuss H., 1996, Contemp. Phys., 207, 51

Davidsson B. J. R., 1999, Icarus, 142, 525

Dawson K. S., et al., 2013, AJ, 145, 10

Debes J. H., Sigurdsson S., 2002, ApJ, 572, 556

Debes J. H., Hoard D. W., Kilic M., Wachter S., Leisawitz D. T., Cohen M., Kirkpatrick J. D., Griffith R. L., 2011, ApJ, 729, 4

Debes J. H., Walsh K. J., Stark C., 2012, ApJ, 747, 148

Demetropoulos I. N., Lawley K. P., 1982, J. Phys. B, 15, 1855

Dennihy E., Debes J. H., Dunlap B. H., Dufour P., Teske J. K., Clemens J. C., 2016, ApJ, 831, 31

Dirac P. A. M., 1926, Proceedings of the Royal Society of London Series A, 112, 661

Dufour P., Bergeron P., Fontaine G., 2005, ApJ, 627, 404

Dufour P., Bergeron P., Schmidt G. D., Liebert J., Harris H. C., Knapp G. R., Anderson S. F., Schneider D. P., 2006, ApJ, 651, 1112

Dufour P., et al., 2007, ApJ, 663, 1291

Dufour P., Kilic M., Fontaine G., Bergeron P., Melis C., Bochanski J., 2012, ApJ, 749, 6

Dufour P., et al., 2015, in Dufour P., Bergeron P., Fontaine G., eds, Astronomical Society of the Pacific Conference Series Vol. 493, 19th European Workshop on White Dwarfs. p. 37

Duncan M. J., Lissauer J. J., 1998, Icarus, 134, 303

Eddington A. S., 1926, The Internal Constitution of the Stars

Eggen O. J., 1968, ApJS, 16, 97

Eisenstein D. J., et al., 2006, ApJS, 167, 40

Euchner F., Reinsch K., Jordan S., Beuermann K., Gänsicke B. T., 2005, A&A, 442, 651

Fabrika S., Valyavin G., 1999, in Solheim S.-E., Meistas E. G., eds, Astronomical Society of the Pacific Conference Series Vol. 169, 11th European Workshop on White Dwarfs. p. 214

Farihi J., 2016, New Astron. Rev., 71, 9

Farihi J., Zuckerman B., Becklin E. E., 2008, ApJ, 674, 431

Farihi J., Barstow M. A., Redfield S., Dufour P., Hambly N. C., 2010a, MNRAS, 404, 2123

Farihi J., Jura M., Lee J., Zuckerman B., 2010b, ApJ, 714, 1386

Farihi J., Dufour P., Napiwotzki R., Koester D., 2011a, MNRAS, 413, 2559

Farihi J., Brinkworth C. S., Gänsicke B. T., Marsh T. R., Girven J., Hoard D. W., Klein B., Koester D., 2011b, ApJ Lett., 728, L8

Farihi J., Gänsicke B. T., Steele P. R., Girven J., Burleigh M. R., Breedt E., Koester D., 2012, MNRAS, 421, 1635

Farihi J., Gänsicke B. T., Koester D., 2013a, Science, 342, 218

Farihi J., Gänsicke B. T., Koester D., 2013b, MNRAS, 432, 1955

Farihi J., Koester D., Zuckerman B., Vican L., Gänsicke B. T., Smith N., Walth G., Breedt E., 2016, MNRAS

Fermi E., 1926, Rendiconti dell'Accademia Nazionale dei Lincei, 3, 145

Finley J., Malmqvist P.-Å., Roos B. O., Serrano-Andrés L., 1998, Chem. Phys. Lett., 288, 299

Fontaine G., van Horn H. M., 1976, ApJS, 31, 467

Fontaine G., Brassard P., Bergeron P., 2001, PASP, 113, 409

Fontaine G., Brassard P., Dufour P., Tremblay P.-E., 2015, in Dufour P., Bergeron P., Fontaine G., eds, Astronomical Society of the Pacific Conference Series Vol. 493, 19th European Workshop on White Dwarfs. p. 113

Foreman-Mackey D., Hogg D. W., Lang D., Goodman J., 2013, PASP, 125, 306

Forster H., Strupat W., Rosner W., Wunner G., Ruder H., Herold H., 1984, Journal of Physics B Atomic Molecular Physics, 17, 1301

Fowler R. H., 1926, MNRAS, 87, 114

Frewen S. F. N., Hansen B. M. S., 2014, MNRAS, 439, 2442

Friedrich S., Oestreicher R., Schweizer W., 1996, A&A, 309, 227

Fuller J., Cantiello M., Stello D., Garcia R. A., Bildsten L., 2015, Sci, 350, 423

Gänsicke B. T., 2011, in Schuh S., Drechsel H., Heber U., eds, American Institute of Physics Conference Series Vol. 1331, AIP Conf. Proc.. pp 211–214 (`arXiv:1101.3946`), doi:10.1063/1.3556202

Gänsicke B. T., Euchner F., Jordan S., 2002, A&A, 394, 957

Gänsicke B. T., Marsh T. R., Southworth J., Rebassa-Mansergas A., 2006, Science, 314, 1908

Gänsicke B. T., Marsh T. R., Southworth J., 2007, MNRAS, 380, L35

Gänsicke B. T., Koester D., Marsh T. R., Rebassa-Mansergas A., Southworth J., 2008, MNRAS, 391, L103

Gänsicke B. T., Koester D., Farihi J., Girven J., Parsons S. G., Breedt E., 2012, MNRAS, 424, 333

Gänsicke B., et al., 2016a, in Skillen I., Balcells M., Trager S., eds, Astronomical Society of the Pacific Conference Series Vol. 507, Multi-Object Spectroscopy in the Next Decade: Big Questions, Large Surveys, and Wide Fields. p. 159

Gänsicke B. T., et al., 2016b, ApJ, 818, L7

Gary B. L., Rappaport S., Kaye T. G., Alonso R., Hambschs F.-J., 2017, MNRAS, 465, 3267

Gates E., et al., 2004, ApJ Lett., 612, L129

Geier S., et al., 2015, Sci, 347, 1126

Genest-Beaulieu C., Bergeron P., 2014, ApJ, 796, 128

Gentile Fusillo N. P., Gänsicke B. T., Greiss S., 2015, MNRAS, 448, 2260

Gentile Fusillo N. P., Gänsicke B. T., Farihi J., Koester D., Schreiber M. R., Pala A. F., 2017, MNRAS, 468, 971

Gentile Fusillo N. P., Tremblay P.-E., Jordan S., Gänsicke B. T., Kalirai J. S., Cummings J., 2018, MNRAS, 473, 3693

Gianninas A., Dufour P., Bergeron P., 2004, ApJ Lett., 617, L57

Gianninas A., Strickland B. D., Kilic M., Bergeron P., 2013, ApJ, 766, 3

Girven J., Brinkworth C. S., Farihi J., Gänsicke B. T., Hoard D. W., Marsh T. R., Koester D., 2012, ApJ, 749, 154

Giusti-Suzor A., Roueff E., 1975, J. Phys. B, 8, 2708

Goodman J., Weare J., 2010, Communications in Applied Mathematics and Computational Science, Vol.˜5, No.˜1, p.˜65-80, 2010, 5, 65

Graham J. R., Matthews K., Neugebauer G., Soifer B. T., 1990, ApJ, 357, 216

Gunn J. E., et al., 2006, AJ, 131, 2332

Guo J., Tziamtzis A., Wang Z., Liu J., Zhao J., Wang S., 2015, ApJ Lett., 810, L17

Gurri P., Veras D., Gänsicke B. T., 2017, MNRAS, 464, 321

Hamada T., Salpeter E. E., 1961, ApJ, 134, 683

Hamers A. S., Portegies Zwart S. F., 2016, MNRAS, 462, L84

Hardersen P. S., Gaffey M. J., Abell P. A., 2005, Icarus, 175, 141

Hardy F., Dufour P., Jordan S., 2017, in Tremblay P.-E., Gaensicke B., Marsh T., eds, Astronomical Society of the Pacific Conference Series Vol. 509, 20th European White Dwarf Workshop. p. 205 (`arXiv:1610.01522`)

Harris M. J., Teegarden B. J., Cline T. L., Gehrels N., Palmer D. M., Ramaty R., Seifert H., 2000, ApJ, 542, 1057

Harris H. C., et al., 2001, ApJ Lett., 549, L109

Harris H. C., et al., 2008, ApJ, 679, 697

Haywood M., Di Matteo P., Lehnert M. D., Katz D., Gómez A., 2013, A&A, 560, A109

Herschel W., 1785, Philosophical Transactions of the Royal Society of London Series I, 75, 40

Hertzsprung E., 1915, ApJ, 42

Herwig F., 2013, Evolution of Solar and Intermediate-Mass Stars. p. 397, doi:10.1007/978-94-007-5615-1˙8

Hintzen P., Tapia S., 1975, ApJ Lett., 199, L31

Holberg J. B., Bergeron P., 2006, AJ, 132, 1221

Holberg J. B., Wesemael F., 2007, Journal for the History of Astronomy, 38, 161

Holberg J. B., Oswalt T. D., Barstow M. A., 2012, AJ, 143, 68

Hollands M. A., Gänsicke B. T., Koester D., 2015, MNRAS, 450, 681

Hollands M. A., Koester D., Alekseev V., Herbert E. L., Gänsicke B. T., 2017, MNRAS, 467, 4970

Horne K., 1986, PASP, 98, 609

Howell S. B., 2006, Handbook of CCD Astronomy

Hubeny I., Lanz T., 1995, ApJ, 439, 875

Jura M., 2003, ApJ Lett., 584, L91

Jura M., Farihi J., Zuckerman B., Becklin E. E., 2007a, AJ, 133, 1927

Jura M., Farihi J., Zuckerman B., 2007b, ApJ, 663, 1285

Jura M., Farihi J., Zuckerman B., 2009, AJ, 137, 3191

Jura M., Xu S., Klein B., Koester D., Zuckerman B., 2012, ApJ, 750, 69

Kawka A., Vennes S., 2004, in Zverko J., Ziznovsky J., Adelman S. J., Weiss W. W., eds, IAU Symposium Vol. 224, The A-Star Puzzle. pp 879–885, doi:10.1017/S1743921305009920

Kawka A., Vennes S., 2006, ApJ, 643, 402

Kawka A., Vennes S., 2011, A&A, 532, A7

Kawka A., Vennes S., 2014, MNRAS, 439, L90

Kawka A., Vennes S., 2016, MNRAS, 458, 325

Kawka A., Vennes S., Thorstensen J. R., 2004, AJ, 127, 1702

Kawka A., Vennes S., Schmidt G. D., Wickramasinghe D. T., Koch R., 2007, ApJ, 654, 499

Kemp J. C., Swedlund J. B., Landstreet J. D., Angel J. R. P., 1970, ApJ Lett., 161, L77

Kepler S. O., et al., 2013, MNRAS, 429, 2934

Kepler S. O., et al., 2015, MNRAS, 446, 4078

Kepler S. O., et al., 2016, MNRAS, 455, 3413

Kilic M., von Hippel T., Leggett S. K., Winget D. E., 2005, ApJ Lett., 632, L115

Kilic M., Patterson A. J., Barber S., Leggett S. K., Dufour P., 2012, MNRAS, 419, L59

Kissin Y., Thompson C., 2015a, ApJ, 808, 35

Kissin Y., Thompson C., 2015b, ApJ, 809, 108

Klein B., Jura M., Koester D., Zuckerman B., Melis C., 2010, ApJ, 709, 950

Klein B., Jura M., Koester D., Zuckerman B., 2011, ApJ, 741, 64

Kleinman S. J., et al., 2004, ApJ, 607, 426

Kleinman S. J., et al., 2013, ApJS, 204, 5

Knox Jr. R., 1970, Meteoritics, 5

Koch K. R., 2007, Introduction to Bayesian Statistics, 2 edn. Springer-Verlag, Heidelberg

Koester D., 2009, A&A, 498, 517

Koester D., 2010, Memorie della Societa Astronomica Italiana,, 81, 921

Koester D., 2013, White Dwarf Stars. Springer, p. 559, doi:10.1007/978-94-007-5615-1˙11

Koester D., Kepler S. O., 2015, A&A, 583, A86

Koester D., Wilken D., 2006a, A&A, 453, 1051

Koester D., Wilken D., 2006b, A&A, 453, 1051

Koester D., Provencal J., Shipman H. L., 1997, A&A, 320, L57

Koester D., Girven J., Gänsicke B. T., Dufour P., 2011, A&A, 530, A114

Koester D., Gänsicke B. T., Farihi J., 2014, A&A, 566, A34

Kowalski P. M., Saumon D., 2006, ApJ Lett., 651, L137

Kramida A., Ralchenko Y., Reader J., NIST ASD Team 2016, NIST Atomic Spectra Database (version 5.4), [Online], `http://physics.nist.gov/asd`

Kreidberg L., et al., 2014a, Nat, 505, 69

Kreidberg L., et al., 2014b, ApJ Lett., 793, L27

Kresak L., 1977, Bulletin of the Astronomical Institutes of Czechoslovakia, 28, 65

Külebi B., Jordan S., Euchner F., Gänsicke B. T., Hirsch H., 2009, A&A, 506, 1341

Külebi B., Jordan S., Nelan E., Bastian U., Altmann M., 2010, A&A, 524, A36

Kupka F., Piskunov N., Ryabchikova T. A., Stempels H. C., Weiss W. W., 1999, A&AS, 138, 119

Landstreet J. D., Angel J. R. P., 1975, ApJ, 196, 819

Latter W. B., Schmidt G. D., Green R. F., 1987, ApJ, 320, 308

Leininger T., Gadéa F. X., Allard N. F., 2015, in Martins F., Boissier S., Buat V., Cambrésy L., Petit P., eds, SF2A-2015: Proceedings of the Annual meeting of the French Society of Astronomy and Astrophysics. pp 397–399

Li N., Thakar A. R., 2008, Computing in Science and Engineering, 10, 18

Liebert J., 1988, PASP, 100, 1302

Liebert J., Wehrse R., 1983, A&A, 122, 297

Liebert J., Dahn C. C., Monet D. G., 1988, ApJ, 332, 891

Liebert J., Bergeron P., Holberg J. B., 2003, AJ, 125, 348

Lindblad B., 1922, ApJ, 55

Lissauer J. J., et al., 2011, Nat, 470, 53

Luyten W. J., 1922a, PASP, 34, 54

Luyten W. J., 1922b, PASP, 34, 132

Luyten W. J., 1922c, PASP, 34, 356

Malmqvist P. Å., Roos B. O., Schimmelpfennig B., 2002, Chem. Phys. Lett., 357, 230

Manser C. J., et al., 2016a, MNRAS, 455, 4467

Manser C. J., Gänsicke B. T., Koester D., Marsh T. R., Southworth J., 2016b, MNRAS, 462, 1461

Margala D., Kirkby D., Dawson K., Bailey S., Blanton M., Schneider D. P., 2015, preprint, (`arXiv:1506.04790`)

Markiel J. A., Thomas J. H., van Horn H. M., 1994, ApJ, 430, 834

Marsh T. R., 1989, PASP, 101, 1032

Matter A., Delbo M., Carry B., Ligori S., 2013, Icarus, 226, 419

McDonough W., 2000, in Teisseyre R., Majewski E., eds, Earthquake Thermodynamics and Phase Transformation in the Earth's Interior. Elsevier Science Academic Press, pp 5–24

McGraw J. T., Robinson E. L., 1975, ApJ Lett., 200, L89

Melis C., Dufour P., 2017, ApJ, 834, 1

Melis C., Jura M., Albert L., Klein B., Zuckerman B., 2010, ApJ, 722, 1078

Melis C., Farihi J., Dufour P., Zuckerman B., Burgasser A. J., Bergeron P., Bochanski J., Simcoe R., 2011, ApJ, 732, 90

Melis C., et al., 2012, ApJ Lett., 751, L4

Mestel L., 1952, MNRAS, 112, 583

Metzger B. D., Rafikov R. R., Bochkarev K. V., 2012, MNRAS, 423, 505

Michaud G., Fontaine G., 1979, apj, 229, 694

Mihalas D., 1978, Stellar atmospheres, second edn. W. H. Freeman & Co, San Francisco

Milne E. A., 1931a, The Observatory, 54, 140

Milne E. A., 1931b, MNRAS, 91, 751

Milne E. A., 1931c, Nat, 127, 16

Monteiro T. S., Cooper I. L., Dickinson A. S., Lewis E. L., 1986, J. Phys. B, 19, 4087

Mosser B., et al., 2012, A&A, 548, A10

Moynier F., Yin Q.-Z., Schauble E., 2011, Science, 331, 1417

Mustill A. J., Villaver E., 2012, ApJ, 761, 121

Mustill A. J., Veras D., Villaver E., 2014, MNRAS, 437, 1404

Neiner C., Folsom C. P., Blazere A., 2014, in Ballet J., Martins F., Bournaud F., Monier R., Reylé C., eds, SF2A-2014: Proceedings of the Annual meeting of the French Society of Astronomy and Astrophysics. pp 163–166 (`arXiv:1410.2755`)

Nordhaus J., Spiegel D. S., Ibgui L., Goodman J., Burrows A., 2010, MNRAS, 408, 631

Nordhaus J., Wellons S., Spiegel D. S., Metzger B. D., Blackman E. G., 2011, Proceedings of the National Academy of Science, 108, 3135

Opik E. J., 1958, Physics of meteor flight in the atmosphere.. New York, Interscience Publishers, 1958.

Ostro S. J., 1985, PASP, 97, 877

Oswalt T. D., Smith J. A., Wood M. A., Hintzen P., 1996, Nat, 382, 692

Palme H., O'Neill H. S. C., 2003, Treatise on Geochemistry, 2, 568

Paquette C., Pelletier C., Fontaine G., Michaud G., 1986a, ApJS, 61, 177

Paquette C., Pelletier C., Fontaine G., Michaud G., 1986b, ApJS, 61, 197

Petrovic J. J., 2001, Journal of Materials Science, 36, 1579

Petrovich C., Muñoz D. J., 2017, ApJ, 834, 116

Piskunov N. E., Kupka F., Ryabchikova T. A., Weiss W. W., Jeffery C. S., 1995, A&AS, 112, 525

Preston G. W., 1970, ApJ Lett., 160, L143

Raddi R., Gänsicke B. T., Koester D., Farihi J., Hermes J. J., Scaringi S., Breedt E., Girven J., 2015, MNRAS, 450, 2083

Rappaport S., et al., 2012, ApJ, 752, 1

Rappaport S., Gary B. L., Kaye T., Vanderburg A., Croll B., Benni P., Foote J., 2016, MNRAS, 458, 3904

Reach W. T., Kuchner M. J., von Hippel T., Burrows A., Mullally F., Kilic M., Winget D. E., 2005, ApJ Lett., 635, L161

Reach W. T., Lisse C., von Hippel T., Mullally F., 2009, ApJ, 693, 697

Rebassa-Mansergas A., Gänsicke B. T., Rodríguez-Gil P., Schreiber M. R., Koester D., 2007, MNRAS, 382, 1377

Redfield S., Farihi J., Cauley P. W., Parsons S. G., Gänsicke B. T., Duvvuri G. M., 2017, ApJ, 839, 42

Reid I. N., Liebert J., Schmidt G. D., 2001, ApJ Lett., 550, L61

Rocchetto M., Farihi J., Gänsicke B. T., Bergfors C., 2015, MNRAS, 449, 574

Roesner W., Wunner G., Herold H., Ruder H., 1984, Journal of Physics B Atomic Molecular Physics, 17, 29

Rogers L. A., Seager S., 2010, ApJ, 712, 974

Roos B. O., Lindh R., Malmqvist P.-A., Veryazov V., Widmark P. O., 2004, J. Chem. Phys., 108, 2851

Ross N. P., et al., 2012, ApJS, 199, 3

Ruder H., Wunner G., Herold H., Geyer F., 1994, Atoms in strong magnetic fields. Springer, Heidelberg

Rudnick R. L., Gao S., 2003, Treatise on Geochemistry, 3, 659

Russell H. N., 1931, MNRAS, 91, 739

Ryabchikova T. A., Piskunov N. E., Kupka F., Weiss W. W., 1997, Baltic Astronomy, 6, 244

Saha M. N., 1920, Nat, 105, 232

Salaris M., 2009, in Mamajek E. E., Soderblom D. R., Wyse R. F. G., eds, IAU Symposium Vol. 258, The Ages of Stars. pp 287–298, doi:10.1017/S1743921309031937

Salaris M., Althaus L. G., García-Berro E., 2013, A&A, 555, A96

Salpeter E. E., 1961, ApJ, 134, 669

Sanchis-Ojeda R., et al., 2015, ApJ, 812, 112

Schaeberle J. M., 1896, AJ, 17, 37

Schatzman E., 1949, ApJ, 110, 261

Schimeczek C., Wunner G., 2014a, Computer Physics Communications, 185, 2655

Schimeczek C., Wunner G., 2014b, ApJS, 212, 26

Schlegel D. J., Finkbeiner D. P., Davis M., 1998, ApJ, 500, 525

Schmidt M., 1959, ApJ, 129, 243

Schmidt G. D., et al., 2003, ApJ, 595, 1101

Sharma S., 2017, ARA&A, 55, 213

Shipman H. L., Greenstein J. L., Boksenberg A., 1977, AJ, 82, 480

Sion E. M., Greenstein J. L., Landstreet J. D., Liebert J., Shipman H. L., Wegner G. A., 1983, ApJ, 269, 253

Sion E. M., Holberg J. B., Oswalt T. D., McCook G. P., Wasatonic R., Myszka J., 2014, AJ, 147, 129

Slyuta E. N., 2013, Solar System Research, 47, 109

Slyuta E. N., Voropaev S. A., 1997, Icarus, 129, 401

Stoner E., 1930, The London, Edinburgh, and Dublin Philosophical Magazine and Journal of Science: Series 7, Volume 9, Issue 60, p. 944-963, 9, 944

Swain M. R., Vasisht G., Tinetti G., 2008, Nat, 452, 329

Thirumalai A., Heyl J. S., 2014, Advances in Atomic Molecular and Optical Physics, 63, 323

Thomas J. H., Markiel J. A., van Horn H. M., 1995, ApJ, 453, 403

Tout C. A., Wickramasinghe D. T., Liebert J., Ferrario L., Pringle J. E., 2008, MNRAS, 387, 897

Tremblay P.-E., Bergeron P., 2009, ApJ, 696, 1755

Tremblay P.-E., Fontaine G., Freytag B., Steiner O., Ludwig H.-G., Steffen M., Wedemeyer S., Brassard P., 2015, ApJ, 812, 19

Tremblay P.-E., Cummings J., Kalirai J. S., Gänsicke B. T., Gentile-Fusillo N., Raddi R., 2016, MNRAS, 461, 2100

Vanderburg A., et al., 2015, Nat, 526, 546

Vanlandingham K. M., et al., 2005, AJ, 130, 734

Vauclair G., Vauclair S., Greenstein J. L., 1979, A&A, 80, 79

Vennes S., Kawka A., 2013, ApJ, 779, 70

Vennes S., Kawka A., Németh P., 2011, MNRAS, 413, 2545

Veras D., Gänsicke B. T., 2015a, MNRAS, 447, 1049

Veras D., Gänsicke B. T., 2015b, MNRAS, 447, 1049

Veras D., Mustill A. J., Bonsor A., Wyatt M. C., 2013, MNRAS, 431, 1686

Veras D., Leinhardt Z. M., Bonsor A., Gänsicke B. T., 2014a, MNRAS, 445, 2244

Veras D., Jacobson S. A., Gänsicke B. T., 2014b, MNRAS, 445, 2794

Veras D., Shannon A., Gänsicke B. T., 2014c, MNRAS, 445, 4175

Veras D., Eggl S., Gänsicke B. T., 2015, MNRAS, 452, 1945

Veras D., Mustill A. J., Gänsicke B. T., Redfield S., Georgakarakos N., Bowler A. B., Lloyd M. J. S., 2016a, MNRAS, 458, 3942

Veras D., Marsh T. R., Gänsicke B. T., 2016b, MNRAS, 461, 1413

Veras D., Carter P. J., Leinhardt Z. M., Gänsicke B. T., 2017a, MNRAS, 465, 1008

Veras D., Georgakarakos N., Dobbs-Dixon I., Gänsicke B. T., 2017b, MNRAS, 465, 2053

Vornanen T., Berdyugina S. V., Berdyugin A., 2013, A&A, 557, A38

Walkup R., Stewart B., Pritchard D. E., 1984, Phys. Rev. A, 29, 169

Wehrse R., Liebert J., 1980, A&A, 86, 139

Weidemann V., 1958, PASP, 70, 466

Weidemann V., 1960, ApJ, 131, 638

Wendell C. E., van Horn H. M., Sargent D., 1987, ApJ, 313, 284

Wesemael F., 1979, A&A, 72, 104

Wesemael F., Truran J. W., 1982, apj, 260, 807

Wickramasinghe D. T., Ferrario L., 2000, Magnetism in Isolated and Binary White Dwarfs

Wilson T. L., Matteucci F., 1992, A&AR, 4, 1

Wilson D. J., Gänsicke B. T., Koester D., Raddi R., Breedt E., Southworth J., Parsons S. G., 2014, MNRAS, 445, 1878

Wilson D. J., Gänsicke B. T., Koester D., Toloza O., Pala A. F., Breedt E., Parsons S. G., 2015, MNRAS, 451, 3237

Winget D. E., Hansen C. J., Liebert J., van Horn H. M., Fontaine G., Nather R. E., Kepler S. O., Lamb D. Q., 1987, ApJ Lett., 315, L77

Woltjer L., 1964, ApJ, 140, 1309

Wyatt M. C., Farihi J., Pringle J. E., Bonsor A., 2014, MNRAS, 439, 3371

Xu S., Jura M., Klein B., Koester D., Zuckerman B., 2013, ApJ, 766, 132

Xu S., Jura M., Koester D., Klein B., Zuckerman B., 2014, ApJ, 783, 79

Xu S., Jura M., Pantoja B., Klein B., Zuckerman B., Su K. Y. L., Meng H. Y. A., 2015, ApJ Lett., 806, L5

Xu S., Jura M., Dufour P., Zuckerman B., 2016, ApJ Lett., 816, L22

Xu S., Zuckerman B., Dufour P., Young E. D., Klein B., Jura M., 2017, ApJ Lett., 836, L7

Zuckerman B., 2015, in Dufour P., Bergeron P., Fontaine G., eds, Astronomical Society of the Pacific Conference Series Vol. 493, 19th European Workshop on White Dwarfs. p. 291 (`arXiv:1410.2575`)

Zuckerman B., Becklin E. E., 1987, Nat, 330, 138

Zuckerman B., Reid I. N., 1998, ApJ Lett., 505, L143

Zuckerman B., Koester D., Reid I. N., Hünsch M., 2003, ApJ, 596, 477

Zuckerman B., Koester D., Melis C., Hansen B. M., Jura M., 2007, ApJ, 671, 872

Zuckerman B., Melis C., Klein B., Koester D., Jura M., 2010, ApJ, 722, 725

Zuckerman B., Koester D., Dufour P., Melis C., Klein B., Jura M., 2011, ApJ, 739, 101

del Peloso E. F., da Silva L., Arany-Prado L. I., 2005, A&A, 434, 301

van Horn H. M., 1971, in Luyten W. J., ed., IAU Symposium Vol. 42, White Dwarfs. p. 97

van Lieshout R., Min M., Dominik C., 2014, A&A, 572, A76

van Maanen A., 1917, PASP, 29, 258

van Maanen A., 1920, Contributions from the Mount Wilson Observatory / Carnegie Institution of Washington, 182, 1

von Hippel T., Kuchner M. J., Kilic M., Mullally F., Reach W. T., 2007, ApJ, 662, 544